Chirped Pulse Fourier Transform Microwave Spectroscopy of Nitrogen-Containing Organic Molecules

Evangelia Gougoula

Thesis submitted in partial fulfilment of the requirements for the award of

Doctor of Philosophy

School of Natural & Environmental Sciences (Chemistry)

Newcastle University

Newcastle upon Tyne, UK

October 2020

Supervisors; Dr Nicholas R. Walker and Dr Antonia E. Carruthers

Abstract

Chirped Pulse Fourier Transform Microwave (CP-FTMW) spectroscopy is a powerful analytical technique. Its versatile applications include molecular structure determination, generating molecular rotational signatures for astrochemistry and probing weak inter- and intra-molecular interactions as well as large amplitude motions. For this thesis, experiments were performed with the CP-FTMW Spectrometer at Newcastle University operating in the 2.0-18.5 GHz region, featuring a pulsed valve for supersonic expansion and a laser ablation source for gas-phase generation of non-volatile species.

The microwave spectra of i) phosphine-carboxamide and a van der Waals complex with argon, ii) two monohydrate isomers of imidazole, iii) methylimidazole isomers and iv) monohydrate complexes of methylimidazole isomers are reported and analyzed. Molecular rotations probed in the microwave spectra are directly correlated to the geometry of these species. Detection of isotopologues, in natural isotopic abundance or by using isotopically enriched samples, allows for full or partial structure determination and rationalization of large amplitude motions.

Phosphine-carboxamide is a phosphorus-bearing analogue of urea. Coordination of an argon atom highlights that the electronic density is concentrated at the amide site. The monohydrate complexes of imidazole exhibit bifunctional hydrogen bonds with imidazole acting either as a proton donor or acceptor. The spectra of methylimidazole isomers exhibit internal rotation of the CH_3 group in each isomer. The relative energy required to surmount the barrier to internal rotation in each isomer is relatable to the position where the CH_3 substitutes on the imidazole ring. The barrier depends on the chemical environment and orbital overlap between the CH_3 group and the adjacent C-H bonds. In the monohydrate complexes of methylimidazole only one type of hydrogen bonding was detected and internal rotation of CH_3 group was observed. Results are supported by *ab initio* and density functional theory (DFT) calculations.

Declaration and Copyrights©

I declare that the work presented in this thesis is my own work, except where references to other works have been made. Contributions by other authors, other than myself, are clearly indicated throughout the text. Whole or part of this thesis has not been submitted as part of previous degree to Newcastle University or any other University or Institute. Parts of this thesis have been published to peer reviewed journals or have been presented to conference audience. I declare that this work was carried out following ethical procedures and guidelines.

The copyrights of this thesis rest with the author. No information or quotation from this thesis may be published by anyone who holds a copy of it without the author's written consent. This thesis may be used by Newcastle University Library and may be copied for consultation and informative purposes.

Acknowledgements

First, I want to thank my supervisor Nick Walker for all the support and guidance over the last four years, first as an MChem student in his group and as a PhD student later. I am extremely thankful to him for seeing potential in me and enabling me to achieve things I never thought I would be capable of. Your always positive perspective on science, even when experiments did not go that well, has been a milestone to become the spectroscopist and person I am today.

Alongside Nick, I also want to thank Tony Legon for bringing in ideas and offering advice throughout my PhD. It has been an honor to work with such dedicated and skilled people.

I am grateful to my parents and sister who have always encouraged and supported me in this journey. Thank you for motivating to move to Newcastle at first place and sticking up for me whenever I needed you.

I am truly thankful to my friend Iago with whom we were also flatmates for the most part of both of our PhDs. It was so helpful to have each other and realize we all go through the same struggles during a PhD. Thank you for making me realize the importance of finding balance between my work and social life.

Special shout out to some very special friends, Liam, John, Su and Johan for always being up for a beer and a chat, during happy days and not so happy days. Special thanks to Abbi, Jayne and Amy with whom I shared our office. You guys have been awesome, and I am so lucky to have had you around. Also, a big thank you goes to everyone in the Chemistry department, in the mechanical and electronic workshops, in the teaching labs, in the reception, all the fellow PhDs, postdocs, MChem students in our lab and people I had the opportunity to work and collaborate with.

Finally, I want to thank my partner and best friend, Chris. You have always been an inspiration and motivation to push myself a step further. Thank you for being part of this.

Contents

List of Tables

List of Figures

Properties of Nuclides

Properties of relevant nuclei reproduced from the IUPAC Green Book.

Atomic number Z	Element symbol	Mass number A	Atomic mass $\frac{m_a}{u}$	Isotopic abundance $100x$	Nuclear spin I	Quadrupole moment $\frac{Q}{fm^2}$
1	H	1	1.00782503207(10)	99.9885(70)	+1/2	
	(D)	2	2.014101777 8(4)	0.0115(70)	+1	+0.286(2)**
	(T)	3*	3.016049277 7(25)		+1/2	
6	C	12	12 (by definition)	98.93(8)	+0	
		13	13.0033548378(10)	1.07(8)	−1/2	
		14*	14.003241989(4)		+0	
7	N	14	14.003074004 8(6)	99.636(20)	+1	+2.001(10)
		15	15.0001088982(7)	0.364(20)	−1/2	
8	O	16	15.99491461956(16)	99.757(16)	+0	
		17	16.99913170(12)	0.038(1)	+5/2	−2.578**
		18	17.9991610(7)	0.205(14)	+0	

12	Mg	24	23.985041700(14)	78.99(4)	+0	
		25	24.98583692(3)	10.00(1)	+5/2	+19.9(2)**
		26	25.982592929(30)	11.01(3)	+0	
15	P	31	30.97376163(20)	100	+1/2	
18	Ar	36	35.967545106(29)	0.3365(30)	+0	
		38	37.9627324(4)	0.0632(5)	+0	
		40	39.962383122 5(29)	99.6003(30)	+0	
29	Cu	63	62.9295975(6)	69.15(15)	−3/2	−21.1(4)**
		65	64.9277895(7)	30.85(15)	−3/2	−19.5(4)

*Asterisk denotes an unstable nuclide (for elements without naturally occurring isotopes it is the most stable nuclide).

** Under quadrupole moment, double asterisk indicates that more than one value is given in the original compilation.

Publications

Molecular geometries and other properties of $H_2O\cdots AgI$ and $H_3N\cdots AgI$ as characterized by rotational spectroscopy and *Ab Initio* calculations; Chris Medcraft, Eva Gougoula, Dror M. Bittner, John Mullaney, Susana Blanco, David P. Tew, Nicholas R. Walker, and Anthony C. Legon, *The Journal of Chemical Physics,* **147**, 234308 (2017)

A chalcogen-bonded complex $H_3N\cdots S{=}C{=}S$ formed by ammonia and carbon disulfide characterized by chirped-pulse broadband microwave spectroscopy; Eva Gougoula, Chris Medcraft, Ibon Alkorta, Nicholas R. Walker, and Anthony C. Legon, *The Journal of Chemical Physics*, **150**, 084307 (2019)

Conformational isomers of *trans*-urocanic acid observed by rotational spectroscopy; Graham A. Cooper, Chris Medcraft, Eva Gougoula, and Nicholas R. Walker, *Physical Chemistry Chemical Physics*, **21**, 9495 (2019)

Barrier to Internal Rotation in Methylimidazole Isomers Determined by Rotational Spectroscopy; Eva Gougoula, Chris Medcraft, Julianne Heitkämper and Nicholas R. Walker, *Journal of Chemical Physics*, **151**, 144301 (2019)

A Chalcogen-Bonded Complex $(CH_3)_3N\cdots S{=}C{=}O$ characterized by Rotational Spectroscopy, Eva Gougoula, Joe A. Moxon, Nicholas R. Walker and Anthony C. Legon, *Chemical Physics Letters*, (2020)

Bifunctional Hydrogen Bonding of Imidazole with Water Explored by Rotational Spectroscopy and DFT Calculations; Eva Gougoula, Daniel J. Cole and Nicholas R. Walker, *Journal of Physical Chemistry A*, **124**, 2649 (2020)

Oral Presentations

Chirped-Pulse Fourier Transform Microwave Spectroscopy; Eva Gougoula and Nicholas R. Walker, Annual Northern Universities Meeting on Chemical Physics, Manchester Metropolitan University, July 2018

Barriers to Internal Rotation and Water/Argon Complex Formation in Methylimidazoles by Broadband Rotational Spectroscopy; Eva Gougoula and Nicholas R. Walker, The University of Nottingham, January 2019

Broadband Rotational Spectroscopy at Newcastle University; Eva Gougoula and Nicholas R. Walker, Newcastle University, May 2019

Barriers to Internal Rotation in Structural Isomers of Methylimidazole; Eva Gougoula, Chris Medcraft, Julianne Heitkämper and Nicholas R. Walker, University of Illinois, June 2018

A chalcogen-bonded complex $H_3N\cdots S{=}C{=}S$ formed by Ammonia and Carbon Disulphide and characterised by Broadband Rotational Spectroscopy; Eva Gougoula, Chris Medcraft, Ibon Alkorta, Nicholas Walker and Anthony C. Legon, University of Illinois, June 2019

Poster Presentations

Broadband Rotational Spectrum of 5-Nitroimidazole and 2-Methyl-5-Nitroimidazole; Eva Gougoula and Nicholas R. Walker, University of Durham, January 2018

Fourier Transform Microwave Spectroscopy at Newcastle University; Eva Gougoula and Nicholas R. Walker, Newcastle University, May 2018

Barriers to Internal Rotation in Methylated Imidazoles Determined by Rotational Spectroscopy; Eva Gougoula and Nicholas R. Walker, Uiversidad del Pais Vasco, September 2018

Chapter 1. Introduction

Observation of light through prisms traces back to the Roman times.[1] The first systematic observations of light, however, only took place in the 17th century when optics technology began to evolve.[2] The idea that white light is comprised by its color components was established with new experiments and improved instrumentation. The main source of light of interest at the time was the sun; soon it was discovered that dark bands exist between the color components of the light emitted by the sun.[3,4] It was later found that chemical elements absorbed light at the position of the dark bands, suggesting that other chemical constituents can absorb light of specific wavelength, too. As technology advanced, invisible light was discovered,[5–7] and the representation of the electromagnetic spectrum as known today was constructed,[8] Quantum mechanical principles were in place to rationalize the observed behavior of light absorbed and emitted by chemical compounds.[9]

The systematic observation of the interaction of electromagnetic radiation emitted or absorbed by matter is known as spectroscopy. Different types of radiation will prompt a different type of response in a molecule, *e.g.* UV light may be absorbed by a molecule and result in fluorescence emission of visible light. Radiation in the 1-300 GHz frequency region, known as microwave (MW) radiation, which is invisible, is associated with molecular rotations.[9] Molecular rotations are directly linked to the molecular structure of the rotating molecule. This makes MW spectroscopy a powerful and sensitive tool in structure determination. The technique is structure specific as it can distinguish between species with the same chemical compositions (*i.e.* methylimidazole isomers,[10] chapter 6), the same molecular weight (imidazole[11] and pyrazole[12], 68 g mol^{-1}) and isotopologues of the same species (^{12}C/^{13}C phosphine carboxamide, chapter 4). Microwave spectroscopy finds applications in molecular structure determination,[13,14] separation of enantiomers,[15–17] study of transient and exotic species,[18] analysis of conformational landscapes,[19,20] monitoring of molecular processes,[21] generation of fingerprint spectra for astrochemistry[22] and benchmarking of quantum chemical calculations.[23]

1.1 Brief History of the technique

The first experiment using MW radiation was conducted by Cleeton and Williams[24] in 1934. The MW spectrum of ammonia was recorded in the 1-4 cm^{-1} region. The inversion vibrational mode of ammonia was probed using a gas cell and a custom-made vacuum magnetron oscillator to generate MW radiation. During WW2 it became necessary to develop more powerful sources of MW radiation as part of radio detection and ranging (RADAR). Klystron sources began to systematically be used in research experiments after WW2 and a series of experiments around ammonia and other molecules were performed.

The need to study transient and short-lived species led to the implementation of supersonic expansion sources. Advances in electronics and vacuum technology in the 1970's made it possible to perform experiments with pulsed supersonic jets containing the gas sample of interest interrogated by pulses of MW radiation. This technique,[25] first used by Ekkers and Flygare, offers the advantage of generating internal temperatures as low as a few Kelvin and shifting the population to low energy rotational states. As a result, these low energy rotational transitions are observed with high intensity. Measuring molecular emissions in the time domain and Fourier transforming to the frequency domain greatly improved the spectral resolution and signal to noise of measured spectra. Supersonic expansion also allows for isolation of complexes and clusters that are stable at low temperatures but dissociate at room temperature, and as such makes them accessible to study.

Balle and Flygare introduced a spectrometer[26] utilizing pulsed supersonic expansion and MW radiation. MW pulses broadcast into a resonant Fabry-Perot cavity and polarize the molecular ensemble in the supersonic jet. The main limitation of that spectrometer is the bandwidth (~ 1 MHz) that can be scanned at once. In 2008, the Chirped Pulse Fourier transform microwave (CP-FTMW) spectrometer was a breakthrough in the field.[27] The spectrometer features an arbitrary waveform generator (AWG) which directly creates chirped MW pulses and allows large bandwidths up to 12 GHz to be scanned at a single spectral acquisition. Travelling wave tube (TWT) amplifiers provide sufficient power to polarize across the entire bandwidth with few losses. The CP-FTMW spectrometer at Newcastle University is based on that design and operates in the 2.0-18.5 GHz frequency range. More information on this design will be given in chapter 3.

Given that microwave spectroscopy is a gas phase technique, the need to study non-volatile molecules made it necessary to reconsider the available experimental methods for gas

phase generation. In the 1950's, ovens were used to generate vapor of species containing refractory metals,[28] Heated reservoirs[29] before or right after the pulse valve, allow relatively large molecules to get into the gas phase. This technique requires the molecule of interest to be placed into a reservoir and whilst heated, the carrier gas passes over and seeds the vapor toward the pulse valve. However, this method may not be suitable for biomolecules as they tend to decompose even at low temperatures (50-60 ˚C) and metals or other solids with high melting points. As an alternative, laser vaporization methods[18,30,31] may be used that allow rapid gas phase generation of molecules from a solid target without destroying the molecular structure. Pulsed Nd:YAG lasers are the most common ones used for this purpose and there is a number of spectrometers around the world that use this technique. Laser vaporization has allowed for observation of metal containing clusters,[18] study of aminoacids[32,33] and other biomolecules,[11,31,34] weakly bound complexes between biomolecules and other smaller molecules[35,36] and formation of exotic species[37] like C_{60}.

1.2 Astrochemistry

Historically, space exploration has always been intriguing and the first observations of stellar objects date thousands of years back. In the 1860's, light emitted by stars revealed that the same elements found on the Earth are also components in stellar regions. The extreme conditions of interstellar space led scientists to believe that atomic elements would be the only species that could survive those environments of ionizing radiation and low temperature. Radioastronomy is a theme that emerged in 1970's and has been a breakthrough to our understanding of space and its complexity. The first molecule to be discovered in the interstellar medium (ISM) was the $CH^{\cdot}$ radical,[38] detected through an electronic transition at 430 nm (700 THz). More than 200 molecules have been detected in the ISM, with that number increasing every year; most of these molecules were detected by means of their microwave spectra. The first detection of a polyatomic molecule in the ISM was in 1968 by Cheung and co-workers,[39] The team discovered ammonia by detection of its microwave spectrum coming from the center of the galaxy.

A crucial part of the process of detecting molecules in the ISM is the generation and understanding of high-quality, microwave molecular laboratory spectra. These spectra are the molecular fingerprints and will drive the assignment of lines measured by radio-telescopes to the correct molecular carrier. Observation of rotational spectral features of a molecular carrier will lead to unambiguous assignment and confirm its presence in a given interstellar environment. Recent detections are concerned with benzonitrile[40] and urea.[41] Benzonitrile is the first aromatic molecule to be detected in the ISM, and its detection supports the assumption that polyaromatic hydrocarbons (PAH's) are abundant in space. Generally, it is thought that diffuse interstellar bands[42] are due to PAH's, however, a definite and explicit assignment is challenging. Detecting PAH's *via* their MW spectrum has so far been unsuccessful due to their low electric dipole moment. Urea was only recently confirmed after tentative and inconclusive assignments.[43] Given the importance of urea in biological systems, its discovery in space gives an insight into life formation on earth.

In a typical astronomical measurement, spectral features that remain unassigned are usually present. A challenge that astronomers are faced with when it comes to these features is the lack of laboratory spectroscopic data of the corresponding molecular carriers that may give rise to these features. Simulating the extreme environments of interstellar space with low temperature and low or high density is also challenging for laboratory

molecular spectroscopists. Exploiting techniques like the electrical discharge source used in Hamburg in conjunction with a millimeter-wave spectrometer[44] and laser vaporization techniques like at Newcastle University may allow for simulation of conditions suitable for ion-neutral or neutral-neutral reactions and potentially identify new candidate molecules.

The microwave spectrum of laser vaporized phosphine carboxamide,[45] a phosphorus analogue of urea, is discussed in chapter 4. Considering the recent discovery of urea, this molecule may be a potential candidate molecule for interstellar detection. A total of six phosphorus-containing molecules have been detected in space. It is unclear where the phosphorus reservoirs in the ISM are and as such limited information is available on the gas phase chemistry of phosphorus. A remarkable example of the unknown and unexpected chemistry of phosphorus is the recent discovery of phosphine gas in the middle atmosphere of Venus by means of its rotational spectrum.[46] On Earth, phosphine is entirely associated with biological and anthropogenic activity and other pathways for its formation would likely require high pressures and temperatures and high concentration of H_2. The middle atmosphere of Venus does not fulfill these conditions and presence of phosphine suggests it is formed *via* pathways that have not been considered or *via* biotic mechanisms. Chapter 4 of this thesis is the beginning of the exploration of organo-phosphorus chemistry in the gas phase. Broadband rotational spectra that extend into the millimeter-wave region may identify reaction products and shed some light on the rich and complex chemistry of phosphorus in the gas phase.

1.3 Hydrogen Bonding of Biomolecules (Microsolvation)

The structure of a biomolecule is strongly linked to its properties and biochemical activity. Distinct chemical sites will favor formation of certain intermolecular interactions, the most common one being hydrogen bonding.[47] Molecules such as amino acids are expected to interact with other molecules like water and other biomolecules in the body. Understanding how larger systems like proteins and lipids interact (conformational and bonding preferences) can be challenging. It is therefore important to establish good understanding around fundamental preferences in bonding and activity by studying the "building blocks" of these larger systems, *i.e.* imidazole is the building block of histidine,[31] histamine,[48] adenine,[34] and various synthetic drugs.[49-52]

The first studies of intermolecular hydrogen bonds were conducted in the 1970's. The detection of the water dimer[53] was one of them and it was significant to establish the donor-acceptor properties of water on a macroscopic scale by probing an isolated neutral cluster. Since then, larger clusters of pure water[13,54-59] have been detected by means of gas phase rotational spectroscopy. The fact that water is abundant and essential for life formation steered research to the direction of exploring gas phase metal-water complexes as well as weakly bound complexes between water and biomolecules. Experiments identified complexes between water and metal halides[18,60,61] and ion metal monohydrates.[62]

MW spectroscopy has been concerned with this field for many years, offering an insight into structure and bonding properties by probing the neutral molecules in an environment free of solvent and lattice effects. This is particularly useful considering that other spectroscopic methods like mass spectrometry and IR dissociation spectroscopy are concerned with the corresponding ion of the molecule of interest. For biomolecules, the surrounding aqueous environment may have a crucial influence on the molecular structure and functionality. This is the so-called solution phase and the molecular behavior in solution may be correlated to the gas phase behavior by means of MW spectroscopy and supersonic expansion methods. Microsolvated complexes of biomolecules,[21,63-65] *i.e.* incrementally encapsulating a solute by solvent molecules, may be formed and probed in a supersonic expansion when both molecules of interest are present. MW spectroscopy is able to detect subtle changes in the structure of the biomolecule induced by attachment of one or more water molecules[66] and *vice versa*; perturbation in the hydrogen bond network formed between the water molecules induced by the biomolecule.

Formamide is a molecule that can form similar hydrogen bonds as those between amino acids in the backbone of proteins and water. The progressive microsolvation of formamide in the gas phase has been studied with rotational spectroscopy to help understand the effects of intermolecular interactions on protein folding, molecular shape, and conformational equilibrium. Various isomers of the monohydrate of formamide were identified. It was shown that the isomer where cooperative hydrogen bonding leads to a pseudo six-membered ring between the carbonyl and amine sites of formamide and water is the most stable one. The water molecule can act both as a proton donor and acceptor by forming hydrogen bonds through the hydrogen and oxygen atoms, respectively. Incrementally adding water molecules to the microsolvated clusters of formamide (formamide-$(H_2O)_n$, n=1,2,3) was shown to result in stronger hydrogen bonds between the oxygen of the carbonyl of formamide and the hydrogen of a water molecule. Similar bond shortening was observed for the amine site too.

The cooperative hydrogen bonding as well as the bifunctional character of water in forming hydrogen bonds will be discussed in chapter 5 in the context of hydrogen bonded complexes between imidazole and water. A previous study with FT-IR spectroscopy in helium identified one isomer of a complex between imidazole and water[67] in which the water molecule is the hydrogen bond donor. An IR laser spectroscopy study in helium droplets detected two isomers of a water-imidazole complex,[68] one of them being common in both studies and one where the water is the hydrogen bond acceptor. The bonding manner was identified in both studies; however, due to the limitations of these methods, a precise insight into the length of the hydrogen bond and the orientation of the two molecules with respect to each other is not given. Structural parameters of those complexes are determined directly from the MW spectra of those isomers and discussed in chapter 5. Monohydrates of various five-membered heteroaromatic rings will also be discussed in chapter 5.

Probing the initial steps of the microsolvation of a biomolecule is not always straight-forward and the majority of studies have been concerned with one, two or three water molecules. However, the first steps of microsolvation in the gas phase will not necessarily give an insight into the structure and function of a microsolvated molecule in the solution phase. Incremental addition of water molecules to a microsolvated cluster is crucial but can be challenging and at risk of compromising the information that can be derived from the rotational structure (rotational resolution may collapse as cluster becomes heavier).

1.4 Internal Motions

MW spectroscopy has been an invaluable tool in studying internal motions in molecules and complexes. The internal motions this thesis will be concerned with are internal rotation of CH_3 groups attached to a molecular framework[69-71] (*i.e. N*-methylimidazole, chapter 6) and large amplitude motions (LAM) in the water molecule attached to biomolecules[72,73] (*i.e.* water···imidazole, chapter 5). Internal motions can couple with the overall molecular rotation and cause certain effects in the MW molecular spectra of a species. Typically, rotational transitions will be split into fine sub-components. The energy difference of these components is sensitive to the potential hindering barrier to the internal motion. It is possible to observed and evaluate these effects with CP-FTMW spectroscopy and thermodynamic methods.[9] The latter are suitable for molecules with high barriers in the range of 1000 cm^{-1} and molecules with no dipole moment. However, this is beyond the scope of this thesis and will not be discussed further.

Probing and understanding internal motions in a molecule or complex may give an insight into its structure and the nature of the intra- and inter-molecular interactions, respectively. For example, internal motions at the water subunit of the water-imidazole complex in chapter 5 are manifested as splitting of the rotational transitions indicating a change in the moment of inertia and mass distribution within the complex. Likewise, evaluating barriers to internal rotation of CH_3 groups may indicate conformational trends. A good example is the study of thioacetic acid.[74] A correlation between the barrier to internal rotation the *syn-/anti-* conformation of the O-H group was reported where the barrier to internal rotation for the latter is approximately 5 times higher than that for the former. Studies have also reported the variation of the barrier to internal rotation in isomers of *i.e.* methylindole[75,76] and methylisooxazole.[77,78] This variation may be expressed as a function of repulsive and attractive interactions between the CH_3 group and the asymmetric molecular framework and the degree of aromaticity. Finally, obtaining experimental values for barriers to internal rotation is a way to benchmark and improve the performance of quantum chemical models.

Internal rotation is addressed in chapter 6 in methylimidazole isomers. A correlation between the barrier to internal rotation of the CH_3 group and the position on which it substitutes on the imidazole ring was observed. These findings are consistent with studies on other methylated five-membered heteroaromatic rings like methylpyrrole,[79,80] methythiazole[81-83] and methyloxazole.[69] It is observed that the heteroatoms in the ring will

dominate the magnitude of the relative barriers to internal rotation and some staggering variations are seen between equivalent isomers of the different methyl-azoles, *e.g.* 2-methylthiazole ($V_3 = 35$ cm^{-1}), 2-methylimidazole ($V_3 = 123$ cm^{-1}), methyloxazole ($V_3 = 252$ cm^{-1}). In chapter 7, internal rotation in methylimidazole isomers is approached in the context of water attachment and hydrogen bond formation. To our best knowledge, this is the first comparative study of monohydrates of methylated heteroaromatic five-membered rings. The broad trend that was reported for the methylimidazole monomers is also observed for the monohydrates, however, attachment of water hinders internal rotation in 2-methylimidazole while the opposite effect is observed in *N*-methylimidazole.

1.5 Thesis Overview

This thesis will be concerned with microwave spectroscopy of non-volatile, organic molecules containing one or two nitrogen atoms. The first molecule to be discussed (chapter 4) is phosphine carboxamide,[45] a phosphorus containing analogue of urea. Laser ablation was used to bring phosphine carboxamide into the gas phase and record its microwave spectrum in the 7.0-18.5 GHz frequency range with the CP-FTMW spectrometer at Newcastle University. A van der Waals complex between phosphine carboxamide and argon, which serves as the carrier gas, was also formed and its spectrum was recorded (chapter 4). Imidazole[11] is an alkaloid featured in many drugs and the building block of adenine,[34] histamine,[48] and histidine.[31] Laser ablated imidazole formed hydrogen bonded complexes with water (chapter 5) and the internal dynamics and bonding patterns a of these complexes are discussed. Functionalizing imidazole with, for example, a methyl group results in molecules with modified physical and chemical properties. The microwave spectra of methylimidazole isomers (chapter 6) are discussed and an insight into the internal rotation dynamics of the methyl group is given. Both heating and laser ablation methods were used individually to introduce a specific methylimidazole isomer into the gas phase. The monohydrate complexes of methylimidazole (chapter 7) are reported and the barriers to internal rotation are evaluated as a function of hydrogen bond formation after attachment of water to the respective methylimidazole monomer.

1.6 References

1 D. Plantzos, Crystals and Lenses in the Graeco-Roman World, *Am. J. Archaeol.*, 1997, **101**, 451–464.

2 P. Fara, Newton shows the light: a commentary on Newton (1672) 'A letter … containing his new theory about light and colours…', *Philos. Trans. R. Soc. A Math. Phys. Eng. Sci.*, 2015, **373**, 20140213.

3 D. Brewster, XVII. Observations on the Lines of the Solar Spectrum, and on those produced by the Earth's Atmosphere, and by the action of Nitrous Acid Gas, *Trans. R. Soc. Edinburgh*, 1834, **12**, 519–530.

4 D. Brewster and J. H. Gladstone, IX. On the lines of the solar spectrum, *Philos. Trans. R. Soc. London*, 1860, **150**, 149–160.

5 W. C. Röntgen, On a new kind of rays, *Nature*, 1896, **53**, 274–276.

6 E. F. J. Ring, The discovery of infrared radiation in 1800, *Imaging Sci. J.*, 2000, **48**, 1–8.

7 L. Gerward, Paul Villard and his Discovery of Gamma Rays, *Phys. Perspect.*, 1999, **1**, 367–383.

8 A. Aspect, From Huygens' waves to Einstein's photons: Weird light, *Comptes Rendus Phys.*, 2017, **18**, 498–503.

9 W. Gordy and R. L. Cook, *Microwave molecular spectra*, John Wiley & Sons, Ltd, New York, 3rd., 1984.

10 E. Gougoula, C. Medcraft, J. Heitkämper and N. R. Walker, Barriers to internal rotation in methylimidazole isomers determined by rotational spectroscopy, *J. Chem. Phys.*, 2019, **151**, 144301.

11 D. Christen, J. H. Griffiths and J. Sheridan, The Microwave Spectrum of Imidazole; Complete Structure and the Electron Distribution from Nuclear Quadrupole Coupling Tensors and Dipole Moment Orientation, *Zeitschrift fur Naturforsch. - Sect. A J. Phys. Sci.*, 1981, **36**, 1378–1385.

12 W. H. Kirchhoff, The Microwave Spectrum and Dipole Moment of Pyrazole, *J. Am. Chem. Soc.*, 1967, **89**, 1312–1316.

13 C. Pérez, S. Lobsiger, N. A. Seifert, D. P. Zaleski, B. Temelso, G. C. Shields, Z. Kisiel and B. H. Pate, Broadband Fourier transform rotational spectroscopy for structure determination: The water heptamer, *Chem. Phys. Lett.*, 2013, **571**, 1–15.

14 K. Inoue, N. Kuze, M. Tanabe, H. Takeuchi, T. Egawa and S. Konaka, Determination of the molecular structure of γ-picoline in the gas phase and in liquid crystal solvents, *J. Mol. Struct.*, 1997, **413–414**, 81–91.

15 D. Patterson, M. Schnell and J. M. Doyle, Enantiomer specific detection of chiral molecules via microwave spectroscopy, *Nature*, 2012, **497**, 1–11.

16 S. R. Domingos, C. Pérez and M. Schnell, Sensing Chirality with Rotational Spectroscopy, *Annu. Rev. Phys. Chem.*, 2018, **69**, 499–519.

17 M. D. Marshall, H. O. Leung, K. Wang and M. D. Acha, Microwave Spectrum and Molecular Structure of the Chiral Tagging Candidate, 3,3,3-Trifluoro-1,2-epoxypropane and Its Complex with the Argon Atom, *J. Phys. Chem. A*, 2018, **122**, 4670–4680.

18 C. Medcraft, E. Gougoula, D. M. Bittner, J. C. Mullaney, S. Blanco, D. P. Tew, N. R. Walker and A. C. Legon, Molecular geometries and other properties of H2O···AgI and H3N···AgI as characterised by rotational spectroscopy and *ab initio* calculations, *J. Chem. Phys.*, 2017, **147**, DOI:10.1063/1.5008744.

19 E. Burevschi, I. Penã and M. E. Sanz, Medium-sized rings: Conformational preferences in cyclooctanone driven by transannular repulsive interactions, *Phys. Chem. Chem. Phys.*, 2019, **21**, 4331–4338.

20 S. R. Domingos, C. Pérez, C. Medcraft, P. Pinacho and M. Schnell, Flexibility unleashed in acyclic monoterpenes: Conformational space of citronellal revealed by broadband rotational spectroscopy, *Phys. Chem. Chem. Phys.*, 2016, **18**, 16682–16689.

21 S. Blanco, J. C. López, A. Lesarri and J. L. Alonso, Microsolvation of Formamide: A Rotational Study, *J. Am. Chem. Soc.*, 2006, **128**, 12111–12121.

22 H. S. P. Müller, B. J. Drouin, J. C. Pearson, M. H. Ordu, N. Wehres and F. Lewen, Rotational spectra of isotopic species of methyl cyanide, CH_3CN, in their $v_8 = 1$ excited vibrational states, *Astron. Astrophys.*, 2016, **586**, DOI:10.1051/0004-6361/201527602.

23 N. Marom, A. Tkatchenko, M. Rossi, V. V. Gobre, O. Hod, M. Scheffler and L. Kronik, Dispersion interactions with density-functional theory: Benchmarking semiempirical and interatomic pairwise corrected density functionals, *J. Chem. Theory Comput.*, 2011, **7**, 3944–3951.

24 C. E. Cleeton and N. H. Williams, Electromagnetic waves of 1.1 cm wave-length and the absorption spectrum of ammonia, *Phys. Rev.*, 1934, **45**, 234–237.

25 J. Ekkers and W. H. Flygare, Pulsed microwave Fourier transform spectrometer, *Rev. Sci. Instrum.*, 1976, **47**, 448–454.

26 T. J. Balle and W. H. Flygare, Fabry-Perot cavity pulsed Fourier transform microwave spectrometer with a pulsed nozzle particle source, *Rev. Sci. Instrum.*, 1981, **52**, 33–45.

27 G. G. Brown, B. C. Dian, K. O. Douglass, S. M. Geyer, S. T. Shipman and B. H. Pate, A broadband Fourier transform microwave spectrometer based on chirped pulse excitation, *Rev. Sci. Instrum.*, 2008, **79**, 53103.

28 M. L. Stitch, A. Honig and C. H. Townes, Microwave Spectroscopy at High Temperature-Spectra of CsCl and NaCl, *Phys. Rev.*, 1952, **86**, 813–814.

29 D. Loru, M. A. Bermúdez and M. E. Sanz, Structure of fenchone by broadband rotational spectroscopy, *J. Chem. Phys.*, 2016, **145**, 74311.

30 Y. Ohshima, Fourier-transform microwave spectroscopy of $^{24}Mg^{35}Cl$ generated by laser ablation, *Chem. Phys. Lett.*, 1993, **213**, 95–100.

31 C. Bermúdez, S. Mata, C. Cabezas and J. L. Alonso, Tautomerism in Neutral Histidine, *Angew. Chemie - Int. Ed.*, 2014, **53**, 11015–11018.

32 E. J. Cocinero, A. Lesarri, J. U. Grabow, J. C. López and J. L. Alonso, The shape of leucine in the gas phase, *ChemPhysChem*, 2007, **8**, 599–604.

33 A. Lesarri, S. Mata, E. J. Cocinero, S. Blanco, J. C. López and J. L. Alonso, The Structure of Neutral Proline, *Angew. Chemie Int. Ed.*, 2002, **41**, 4673–4676.

34 R. D. Brown, P. D. Godfrey, D. McNaughton and A. P. Pierlot, A study of the major gas-phase tautomer of adenine by microwave spectroscopy, *Chem. Phys. Lett.*, 1989, **156**, 61–63.

35 J. C. Mullaney, D. P. Zaleski, D. P. Tew, N. R. Walker and A. C. Legon, Geometry of an Isolated Dimer of Imidazole Characterised by Rotational Spectroscopy and *Ab Initio* Calculations, *ChemPhysChem*, 2016, **17**, 1154–1158.

36 J. C. Mullaney, C. Medcraft, D. P. Tew, L. Lewis-Borrell, B. T. Golding, N. R. Walker and A. C. Legon, Cooperative hydrogen bonds form a pseudocycle stabilizing an isolated complex of isocyanic acid with urea, *Phys. Chem. Chem. Phys.*, 2017, **19**, 25080–25085.

37 H. W. Kroto, J. R. Heath, S. C. O'Brien, R. F. Curl and R. E. Smalley, C60: Buckminsterfullerene, *Nature*, 1985, **318**, 162–163.

38 O. E. H. Rydbeck, J. Elldér and W. M. Irvine, Radio detection of interstellar CH, *Nature*, 1973, **246**, 466–468.

39 A. C. Cheung, D. M. Rank, C. H. Townes, D. D. Thornton and W. J. Welch, Detection of NH_3 molecules in the interstellar medium by their microwave emission, *Phys. Rev. Lett.*, 1968, **21**, 1701–1705.

40 B. A. McGuire, A. M. Burkhardt, S. Kalenskii, C. N. Shingledecker, A. J. Remijan, E. Herbst and M. C. McCarthy, Detection of the aromatic molecule benzonitrile (c-C_6H_5CN) in the interstellar medium, *Science*, 2018, **359**, 202–205.

41 A. Belloche, R. T. Garrod, H. S. P. Müller, K. M. Menten, I. Medvedev, J. Thomas and Z. Kisiel, Re-exploring Molecular Complexity with ALMA (ReMoCA): interstellar detection of urea, *A&A*, 2019, **628**

42

43 I. Fourré, L. Rosset, H. Chevreau and Y. Ellinger, About the detection of urea in the interstellar medium: the energetic aspect, *A&A*, 2016, **589**

44 B. E. Arenas, S. Gruet, A. L. Steber, B. M. Giuliano and M. Schnell, Chirped-pulse Fourier transform millimeter-wave spectroscopy of ten vibrationally excited states of i-propyl cyanide: exploring the far-infrared region, *Phys. Chem. Chem. Phys.*, 2017, **19**, 1751–1756.

45 A. R. Jupp and J. M. Goicoechea, Phosphinecarboxamide: A Phosphorus-Containing Analogue of Urea and Stable Primary Phosphine, *J. Am. Chem. Soc.*, 2013, **135**, 19131–19134.

46 J. S. Greaves, A. M. S. Richards, W. Bains, P. B. Rimmer, H. Sagawa, D. L. Clements, S. Seager, J. J. Petkowski, C. Sousa-Silva, S. Ranjan, E. Drabek-Maunder, H. J. Fraser, A. Cartwright, I. Mueller-Wodarg, Z. Zhan, P. Friberg, I. Coulson, E. Lee and J. Hoge, Phosphine gas in the cloud decks of Venus, *Nat. Astron.*, 2020, DOI:10.1038/s41550-020-1174-4.

47 S. Gruet, C. Pérez, A. L. Steber and M. Schnell, Where's water? The many binding sites of hydantoin, *Phys. Chem. Chem. Phys.*, 2018, **20**, 5545–5552.

48 B. Vogelsanger, P. D. Godfrey and R. D. Brown, Rotational spectra of biomolecules: histamine, *J. Am. Chem. Soc.*, 1991, **113**, 7864–7869.

49 H. Takahashi, M. Abe, T. Sugawara, K. Tanaka, Y. Saito, S. Fujimura, M. Shibuya and Y. Sato, Clotrimazole, an imidazole antimycotic, is a potent inhibitor of angiogenesis, *Japanese J. Cancer Res.*, 1998, **89**, 445–451.

50 Beena, N. Kumar, R. K. Rohilla, N. Roy and D. S. Rawat, Synthesis and antibacterial activity evaluation of metronidazole-triazole conjugates, *Bioorganic Med. Chem. Lett.*, 2009, **19**, 1396–1398.

51 M. Garner, D. R. Armstrong, J. Reglinski, W. E. Smith, R. Wilson and J. H. McKillop, The structure of methimazole and its consequences for current therapeutic models of graves' disease., *Bioorganic Med. Chem. Lett.*, 1994, **4**, 1357–1360.

52 S. Ganguly, V. V. Vithlani, A. K. Kesharwani, R. Kuhu, L. Baskar, P. Mitramazumder, A. Sharon and A. Dev, Synthesis, antibacterial and potential anti-HIV activity of some novel imidazole analogs, *Acta Pharm.*, 2011, **61**, 187–201.

53 T. R. Dyke and J. S. Muenter, Microwave spectrum and structure of hydrogen bonded water dimer, *J. Chem. Phys.*, 1974, **60**, 2929–2930.

54 M. R. Viant, J. D. Cruzan, D. D. Lucas, M. G. Brown, K. Liu and R. J. Saykally, Pseudorotation in Water Trimer Isotopomers Using Terahertz Laser Spectroscopy, *J. Phys. Chem. A*, 1997, **101**, 9032–9041.

55 J. D. Cruzan, M. R. Viant, M. G. Brown and R. J. Saykally, Terahertz Laser Vibration−Rotation Tunneling Spectroscopy of the Water Tetramer, *J. Phys. Chem. A*, 1997, **101**, 9022–9031.

56 K. Liu, M. G. Brown, J. D. Cruzan and R. J. Saykally, Terahertz Laser Spectroscopy of the Water Pentamer: Structure and Hydrogen Bond Rearrangement Dynamics, *J. Phys. Chem. A*, 1997, **101**, 9011–9021.

57 C. Pérez, M. T. Muckle, D. P. Zaleski, N. A. Seifert, B. Temelso, G. C. Shields, Z. Kisiel and B. H. Pate, Structures of cage, prism, and book isomers of water hexamer from broadband rotational spectroscopy, *Science (80-.).*, 2012, **336**, 897–901.

58 W. T. S. Cole, J. D. Farrell, D. J. Wales and R. J. Saykally, Structure and torsional dynamics of the water octamer from THz laser spectroscopy near 215 μm, *Science (80-.).*, 2016, **352**, 1194 LP-1197.

59 C. Pérez, D. P. Zaleski, N. A. Seifert, B. Temelso, G. C. Shields, Z. Kisiel and B. H. Pate, Hydrogen Bond Cooperativity and the Three-Dimensional Structures of Water Nonamers and Decamers, *Angew. Chemie Int. Ed.*, 2014, **53**, 14368–14372.

60 V. A. Mikhailov, F. J. Roberts, S. L. Stephens, S. J. Harris, D. P. Tew, J. N. Harvey, N. R. Walker and A. C. Legon, Monohydrates of cuprous chloride and argentous chloride: H2O···CuCl and H2O···AgCl characterized by rotational spectroscopy and ab initio calculations, *J. Chem. Phys.*, 2011, **134**, 134305.

61 S. L. Stephens, D. P. Tew, N. R. Walker and A. C. Legon, Monohydrate of argentous fluoride: H2O···AgF characterised by rotational spectroscopy and ab initio calculations, *J. Mol. Spectrosc.*, 2011, **267**, 163–168.

62 N. R. Walker, R. S. Walters, E. D. Pillai and M. A. Duncan, Infrared spectroscopy of V+(H2O) and V+(D2O) complexes: Solvent deformation and an incipient reaction, *J. Chem. Phys.*, 2003, **119**, 10471–10474.

63 P. Pinacho, A. Krin, C. Pérez, S. Zinn, J. C. López, S. Blanco and M. Schnell, Microsolvated complexes of ibuprofen as revealed by high-resolution rotational spectroscopy, *Phys. Chem. Chem. Phys.*, 2018, **20**, 15635–15640.

64 P. Pinacho, J. C. López, Z. Kisiel and S. Blanco, Microsolvation of ethyl carbamate conformers: effect of carrier gas on the formation of complexes, *Phys. Chem. Chem. Phys.*, 2020, **22**, 18351–18360.

65 P. Pinacho, S. Blanco and J. C. López, The complete conformational panorama of formanilide-water complexes: The role of water as a conformational switch, *Phys. Chem. Chem. Phys.*, 2019, **21**, 2177–2185.

66 E. G. Schnitzler, N. A. Seifert, S. Ghosh, J. Thomas, Y. Xu and W. Jäger, Hydration of the simplest α-keto acid: a rotational spectroscopic and ab initio study of the pyruvic acid–water complex, *Phys. Chem. Chem. Phys.*, 2017, **19**, 4440–4446.

67 J. Zischang, J. J. Lee and M. A. Suhm, Communication: Where does the first water molecule go in imidazole?, *J. Chem. Phys.*, 2011, **135**, 61102.

68 M. Y. Choi and R. E. Miller, Infrared laser spectroscopy of imidazole complexes in helium nanodroplets: Monomer, dimer, and binary water complexes, *J. Phys. Chem. A*, 2006, **110**, 9344–9351.

69 E. Fliege, H. Dreizler, M. Meyer, K. Iqbal and J. Sheridan, 14N Nuclear Quadrupole Coupling and Methyl Internal Rotation of 2-, 4-, and 5-Methyl Oxazole, *Zeitschrift fur Naturforsch. - Sect. A J. Phys. Sci.*, 1986, **41**, 623–636.

70 T. Ogata and K. Kozima, Microwave spectrum, barrier height to internal rotation of methyl group of 3-methylthiophene, and dipole moments of 3-methylthiophene and thiophene, *J. Mol. Spectrosc.*, 1972, **42**, 38–46.

71 S. Huber, T. K. Ha and A. Bauder, Microwave spectra of isotopic N-methylpyrroles, quadrupole coupling constants and substitution structure, *J. Mol. Struct.*, 1997, **413–414**, 93–100.

72 S. Blanco, J. C. Lopez, J. L. Alonso, P. Ottaviani and W. Caminάti, Pure rotational spectrum and model calculations of indole–water, *J. Chem. Phys.*, 2003, **119**, 880–886.

73 R. B. Mackenzie, C. T. Dewberry, R. D. Cornelius, C. J. Smith and K. R. Leopold, Multidimensional large amplitude dynamics in the pyridine-water complex, *J. Phys. Chem. A*, 2017, **121**, 855–860.

74 C. J. Smith, A. K. Huff, H. Zhang, Y. Mo and K. R. Leopold, A strong dependence of the CH3 internal rotation barrier on conformation in thioacetic acid: Microwave measurements and an energy decomposition analysis, *J. Chem. Phys.*, 2019, **150**, 134302.

75 R. M. Gurusinghe and M. J. Tubergen, Probing the Electronic Environment of Methylindoles using Internal Rotation and 14N Nuclear Quadrupole Coupling, *J. Phys. Chem. A*, 2016, **120**, 3491–3496.

76 D. M. Sammeth, S. S. Siewert, P. R. Callis and L. H. Spangler, Methyl rotor effects in 3- and 5-methylindole, *J. Phys. Chem.*, 1992, **96**, 5771–5778.

77 E. Fliege, H. Dreizler, J. Sheridan and C. T. Walls, Internal rotation and 14N quadrupole coupling of 3- and 5-methylisoxazole, *J. Mol. Spectrosc.*, 1985, **113**, 362–372.

78 P. J. Mjöberg, W. M. Ralowski and S. O. Ljunggren, Microwave Spectrum and Barrier to Internal Rotation of 5-Methylisoxazole, *Zeitschrift fur Naturforschung - Sect. A J. Phys. Sci.*, 1975, 30, 1279–1281.

79 T. Nguyen, C. Dindic, W. Stahl, H. V. L. Nguyen and I. Kleiner, 14N Nuclear quadrupole coupling and methyl internal rotation in the microwave spectrum of 2-methylpyrrole, *Mol. Phys.*, 2020, **118**, 1668572.

80 J. Makarewicz, S. Huber, B. Brupbacher-Gatehouse and A. Bauder, Internal rotation dependent quadrupole hyperfine splittings of rotational transitions of N-methylpyrrole, *J. Mol. Struct.*, 2002, **612**, 117–123.

81 J. U. Grabow, H. Hartwig, N. Heineking, W. Jäger, H. Mäder, H. W. Nicolaisen and W. Stahl, The microwave spectrum of 2-methylthiazole: Methyl internal rotation and 14N nuclear quadrupole coupling, *J. Mol. Struct.*, 2002, **612**, 349–356.

82 W. Jäger and H. Mäder, The Microwave Spectrum of 4-Methylthiazole: Methyl Internal Rotation, 14N Nuclear Quadrupole Coupling and Electric Dipole Moment, *Zeitschrift für Naturforsch. A*, 1987, 42, 1405.

83 W. Jäger and H. Mäder, The microwave spectrum of 5-methylthiazole: methyl internal rotation, 14 N nuclear quadrupole coupling and electric dipole moment, *J. Mol. Struct.*, 1988, **190**, 295–305.

Chapter 2. Theory

In this chapter, the fundamental concepts of rotational spectroscopy will be discussed. Both classical and quantum mechanical treatments will be considered, from polarization of rotational transitions with microwave radiation to determination of rotational constants followed by determination of molecular properties. The molecules and complexes considered in this thesis are asymmetric rotors (tops), so only brief insights into the theoretical aspects of other types of rotors will be given. This chapter is based on Gordy and Cook's *Microwave Molecular Spectra*,[1] Hollas' *Modern Spectroscopy*[2] and *High-Resolution Spectroscopy*[3] and Townes and Kroto's *Molecular Rotation Spectra*[4] books. These are representative and authoritative sources regarding the underpinning theory of rotational spectroscopy.

Analysis of a rotational spectrum relies on quantum mechanical principles. Radiation in the 1-300 GHz region is associated with rotational motions of molecules. When a molecule encounters this radiation, a photon will be absorbed if it is resonant with a rotational transition of that molecule. It is required that molecules possess a permanent dipole moment in order to absorb microwave radiation. The energy of a photon (E_p) is quantized and is given by the expression;

$$E_p = hv = h\frac{c}{\lambda} \qquad (Eq.\,2.1)$$

where h is the Planck constant, v and λ are the frequency and wavelength of the light, respectively, and c is the speed of light in vacuum. The experiments in this thesis are concerned with both absorption and emission of microwave light. As it will be described in chapter 3, after the halt of the polarizing radiation that excites molecules from their ground state to higher rotational energy levels, molecular relaxation is detected as a decaying signal in the form of a free induction decay (FID). The advantages of detecting emission instead of absorption of photons have been discussed in the previous chapters.

2.1 Classical Mechanics and Moment of Inertia

Quantum mechanical treatment of molecular rotation emerges from fundamental concepts of classical mechanics. Structure determination methods that will be discussed in section 2.10 evaluate molecular structure from the moments of inertia of a molecule which are derived from measured rotational constants. For any molecule, the moment of inertia about anyaxis going through the center of mass may be expressed by the relationship;

$$I = \sum_i m_i r_i^2 \qquad (Eq.\,2.2)$$

where m_i is any mass point about a given principal axis and r_i is the distance between m_i and the center of mass of the molecule. Conventionally, we define three mutually perpendicular axes labeled as *a*, *b* and *c*. It follows that for each of the *a*-, *b*- and *c*-axes, a corresponding moment of inertia I_{aa}, I_{bb} and I_{cc} may be defined by means of equation 2.2. Conventionally, it holds that $I_{cc} \geq I_{bb} \geq I_{aa}$, meaning that the largest mass distribution is observed about the *c*-axis whereas the minimum mass distribution is found about the *a*-axis, with the *b*-axis being the intermediate case.

According to classical mechanics, the angular momentum of a rigid rotating molecule where each atom is considered a point mass is expressed as;

$$P = \omega \times I \qquad (Eq.\,2.3)$$

where ω is the angular velocity and I is the moment of inertia tensor as defined in equation 2.2. As the rotor undergoes rotation about its center of mass, each point rotates at the same velocity. The moment of inertia may be expressed in terms of the *a*-, *b*- and *c*-axes system as a matrix;

$$I = \begin{pmatrix} I_{aa} & I_{ab} & I_{ac} \\ I_{ba} & I_{bb} & I_{bc} \\ I_{ca} & I_{cb} & I_{cc} \end{pmatrix} \qquad (Eq.\,2.4)$$

The mutually perpendicular *a*-, *b*- and *c*-axes are conventionally placed on the center of mass of the rotating molecule, and so the off-diagonal components vanish, leaving the diagonal components known as the principal moments of inertia. It follows that;

$$I = \begin{pmatrix} I_{aa} & 0 & 0 \\ 0 & I_{bb} & 0 \\ 0 & 0 & I_{cc} \end{pmatrix} \qquad (Eq.\,2.5)$$

The individual moments of inertia are expressed as;

$$I_{aa} = \sum_i m_i(b_i^2 + c_i^2) \qquad (Eq.2.6)$$

$$I_{bb} = \sum_i m_i(a_i^2 + c_i^2) \qquad (Eq.2.7)$$

$$I_{cc} = \sum_i m_i(a_i^2 + b_i^2) \qquad (Eq.2.8)$$

The individual components of angular momentum are noted as;

$$P_a = \omega_{aa} \times I_{aa} \qquad (Eq.2.9)$$

$$P_b = \omega_{bb} \times I_{bb} \qquad (Eq.2.10)$$

$$P_c = \omega_{cc} \times I_{cc} \qquad (Eq.2.11)$$

The rotational kinetic energy in the principal axes system is;

$$E_r = \frac{1}{2}\omega^2 I = \frac{1}{2}\left(\frac{P_a^2}{I_{aa}}\right) + \frac{1}{2}\left(\frac{P_b^2}{I_{bb}}\right) + \frac{1}{2}\left(\frac{P_c^2}{I_{cc}}\right) \qquad (Eq.2.12)$$

When a torque is applied to a molecule, a molecular rotation is induced and the rate of change of the angular momentum is equal to the applied torque. The Euler equations of motion for a freely rotating body with no torque from the external field are;

$$\frac{dP_a}{dt} + \left(\frac{1}{I_{bb}} - \frac{1}{I_{cc}}\right) P_b P_c = 0 \qquad (Eq.2.13)$$

$$\frac{dP_b}{dt} + \left(\frac{1}{I_{cc}} - \frac{1}{I_{aa}}\right) P_c P_a = 0 \qquad (Eq.2.14)$$

$$\frac{dP_c}{dt} + \left(\frac{1}{I_{aa}} - \frac{1}{I_{bb}}\right) P_a P_b = 0 \qquad (Eq.2.15)$$

and it follows from these equations that the total kinetic energy remains constant. For linear and symmetric tops, rotation is constant about the symmetry axis. This condition is not true for asymmetric tops, although the total angular momentum is constant and

independent of the coordinate system it is expressed in. Discrimination of linear, symmetric, and asymmetric tops follows in section 2.2.

2.2 Types of Rotors

2.2.1 Linear Tops

Considering a linear molecule, e.g. AgI, OCS, HCN, it holds that $I_{cc} = I_{bb} > I_{aa} \cong 0$, with the principal axes being mutually perpendicular at the center of mass of AgI, figure 2.1. If the Ag and I atoms are considered as point masses on the a-axis, I_{aa} is very small,

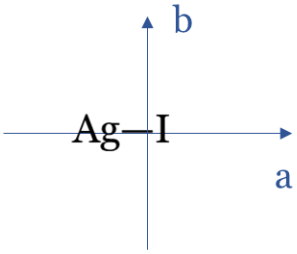

Figure 2.1. The linear diatomic silver iodide (AgI). The a-inertial axis is aligned with the Ag-I bond resulting in a I_{aa} value of effectively zero.

approaching zero.

2.2.2 Symmetric Tops

Symmetric tops may be classified as a prolate or an oblate symmetric top where two of the moments of inertia are equal whilst the third one is non-zero. For a prolate symmetric top, it holds that;

$$I_{cc} = I_{bb} > I_{aa} \qquad (Eq. 2.16)$$

An example of a prolate symmetric top is acetonitrile (methyl cyanide) H_3CCN. The C–C and C–N bonds of the molecule are aligned with the a-inertial axis while the contributions to the I_{aa} made by the C–H bonds are negligible.

Benzene is the prototype example of an oblate symmetric top. It follows that for an oblate symmetric top;

$$I_{aa} = I_{bb} < I_{cc} \qquad (Eq. 2.17)$$

A prerequisite for a molecule to be classed as a symmetric top is that it has a C_n axis where $n > 2$. A C_3 axis is present within acetonitrile which is aligned with the a-inertial axis of the molecule. As for benzene, a C_6 axis is observed through the aromatic plane, aligned with the c-inertial axis.

2.2.3 Asymmetric Tops

In the case of asymmetric tops, all principal inertial components are unequal;

$$I_{cc} \neq I_{bb} \neq I_{cc} \qquad (Eq. 2.18)$$

The majority of asymmetric tops are known as prolate near-symmetric rotors with;

$$I_{cc} \approx I_{bb} > I_{aa} \qquad (Eq. 2.19)$$

An example of prolate near-symmetric rotor is *N*-methylimidazole (chapter 6).

We may also come across molecules such as imidazole (chapter 5) that are classed as oblate near-symmetric tops for which we observe;

$$I_c > I_b \approx I_a \qquad (Eq. 2.20)$$

Any set of *x*, *y*, *z* cartesian axes can be placed on a molecule which may or may not coincide with the principal *a*-, *b*-, and *c*-inertial axes. The most common convention is the I^r representation where (*x, y, z*) ≡ (*a, b, c*). Other possible representations are;

	I^r	II^r	III^r	I^l	II^l	III^l
x	*b*	*c*	*a*	*c*	*a*	*b*
y	*c*	*a*	*b*	*b*	*c*	*a*
z	*a*	*b*	*c*	*a*	*b*	*c*

The representations refer to the axes orientation in the rotational Hamiltonian which will be discussed in the following sections.

2.3 Born-Oppenheimer Approximation

The total energy of a diatomic or polyatomic molecule is the sum of its kinetic T and potential energy V. The kinetic energy includes contributions made by electronic and nuclear motions. Coulombic repulsions between electrons and between nuclei as well as attractive forces between electrons and nuclei, comprise the potential energy. According to the Born-Oppenheimer approximation, electronic and nuclear motions are treated independent of one another because they occur on different timescales. Nuclei are much heavier than electrons so electronic motions are separated from nuclear motions and nuclei are effectively treated as static. Internal motions of a system and their corresponding energies can also be treated separately. The Hamiltonian for a molecular system describes these internal motions and is written as:

$$\hat{\mathrm{H}}_{total} = \hat{\mathrm{H}}_{el} + \hat{\mathrm{H}}_{vib} + \hat{\mathrm{H}}_{rot} + \hat{\mathrm{H}}_{trans} \qquad (Eq.\,2.21)$$

where el: electronic, vib: vibrational, rot: rotational and $trans$: translational the relevant Hamiltonians in the overall Hamiltonian. Likewise, the total wavefunction and eingenvalues that describe a molecular system are expressed as:

$$\psi_{total} = \psi_{el}.\psi_{vib}.\psi_{rot}.\psi_{trans} \qquad (Eq.\,2.22)$$

and

$$E_{total} = E_{el} + E_{vib} + E_{rot} + E_{trans} \qquad (Eq.\,2.23)$$

respectively.

This work will only be concerned with rotational motions for the electronic and vibrational ground state of molecules for which the time-independent Schrödinger equation will be solved. The time-independent equation can only be solved for one-electron atomic systems. The generalized solution for the time-independent equation for a molecular rotor is;

$$\hat{\mathrm{H}}_{rot}\psi_{rot} = E_{rot}\psi_{rot} \qquad (Eq.\,2.24)$$

where ψ_{rot} is the rotational eigenfunction and E_{rot} is the eigenvalues of the Hamiltonian.

A Hamiltonian can be formulated to account for internal and large amplitude motions (LAM). The internal rotation Hamiltonian will be discussed in more detail in section 2.9.

2.4 The Rigid Rotor Approximation

In quantum mechanics, a torque is applied by a resonant photon hv. The classical Hamiltonian represents the total energy of a system and consists of kinetic and potential energy;

$$H = T + V \qquad (Eq. 2.25)$$

where $T = \frac{J^2}{2m}$ and J is the total momentum and m is the mass of the system. It was discussed in section 2.2 that the potential energy is not included in the wavefunction of a rotating molecule. In a molecule with *a*-, *b*-, and *c*-inertial axes, the angular momenta in the rotational Hamiltonian are replaced by their relevant angular momentum operators which are formulated to include $\hbar$, $\hat{P} = -i\hbar\nabla$. The eigenvalues that solve the Hamiltonian operators are the quantized rotational energy levels measured in the microwave spectrum and are specific for a given molecule. The Hamiltonian operator is;

$$\hat{\mathrm{H}}_{rot} = \frac{1}{2}\left(\frac{\hat{P}_a^2}{I_{aa}} + \frac{\hat{P}_b^2}{I_{bb}} + \frac{\hat{P}_c^2}{I_{cc}}\right) \qquad (Eq. 2.26)$$

The case of a simple diatomic performing an end-over-end rotation may be described by the rigid rotor approximation. According to that concept, the two mass point atoms are joined by a weightless, rigid, non-distortable bond. If that bond were to coincide with an inertial axis of that diatomic, *i.e.* the *a*-axis, then the rotation depends on the mass distribution about that axis. The model can extend to polyatomic molecules performing rotations about the *a*-, *b*-, and *c*-inertial axis which are placed on its center of mass. The quantum mechanical rigid rotor Hamiltonian is also expressed as;

$$\hat{\mathrm{H}}_{rot} = A\hat{P}_a^2 + B\hat{P}_b^2 + C\hat{P}_c^2 \qquad (Eq. 2.27)$$

where A, B, and C are the rotational constants specific to each inertial axis and $\hat{P}_a$, $\hat{P}_b$, and $\hat{P}_c$ are the angular momenta operators. For convenience, the rotational constants are expressed in units of h;

$$A = \frac{h}{8\pi^2 I_{aa}},\ B = \frac{h}{8\pi^2 I_{bb}},\ \text{and}\ C = \frac{h}{8\pi^2 I_{cc}} \qquad (Eq. 2.28)$$

where h is the Planck constant and I_{aa}, I_{bb}, and I_{cc} are the principal moment moments of inertia as described in section 2.1. The rotational constant is inversely proportional to the corresponding moment of inertia.

2.5 Ray's Asymmetry Parameter

Ray's asymmetry parameter, κ, provides a measurement of the asymmetry of a molecule by giving a quantitative insight into how far from the prolate or oblate limit it lies. It is defined as;

$$\kappa = \frac{2B - A - C}{A - C} \qquad (Eq.\,2.29)$$

and may take values $-1 \leq \kappa \leq 1$. At the prolate limit, it holds that $\kappa = -1$ and $A > B = C$, whilst for an oblate we have $\kappa = 1$ and $A = B > C$ (figure 2.2). At the intermediate case where $\kappa = 0$, the molecule exhibits the highest degree of asymmetry.

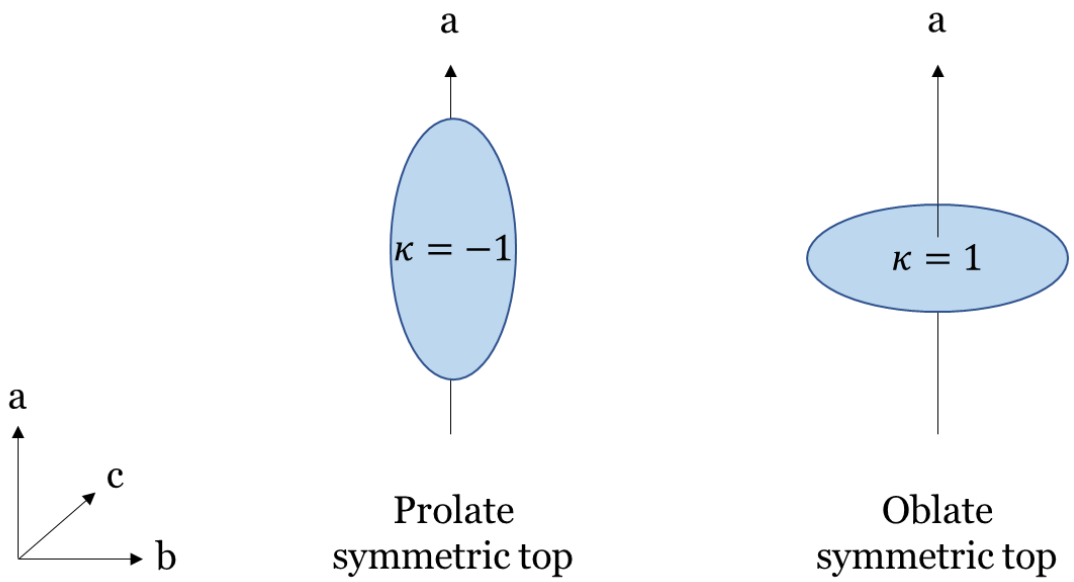

Figure 2.2. Schematic representations of a prolate (rugby ball) and an oblate (frisbee) symmetric top.

2.6 Rotational Transitions and Energy Levels

Generally, the energy of a transition between subsequent energy levels is described as;

$$E_1 - E_2 = hv \qquad (Eq. 2.30)$$

which is equal to the energy of the resonant photon that excites that transition.

Within the rigid rotor approximation, the eigenvalues of the rotational energy levels that are solutions to the time-independent Schrödinger equation are given by the relationship;

$$E_r = \frac{h^2}{8\pi^2 I} J(J+1) \qquad (Eq. 2.31)$$

where h is the Planck constant, the moment of inertia $I = \mu r^2$ with $\mu = \frac{m_1 m_2}{m_1 + m_2}$ being the reduced mass of the diatomic and $J = 0,1,2,\ldots$ is the rotational quantum number and describes the total angular momentum in units of $h/2\pi$. In microwave spectroscopy, frequency units (Hz, MHz, GHz converted from energy by dividing by h) are used to describe the different energy levels $E(J)$;

$$E(J) = \frac{E_r}{h} = \frac{h}{8\pi^2 I} J(J+1) = BJ(J+1) \qquad (Eq. 2.32)$$

Allowed rotational transitions for both emission and absorption spectra comply with the selection rule;

$$\Delta J = \pm 1 \qquad (Eq. 2.33)$$

meaning photons can be emitted or absorbed between subsequent rotational energy levels. It is also crucial that the molecules of interest possess a permanent dipole moment ($\mu \neq 0$) in order to absorb a photon. For asymmetric rotors, rotational emission transitions will be described by the notation;

$$J' \longrightarrow J'' \qquad (Eq. 2.34)$$

which indicates a change in the angular momentum of the rotating molecule. Single prime " $'$ " indicates the upper state and double prime " $''$ " the lower state.

For symmetric and asymmetric tops, the energy levels become more complex compared to those of a linear molecule. It is necessary to introduce the quantum number K which describes the projection of the total angular momentum along an axis of symmetry. For a prolate top, *i.e.* methyl cyanide, the vector of the angular momentum P may orientate in

any direction. The expression for the energy levels of a symmetric top including a term that accounts for K is;

$$E(J,K) = BJ(J+1) + (A-B)K^2 \qquad (Eq.2.35)$$

For an oblate symmetric top, the energy expression becomes;

$$E(J,K) = BJ(J+1) + (C-B)K^2 \qquad (Eq.2.36)$$

Due to the K^2 term in equations 2.35 and 2.36, the values K may take are $K = 0, \pm1, \pm2, \ldots, \pm J$ and the K levels are doubly degenerate. For asymmetric molecules, the degeneracy is lifted and the above expressions are modified as;

$$E(J,K) \cong B_{bar}J(J+1) + (A-B_{bar})K^2 \qquad (Eq.2.37)$$

and

$$E(J,K) \cong B_{bar}J(J+1) + (C-B_{bar})K^2 \qquad (Eq.2.38)$$

for a near-prolate and a near-oblate top, respectively. B_{bar} is defined as $\frac{1}{2}(B+C)$ and $\frac{1}{2}(A+B)$, respectively. This thesis will be concerned with near-prolate tops. The rotational emission transitions will be hereby labelled as;

$$J'_{K'_{-1}K'_1} \rightarrow J''_{K''_{-1}K''_1} \qquad (Eq.2.39)$$

K_{-1} and K_1 are labels linking the energy levels to the prolate and oblate limits, essentially describing the intermediate case of an asymmetric top. The K levels are no longer degenerate, and their energy difference tends to decrease with increasing value of K_{-1}. Selection rules of allowed rotational transitions of an asymmetric top are listed in table 2.1. Figure 2.3 is a schematic representation of the *a*-type rotational energy levels of an asymmetric top at the prolate and oblate limit as a function of the molecule's asymmetry κ.

The asymmetric Hamiltonian may be rearranged and expressed as a function of κ;

$$\hat{\mathrm{H}}_{rot} = \frac{1}{2}(A+C)\hat{P}^2 - \frac{1}{2}(A-C)\hat{H}_\kappa \qquad (Eq.2.40)$$

where $\hat{H}_\kappa = \hat{P}_a^2 + \kappa\hat{P}_b^2 - \hat{P}_c^2$.

The rotational Hamiltonian for an asymmetric top is typically expressed as a matrix, followed by diagonalization. When the matrix element of the rotational Hamiltonian are known, the rotational energy levels can be found which are the eigenvalues. Depending on

the orientation of the electric dipole moment, whether that is along the *a*-, *b*- or *c*-inertial axes, the respective type of transition will be yielded, namely *a*-, *b*- or *c*-type transitions. Selection rules and transitions are shown in table 2.1.

Table 2.1. Selection rules for transitions of asymmetric-top molecules.

Dipole Component	Type	ΔJ[a]	ΔK_{-1}	ΔK_1
$\mu_a \neq 0$	*a*-type	0, ±1	0, ±2, …	±1, ±3, …
$\mu_b \neq 0$	*b*-type	0, ±1	±1, ±3, …	±1, ±3, …
$\mu_c \neq 0$	*c*-type	0, ±1	±1, ±3, …	0, ±2, …

[a] $\Delta J = 1$ and 0 correspond to R- and Q-branch transitions, respectively. Transitions with ΔK_{-1} and $\Delta K_1 \geq 2$ are usually not observable in MW spectroscopy. A detailed list of selection rules may be found in the work of Cooke and Ohring.[5]

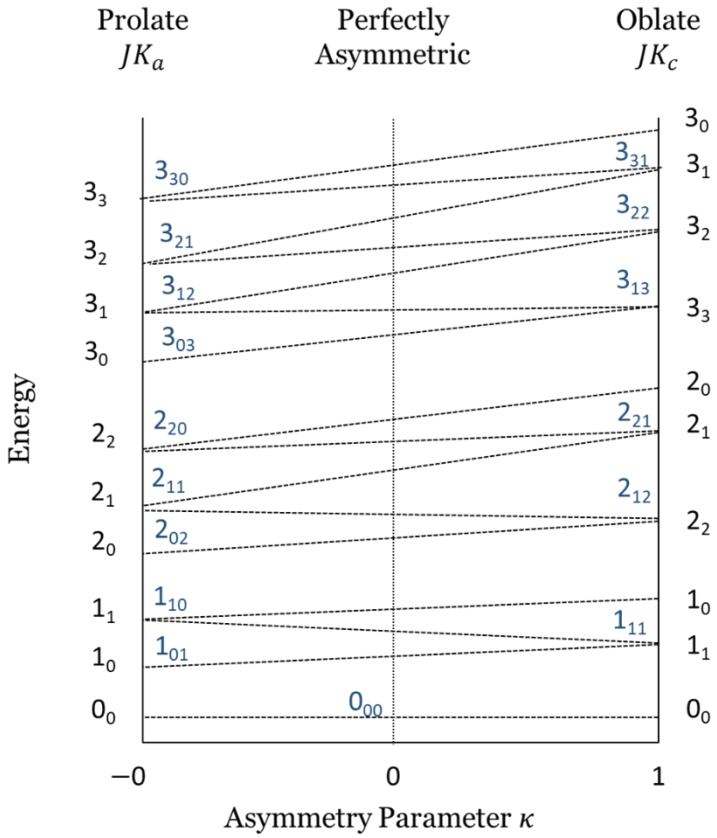

Figure 2.3. Correlation diagram of the energy levels of an asymmetric top at the prolate and oblate end. The energy levels are expressed as a function of the asymmetry parameter κ.

2.7 The Distortable Rotor and the Reduced Hamiltonian

Within the rigid rotor approximation, atoms are considered as point masses held together by rigid, weightless bonds. Real molecules undergoing rotation will experience distortion in their bonds and angles because of centrifugal forces. These restoring forces also give rise to the structural differences between equilibrium and zero-point structures. The effects of centrifugal distortion become more complicated as the molecular networks becomes more complex. In microwave spectroscopy, the effects of centrifugal distortion are depicted on the position of rotational transitions which may become perturbed. However, as it will be seen in the Hamiltonian for a distortable rotor, for lower J transitions, the effects of centrifugal distortion only comprise a small portion of the rotational energy so the deviations from rigid rotor behavior may be subtle.

The energy levels of a semi-rigid diatomic rotor can be expressed by modification of equation 2.31 and addition of centrifugal distortion terms that correct the energy. This is written as;

$$E(J) = BJ(J+1) - DJ^2(J+1)^2 + HJ^3(J+1)^3 + \cdots \qquad (Eq.\,2.41)$$

where D and H are the quartic and sextic order centrifugal distortion constants, respectively.

The quantum number K which is necessary to describe the energy levels of symmetric and asymmetric tops was introduced in section 2.6. The rotational transitions arising from the projection of the angular momentum on the symmetry axis are doubly degenerate for symmetric tops. The degeneracy is lifted in the case of asymmetric tops and transitions with $K = 1,2,3 \ldots$ are split into two components and their energy differences typically decreases with increasing K.

For asymmetric tops, there are two reduced, quantum mechanical Hamiltonians, namely Watson's A- and S-reduced Hamiltonians, where A- stands for asymmetric top and S- for symmetric top. These Hamiltonians consider centrifugal distortion forces and their effect on the total rotational energy. The advantage of the reduced Hamiltonian is that it allows for least square fitting of rotational transitions and any parameters that are only poorly determined may be removed from the expansion. The A-reduction which contains the rotational Hamiltonian and terms that account for the centrifugal distortion is written as;

$$H^A = 1/2(B^A + C^A)J^2 + \left(A^A - 1/2(B^A + C^A)\right)J_z^2 + 1/2(B^A + C^A)\left(J_x^2 - J_y^2\right) + \Delta_J J^4 - \Delta_{JK} J^2 J_z^2 - \Delta_K J_z^4 - 2\delta_J J^2\left(J_x^2 - J_y^2\right) - \delta_K\left(J_z^2\left(J_x^2 - J_y^2\right) + \left(J_x^2 - J_y^2\right)J_z^2\right) + \Phi_J J^6 + \Phi_{JK} J^4 J_z^2 + \Phi_{KJ} J^2 J_z^4 + \Phi_K J_z^6 + \cdots \quad (Eq. 2.42)$$

where J_x, J_y, and J_z are the angular momentum vectors along the principal inertial axes and $J^2 = J_x + J_y + J_z$.

The S-reduction is written as;

$$H^S = 1/2(B^S + C^S)J^2 + \left(A^S - 1/2(B^S + C^S)\right)J_z^2 + 1/4(B^S - C^S)(J_+^2 - J_-^2) - D_J J^4 - D_{JK} J^2 J_z^2 - D_K J_z^4 - 2\delta_1 J^2 (J_+^2 - J_-^2) - \delta_2 (J_+^4 - J_-^4) + H_J J^6 + H_{JK} J^4 J_z^2 + H_{KJ} J^2 J_z^4 + H_K J_z^6 + \cdots \quad (Eq. 2.43)$$

where $J_+^2 + J_-^2 = 2\left(J_x^2 - J_y^2\right)$.

Both A- and S-Hamiltonians are used throughout this thesis and it will be indicated which one was used for each molecule. Typically, the S-reduction is more suitable for asymmetric top that approach the oblate or prolate limit, *i.e.* $\kappa \to 1$ or -1. The A-reduction is more appropriate when the asymmetry of a molecule is high, *i.e.* $\kappa \to 0$.

Terms beyond the sextic are often omitted in microwave spectroscopy as these terms have a more significant effect in millimeter-wave and THz spectroscopy. The effect of the sectic and octic terms is more profound with higher J.

2.8 Hyperfine Structure- Nuclear Quadrupole Coupling

The rotational spectra of the molecules that will discussed in this thesis exhibit hyperfine structure due to the presence of one or more nuclei with non-spherical distribution of nuclear charges. This type of distribution generates the nuclear electric quadrupole moment, eQ, and an electric field gradient (EFG) on that nucleus. The hyperfine structure that will be observed here arises through coupling of the nuclear electric quadrupole moment of a nucleus with spin $I \geq \frac{1}{2}$ with the EFG of the oscillating electric field. In the semi-rigid Hamiltonians used in this thesis, this interaction is expressed as;

$$H_Q = \frac{1}{6} Q(X) : \nabla E(X) \qquad (Eq. 2.44)$$

where Q and ∇E are the electric quadrupole moment and electric field tensors of a nucleus X with $I \geq \frac{1}{2}$, respectively. This interaction is not observed for nuclei with spherical distribution of nuclear charges with $I = 0$ or $1/2$. When more than one quadrupolar nuclei are present, additional terms are included in the Hamiltonian.

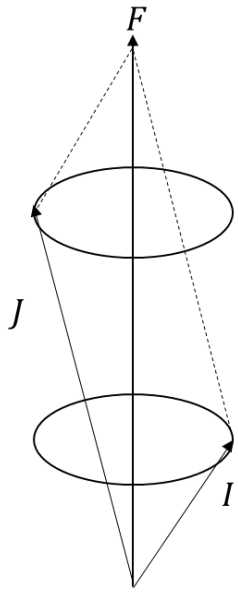

Figure 2.4. Schematic representation of coupling between angular momentum J and nuclear spin I resulting in the total angular momentum F.

Considering a rotating molecule with one quadrupolar nucleus in an electric field where the nuclear spin I couples to the angular momentum of the molecular rotation J which results in the total angular momentum F. A graphic representation of the coupling interaction is given in figure 2.4.

$$F = J + I \qquad (Eq. 2.45)$$

The resulting quantum numbers I, J and F are related in the following manner;

$$F = J + I, J + I - 1, J + I - 2, \ldots\ldots, |J - I| \qquad (Eq. 2.46)$$

which is an expression for the total angular momentum.

We also have M_F which may adopt values $M_F = F, F - 1, F - 2, \ldots\ldots, -F$.

Selection rules for allowed hyperfine transitions in rotational emission spectra are $\Delta J = 1$, $\Delta F = 0, \pm 1$, and $\Delta I = 0$.

In rotational spectroscopy, for a coupling nucleus X in an asymmetric top the coupling (eQq) components are labelled as;

$$\chi_{aa} = eQq_{aa} \qquad (Eq. 2.47)$$

$$\chi_{bb} = eQq_{bb} \qquad (Eq. 2.48)$$

$$\chi_{cc} = eQq_{cc} \qquad (Eq. 2.49)$$

These are the diagonal components of the recurrent three-by-three matrix;

$$\chi = \begin{pmatrix} \chi_{aa} & \chi_{ba} & \chi_{ca} \\ \chi_{ab} & \chi_{bb} & \chi_{cb} \\ \chi_{ac} & \chi_{bc} & \chi_{cc} \end{pmatrix} \qquad (Eq. 2.50)$$

for which the Laplace condition holds;

$$\chi_{aa} + \chi_{bb} + \chi_{cc} = 0 \qquad (Eq. 2.51)$$

The off-diagonal components χ_{ab}, χ_{ac}, χ_{cb},... are often small and only very poorly determined with rotational spectroscopy, particularly for nuclei with small quadrupole moments. Where off-diagonal terms are necessary to be used for generating diagonalized components (see section 2.8.2) in this thesis, these will be calculated *ab initio* or with DFT. Information about the electronic environment in different molecules may be obtained by the measured values of χ_{aa}, χ_{bb} and χ_{cc}, which are sensitive to subtle changes in electronic distributions, *i.e.* between structural isomers. The measured values of χ_{aa}, χ_{bb} and χ_{cc} are typically more sensitive to low J transitions as the hyperfine lines tend to be blended at higher J.

2.8.1 Molecules with two or more Quadrupolar Nuclei

The hyperfine structure of molecular transitions becomes more complicated in the case where two quadrupolar nuclei are present within a molecule or a complex. The majority of molecules and complexes that will be discussed in this thesis possess two quadrupolar

nuclei, in particular, two N nuclei with $I = 1$. It was explained above that additional terms are included in the Hamiltonian to account for the coupling interactions. The total angular momentum, J, is now coupled by I_1 and I_2 which are the nuclear spins of two quadrupolar nuclei which result in F_1 and F.

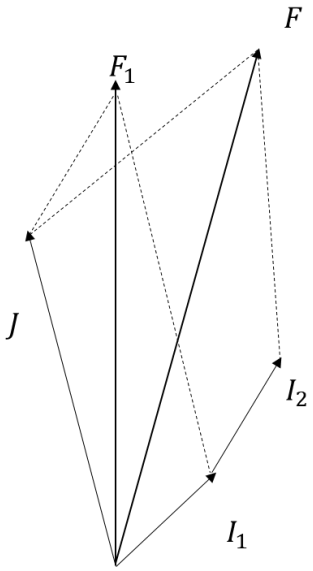

Figure 2.5. Schematic representation of coupling between the angular momentum J and the nuclear spin on two quadrupolar nuclei, I_1 and I_2, resulting in the total angular momentum F.

2.8.2 Principal Nuclear Axes

Often, the measured values of χ_{aa}, χ_{bb} and χ_{cc} do not provide sufficient information for a direct comparison of the electronic environment of nuclei in different molecules. This is because these components are referenced against the *a*-, *b*-, and *c*-inertial axes which are unique for each molecule. A common reference system is necessary where a set of mutually perpendicular axes *x*, *y*, and *z*, which are also the axes of the field gradient, are placed on each quadrupolar nucleus. The resulting diagonalized coupling components are now χ_{xx}, χ_{yy} and χ_{zz} with all the rest of the components being equal to zero;

$$\chi = \begin{pmatrix} \chi_{zz} & 0 & 0 \\ 0 & \chi_{yy} & 0 \\ 0 & 0 & \chi_{zz} \end{pmatrix} \qquad (Eq.\,2.52)$$

The transformation should rely on the following relationships;

$$\chi_{aa} = \chi_{xx}cos^2\theta_{xa} + \chi_{yy}cos^2\theta_{ya} + \chi_{zz}cos^2\theta_{za} \qquad (Eq.\,2.53)$$

$$\chi_{bb} = \chi_{xx}cos^2\theta_{xb} + \chi_{yy}cos^2\theta_{yb} + \chi_{zz}cos^2\theta_{zb} \qquad (Eq.\,2.54)$$

$$\chi_{cc} = \chi_{xx}cos^2\theta_{xc} + \chi_{yy}cos^2\theta_{yc} + \chi_{zz}cos^2\theta_{zc} \qquad (Eq.\,2.55)$$

however, these equations cannot be solved directly. It is necessary to have a value for at least one off-diagonal component χ_{ab}, χ_{ac}, χ_{cb},... but as described above, these typically cannot be determined from the rotational hyperfine structure. A calculated value of χ_{ab} may be used instead.

In the case where a coupling tensor coincides with a bond axis or an inertial axis, for example, for the *z*-axis it holds that $\chi_{xx} = \chi_{yy} = -\frac{1}{2}\chi_{zz}$, then there is only one dependent constant. The above equations 2.53-2.55 are expressed as;

$$\chi_{aa} = -\frac{1}{2}\chi_{zz}(3cos^2\theta_{za} - 1) \qquad (Eq. 2.56)$$

$$\chi_{bb} = -\frac{1}{2}\chi_{zz}(3cos^2\theta_{zb} - 1) \qquad (Eq. 2.57)$$

$$\chi_{cc} = -\frac{1}{2}\chi_{zz}(3cos^2\theta_{zc} - 1) \qquad (Eq. 2.58)$$

The molecules and complexes discussed in this thesis possess a plane of symmetry. The axis that goes through that plane is the c-axis (or the *a*-axis when it comes to Ar van der Waals complexes). That axis will be colinear with a principal axis of the field gradient or coupling. Then it holds that;

$$\chi_{aa} = \chi_{xx}sin^2\theta_{za} + \chi_{zz}cos^2\theta_{za} \qquad (Eq. 2.59)$$

$$\chi_{bb} = \chi_{xx}cos^2\theta_{za} + \chi_{zz}sin^2\theta_{za} \qquad (Eq. 2.60)$$

This method is implemented in Kisiel's program QDIAG which will be used throughout this thesis. The program is available from the PROSPE website. The measured values of χ_{aa}, χ_{bb} and χ_{cc} and a calculated value of χ_{ab} are evaluated to generate χ_{xx}, χ_{yy} and χ_{zz}.

2.9 Internal Rotation

It is common for molecules that contain groups with 3-fold symmetry, *i.e.* CH_3 groups, to exhibit internal rotation of that group coupling to the overall rotation, provided that the surrounding energy is sufficient to surmount the barrier height to internal rotation. The potential energy surface of a CH_3 rotating internally can be expressed as a periodic function of α, which repeats over 120° intervals, $2\pi/N$ where N is the N-fold symmetry of the rotating group which is equal to 3 in the case of CH_3. It can be expressed as;

$$V(\alpha) = \frac{V_3}{2}(1 - cos3\alpha) + \frac{V_6}{2}(1 - cos6\alpha) + \cdots \qquad (Eq.\,2.61)$$

This thesis will be concerned with molecules with 3-fold barriers so the higher terms vanish retaining expression 2.61 to;

$$V(\alpha) = \frac{V_3}{2}(1 - cos3\alpha) \qquad (Eq.\,2.62)$$

The barrier to a three-fold internal rotation will hereafter be denoted as V_3. The V_3 barrier to internal rotation was calculated for *N*-methylimidazole at the B3LYP(D3BJ)/aug-cc-PVTZ level and the shape of the sinusoidal hindering potential is shown in figure 2.6.

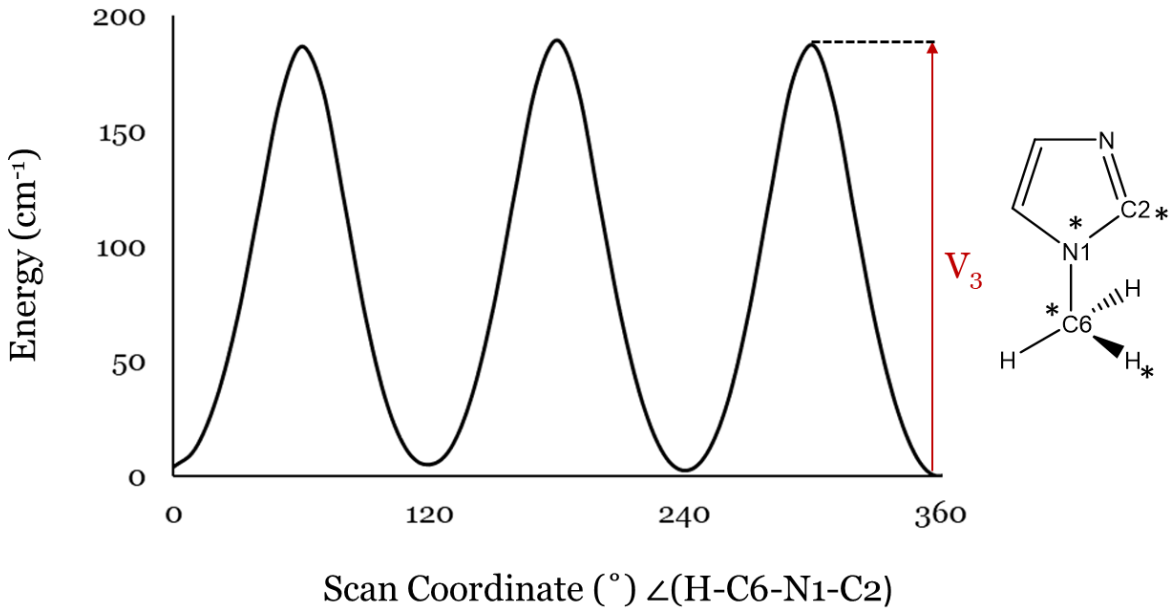

Figure 2.6. Calculated representation of the V_3 hindering potential in *N*-methylimidazole. Identical minima are repeated over 120° rotations of the (H-C6-N1-C2) dihedral angle.

The torsional energy levels for a system with internal rotation of a three-fold group are given by;

$$-F\frac{d^2U(\alpha)}{d\alpha}+\left[\frac{V_3}{2}(1-cos3\alpha)-E\right]U(\alpha)=0 \qquad (Eq.2.63)$$

where $F=\frac{\hbar^2}{2I_r}$ is the rotational constant and $I_r=\frac{I_iI_r}{I_i+I_r}$ the reduced mass of internal rotor-molecular framework, E is the total energy of the system and $U(\alpha)$ the periodic wavefunction of internal rotation. In order to find the relative torsional levels, we may consider two limiting cases; i) very low barrier resulting in essentially free internal rotation ($V_3\rightarrow 0$) and ii) very high barrier with a rigid internal rotor ($V_3\rightarrow\infty$).

For $V_3\rightarrow 0$, expression 2.63 is simplified to ;

$$\frac{d^2U(\alpha)}{d\alpha}+\frac{1}{F}EU(\alpha)=0 \qquad (Eq.2.64)$$

and

$$U(\alpha)-Ae^{im\alpha}=A\big(cos(m\alpha)+i\,sin(m\alpha)\big) \qquad (Eq.2.65)$$

where A is a normalization factor and $m=0,\pm1,\pm2,\pm3,\ldots$ is the internal rotation quantum number. The energy is given by;

$$E=Fm^2 \qquad (Eq.2.66)$$

and it follows that torsional states are doubly degenerate except for $m=0$.

For $V_3\rightarrow\infty$, internal motions will be restricted to low energy oscillations about the minima of the potential well. The torsional levels approximate those of a harmonic oscillator with frequencies;

$$v=\frac{3}{2\pi}\left(\frac{V_3}{2I_r}\right)^{1/2} \qquad (Eq.2.67)$$

The limiting case of a rigid internal rotor is beyond the scope of this thesis.

At the free rotor limit, each torsional state v is three-fold degenerate. At the intermediate case of finite barrier, quantum mechanical tunnelling effects lift the degeneracy, and a splitting is induced. Since the barrier is finite, the probability of tunnelling through the barrier is also finite. Tunnelling through the potential barrier results in splitting of the three-fold degenerate torsional levels into an *A*-state ($m=0$) and a doubly degenerate *E*-state ($m=\pm1$).

The Hamiltonian for an asymmetric molecule with a three-fold internal rotor is written as;

$$\mathcal{H} = H^A + H_{IR} \qquad (Eq.\,2.68)$$

where H^A is Watson's A-reduced Hamiltonian and H_{IR} is the internal rotation Hamiltonian defined as;

$$H_{IR} = F\left(\hat{P}_a - \hat{P}\right)^2 + V(\alpha) \qquad (Eq.\,2.69)$$

Two methods were used to approach internal rotation in this thesis; the principal axes method (PAM) and the internal axes method (IAM), the main difference being the reference system used in each one. In the PAM, the principal axes of the molecule of interest are used as the reference system. The advantage is that the components of the moments of inertia remain diagonalized. It is required that the local C_3 axis of the CH_3 group is co-linear or almost co-linear with one of the principal axes of the molecule. In the IAM, the C_3 axis of the CH_3 group is chosen as one of the reference axes and the polar coordinates are chosen such that internal rotation-rotation coupling is minimized.

2.9.1 Principal Axes Method (PAM)

The PAM[1] was used as complementary approach to the barriers to internal rotation in methylimidazole isomers and is described in detail in chapter 6. The method is generally more appropriate for molecules with low V_3 barriers and molecules where vibrational contributions are negligible at the zero-point. It is also important that the local C_3 axis of the internal rotor is aligned or almost aligned with one of the principal inertial axes of the molecule. The method evaluates how the measured rotational constants determined through fitting of *A*-state transitions deviate from the limiting case of free internal rotation with $V_3 \to 0$ or fixed internal rotor $V_3 \to \infty$ and estimates the actual V_3 barrier to internal rotation.

2.9.2 Internal Axes Method (IAM)

The IAM[1] is implemented in the program XIAM[6], available from the PROSPE website[7]. This method will be the predominant tool to analyze internal rotation in this thesis. The Hamiltonian implemented in XIAM is based on the one described in section 2.9 and the complete form is discussed here[6]. Unlike in the PAM, the local C_3 axis of the CH_3 group as a reference and the angles between that and the principal inertial axes of the molecule are of interest. The polar coordinates are defined as δ and ε, which are the angles between the C_3 axis and the *a*-inertial axis and between the *b*-axis and the projection of C_3 onto the *bc*-plane, respectively.

2.10 Structure determination methods

Experimentally measured rotational constants give an insight into the molecular structure of a molecule or complex. In section 2.5, it was shown that Ray's asymmetry parameter gives a quantitative measure of the asymmetry of an asymmetric top molecule by evaluating the A, B, and C rotational constants. In sections 2.1 and 2.4 it was discussed that the measured rotational constants are inversely proportional to the moment of inertia around the corresponding inertial axis. It will be shown in section 2.10.1 that the moments of inertia may be evaluated to calculate planar moments that give a more straight-forward insight into the mass distribution. It is possible to determine the precise position of an atom within a molecule by measuring the rotational constants of the molecule with an atom replaced by a heavier or lighter isotope, *i.e.* $^{12}C/^{13}C$. The Kraitchman method (2.10.2) evaluates changes in the moments of inertia caused by single isotopic substitution and requires no assumptions about the molecular structure. The effective structure (2.10.3) can deal with multiple atoms substituted by their heavier isotopes at once; however, it is necessary to make assumptions about the molecular structure when there is not sufficient isotopic information about each atom in a molecule.

2.10.1 Planar (Second) Moments and Inertial Defect

It has been shown how the rotational constants relate to the principal moments of inertia of a molecule, which are a direct measure of mass distribution. Often, a more intuitive, initial insight into the structure of a molecule or complex that allows for more direct comparisons is obtained through the evaluations of planar (or second) moments[8] P_{aa}, P_{bb}, and P_{cc}. These are related to the principal moments of inertial *via* the expressions;

$$P_{aa} = \sum_i m_i a_i^2 = (I_{bb} + I_{cc} - I_{aa})/2 \qquad (Eq. 2.70)$$

$$P_{bb} = \sum_i m_i b_i^2 = (I_{aa} + I_{cc} - I_{bb})/2 \qquad (Eq. 2.71)$$

$$P_{cc} = \sum_i m_i c_i^2 = (I_{aa} + I_{bb} - I_{cc})/2 \qquad (Eq. 2.72)$$

Conversion relies on the $(h/8\pi^2)N_A$ factor which relates the rotational constants A, B, and C (in MHz) to the principal moments of inertia I_{aa}, I_{bb} and I_{cc} (in u Å^2) and to subsequently to P_{aa}, P_{bb}, and P_{cc} (in u Å^2), where N_A is Avogadro's number.

The inertial defect Δ is often used as a measure of the planarity of a molecule or complex. It is defined as;

$$\Delta = I_{cc} - I_{aa} - I_{bb} = -P_{cc} \qquad (Eq. 2.73)$$

For a planar molecule at equilibrium, $\Delta = 0$. Given that this thesis will be concerned with molecules at the zero-point, deviations from zero are expected because of low-lying vibrations. In general, in plane vibrations have a positive contribution to Δ whilst out-of-plane vibrations result in negative values of Δ. The planar molecules with one CH_3 group that does not perform internal rotation, the inertial defect is expected to be approximately 3.2 u Å^2. Δ may assist with determination of heights of barriers to internal rotation in molecules with CH_3 groups (PAM).

2.10.2 Substitution Structure (r_s) and Kraitchman Equations

Single isotopic substitution of an atom in a molecule, allows for determination of the atomic coordinates of that atom in the parent molecule in the principal *a*-, *b*- and *c*-axis system. The atomic coordinates are evaluated with Kraitchman's equations[9,10] which are implemented in the program KRA. The equations can be specified for linear, symmetric, and asymmetric rotors by evaluating the measured zero-point rotational constants. The resulting structure is called the r_s (s: substitution) structure. The calculations consider changes in the moments of inertia caused by isotopic substitution and only the relative magnitudes of the coordinates are calculated. The method does not account for rotation-vibration effects, typically resulting in the r_s structure being closer to equilibrium. Costain's errors[10,11] can be calculated by means of $\delta z = 0.0015/|z|$, which are expressed as a fractional uncertainty of the magnitude of the coordinate, where $|z|$ is the magnitude of the relative coordinate. The method may perform poorly when determining the position of atoms close to the center of mass or an inertial axis by returning imaginary numbers.

The Kraitchman method assumes that the molecular structure does not change upon isotopic substitution. As it will be discussed later, this is not true for H/D substitution where an elongation of the bond-length is observed with D. The Kraitchman equations are;

$$|a| = \left[\frac{\Delta P_a}{\mu}\left(1+\frac{\Delta P_b}{I_a - I_b}\right)\left(1+\frac{\Delta P_c}{I_a - I_c}\right)\right]^{1/2} \qquad (Eq.2.74)$$

$$|b| = \left[\frac{\Delta P_b}{\mu}\left(1+\frac{\Delta P_c}{I_b - I_c}\right)\left(1+\frac{\Delta P_a}{I_b - I_a}\right)\right]^{1/2} \qquad (Eq.2.75)$$

$$|c| = \left[\frac{\Delta P_c}{\mu}\left(1+\frac{\Delta P_a}{I_c - I_a}\right)\left(1+\frac{\Delta P_b}{I_c - I_b}\right)\right]^{1/2} \qquad (Eq.2.76)$$

where $\Delta P_a = \frac{1}{2}(-\Delta I_a + \Delta I_b + \Delta I_c)$, $\Delta P_b = \frac{1}{2}(-\Delta I_b + \Delta I_c + \Delta I_a)$, and $\Delta P_c = \frac{1}{2}(-\Delta I_c + \Delta I_a + \Delta I_b)$ and $\Delta I_a = I'_a - I_a$, $\Delta I_b = I'_b - I_b$, and $\Delta I_c = I'_c - I_c$, where μ is the mass difference between the parent and the isotopically substituted molecule, I_a, I_b, I_c and I'_a, I'_b, I'_c are the moments of inertia, respectively. The quantities $|a|$, $|b|$ and $|c|$, represent the atom coordinates along the *a*-, *b*-, and *c*-axis.

2.10.3 Effective Structure (r_0)

The effective r_0 structure is calculated by least square fitting of structural parameters to the experimentally determined moments of inertia derived from the zero-point rotational constants of the available isotopologues. The method does not consider changes that may be induced to the structure by isotopic substitution or large amplitude motions. The method is implemented in STRFIT[12] and a detailed description of the method and program may be found in reference 12. The starting geometry of the molecule of interest is input as a *z*-matrix. Assumptions for the structure need to be made when there is not sufficient amount of isotopic information.

2.11 Quantum Chemical Calculations

A brief description of the quantum chemical methods that were used for this thesis is given here. All calculations were performed with the GAUSSIAN09 package.[13] The performance of the methods is benchmarked against experimental results in chapters 4-7. A complete description of the methods and interpretation of the performance is beyond the scope of this thesis.

In rotational spectroscopy, particularly for complex asymmetric rotors, quantum chemical calculations greatly assist with spectral analysis. A typical broadband rotational spectrum consists of hundreds or even thousands of spectral lines. Molecules in the ground vibrational state co-exist as a gas phase mixture and are probed simultaneously. As a result, the spectral patterns usually overlap and identifying them is not straight forward. Quantum chemical calculations provide a starting point for the A, B and C rotational constants of a molecule and when combined with the appropriate dipole moment component, the relevant energy levels can be estimated, identified in the spectra and quantum numbers can be assigned. Quantum chemical calculations assist with estimation of energetic barriers, *i.e.* calculating the V_3 barrier to internal rotation in methylimidazole isomers in chapter 6. Conformations beyond the global minimum of a molecular carrier can be investigated by examining local minima of a potential energy surface. In the case where a fully experimental structure is not available, *i.e.* in chapter 6 in methylimidazole isomers where no experimental data is available for the position of the hydrogen atoms, their position is based on their calculated equilibrium structure. Finally, vibrational modes can be identified which may indicate whether the structure of interest is a global or local minimum, or give an insight into internal motions (wag and torsion of the water subunit in chapter 5) and predict the centrifugal distortion constants.

For this thesis, Density Functional Theory (DFT) and *ab initio* calculations were performed. The DFT functional of Becke, Lee-Yang-Parr (B3LYP)[14-17] is based on a combination of the exact Hartree-Fock functional and electron-electron exchange correlation to describe a molecular system. The method treats the molecular structure as a system of non-interacting electrons as a function of density. The energy is minimized such that the true ground state density is found. The B3LYP functional is used in conjunction with D3BJ empirical correction[15, 18, 19] that accounts for dispersion interactions by avoiding repulsive interatomic forces. The long-range corrected functional ωB97X-D[20] which includes empirical correction for dispersion interactions is also used. The *ab initio* second

order Møller-Plesset perturbation theory (MP2) was also used. The method considers electron correlation effects and as such dispersion interactions are accounted for.

Each functional must be used in conjunction with a basis set, which is made up by linear combination of functions which represent the orbitals in a molecular system. Dunning type basis sets,[21-23] augmented with functions that account for core electron correlation (aug-cc-pVnZ, n=2,3) are used here. Ahlirichs' Def2-TZVP basis set[24] is also used; the valence shells are described by three functions whilst only one is used for the inner shells.

The exact functional-basis set combinations are indicated in each chapter for each molecular system.

2.12 Spectral Analysis and Fitting

Spectral analysis is performed with Watson's PGOPHER.[25] Watson's A- and S-reduced Hamiltonians[26] are implemented in PGOPHER. Rotational constants, centrifugal distortion constants up to the octic and nuclear quadrupole coupling constants can be determined through least square fitting of transition frequencies. The program allows for interactive viewing of measured broadband spectra alongside a simulation that is based on rotational constants calculated as described in section 2.4. Quantum numbers are assigned to measured transition frequencies and the spectroscopic parameters are least-squares fitted. It is crucial to use as few constants as possible for as many transition frequencies as possible with experimental accuracy of a few kHz. As a rule of thumb, the accuracy of the fit should be approximately 1/10 of the linewidth of a well resolved line at full width at half maximum. However, this will be somewhat dependent on the molecule, the number of fitted transitions, internal motions, and hyperfine splitting.

PGOPHER is not programmed to deal with internal motions like internal rotation. For the problem of internal rotation, the XIAM program is used where simultaneous fitting of *A*- and *E*-states is possible. The A- and S-reduced Hamiltonians are implemented in XIAM and the fitting procedure is essentially the same as with PGOPHER; however, no graphical interface is available with XIAM.

2.13 References

1 W. Gordy and R. L. Cook, *Microwave molecular spectra*, John Wiley & Sons, Ltd, New York, 3rd., 1984.

2 E. W. Castner, *Modern Spectroscopy*, 4th Edition (J. Michael Hollas), J. Chem. Educ., 2005, 82, 43.

3 J. M. Hollas, in *High Resolution Spectroscopy*, Butterworth-Heinemann, 1982, pp. 87–148.

4 W. Zeil, H. W. Kroto: *Molecular Rotation Spectra*, John Wiley & Sons, Ltd., London-New York-Sydney-Toronto 1975, 311 Seiten, *Berichte der Bunsengesellschaft für Phys. Chemie*, 1976, **80**, 99.

5 S. A. Cooke and P. Ohring, *Decoding pure rotational molecular spectra for asymmetric molecules*, 2013, vol. 1.

6 H. Hartwig and H. Dreizler, Zeitschrift fur Naturforsch. - *Sect. A J. Phys. Sci.*, 1996, **51**, 923–932.

7 Z. Kisiel, PROSPE - Programs for ROtational SPEctroscopy, http://www.ifpan.edu.pl/~kisiel/prospe.htm.

8 R. K. Bohn, J. A. Montgomery, H. H. Michels and J. A. Fournier, Second moments and rotational spectroscopy, *J. Mol. Spectrosc.*, 2016, **325**, 42–49.

9 J. Kraitchman, Determination of Molecular Structure from Microwave Spectroscopic Data, *Am. J. Phys.*, 1953, **21**, 17–24.

10 C. C. Costain, Determination of molecular structures from ground state rotational constants, *J. Chem. Phys.*, 1958, **29**, 864–874.

11 C. C. Costain, Further comments on the accuracy of rs substitution structures., *Trans. Am. Crystallogr. Assoc.*, 1966, **2**, 157–61, discussion 161-4.

12 Z. Kisiel, Least-squares mass-dependence molecular structures for selected weakly bound intermolecular clusters, *J. Mol. Spectrosc.*, 2003, **218**, 58–67.

13 M. J. Frisch, G. W. Trucks, H. B. Schlegel, G. E. Scuseria, M. A. Robb, J. R. Cheeseman, G. Scalmani, V. Barone, B. Mennucci, G. A. Petersson, H. Nakatsuji, M. Caricato, X. Li, H. P. Hratchian, A. F. Izmaylov, J. Bloino, G. Zheng, J. L. Sonnenberg,

M. Hada, M. Ehara, K. Toyota, R. Fukuda, J. Hasegawa, M. Ishida, T. Nakajima, Y. Honda, O. Kitao, H. Nakai, T. Vreven, J. A. J. Montgomery, J. E. Peralta, F. Ogliaro, M. Bearpark, J. J. Heyd, E. Brothers, K. N. Kudin, V. N. Staroverov, T. Keith, R. Kobayashi, J. Normand, K. Raghavachari, A. Rendell, J. C. Burant, S. S. Iyengar, J. Tomasi, M. Cossi, N. Rega, J. M. Millam, M. Klene, J. E. Knox, J. B. Cross, V. Bakken, C. Adamo, J. Jaramillo, R. Gomperts, R. E. Stratmann, O. Yazyev, A. J. Austin, R. Cammi, C. Pomelli, J. W. Ochterski, R. L. Martin, K. Morokuma, V. G. Zakrzewski, G. A. Voth, P. Salvador, J. J. Dannenberg, S. Dapprich, A. D. Daniels, O. Farkas, J. B. Foresman, J. V. Ortiz, J. Cioslowski and D. J. Fox, 2013.

14 K. S. Thanthiriwatte, E. G. Hohenstein, L. A. Burns and C. D. Sherrill, Assessment of the performance of DFT and DFT-D methods for describing distance dependence of hydrogen-bonded interactions, *J. Chem. Theory Comput.*, 2011, **7**, 88–96.

15 L. Goerigk and S. Grimme, A thorough benchmark of density functional methods for general main group thermochemistry, kinetics, and noncovalent interactions, *Phys. Chem. Chem. Phys.*, 2011, **13**, 6670–6688.

16 A. D. Becke, Density-functional thermochemistry. III. The role of exact exchange, *J. Chem. Phys.*, 1993, **98**, 5648–5652.

17 B. Miehlich, A. Savin, H. Stoll and H. Preuss, Results obtained with the correlation energy density functionals of Becke and Lee, Yang and Parr, *Chem. Phys. Lett.*, 1989, **157**, 200–206.

18 S. Grimme, S. Ehrlich and L. Goerigk, Effect of the damping function in dispersion corrected density functional theory, *J. Comput. Chem.*, 2011, **32**, 1456–1465.

19 D. Bernhard, M. Fatima, A. Poblotzki, A. L. Steber, C. Pérez, M. A. Suhm, M. Schnell and M. Gerhards, Dispersion-controlled docking preference: multi-spectroscopic study on complexes of dibenzofuran with alcohols and water, *Phys. Chem. Chem. Phys.*, 2019, **21**, 16032–16046.

20 J.-D. Chai and M. Head-Gordon, Long-range corrected hybrid density functionals with damped atom–atom dispersion corrections, *Phys. Chem. Chem. Phys.*, 2008, **10**, 6615–6620.

21 T. H. Dunning, Gaussian basis sets for use in correlated molecular calculations. I. The atoms boron through neon and hydrogen, *J. Chem. Phys.*, 1989, **90**, 1007–1023.

22 T. Hashimoto, K. Hirao and H. Tatewaki, Comment on Dunning's correlation-consistent basis sets, *Chem. Phys. Lett.*, 1995, **243**, 190–192.

23 A. K. Wilson, D. E. Woon, K. A. Peterson and T. H. Dunning, Gaussian basis sets for use in correlated molecular calculations. IX. The atoms gallium through krypton, *J. Chem. Phys.*, 1999, **110**, 7667–7676.

24 F. Weigend and R. Ahlrichs, Balanced basis sets of split valence, triple zeta valence and quadruple zeta valence quality for H to Rn: Design and assessment of accuracy, *Phys. Chem. Chem. Phys.*, 2005, **7**, 3297–3305.

25 C. Western, PGOPHER, a program for rotational, vibrational and electronic spectra, *J. Quant. Spectrosc. Radiat. Transf.*, 2015, **186**, 221–242.

26 J. K. G. Watson, Determination of centrifugal distortion coefficients of asymmetric-top molecules. III. Sextic coefficients, *J. Chem. Phys.*, 1968, **48**, 4517–4524.

Chapter 3. Experimental Methods

3.1 The CP-FTMW Spectrometer at Newcastle University

In this chapter a detailed description of the CP-FTMW spectrometer at Newcastle University[1–3] will be provided. The instrument is designed to record broadband rotational spectra in a highly automated manner. The design of the spectrometer is based on an original design by Pate and co-workers[4] with some modifications and additions. The spectrometer operates in the 2.0 to 18.5 GHz frequency range alongside an Arbitrary Waveform Generator (AWG) which is used for frequency signal generation. The two bands, 2.0-8.0 GHz and 7.0-18.5 GHz are covered in two different setups which can be interchanged by modification of the microwave circuit. A detailed description and a schematic of the circuit are given in the sections to follow. A bespoke laser ablation source using a pulsed laser is also installed in our spectrometer.

Advances in microwave spectroscopy have relied upon technological advances and the need to record spectra of transient and short-lived species. In 1934, Cleeton and Williams[5] recorded the absorption spectrum of ammonia in the 1-3 cm region using continuous radiation. That was one of the first microwave spectroscopy experiments to be performed with such short wavelengths. In 1975, Ekkers and Flygare[6] reported a microwave spectrometer that operated using short microwave pulses from Travelling-Wave Tube Amplifiers (TWTA) as opposed to continuous sample irradiation. Their design also featured time domain measurements which offered significant improvements in the signal to noise of molecular signals.

As vacuum technology evolved, in 1981, Balle and Flygare[7] implemented a pulse valve molecular source allowing molecules of interest to adiabatically expand into a vacuum chamber enclosing a Fabry-Perot cavity. The gas pulse is followed by a short microwave pulse resonating in the cavity which polarizes a frequency band, typically approximately 1 MHz bandwidth. Detection of molecular emissions after the halt of the polarizing pulse is also performed in the time domain and Fourier transformed to the frequency domain rotational spectrum. The spectrometer designed by Pate and co-workers[4] was introduced in 2008 and allowed to scan large bandwidths of up to 12 GHz in a single acquisition shot using chirped microwave pulses. The Fabry-Perot cavity of the Balle and Flygare spectrometer is replaced by microwave horn antennas.

Given that the design of the CP-FTMW spectrometer at Newcastle University is based on existing setups, the experimental cycle consists of a sequence of events with the insertion of gas phase molecules into the vacuum chamber being the first one in line. If the molecules of interest are solid at room temperature (~20°C), a laser pulse can follow which will rapidly vaporize molecules into the gas phase. A microwave excitation pulse polarizes the gas phase molecules, and their molecular emissions are recorded at the detection end after the halt of the polarizing pulse. Typically microwave pulses broadcast through horn antennas and perpendicularly to the direction of the expanding gas. An exception to that is the spectrometer described by Finneran *et al.* in which the microwave pulse travels coaxially to the gas sample.[8]

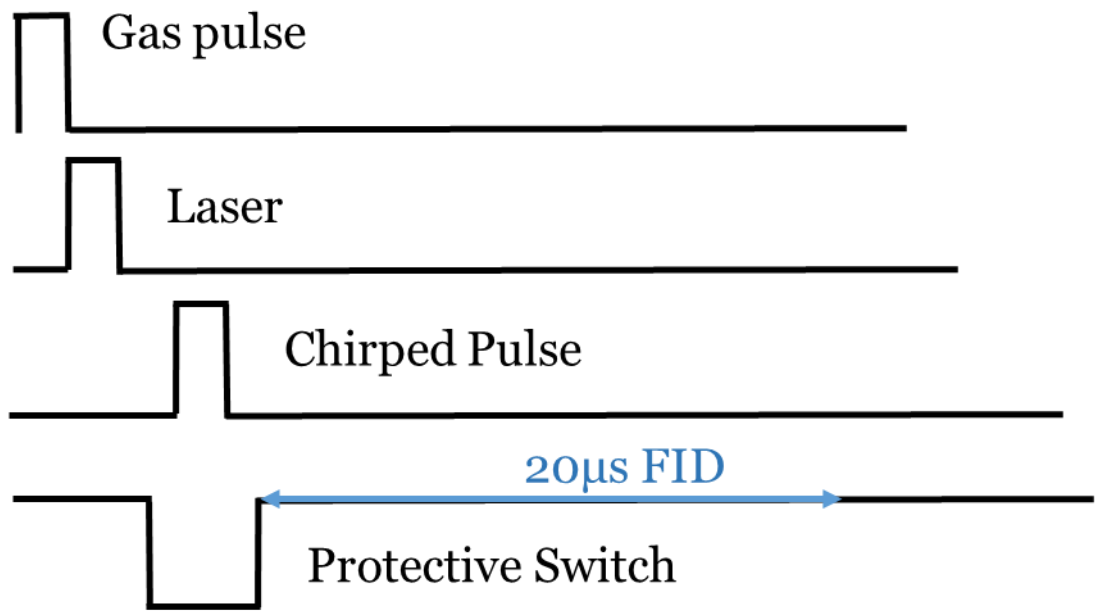

Figure 3.1. Schematic of the various events in the experimental cycle. Note that the protective switch remains open for the duration of the chirped pulse and before and after the pulse.

3.2 Supersonic expansion

In this work, the term supersonic expansion refers to a gas or gas mixture expanding into a vacuum chamber at a speed greater than that of sound. Supersonic expansion allows efficient conversion of enthalpy to direct mass flow, which generates an environment of rotationally cooled species (~ 2-3 K) free of solvent and lattice effects. Low internal temperature results in population of low energy states which significantly simplifies the spectral patterns we observe. An outstanding example that highlights the benefits of rotational cooling was discussed by Smalley and co-workers.[9] In optical spectroscopy, matrix isolation experiments are common and allow study of complex molecules. However, the matrix can induce perturbations in the spectra and information carried in the rotational structure is lost. Supersonic expansion methods allowed for observation of the fluorescence absorption spectrum of NO_2 with individually resolved vibronic and rovibronic bands identifiable in the spectrum.

As the supersonic jet propagates, the molecular velocities can exceed that of sound resulting in supersonic speeds with $M > 1$, where M is the Mach number describing the ratio of the speed of the expanding jet to the local speed of sound.[10] As the gas expands, the collision free zone or zone of silence is approached, and molecular collisions are effectively halted. At that point, the jet has reached its lowest internal temperature and optimal conditions for the sample to interact with the microwave pulse are provided. Measurements under high vacuum conditions could elongate the collision free zone and position it directly between the two horn antennae (approximately 30 cm from the orifice of the pulse valve which is described below) for efficient radiation-sample interrogation. The vacuum system is described in detail in section 3.4.

A pulsed valve (Parker General Valve, series 9) is employed for supersonic expansion throughout this thesis. The valve opening time (800-1000 μs) and repetition rate (1-2 Hz) are controlled by a valve driver (Parker, IOTA ONE, Micro fluidic valve driver). Gas expands through the 0.7 mm orifice of the valve and into the vacuum chamber. Typically, an inert carrier gas such as He, Ne or Ar is kept at high backing pressure and acts as a means of cooling the expanding jet.

The interactions between molecules and inert gas atoms in a supersonic expansion can be complicated. Switching between carrier gases can have a drastic effect on the temperature of the expanding jet and therefore affect the population of species for different rotational states. In the spectra, this is depicted as a change in the signal strength of rotational transitions. The effect of the carrier gas on conformational relaxation was examined in conformational isomers of *trans*-urocanic acid.[11] The four possible conformers of *trans*-urocanic acid are observed when neon is used as the carrier gas. The relative intensity of rotational transitions of the conformers is analogous to their calculated energies. The high energy conformers relax into a more stable configuration when neon is substituted by argon. However, the relative energy of the conformers is not the only factor that influences the relative intensity, *i.e.* dipole moment, power and duration of polarizing pulse (section 3.12).

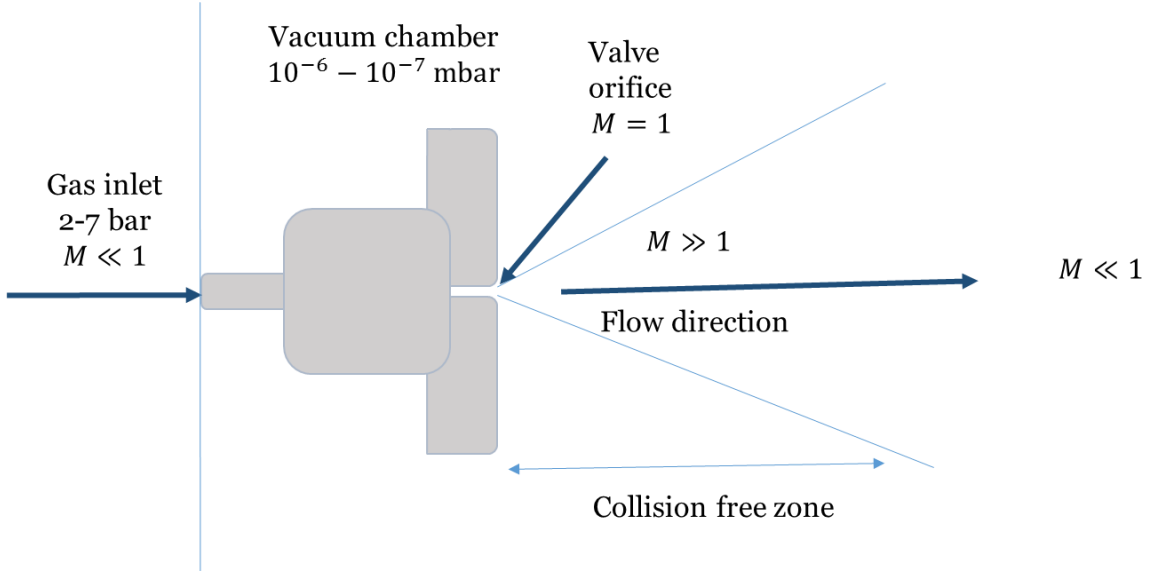

Figure 3.2. Supersonic expansion schematic (not to scale).

Relaxation is a result of efficient cooling of molecular species in the supersonic expansion. Molecular species that are high in energy may relax into a more stable configuration due to energy transfer through inelastic collisions with the inert carrier gas atoms. Energy that is equal to the energy difference between a high energy configuration and a relaxed configuration may be redistributed internally in the molecule or absorbed by the carrier gas atoms. Typically, the heavier the carrier gas, the more efficient the cooling may become, with krypton being able to relax molecules with high energy barriers. Following this basis, helium and neon would be the choice of carrier gas in order to study high energy conformers, excited and meta-stable species.

In some cases, during the collisional process, molecules may interact with inert gas atoms. During supersonic expansion, mixed weakly-bound complexes of the molecules of interest and an inert gas atom can be "frozen" out and isolated. The energy required for complex formation is absorbed by the unreacted carrier gas atoms. Adiabatic cooling allows for weakly-bound complexes[12] such as the Ar···AgI and the phosphine carboxamide···Ar complexes (chapter 4), to be isolated and spectroscopically characterized. It is also common to observe complexes formed between the molecules of interest and other molecules that may be present in the supersonic expansion, *i.e.* the imidazole-water complex (chapter 5) and the methylimidazole···water complexes (chapter 7).

The maximum velocity of an expanding inert gas is determined by the relationship;

$$u_{max} = \sqrt{\frac{2C_pT_0}{m}} \qquad (Eq.\,3.1)$$

where $C_p = \frac{5}{2}R$ is the constant-pressure molar heat capacity, T_0 is the temperature of the gas reservoir (in our case, room temperature ~ 20-21 ˚C) and m is the molar mass of the molecules. The maximum velocity of Ar is calculated to be 5.5231×10^4 cm s^{-1} which is greater than that of sound, 3.34×10^4 cm s^{-1}.

For the experiments described here, a free pulsed jet expansion was used where an inert carrier gas (Ar) is kept at a high backing pressure (2-7 bar) at one end and expands into a high vacuum chamber (low pressure 10^{-6}-10^{-7} mbar).

3.3 Heated Reservoirs and Band Heaters

Figure 3.3. General pulse valve and bespoke reservoir that attaches onto the face plate of the valve. Gas expands through the 0.7 mm orifice. (Design 1)

A bespoke heated reservoir that attaches onto the face plate of the pulse valve can be used for the study of liquid samples, as seen in figure 3.3. Molecules can be seeded directly into the flow of the expanding jet of the inert gas. The reservoir provides high control over the amount of sample that is used during an experiment and this will be further discussed in the chapters to follow when where heavy water D_2O and $H_2{}^{18}O$ were used.

The initial design (Design 1) of the reservoir is displayed in figure 3.3. The face plate of a general pulse valve was modified by the mechanical workshop at Newcastle university so that the four holes (~0.05 mm in diameter) that serve for seeding molecules into the gas flow are surrounding the orifice. A brass reservoir was machined so that it can be mounted on the modified face plate. The orifice channel on the brass reservoir is exactly in line with the orifice on the face plate so that supersonic expansion can be achieved despite the modifications and additions. An o-ring is placed around the reservoir so that the face plate-reservoir assembly can be pressurized without any gas or sample leaks. A schematic representation of sample seeding into the carrier gas flow is illustrated in figure 3.5.

It was necessary to rebuild the reservoir due to significant wear and tear damage to the o-ring groove on the brass part. High pressures in the reservoir caused the walls of the groove

to bend and eventually break leading to sample leaks. For the advanced reservoir design (Design 2), it was crucial not to place any o-rings on the brass parts. Instead, the o-ring was placed on the face plate. Design 2 of the reservoir and face plate are displayed in figure 3.4. This version of the reservoir combined with a band heater was used to improve the recorded spectrum of *N*-methylimidazole, as discussed in chapter 7. It was seen that filling the reservoir with glasswool before placing the liquid *N*-methylimidazole in, significantly extended the sample lifetime and allowed for long measurements (~72 h) without replacing the sample in reservoir.

Figure 3.4. The modified faceplate and reservoir assembly. The o-rings are placed on the steel faceplate instead of on the brass reservoir.

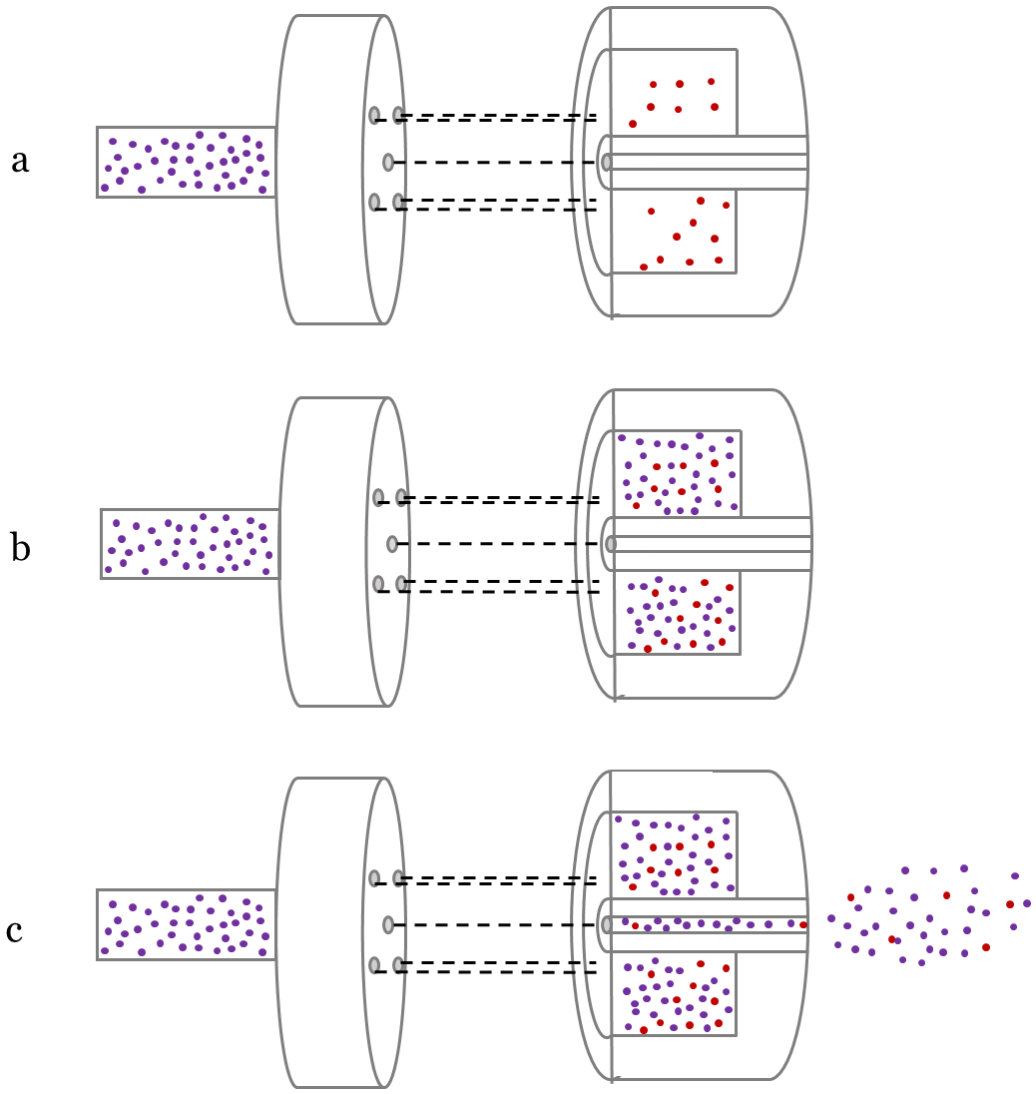

Figure 3.5. Schematic representation of the reservoir function illustrating how the sample (red dots) is seeded into the expanding jet of argon (purple dots). The dashed lines trace from the openings of the faceplate and onto the reservoir. (a) the pressurized argon buffer is in the gas line behind the reservoir. The sample is at 1 atm in the reservoir. (b) the reservoir is pressurized, and the sample is mixed with the argon buffer. (c) the argon-sample mix expands into the vacuum chamber.

3.4 Diffusion Pump and Vacuum Chamber

Gas phase measurements and supersonic expansion require a high vacuum chamber. The chamber is built from a stainless steel six-way cross with ISO 250 ports. The horn antennas attach on both sides of the chamber as shown in figure 3.6 while the vacuum system connects to the bottom port. The gas feedthrough to the pulse valve, the laser ablation source (section 3.5) and their power supplies are found on the back flange. A viewport on the front flange allows monitoring of the experiment and easy access to the chamber's interior. High vacuum (~10^{-6}-10^{-7} mbar) is achieved by use of a water-cooled diffusion pump (Edwards Diffstak 250) alongside two rotary mechanical pumps (Edwards EH250 and EM240). The pressure inside the chamber is constantly monitored by two pressure gauges (Pirani gauge, Edwards APG100 and Magnetron gauge) as it is crucial that it remains low so that the supersonic jet is cooled down efficiently. The chamber's interior is layered with microwave absorbent polyurethane foam to minimize background reflections interfering with molecular signals.

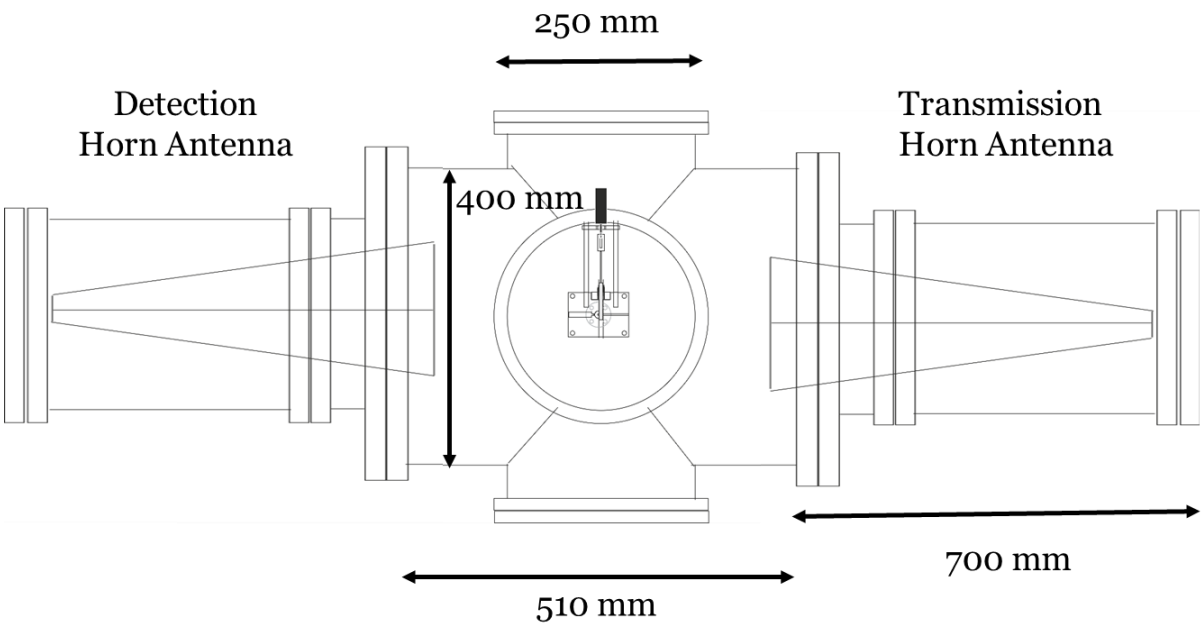

Figure 3.6. Front on schematic representation of the vacuum chamber. The transmission and detection horn antennas are found on both sides of the chamber.

3.5 Laser Ablation Source and Rod Preparation

Rapid gas phase generation of solid compounds is achieved by employing a pulsed nanosecond Nd:YAG laser (Photonics Solutions, Continuum, Minilite II) and a bespoke laser ablation source. The laser beam is focused on a rotating target rod which contains the molecules of interest and vaporizes material without destroying the molecular structure. The rod is positioned approximately 2-3 mm from the orifice of the pulse valve. A motor and a switch ensure that the rod is rotating and translating so that material from all over its length is exploited. A fresh surface of material is exposed to every laser pulse which was shown to increase the intensity of molecular signals. The target rods are prepared by grinding the solid samples of interest and mixing them with a small amount of metal powder (e.g Cu) which acts as a binder. The mixtures are then pressed into 5 or 13 mm diameter rods by a hydraulic bench press.

It was discovered that mixing in a small amount of desiccant such as $MgSO_4$ with hygroscopic and low melting point (~ 30-45 °C) substances significantly increases the lifetime and quality of the rods. The melting point of the tautomeric mixture of 4(5)-methylimidazole (Sigma-Aldrich, 98%) is 44-47 °C. The mixture was also moderately hygroscopic which made it impossible to press into a rod. Exposure to air and mixing with Cu powder turned the mixture into a paste. Besides Cu powder, $MgSO_4$, which has a high affinity for water, was used to bind the rod. Figure 3.7 shows the rod (A) containing 4(5)-methylimidazole: Cu powder: $MgSO_4$ (1:1:1 by mass) attached on the bespoke laser ablation source. Important parts of the ablation source are also labelled. The ablation source attaches onto the back flange of the vacuum chamber. The pulse valve attaches behind the block and the target rod so that the gas can expand through the orifice of the block (B) and efficiently entrain laser vaporized material into the supersonic jet.

The motor (C) (Faulhaber, DC 1524 024 SR) is found at the top of the source and translates the rod downwards until it reaches its limit and hit the switch (D) which will change the direction of translation and rotation. A bespoke power supply box, referred to as Laser Ablation Controller, is shown in figure 3.8 and allows control over the rotation speed (F) of the rod and reverse translation timings. Three control modes (G) referring to the length of the rod, short (< 2 cm), medium (> 2 cm, < 3 cm) and large (> 3 cm) are implemented and alongside the time dial (H) the reverse translation duration is controlled. Reverse translation can also be induced by pressing the start button (I) and paused by the stop button, a particularly useful function that allows fine optimization of the ablation source.

The laser beam (E, red dashed line) approaches the sample rod from the side and perpendicularly to the direction of the expanding gas.

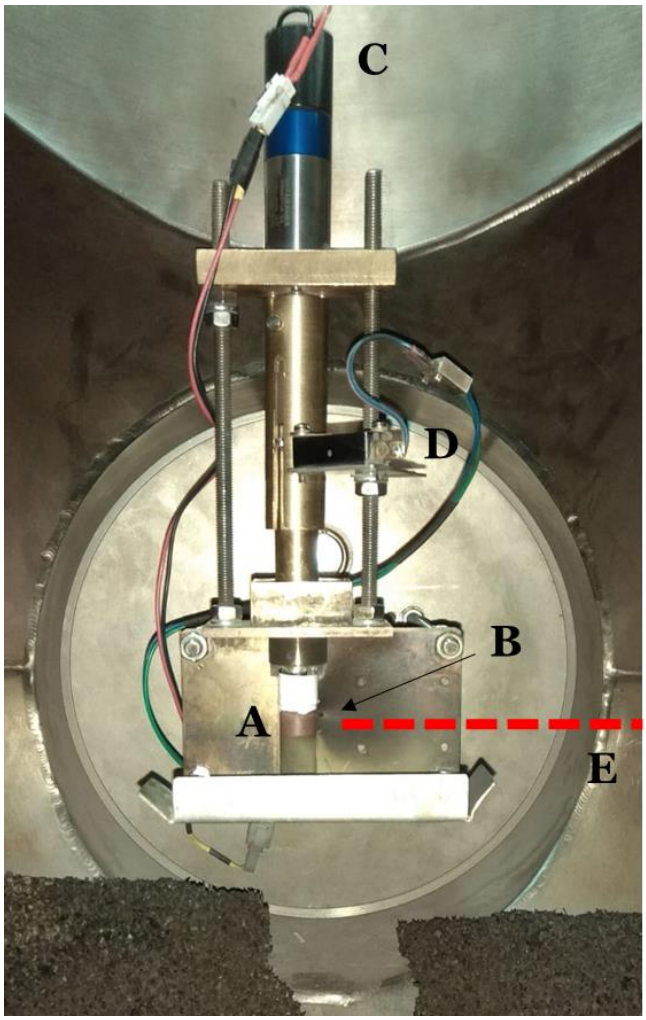

Figure 3.7. The bespoke laser ablation source attached on the back flange of the vacuum chamber. A: Rotating target rod, B: 0.7 mm orifice for gas expansion, C: DC motor, E: Pulsed laser beam.

Figure 3.8. The laser ablation controller.

Recent modifications of the laser ablation source include the use of the fundamental harmonic (1064 nm, 42 mJ/pulse, 10 ns) of the pulsed Nd:YAG laser. Previous laser ablation experiments within the group exclusively exploited the 2nd harmonic (532 nm, 15 mJ/pulse, 10 ns). It was shown that the 1064 nm wavelength could provide good conditions for organic complex formation and significantly boost molecular signals, for example, imidazole (chapter 5) and 4(5)-methylimidazole (chapter 6). The signal to noise ratio of the 4(5)-methylimidazole spectrum was improved by approximately a factor of 100 when the 1064 nm wavelength was used. It is not clear whether the wavelength doubling or the increase in output power have the most profound effect on the signal intensity. A test where the laser power is adjusted to approximately 15 mJ/pulse, equal to the power output of the 2nd harmonic, is necessary to answer that question. A portion of the spectrum is shown in figure 3.9 and some improved molecular signals are marked with asterisks (purple asterisk: 4-methylimidazole, green asterisk: 5-methylimidazole).

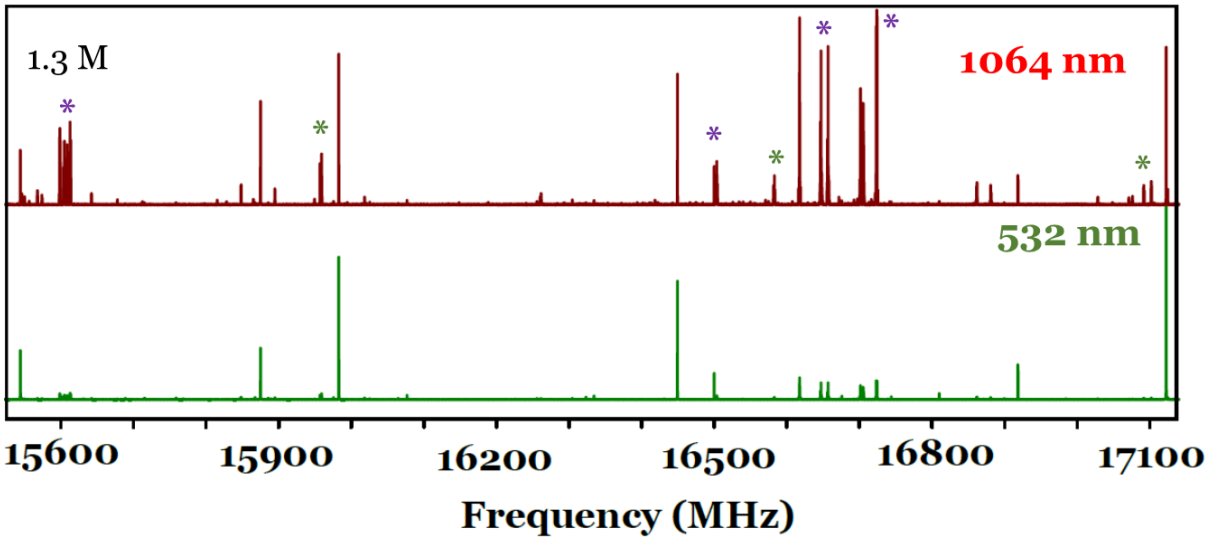

Figure 3.9. (top panel) The spectrum collected when vaporizing a rod made of 4(5)-methylimidazole: Cu: $MgSO_4$ (1:1:1 ratio) with the 1064 nm of the pulsed Nd:YAG laser. (bottom panel) The spectrum collected using the same rod composition with 532 nm wavelength. Some transitions for 4-methylimidazole and 5-methylimidazole are marked with purple and green asterisks, respectively. The scale on the *y*-axis is the same for both panels and the intensity units are arbitrary.

3.6 Excitation Circuit

3.6.1 The 7.0-18.5 GHz region

A chirped pulse spanning between 12.0 and 0.5 GHz is generated by a 20 GS/s AWG (Tektronix AWG7102) and passes through a low pass filter (Lorch, 12.2 GHz) and a triple balance mixer (MITEQ, TBO 440LWI-R). The chirped pulse is mixed against a 19 GHz reference signal provided by a Phase Locked Dielectric Resonant Oscillator (Herley CTI, PDRO, XPDRO-14373). The resulting higher frequency sideband (31.0-19.5 GHz) is filtered out (K&L Microwave, 3C60-19000/T100-O/O). Only the lower frequency band between 7.0 and 18.5 GHz which passes through a pre-amplifier (MITEQ, AMF-5F-080018-14-10P-R) can reach a 300 W Travelling-Wave Tube Amplifier (TWTA). Attenuation prior to amplification is required to protect the TWTA from high input signals. The chirped pulse broadcasts through a horn antenna (ATM 750-442-C3) to polarize the molecular ensemble formed by supersonic expansion inside the vacuum chamber.

3.6.2 The 2.0-8.0 GHz region

A chirped pulse spanning between 2.0 and 8.0 GHz is generated by a 20 GS/s AWG. No mixing is required, and the chirped pulse is attenuated and sent directly to the TWTA for amplification. It subsequently broadcasts via the horn antenna into the vacuum chamber. The PDRO and low pass filters are removed from the circuit.

3.7 Sample polarization

The excitation microwave pulse propagates perpendicularly to the flow direction of the supersonic expanding jet that contains the molecules of interest. The oscillating electric field of the microwave photons couples the electric field gradient of the polar molecules and energy is provided to induce molecular resonant rotations. The sample is polarized for 1 μs half-way between the horn antennas which are placed approximately 50 cm apart, as displayed in figure 3.6. The horn antennas are fixed in the vacuum chamber and do not require adjustment during measurements in either frequency range.

3.8 Detection Circuit

3.8.1 The 7.0-18.5 GHz region

Molecular emissions are detected in the form of a free induction decay (FID) after the pause of the microwave excitation pulse. The FID's are recorded by a second horn antenna. A pin diode limiter (ACLM-4539C6R1K) and a pin diode switch (Arra H8753-8OD) which only remains open during the collection of the FIDs, are used to protect the detection end from powerful microwave pulses. Molecular signals are amplified by a low noise amplifier (MITEQ, AMF-5F-08001800-14-10P-R). Given the frequency range of the oscilloscope (0.0-12.5 GHz), mixing prior to digitization is required at the detection end too. Mixing against the 19 GHz reference provided by the PDRO proceeds *via* a triple balance mixer and a low pass filter eliminates frequencies above 12 GHz. The input signal 12.0-0.5 GHz is digitized by a 100 GS/s oscilloscope (Tektronix DPO72304XS). The first 20 μs of the FID are digitally recorded in the time domain and then Fourier transformed to the frequency domain spectrum.

3.8.2 The 2.0-8.0 GHz region

The same principles mentioned above apply for the detection circuit of the 2.0-8.0 GHz range, but mixing is not required. Thus, the PDRO and low pass filters are removed from the detection end of the microwave circuit.

3.9 Nyquist Limit and Sampling

The bandwidth that is detectable by the oscilloscope in a single experimental cycle is dependent on the sampling rate and the Nyquist limit.[13] Sampling refers to the conversion of a continuous signal to a discrete signal. A sample is a datapoint of the resulting wavefunction. The maximum bandwidth that the oscilloscope is required to cover is 11.5 GHz. To achieve this bandwidth, the oscilloscope is set to operate at a sampling rate of 25 GS/s at most. This is referred to as the Nyquist frequency which is approximately half of the sampling rate. The sampling rate could be increased; however, this would compromise the digitizing and Fourier Transform speed.

3.10 Triggers and Timings (Fast Frame Acquisition Mode)

Fine control over the timings and duration of the different events of the experimental cycle is important in order to obtain high quality spectra and protect the spectrometer from irreversible damage. Timings are controlled by two delay generators, A (Quantum Composers, 9520 Series) and B (Quantum Composers, 9518 Series) and the AWG. These instruments provide high accuracy and phase stability in the time domain with less than 50 ps and 30 ps phase jitters, respectively.

The valve driver is triggered by Channel A of delay generator A which is set on internal trigger and that determines the T_0 point of the experiment. Typically, the duration of the gas pulse is determined by the inert gas in which the molecules of interest are seeded. In the case of Ar and Ne, the pulse duration is approximately 2 μs. The AWG is triggered for 51 μs by Channel B of the same delay generator approximately 1400 μs after T_0. To assist generation of intense molecular signals, the trigger delay to the AWG can be adjusted and it depends on i) the valve tension (*i.e.* how tight the valve is and how much gas flows through it), and ii) whether it is a laser ablation experiment. Usually, in a laser ablation experiment the trigger to the AWG is further delayed so that more time is allowed for the supersonic jet to interact with the laser plasma. The Q-Switch of the Nd:YAG is triggered for 100 μs by channel C, 1300 μs after T_0 and, as in Channel B, the delay can be adjusted with respect to the valve tension. As a rule of thumb, $100 - 400$ μs are allowed between the two trigger pulses. The flashlamps are controlled by Channel D and triggered 164 μs before the Q-Switch which was found to be the optimal delay for maximum laser power output.

The delay generator B is triggered externally by Channel 1 of the AWG (master trigger) operating at interleaved mode to exploit its sampling rate (20 GS/s) to the full. Channel A of delay generator B controls the opening times of the pin diode switch which must remain open during the high-power excitation pulse to protect the oscilloscope from damage. The switch remains opens for 2 μs with a 0.75 μs delay relative to the master trigger. A 1.5 μs trigger pulse is sent to the TWT by Channel B with 1 μs delay. When the switch is closed 2.75 μs after the master trigger, the first channel of the oscilloscope is triggered by Marker 1 of the AWG to collect a 20 μs FID.

Molecules in the supersonic jet remain in the collision free zone for approximately 200 μs. Considering the duration of the excitation pulse and the FID, the oscilloscope's fast frame

operation mode can be used. Each gas pulse can be polarized eight times, each followed by an FID collection. The AWG sends eight trigger pulses to delay generator B and to the oscilloscope which collects eight frames of FID's. The FIDs are co-added in the time domain and Fourier transformed to the frequency domain spectrum using a high-resolution window provided by Tektronix. Spectra are saved at given real time intervals by a Python script.

The pulsing rate of the valve and thus the repetition rate of the experiment is typically 2 Hz, which can be controlled by delay generator A. The maximum repetition rate that can be achieved is 4.5 Hz and this is limited by the pumping speed and the sampling rate of the oscilloscope.

3.11 Linewidths and Resolution (*x*-axis)

The linewidths and resolution of the frequency domain spectra are dependent on several factors. The linewidth at full width half maximum (FWHM) of the line intensity is inversely proportional to the FID duration. Given that the FID is recorded for 20 μs the resulting linewidths should be in the range of 50-60 kHz. It should be considered that the molecules travel inside the vacuum chamber and are not treated as stationary points. Phase jitters in the time domain in the range of 30 ps can also induce line broadening. Finally, the Fourier transform methods should be considered. Throughout this thesis, high resolution and Kaisser-Bessel windows were used, each offering different advantages. Sharper lines and accuracy in peak position is offered by the high-resolution window which also provides an increase in spectral resolution by approximately 10 kHz. The latter provides a better baseline resolution and allows to distinguish between molecular signals and noise. A decrease in spectral resolution is observed by broadening the FWHM by approximately 10 kHz. Considering all these factors, the reported linewidths are approximately 100 kHz. Typically, the error associated with recorded lines is approximately 10% of the linewidth. These arguments are only true for well isolated and well resolved lines, excluding effects that can be induced by presence of quadrupolar nuclei, *i.e.* nitrogen and deuterium which are known to cause hyperfine splittings, sometimes in the range of only a few kHz.

Accuracy in the measured transition frequencies and phase coherence in the time domain is provided by a Rb-clock (SRS FS725) to which the AWG, the PDRO and the oscilloscope are phase locked. The Rb-clock provides a 10 MHz reference signal with $\pm 5 \times 10^{-11}$ $\Delta f/f$ accuracy.

3.12 Spectral Intensity (*y*-axis)

It was discussed earlier that signal intensity of *e.g.* conformers may be reflected through their relative energies. The intensity of measured lines is also proportional to the square of the dipole moment of the molecule responsible for a molecular signal[13,14]. In CP-FTMW the intensity units in the *y*-axis are arbitrary. Conclusions about relative intensities of different species in the spectra can be drawn, however, insufficient information is provided so no arguments can be made regarding number density of a molecular species in the molecular ensemble.

In chapter 2, it was discussed that molecules are required to possess a permanent electric dipole to be studied with rotational spectroscopy. Intensities also depend on the population of the lower state of a transition. The ratio of the population between two states is given by;

$$\frac{N_J}{N_0} = (2J+1)exp\left(-\frac{E_J}{kT}\right) \qquad (Eq.3.2)$$

where N_0 is the number of molecules at equilibrium and N_J the number of molecules in a rotationally excited state.

Intensity of measured lines also depends on the power of the polarizing pulse and the pulse duration. This traces to a concept know as fast passage which arises when a frequency or range of frequencies are swept in a time relatively short to the dephasing time, *i.e.* FID. Chirped pulses must maintain phase coherence so that molecular emissions are also phase coherent and can be averaged in the time domain, as explained earlier. McGurk *et al.*[15] and Dreizler[16] approached molecular polarization by a chirped pulse by solving the optical Bloch equations modified to describe the electric dipole moment, equivalent to unpaired electrons in NMR. The molecular ensemble can be approximated as a two-level system of N molecules which undergo macroscopic polarization. The total component of the macroscopic dipole moment of the ensemble may be denoted as $\dot{P}$ and consists of two components, P_r and P_i. P_r is aligned with the direction of the electric field of the chirped pulse and P_i is $\pi/2$ phase separated. The populations of the two states are denoted as N_a and N_b, respectively, with $\Delta N = N_a - N_b$. A dephasing time is associated with each of N_a and N_b; these are T_1 and T_2. The Bloch equations, tailored to describe chirped pulse excitation followed by relaxation, are;

$$P_r + (\omega_0 - \omega)P_i + \frac{P_r}{T_2} = 0 \qquad (Eq. 3.3)$$

$$P_i - (\omega_0 - \omega)P_r + k\varepsilon\frac{\hbar}{4}k\Delta N + \frac{P_i}{T_2} = 0 \qquad (Eq. 3.4)$$

$$\frac{\hbar}{4}k\Delta N - k\varepsilon P_i + \frac{\hbar}{4}\frac{\Delta N - \Delta N_0}{T_1} = 0 \qquad (Eq. 3.5)$$

where $k = 2\mu_{ab}/\hbar$ with μ_{ab} being a matrix element of the dipole moment operator of a Hamiltonian[A] that includes the time-dependent perturbation element of the MW field and 2ε being the MW field amplitude.

Assuming that the experiment is concerned with fast passage phenomena, the MW pulse duration, t_p, will be much shorter than T_1 and T_2 relaxation times. Then equations 3.3-3.5 can be approximated to;

$$P_r + \Delta\omega P_i = 0 \qquad (Eq. 3.6)$$

$$P_i - \Delta\omega P_r + k^2\varepsilon\frac{\hbar}{4}\Delta N = 0 \qquad (Eq. 3.7)$$

$$\frac{\hbar}{4}\Delta N - \varepsilon P_i = 0 \qquad (Eq. 3.8)$$

If $P_r = 0$ and $P_i = 0$, it gives a solution to equations 3.6-3.8. It was shown that the maximum signal for a transition can be obtained for a resonant MW pulse is;

$$k\varepsilon t_p = (2n+1)\pi/2 \qquad n = 1,2,\ldots \quad (Eq. 3.9)$$

The electric field of a chirped pulse is given by;

$$E(t) = E_{max}e^{i\left(\omega_0 t_p + \frac{1}{2}\alpha t_p^2\right)} \qquad (Eq. 3.10)$$

where E_{max} is the maximum strength of the polarizing pulse, α is the sweep rate, and ω_0 is the initial frequency. The frequency range of the pulse, $\Delta\omega$, is proportional to the pulse duration, t_p;

$$\Delta\omega = \alpha t_p \qquad (Eq. 3.11)$$

The signal intensity can be expressed as a function of the sweep rate, α;

[A] The generalized Hamiltonian is $\hat{H} = \hat{H}_0 + \hat{H}_1$ where $\hat{H}_1$ is the time-dependence of the MW field.

$$Signal \propto \omega \mu^2 E_{max} \Delta N_0 \left(\frac{\pi}{\alpha}\right)^{\frac{1}{2}} \qquad (Eq. 3.12)$$

where ω is the frequency, μ is the electric dipole moment, E_{max} is the maximum strength of the polarizing pulse, and ΔN_0 is the population difference between states.[17–19]

In comparison to previous techniques such as that developed by Balle and Flygare, CP-FTMW requires more peak power to polarize a molecular ensemble. The Farby-Perot cavity of the Balle-Flygare spectrometer creates a resonance with the polarizing MW pulse that amplifies the signal to cover the bandwidth of approximately 1 MHz. The large bandwidth that is covered by CP-FTMW spectrometers requires alternative high-power sources such as TWT amplifiers discussed earlier.

3.13 References

1 S. L. Stephens, W. Mizukami, D. P. Tew, N. R. Walker and A. C. Legon, Molecular geometry of OC···AgI determined by broadband rotational spectroscopy and *ab initio* calculations, *J. Chem. Phys.*, 2012, **136**, 64306.

2 C. Medcraft, E. Gougoula, D. M. Bittner, J. C. Mullaney, S. Blanco, D. P. Tew, N. R. Walker and A. C. Legon, Molecular geometries and other properties of H_2O···AgI and H_3N···AgI as characterised by rotational spectroscopy and ab initio calculations, *J. Chem. Phys.*, 2017, **147**, 234308.

3 E. Gougoula, C. Medcraft, J. Heitkämper and N. R. Walker, Barriers to internal rotation in methylimidazole isomers determined by rotational spectroscopy, *J. Chem. Phys.*, 2019, **151**, 144301.

4 G. G. Brown, B. C. Dian, K. O. Douglass, S. M. Geyer, S. T. Shipman and B. H. Pate, A broadband Fourier transform microwave spectrometer based on chirped pulse excitation, *Rev. Sci. Instrum.*, 2008, **79**, 53103.

5 C. E. Cleeton and N. H. Williams, Electromagnetic waves of 1.1 cm wave-length and the absorption spectrum of ammonia, *Phys. Rev.*, 1934, **45**, 234–237.

6 J. Ekkers and W. H. Flygare, Pulsed microwave Fourier transform spectrometer, *Rev. Sci. Instrum.*, 1976, **47**, 448–454.

7 T. J. Balle and W. H. Flygare, Fabry-Perot cavity pulsed Fourier transform microwave spectrometer with a pulsed nozzle particle source, *Rev. Sci. Instrum.*, 1981, **52**, 33–45.

8 I. A. Finneran, D. B. Holland, P. B. Carroll and G. A. Blake, A direct digital synthesis chirped pulse Fourier transform microwave spectrometer, *Rev. Sci. Instrum.*, 2013, **84**, 83104.

9 R. E. Smalley, B. L. Ramakrishna, D. H. Levy and L. Wharton, Laser spectroscopy of supersonic molecular beams: Application to the NO2 spectrum, *J. Chem. Phys.*, 1974, **61**, 4363.

10 J. M. Hayes and G. J. Small, Supersonic Jets, Rotational Cooling, and Analytical Chemistry, *Anal. Chem.*, 1983, **55**, 565A–574A.

11 G. A. Cooper, C. Medcraft, E. Gougoula and N. R. Walker, Conformational isomers of trans -urocanic acid observed by rotational spectroscopy, *Phys. Chem. Chem. Phys.*, 2019, **21**, 9495–9503.

12 C. Medcraft, J. C. Mullaney, N. R. Walker and A. C. Legon, A complex Ar···AgI produced by laser ablation and characterised by rotational spectroscopy and ab initio calculations: Variation of properties along the series Ar···AgX (X=F, Cl, Br and I), *J. Mol. Spectrosc.*, 2017, **335**, 61–67.

13 W. Gordy and R. L. Cook, *Microwave molecular spectra*, John Wiley & Sons, Ltd, New York, 3rd., 1984.

14 J. M. Hollas, *High Resolution Spectroscopy*, Butterworth-Heinemann, 1982, pp. 87–148.

15 J. C. McGurk, T. G. Schmalz and W. H. Flygare, *Adv. Chem. Phys.*, 1974, **25**, 1–68.

16 H. Dreizler, Experiences with microwave Fourier transform spectroscopy of molecular gases, *Mol. Phys.*, 1986, **59**, 1–28.

17 S. T. Shipman and B. H. Pate, *Handb. High-resolution Spectrosc.*, 2011.

18 V. V Khodos, D. A. Ryndyk and V. L. Vaks, Fast-passage microwave molecular spectroscopy with frequency sweeping, *Eur. Phys. J. Appl. Phys.*, 2004, **25**, 203–208.

19 J. C. McGurk, T. G. Schmalz and W. H. Flygare, Fast passage in rotational spectroscopy: Theory and experiment, *J. Chem. Phys.*, 1974, **60**, 4181–4188.

Chapter 4. Spectrum of Phosphine Carboxamide and its Van der Waals Complex with Argon

4.1 Introduction

Primary phosphines are a class of chemicals with potential versatile applications in the synthesis of functionalized phosphorus compounds. The P–H bonds in primary phosphines can be extremely reactive allowing a number of compounds to be accessed[1]. However, primary phosphines, particularly those with low molecular weight, are notorious for being difficult to handle. Air sensitivity, noxious character, high toxicity, spontaneous combustion, and unpleasant, garlic-like odor are namely a few of the reasons why there is only a limited number of phosphorus-functionalized compounds.

In 2013, Jupp and Goicoechea[2] reported the synthesis of a primary phosphine that exhibits remarkable air and moisture stability. The compound, namely phosphine carboxamide (PCA) figure 4.2, is a phosphorus containing analogue of urea and thiourea arising from reaction of ammonium salts with 2-phosphaethynolate ions. Typically, the stability of primary phosphines arises from bulky groups surrounding the $–PH_2$ group or electronic effects stabilizing the lone pair of phosphorus. However, it was shown that the stability of PCA may arise due to a large bandgap between HOMO and LUMO and mixing of π-orbitals. NMR studies suggest an essentially planar arrangement in the carboxamide sub-unit with significant lone pair delocalization over the carbonyl and amide sites. Some minor delocalization is observed on the phosphine site with minimal interactions between

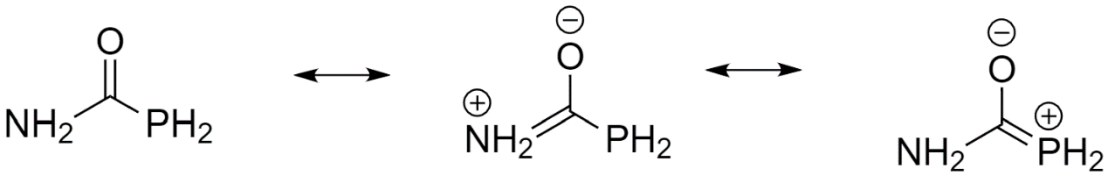

Figure 4.1. Schematic representation of the resonance canonicals of PCA.

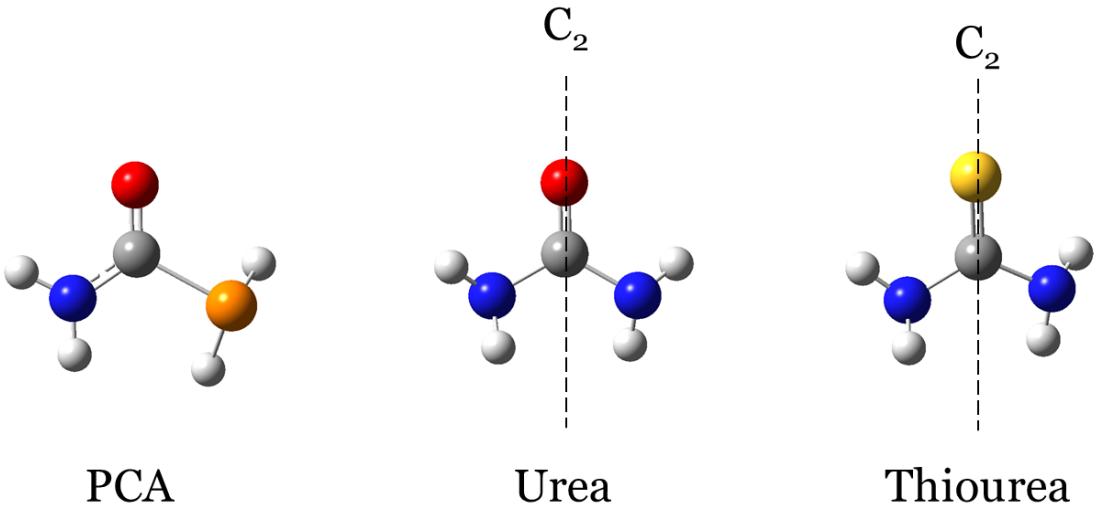

Figure 4.2. The structure of PCA and its structural analogues, urea and thiourea. Absence of a C_2 axis in PCA highlights the asymmetry of the molecule.

the phosphine lone pair and the carbonyl carbon. The resonance canonicals and chemical composition of PCA are depicted in figure 4.1.

Phosphorus is a biochemically significant element found in phospholipids, DNA, RNA and cell membranes.[3,4] It is the 18th most abundant element in the interstellar medium (ISM), behind carbon, nitrogen and oxygen.[5] Knowledge around the gas phase chemistry of P is limited but it is thought that P is formed at massive star regions and thrown into the ISM through supernovae explosions.[5] Up to date, a total of six P-containing compounds[6–11] have been detected in the ISM by means of their rotational spectrum, including PN, CP, HCP, PO, CCP and PH_3, in chronological detection order, in circumstellar envelopes around evolved stars. Only PN was detected at hot and dense regions of interstellar clouds[6] like Orion-KL and SgrB2. Formation of these compounds is yet to be fully comprehended but would likely require large activation energies involving endothermic and bond cleavage reactions of larger molecules.

These compounds account for a very small percentage of the total cosmic P suggesting that the rest of P is elsewhere or in a different form, *i.e.* condensed onto ice grains or in meteorites in the solid state. The main source of P in some meteorites is in the form of minerals like $(Fe, Ni)_3P$ (schreibersite) and phosphoric acids. Also, PH_3 is detected in the atmospheres of Jupiter and Saturn[12–14] whilst P^+ has been detected in diffuse clouds.[15] Given the limited number of confirmed P sources, it is no surprise that much research still needs to be done in order to unravel the gas phase chemistry of P compounds.

Unlike P, *N*-containing molecules are abundant in the ISM compared to P and significant steps have been made towards understanding the chemical reactions behind their formation. Linear unsaturated nitriles[16,17] are amongst the most common *N*-bearing molecules in the ISM. More complex molecules such as formamide[18] and *N*-methylformamide[19] have also been detected in both the ISM and comets and these are thought to play an important role in life formation on Earth. Urea (figure 4.2) was unambiguously detected in the ISM in 2019 by Belloche and co-workers[20] at SgrB2 by means of its rotational spectrum after a number of inconclusive studies.[21] Given that N and P are both group 15 elements, it is worth exploring whether more P-analogues of *N*-bearing compounds are detectable in the ISM. Here, we wish to bring PCA, a urea analogue, to the attention of astronomers and astrochemists as a possible interstellar P-containing candidate molecule.

Microwave spectroscopy studies of urea[22–25] and thiourea[26] allowed for interstellar detection of the former[20] and precise structure determination of both molecules in the gas phase. A planar arrangement between the heavy atoms O, C, N1 and N2 and S, C, N1 and N2, respectively, is reported for both molecules. A slightly pyramidal configuration is observed at the $–NH_2$ sites resulting in an overall C_2 point group for both urea and thiourea.[27] Solid phase urea and thiourea, however, are planar with C_{2v} geometry. A rigidly pyramidal configuration is adopted around the $–PH_2$ site of PCA, according to NMR and crystallography studies, giving rise to the asymmetry of the molecule. As in urea and thiourea, a planar O, C, N and P heavy atoms skeleton is reported for PCA.

A recent study by Mullaney *et al.* reported the formation of a hydrogen bonded complex between urea and isocyanic acid following laser ablation of urea in a supersonic expansion.[28] Thermal decomposition of urea results in formation of ammonia and isocyanic acid.[29] It is therefore suggested that isocyanic acid was generated as a side product of laser ablation of urea. It is reported that PCA will decompose to PH_3 and isocyanic acid when heated to 55-60 ˚C. Given that neither PH_3 nor isocyanic acid[30–33] have any detectable transitions in the frequency range covered by the CP-FTMW spectrometer at Newcastle University, it is not possible to say whether these products are formed as a result of laser ablation of PCA.

In this chapter, the microwave spectrum of three isotopologues of PCA (parent, ^{13}C, ^{15}N) are reported and spectroscopically characterized for the first time. The spectrum of a van der Waals complex between PCA and Ar was also recorded simultaneously and is reported

and characterized here. Typically, an Ar atom will coordinate with a molecule at the site where the largest electronic density is found. A plethora of such Ar complexes with both aromatic and non-aromatic molecules[34–41] have been studied with microwave spectroscopy. These systems can be exceptionally interesting giving rise to complex internal dynamics and given the symmetric charge distribution around Ar, they may assist with experimental benchmarking of quantum chemical calculations. Here, we explore the geometry of the PCA···Ar complex and compare the non-covalent interaction to that of urea···Ar and thiourea···Ar (unpublished work by Mullaney *et al.*).

4.2 Experimental

The microwave spectra of PCA and PCA···Ar were recorded in the 7.0-18.5 GHz frequency range. PCA was synthesized and provided by the group of Professor Jose M. Goicoechea at the University of Oxford and was used with no further purification. At ambient conditions, it is a white crystalline solid and, according to the Goicoechea group, decomposes at approximately 55-60 ˚C. To avoid decomposition due to heating, the preferred method of gas phase generation of PCA is laser ablation. Given that PCA is a non-commercial compound, limited information is known around its toxicity and other health hazards. The main concern around it was its behavior under high pressures applied by the hydraulic bench press used for solid sample preparation as described in chapter 3.

Conversations around safety and handling of primary phosphines were held with Dr Lee Higham (Newcastle University) prior to any experiments in order to assess and minimize risks. Initially, to avoid potential release of toxic PH_3, PCA was transferred from a glass sealed ampule into a Young flask and kept under a gentle N_2 flow. PCA powder was gently mixed with Zn powder (Sigma-Aldrich, ACS reagent, ≥99.9%, granular) in 1:1 by mass ratio and deposited on a solid Teflon core (5 mm diameter) covered in PVA glue (no dilution with water). The above method of sample preparation generated the initial spectrum of PCA and allowed for assignment of a significant number of molecular transitions. However, the PCA and Zn mix fell off the Teflon core within 10-15 minutes of laser ablation.

An alternative approach to sample preparation was taken where several 5 mm diameter rods containing PCA and Zn in an approximate 1:1 by mass ratio were prepared into a dye mold and pressing with the hydraulic bench press. A total of approximately 900 mg of PCA was available in three batches of 300 mg in vacuum sealed ampules. A total of five test rods were prepared, each containing approximately 18, 60, 100, 140 and 300 mg of PCA mixed with an equal amount of Zn. Given that PCA was a brand-new substance for our lab, the purpose of iteratively increasing its amount in the solid rod was to minimize any risks that might arise during sample preparation. Pressing of solid substances is the preferred method of generating solid rods for laser ablation.

To further mitigate the risks that may be imposed during sample preparation, the hydraulic bench pressed was moved into a fume cupboard. The pressing chamber was purged with N_2 prior, during and after sample pressing. The 5 mm dye mold was kept connected to a vacuum exhaust prior, during and for a few minutes after pressing to remove any PH_3. It

was found that with this method, it is safe to apply ~ 2 tons of pressure to a mixture containing approximately 300 mg of PCA and 300 mg of Zn.

4.3 Density Functional Theory

Geometry optimizations of PCA and PCA···Ar were performed. The starting geometry of PCA is according to the proposed structure. The B3LYP functional was used in conjunction with Dunning's aug-cc-pVTZ and D3BJ dispersion correction. The optimized geometries of PCA and PCA···Ar are displayed in figure 4.3 and the calculated spectroscopic parameters are in table 4.1. Atomic coordinates for the complete calculated geometry are given in appendix A.

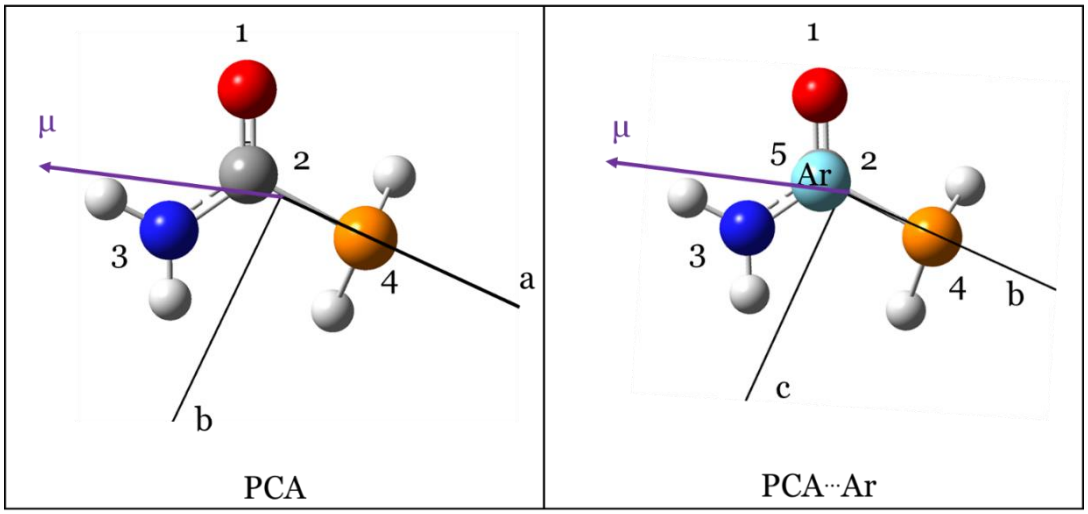

Figure 4.3. Calculated geometries of PCA and PCA···Ar at the B3LYP(D3BJ)/aug-cc-pVTZ level. The principal inertial axes are indicated as *a*, *b*, and *c* and the total dipole moment components μ expand from positive to negative partial charge.

Table 4.1. Calculated spectroscopic parameters at the B3LYP(D3BJ)/aug-cc-pVTZ level.

	PCA	PCA···Ar
A_e (MHz)[a]	10604	3405
B_e (MHz)	4550	1280
C_e (MHz)	3255	1119
$\chi_{aa}(N)$ (MHz)[b]	2.0561	–3.429
$\chi_{bb}(N) - \chi_{cc}(N)$ (MHz)	6.3238	–0.766
χ_{ab} (MHz)	–0.1719	2.0228
$\lvert\mu_a\rvert$, $\lvert\mu_b\rvert$, $\lvert\mu_c\rvert$ (D)[c]	0.2, 3.6, 0.8	0.9,0.1, 3.7

[a] Calculated rotational constants at equilibrium A_e, B_e and C_e.

[b] Calculated nuclear quadrupole coupling constants $\chi_{aa}(N)$ and $\chi_{bb}(N) - \chi_{cc}(N)$.

[c] Calculated dipole moments along the *a*-, *b*- and *c*-inertial axes.

4.4 Spectral analysis

4.4.1 Phosphine Carboxamide (PCA)

The jet-cooled microwave spectrum of PCA was recorded in the 7.0-18.5 GHz frequency range over the course of 50k FID's under the conditions described in section 4.2 and is displayed in figure 4. Several intense features are immediately observable alongside tens of less intense lines which are visible upon magnification of the spectrum. Examining the DFT calculated geometry (figure 3), PCA is a near-prolate asymmetric-top with the total dipole moment vector orienting from the carbonyl carbon to the direction of the amine group. The main dipole moment component is calculated to be closely aligned with the *b*-inertial axis of the molecule suggesting that the most intense lines will be ascribed to *R*- and *Q*-branch, *b*-type transitions of the patterns $J'_{1,J'-1} \rightarrow J''_{0,J''}$ and $J_{2,J-2} \rightarrow J_{1,J-1}$, respectively. These transitions were identified and exhibit hyperfine structure consistent with the presence of a N nucleus ($I = 1$) within PCA. The transitions were fit to Watson's A-reduced Hamiltonian[42] in the I^r representation as implemented in Western's Pgopher[43]. The overall Hamiltonian can be expressed as follows;

$$\mathcal{H} = \mathcal{H}_{\mathrm{R}} - \frac{1}{6}\boldsymbol{Q}(\mathrm{N}):\nabla\mathbf{E}(\mathrm{N})$$

where $\mathcal{H}_{\mathrm{R}}$ is the energy operator for a semi-rigid asymmetric top carrying information on the rotational and centrifugal distortion constants. The nuclear quadrupole moment dyadic is expressed as $\boldsymbol{Q}$ and $\nabla\mathbf{E}$ is the electric field gradient dyadic describing the coupling of the electric field gradient at the N nucleus with the applied electric field. The Hamiltonian has been discussed in detail chapter 2. The initial fit of the most intense transitions allowed for detection of several more *b*-type, as well as some *a*- and *c*-type transitions. A total of 99 hyperfine components were fit to yield the rotational constants A_0, B_0 and C_0, quartic centrifugal distortion constants Δ_J, Δ_{JK}, d_J and d_K, and nuclear quadrupole coupling constants $\chi_{aa}(N)$ and $\chi_{bb}(N) - \chi_{cc}(N)$ of table 4.4. The experimentally determined constants are in good agreement with the calculated constants. The values and the magnitude of the obtained centrifugal distortion constants are comparable to those determined for urea and thiourea which are structural analogues of PCA. Observation of *c*-type transitions is consistent with the proposal that a rigidly pyramidal configuration is

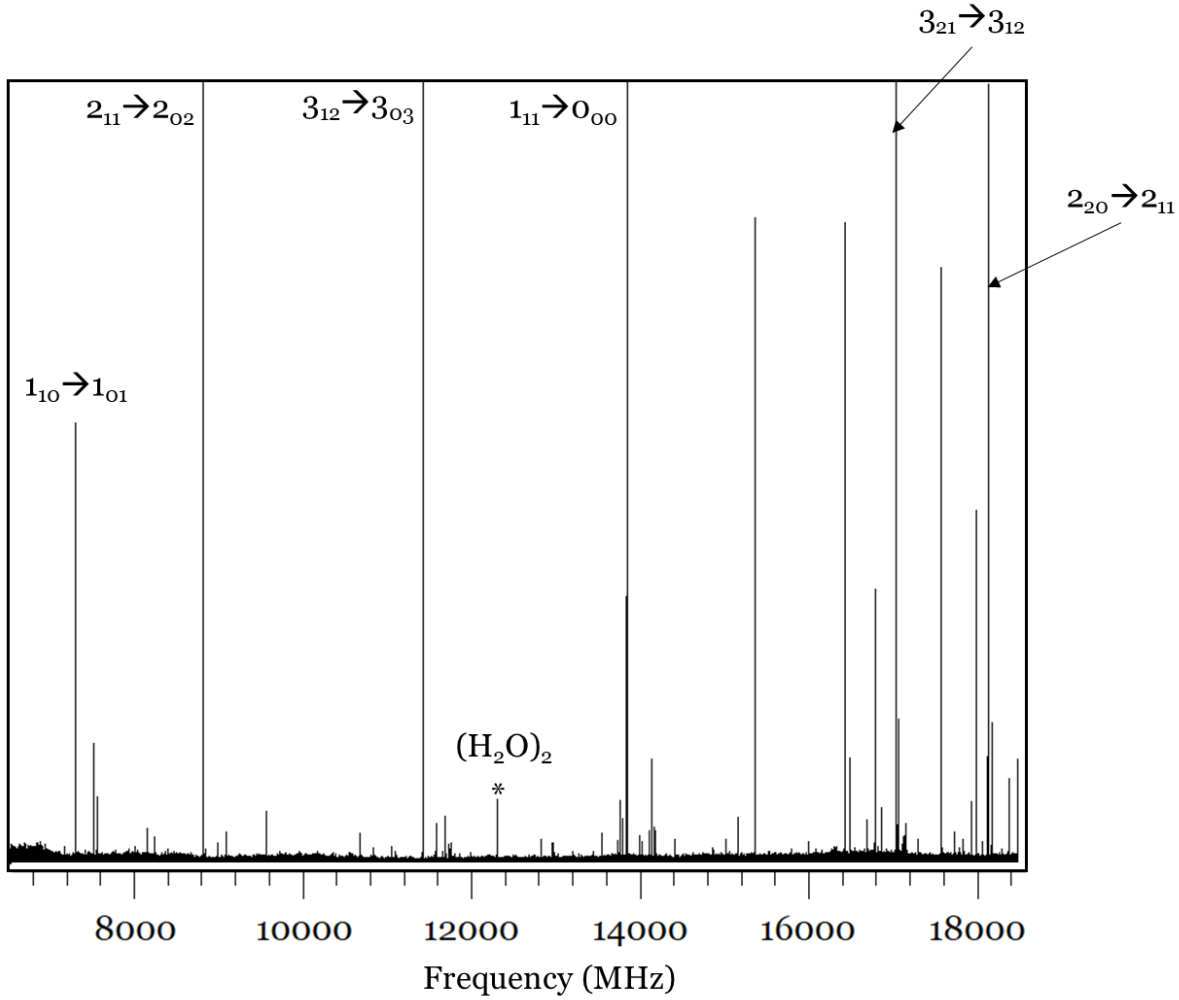

Figure 4.4. The broadband microwave spectrum of PCA recorded in the 7.0-18.5 GHz frequency range over the course of 50k FID's under the conditions described in the experimental section and the apparatus described in chapter 3. Some intense transitions of PCA are labelled with the appropriate quantum numbers. The black asterisk highlights a detectable transition for the $(H_2O)_2$.

adopted around the P atom leading the phosphine protons to point out of the *ab*-plane defined by the O, C, N and P atoms of PCA. *C*-type transitions were not reported in the spectra of urea and thiourea, consistent with the presence of a C_2 axis aligned with the carbonyl and the proposal of *syn* and *anti* -NH_2 groups resulting in cancelation of the relative dipole moment component. The barrier to inversion to planarity at the -PH_2 site was calculated to be 112.7 kJ mol^{-1} which cannot be surmounted at the temperature of the supersonic expansion (approximate rotational temperature is 2 K).

Transitions for HC_3N, CH_3CN and CH_2=CHCN (vinyl cyanide)[44–46] are also identified and these fragments are potentially side products of laser ablation of PCA in the solid target. Some transitions for the $(H_2O)_2$ are also readily identified with references to relevant

literature.[47] The spectra were examined for the presence of other P-bearing species such as HPCO, HC_3P and HC_5P which have previously been studied with rotational spectroscopy[48–50] but none of them could confidently be identified. Species of astrochemical importance such as PN, CP, HCP, PO and CCP do not yield any transitions in the frequency range covered by the Newcastle University Spectrometer so no conclusions can be drawn on whether these may be formed

The most intense peaks of parent PCA were observed with a signal to noise (S:N) ratio of 480:1. This allowed for observation of the ^{13}C and ^{15}N isotopologues of PCA in their natural isotopic abundance, 1.1% and 0.4%, respectively. Transitions of the ^{13}C and ^{15}N isotopologues of PCA were fitted with Watson's A-reduced Hamiltonian as described for the parent PCA. The centrifugal distortion constants were kept fixed at the values determined for the parent PCA and $\chi_{aa}(N)$ and$\chi_{bb}(N) - \chi_{cc}(N)$ were determined for ^{13}C.

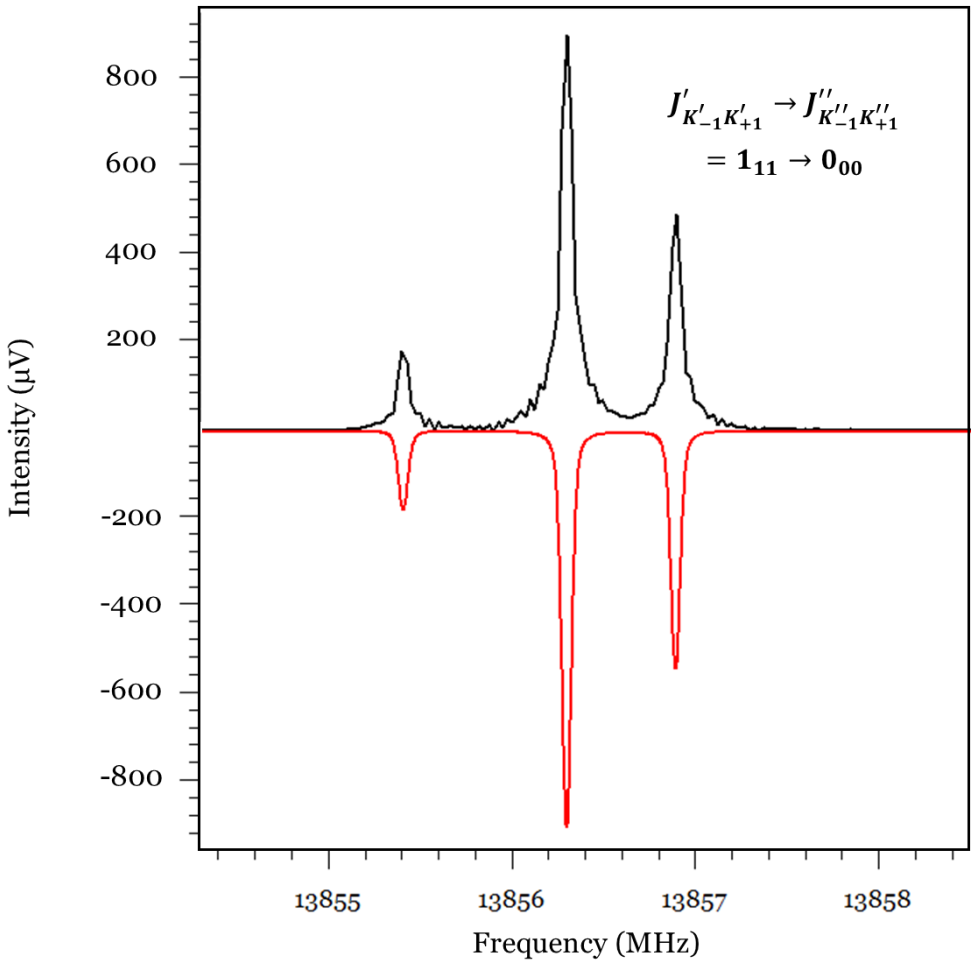

Figure 4.5. The $1_{11} \rightarrow 0_{00}$ transition of PCA parent isotopologue. Positive trace is a portion of the experimental spectrum and negative trace in red is the simulation produced with Pgopher.

Given that ^{15}N is not a quadrupolar nucleus ($I = 1/2$), hyperfine structure was not observed for that isotopologue. Isotopic shifts in rotational constants will be evaluated in order to determine atomic coordinates of the C and N atoms within PCA and subsequently determine a partial structure of gas phase PCA in section 4.5.1.

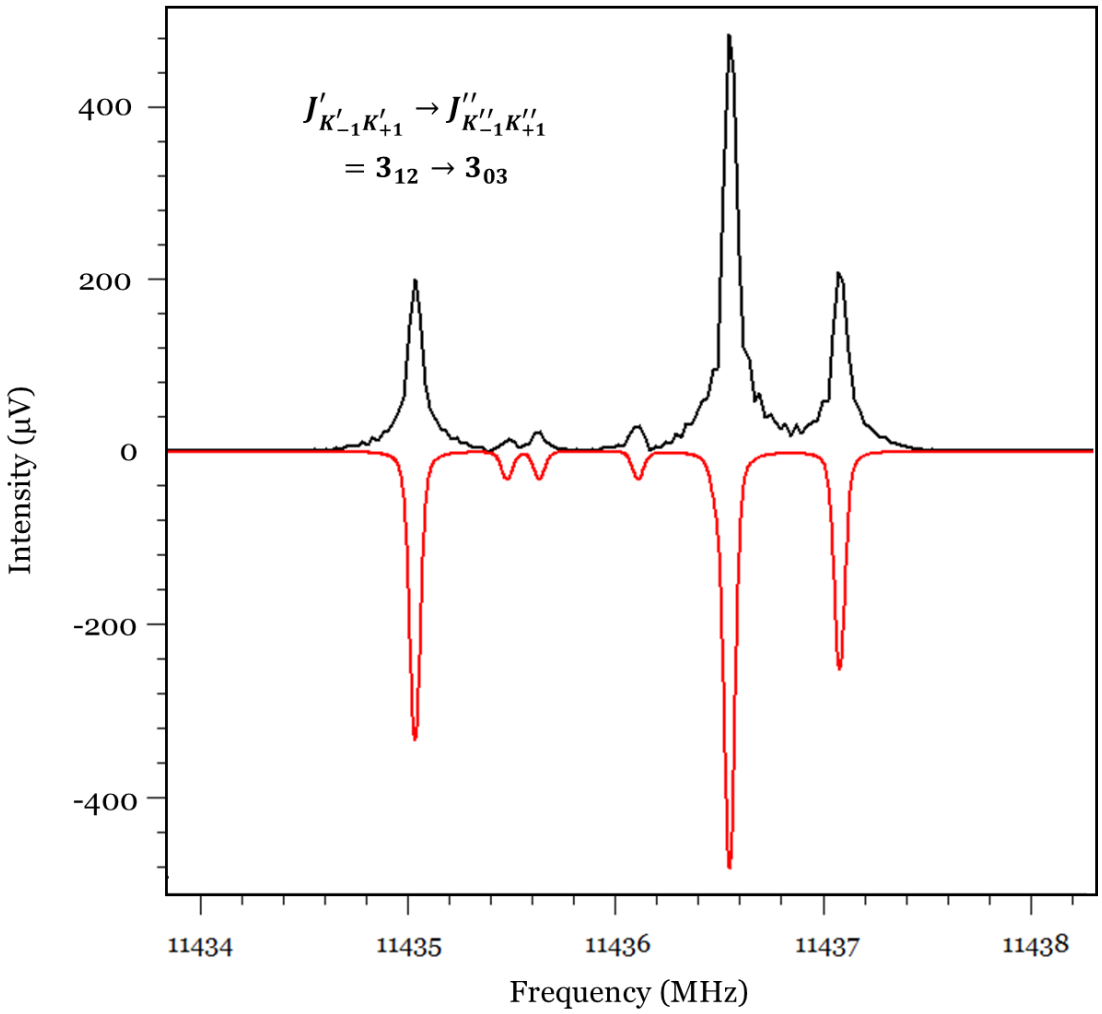

Figure 4.6. The $3_{12} \rightarrow 3_{03}$ transition of PCA parent isotopologue. Positive trace is a portion of the experimental spectrum and negative trace in red is the simulation produced with Pgopher.

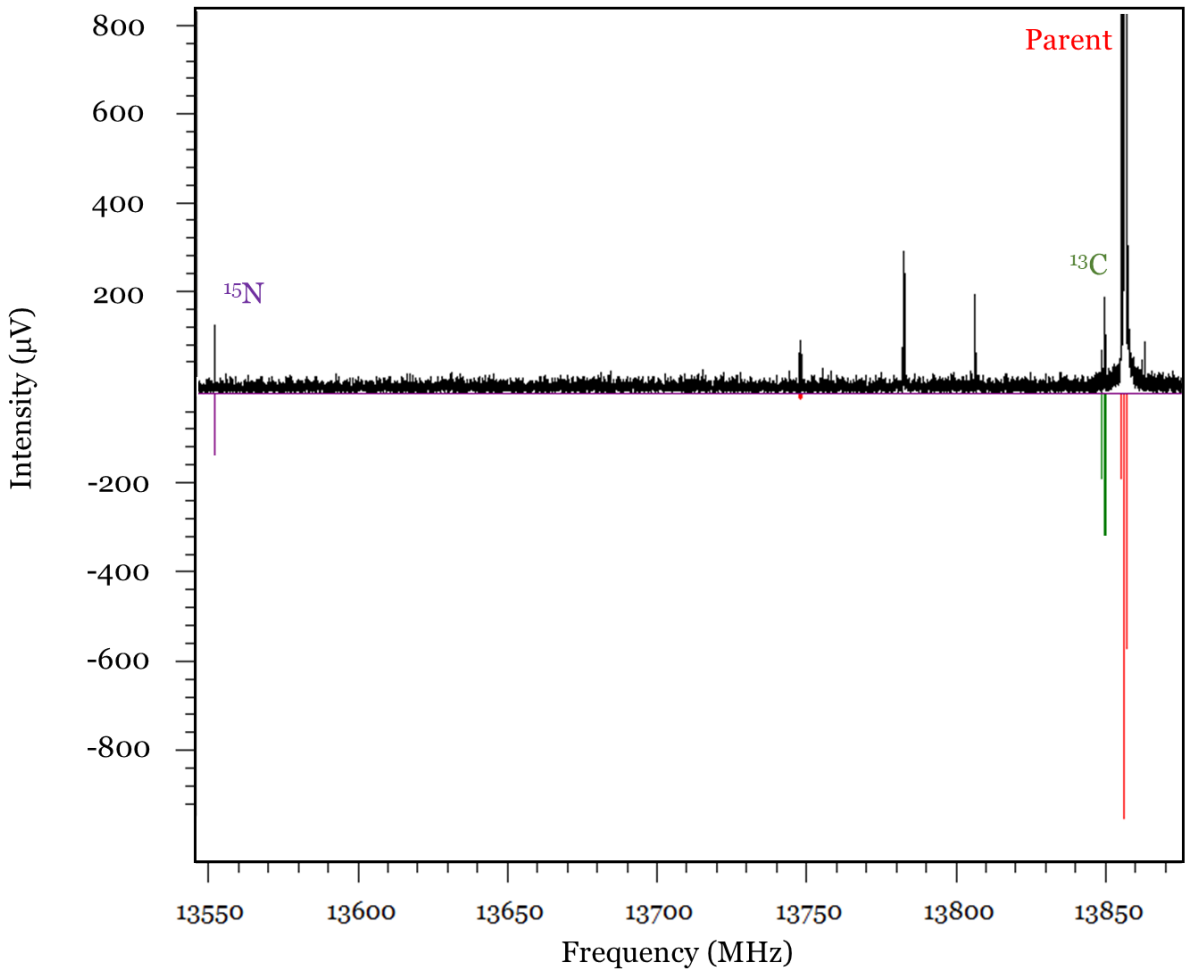

Figure 4.7. Expanded portion of the spectrum of PCA recorded over the course of 50k FID's. The $1_{11} \rightarrow 0_{00}$ transition of parent PCA and its ^{13}C and ^{15}N isotopologues are simulated in red, green and purple, respectively. The transitions for ^{13}C and ^{15}N are shifted according to predicted isotopic shifts. The intensities are also consistent with their relative isotopic abundances. The lines around 13800 MHz (no simulation at the negative trace) remain unassigned and may be attributed to species formed during laser ablation and supersonic expansion or contamination.

Table 4.2. Experimentally determined spectroscopic parameters generated by fitting the transition frequencies of PCA to Watson's A-reduced Hamiltonian with Pgopher. The percentage deviation from the calculated values for some parameters are shown in the third column.

	PCA	%
A_0 (MHz)	10581.3997(11) [a]	0.21%
B_0 (MHz)	4598.54643(50)	–1.07%
C_0 (MHz)	3275.00784(44)	–0.62%
Δ_J (kHz)	1.295(12)	-
Δ_{JK} (kHz)	6.949(87)	-
d_J (kHz)	0.398(11)	-
d_K (kHz)	5.01(16)	-
$\chi_{aa}(N)$ (MHz)	1.8974(39)	7.72%
$\chi_{bb}(N) - \chi_{cc}(N)$(MHz)	5.8660(69)	7.24%
χ_{ab} (MHz)	[–0.1719][b]	-
Δ_0 (u Å^2) [c]	–3.34689(2)	-
P_{cc} (u Å^2) [c]	1.67345(1)	-
κ [c]	–0.6377039(2)	-
N [d]	99	-
σ_{RMS} (kHz) [e]	7.6	-

[a] Numbers in parentheses are one standard deviation in units of the last significant figures.

[b] The off-diagonal χ_{ab} quadrupole component in square brackets is fixed to its DFT calculated value for the optimized geometry of PCA.

[c] Derived parameters. Inertial defect $\Delta_0 = I_c - I_b - I_c$, planar moment $P_{cc} = -\frac{1}{2}\Delta_0$ and Ray's asymmetry parameter $\kappa = \frac{2B_0 - A_0 - C_0}{A_0 - B_0}$ derived by evaluating the ground state rotational constants determined for PCA.

[d] Number of total hyperfine components included in the fit.

[e] Root mean square deviation of the fit.

Table 4.3. Experimentally determined spectroscopic parameters generated by fitting the transition frequencies of ^{13}C and ^{15}N isotopologues of PCA to Watson's A-reduced Hamiltonian with Pgopher.

	PCA ^{13}C	PCA ^{15}N
A_0 (MHz)	10580.6658(15) [a]	10332.8805(23)
B_0 (MHz)	4586.87320(84)	4535.9236(11)
C_0 (MHz)	3269.02618(84)	3219.3326(11)
Δ_J (kHz)	[1.295(12)] [b]	[1.295(12)]
Δ_{JK} (kHz)	[6.949(87)]	[6.949(87)]
d_J (kHz)	[0.398(11)]	[0.398(11)]
d_K (kHz)	[5.01(16)]	[5.01(16)]
$\chi_{aa}(N)$ (MHz)	1.884(17)	-
$\chi_{bb}(N) - \chi_{cc}(N)$(MHz)	5.866(20)	-
χ_{ab} (MHz)	{–0.1719} [c]	-
N [d]	18	6
σ_{RMS} (kHz) [e]	8.4	6.7

[a] Numbers in parentheses are one standard deviation in units of the last significant figures.

[b] Numbers in square brackets are fixed to the values determined for the parent PCA.

[c] The off-diagonal χ_{ab} quadrupole component in square brackets is fixed to its DFT calculated value for the optimized geometry of PCA.

[d] Number of total hyperfine components included in the fit.

[e] Root mean square deviation of the fit.

4.4.2 The PCA···Ar complex

After assignment of the spectrum of PCA and its ^{13}C and ^{15}N isotopologues and the fragmentation side-products, several lines remain unassigned at a S:N ratio of approximately 20:1. The observed patterns for these lines suggest that their molecular carrier will be heavier than PCA. Additionally, considering their hyperfine structure, it is likely that the molecular carrier will contain PCA and some other lighter molecule. Given that the signal intensity for $(H_2O)_2$ is low whereas argon is abundant in the supersonic expansion, this chapter will proceed on the basis that a complex between PCA and Ar is responsible for the origin of these lines. Structural analysis and evalution of rotational constants and nuclear quadrupole coupling will support this assumption in the sections to follow. Typically, presence of $(H_2O)_2$ in a spectrum, with reference to previously measured transitions[47], may result in the formation of complexes containing water (see chapter 7).

The calculated geometry of the PCA···Ar complex is a near prolate asymmetric top. Given the symmetric electron distribution of an Ar atom, it will typically interact with a molecule at the site where the most π-electron density is located. In PCA, Ar can coordinate above or below the plane defined by the O, C, N and P atoms. As a result, the inertial axes are positioned on the center of mass in the manner shown in figure 4.3. The *a*-axis is now going through the plane of PCA and is almost co-linear with the non-covalent bond between PCA and Ar. The strongest dipole moment component is expected to lie closely to the *c*-inertial axis and thus yield *c*-type transitions of the $J'_{1,J'-1} \rightarrow J''_{0,J''}$ series. Assignement of transitions was assisted by the rotational constants calculated at the B3LYP(D3BJ)/aug-cc-pVTZ level in table 4.1. Transitions were fitted to Watson's A reduced Hamiltonian as implemented in Pgopher and the form of the Hamiltonian was described earlier. Rotational constants A_0, B_0 and C_0, quartic centrifugal distortion constants Δ_J, Δ_{JK}, Δ_K, d_J and d_K, and nuclear quadrupole coupling constants $\chi_{aa}(N)$ and $\chi_{bb}(N) - \chi_{cc}(N)$ were determined and summarized in table 4.4. An expanded portion of the spectrum of PCA···Ar is shown in figure 4.8. The calculated rotational constants deviate by approximately 3-5% from the experimentally determined ones. The magnitude and the values of the centrifugal distortion constants are relatively large compared to those for the PCA monomer, consistent with the presence of a non-covalent bond between PCA and Ar. They are also comparable to those determined for urea···Ar and thiourea···Ar (unpublished work by J. C. Mullaney *et al.*)

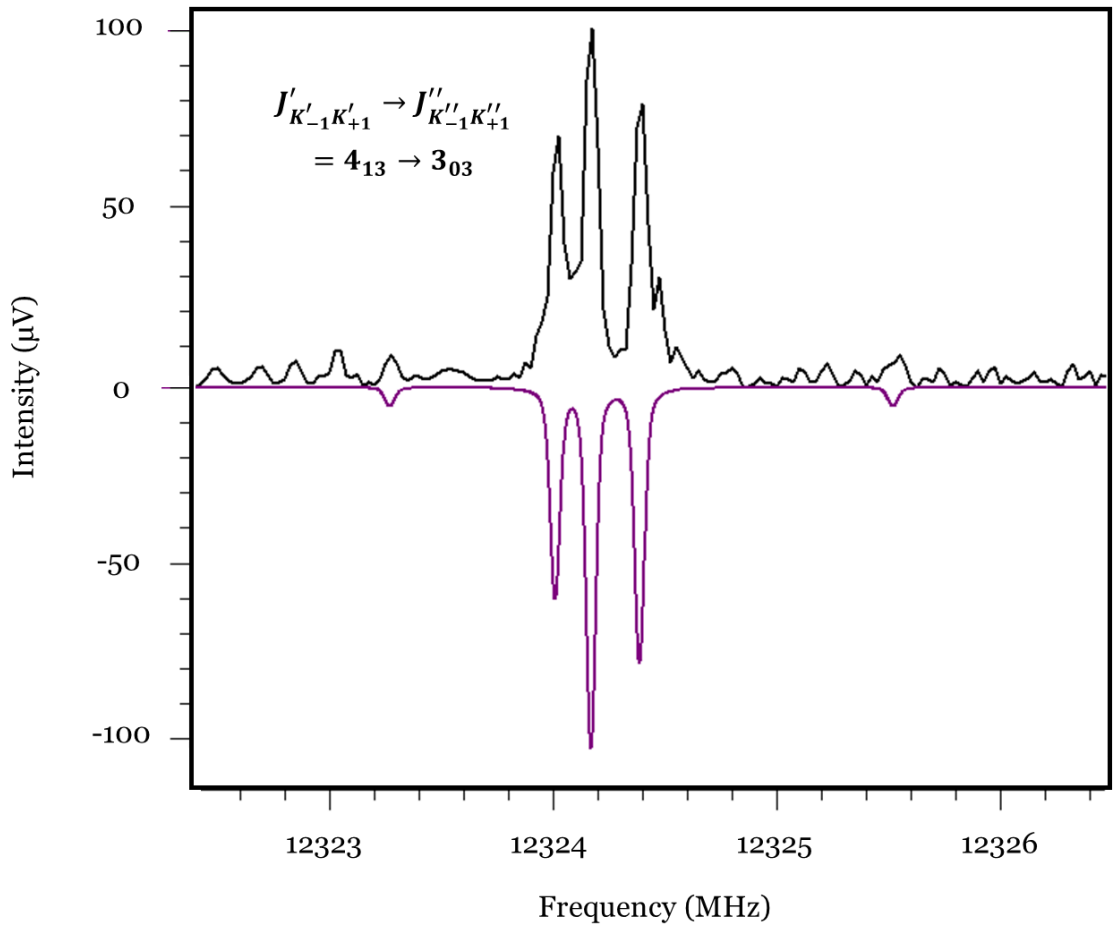

Figure 4.8. The $4_{13} \rightarrow 3_{03}$ *c*-type transition of the PCA···Ar complex. Upward trace (black) is the expanded portion of the experimental spectrum and downward trace (purple) is the simulated transition.

Table 4.4. Experimentally determined spectroscopic parameters generated by fitting the transition frequencies of PCA···Ar to Watson's A-reduced Hamiltonian with Pgopher.

	PCA···Ar	% [f]
A_0 (MHz)	3502.8520(10) [a]	–2.87%
B_0 (MHz)	1226.93915(45)	4.15%
C_0 (MHz)	1080.55182(70)	3.44%
Δ_J (kHz)	4.4561(48)	–
Δ_{JK} (kHz)	29.283(26)	–
Δ_K (kHz)	–1.228(98)	–
d_J (kHz)	0.6776(25)	–
d_K (kHz)	11.51(13)	–
$\chi_{aa}(N)$ (MHz)	–3.3338(99)	2.78%
$\chi_{bb}(N) - \chi_{cc}(N)$(MHz)	–0.396(16)	69.54%
χ_{ab} (MHz)	[2.0286]	–
Δ_0 (u Å^2) [c]	–88.47207(34)	–
P_{cc} (u Å^2) [c]	44.23604(17)	–
κ [c]	–0.8791336(7)	–
N [d]	76	–
σ_{RMS} [e]	11.6	–

[a] Numbers in parentheses are one standard deviation in units of the last significant figures.

[b] The off-diagonal χ_{ab} quadrupole component in square brackets is fixed to its DFT calculated value for the optimized geometry of PCA···Ar.

[c] Derived parameters. Inertial defect $\Delta_0 = I_c - I_b - I_c$, planar moment $P_{cc} = -\frac{1}{2}\Delta_0$ and Ray's asymmetry parameter $\kappa = \frac{2B_0 - A_0 - C_0}{A_0 - B_0}$ derived by evaluating the ground state rotational constants determined for PCA···Ar.

[d] Number of total hyperfine components included in the fit.

[e] Root mean square deviation of the fit.

[f] Percentage deviations of experimental and calculated constants as $\frac{A_{calc} - A_{exp}}{Aexp} \times 100$

4.5 Structure Determination

4.5.1 Geometry Interpretation of PCA

The asymmetry of PCA is evaluated in terms of Ray's asymmetry parameter which was defined in chapter 2 by means of equation 2.30. A value of –0.6377039(2) is obtained, consistent with the earlier assumption that PCA lies relatively close to the prolate limit. An insight into the gas phase structure of PCA can be provided by considering the planar (or second) moments. These can be calculated by means of equation 2.70. The degree of planarity in PCA can be evaluated by P_{cc}, as well as by the inertial defect $\Delta_0 = I_c - I_b - I_c$ (and therefore $P_{cc} = -\frac{1}{2}\Delta_0$ because of equation 2.73). For a planar molecule at equilibrium, the value of Δ_0 will be zero (and subsequently, $P_{cc} = 0$). Generally, in-plane vibrations at the zero-point will have a positive contribution to Δ_0 whilst out-of-plane vibrations (and mass distribution) result in a negative Δ_0 value.

For PCA, evaluating the rotational constants summarized table 4.3 by means of equation 2.72, we obtain a P_{cc} value of 1.67345 u Å^2. This value primarily arises by the PH_2 protons, supporting the previously observed geometry where a rigidly pyramidal configuration is adopted at the P atom. The barrier to inversion at the PH_2 site was calculated to be 112.7 kJ mol^{-1} (9421 cm^{-1}). Isotopic substitution with ^{13}C and ^{15}N does not significantly affect the value of P_{cc} which is consistent with the proposal that the heavy atoms O, C, N and P lie close to the *ab*-inertial plane. The P_{cc} values for the PCA analogues, urea and thiourea, are respectively 0.21285(8) u Å^2 and 0.05749(6) u Å^2 consistent with a planar geometry around the heavy atoms. In the solid state, the urea and thiourea monomers are planar at each NH_2 group with overall C_{2v} symmetry. However, in the gas phase, the lowest energy conformers have a C_2 symmetry with a pyramidal arrangement at each NH_2 group with the protons pointing at opposite sides of the heavy atoms plane. An alternative low-energy conformer with C_s symmetry is also possible. The NH_2 protons are pointing at the same side of the plane but with a low barrier to inversion at the NH_2 resulting in the planar C_{2v} conformer. Given the lack of data on deuterated isotopologues of PCA, it is not possible to establish the actual position of the NH_2 and PH_2 protons.

Table 4.5. Structural parameters derived by evaluating the ground state rotational constants PCA, urea and thiourea.

	PCA	Urea	Thiourea
κ	–0.63770354(28) [a]	0.702936(4)	–0.5280918(13)
Δ_0 (u Å^2)	–3.34685(4)	–0.42571(16)	–0.11499(11)
P_{cc} (u Å^2)	1.673427(21)	0.21285(8)	0.05749(6)
c-type [b]	yes	no	no

[a] Numbers in parentheses are one standard deviation in units of the last significant figure.

[b] Absence or presence of *c*-type transitions in the spectra is indicated by yes or no, respectively.

Considering the ground state rotational constants given in tables 4.2 and 4.3 for PCA and its ^{13}C and ^{15}N isotopologues, we can obtain structural information on the geometry of PCA. Upon ^{13}C isotopic substitution, the shift in rotational constants, particularly for A_0 is small, suggesting that C is positioned very close to the center of mass of PCA. The shifts in rotational constants caused by ^{13}C and ^{15}N isotopic substitution allow for calculation of the atomic r_s coordinates of the C and N atoms in PCA using Kraitchman's structure determination method[51–53] described in section 2.10.2. The method is implemented in the program KRA which is available from the PROSPE website.[54] The r_s coordinates derived from the ground state rotational constants of the available isotopologues are shown in table 4.6 alongside their fractional uncertainties expressed as Costain errors[55] in parentheses to account for the semi-rigid rotor behavior and vibration-rotation effects. The method can only generate the absolute values of the coordinates and for that reason the signs were implied by the DFT calculated geometry of PCA. Good agreement is observed between r_s and DFT calculated r_e coordinates. The C atom is positioned very close to the center of mass of PCA so the magnitudes of its atomic coordinates are small, consistent with the small shift in rotational constants caused by ^{13}C isotopic substitution. The *c*-coordinate of the N atom is calculated to be an imaginary number, suggesting that the N atom essentially lies in the *ab*-inertial plane, and it was therefore set to zero.

Table 4.6. Calculated (r_e) and experimentally determined (r_s, r_0) atomic coordinates of the C and N atoms of PCA.

	C(2)			N(3)		
	a/Å	b/Å	c/Å	a/Å	b/Å	c/Å
r_e	−0.5503	−0.0837	0.0207	−1.2301	1.0934	−0.0082
r_s	−0.5311(28)	−0.055(27)	0.018(84)	−1.2306(12)	1.0941(14)	0.0*
r_0	−0.57078(95)	−0.0667(16)	−0.0131(9)	−1.238(52)	1.086(27)	−0.0348(2)

Despite the limited amount of isotopic data, it is possible to partially evaluate the gas phase structure of PCA by making some structural assumptions. These assumptions are based on the r_s, r_e and X-ray structure of PCA[2] as well as on the gas phase structure of urea at the zero-point.[22–24] The partial effective r_0 structure of PCA is determined using Kisiel's STRFIT[56] available from the PROSPE website. The r_0 method, as described in section 2.10.3, proceeds through least-squares fitting of the experimental moments of inertia of the various isotopologues of PCA to a structure. The input *z*-matrix was constructed assuming the r_s bond length of the $(N-C)$ bond of PCA which is evaluated to be 1.346(23) Å. Given the structural similarities between PCA and urea, the carbonyl bond length was set to that determined for the gas phase urea at the zero-point. Likewise, the values for the $\angle(O-C-N)$ angle and the $r(N-H)$ bonds were set to the values for urea. The $\angle(O-C-N-P)$ dihedral angles was set to its DFT value 174.5°. The respective dihedral in urea and thiourea is 180°. Some subtle deviation from planarity is expected for PCA given the asymmetry and the low charge delocalization over the P center increasing the sp^3 character at the phosphine site. Finally, the $r(P-H)$ bond lengths were based on their DFT values rather than X-ray values; shortening of these bonds is expected due to crystal packing effects.

The *z*-matrix described above allows for determination of the $r_0(N-C)$, $\angle(N-C-P)$ and $\angle(N-C-O)$ structural parameters of PCA. These are summarized in Appendix A, table A3 alongside some r_s, r_e and X-ray data for PCA and some geometrical parameters for urea and thiourea determined with microwave spectroscopy. The experimentally determined r_0 parameters are consistent with the r_e geometry of PCA as well as with the X-ray structure. As it is expected, the X-ray value for the $r(N-C)$ bond is somewhat smaller than its r_s and r_0 value, possibly due to crystal and lattice effects.

The structures of urea and thiourea have been established by microwave spectroscopy[22–26] and X-ray crystallography.[27] Both molecules exhibit C_2 symmetry in the gas phase with the two NH_2 groups adopting a pyramidal configuration at the N atom at the zero-point. The main C_2 axis goes down the C=O bond resulting in the two N atoms being equivalent within each molecule. However, isotopic experiments with D indicated that the H atoms are not equivalent with one other, ruling out a possible planar structure and supporting the argument that a *syn-* and *anti-* configuration is adopted by each NH_2 group. Isotopic experiments with D-enriched PCA are pending and these will confirm the orientation of the protons in the NH_2 and PH_2 sites

4.5.2 Geometry Interpretation of PCA···Ar

To interpret the geometry of the PCA···Ar complex, it will be assumed that the structure of the PCA subunit remains unchanged upon complexation. This is a common approach that has been adopted for similar complexes reported in previous works cited here.[57–59] The polar coordinates, R_{cm}, ϑ and φ, depicted in figure 4.9 are employed and these are referenced with respect to the principal axes of PCA which will be denoted as α, β and γ, corresponding to the a, b and c-axes, respectively. R_{cm}, ϑ and φ are defined as the distance between the centers of mass of PCA and Ar, the angle between a vector along R_{cm} and the α-axis of PCA and the angle between the β-axis of PCA and the projection of R_{cm} on the $\beta\gamma$-plane of PCA, respectively. The program RGDFIT[59] available from the PROSPE website[54] was used to calculate the coordinates of the Ar atom within the frame of reference by fitting the rotational constants of PCA and PCA···Ar to a set of moments of inertia. The program calculates the position of the Ar atom by adding a point mass to the PCA monomer so that the coordinates of the added atom can be reproduced by the moments of inertia resulting from the rotational constants of PCA and PCA···Ar. The limitation of the program is that rotation-vibration effects are not accounted for so for this reason, Costain errors will be calculated based on the final geometry.

Given that inertial tensors are invariant over a 180° rotation about a principal inertial axis,[53] four possible sets of solutions are generated all of which can reproduce the experimentally determined zero-point rotational constants of PCA and PCA···Ar. This traces back to the Kraitchman method where only the relative magnitudes of each coordinate are generated. The four possible solutions are collected in table 4.8. Two of them can be ruled out by simple geometry considerations. The two sides of the heavy atoms plane of PCA are not equivalent due to the rigidly pyramidal arrangement at the PH_2 site. Solutions 3 and 4 require the Ar atoms to coordinate at the side of the plane where the PH_2 protons are directed. Considering the possible distance between Ar and the PH_2 protons, this distance is approximately 2 Å which would account for a relatively short van der Waals interaction. Solution 2 can also be ruled out as it requires the Ar atom to coordinate almost directly above the P atom. As it will be discussed later, the electronic density over the P site is low so based on trends observed in other Ar-containing complexes, this position is not favorable for Ar coordination. This is consistent with the proposal made by Goichoechea *et al.* that the PH_2 site exhibits more sp^3 character and lower delocalization of electronic charges,[2]

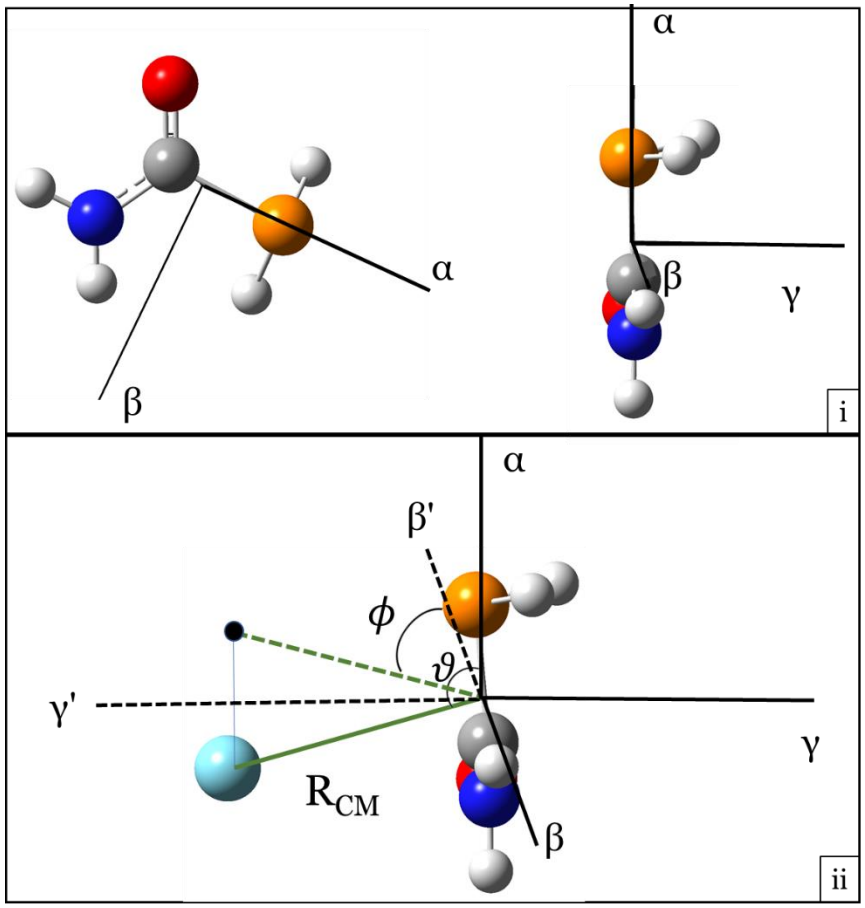

Figure 4.9. Calculated geometries of PCA and PCA···Ar. Definition of the α-, β-, and γ-axes of PCA (panel i) and definition of the polar coordinates R_{CM}, ϑ and φ in PCA···Ar with respect to the axes of PCA (panel ii).

Table 4.7. The possible solutions for the position of the Ar atom with respect to the inertial axes framework of PCA.

	R_{cm} (Å)	ϑ (˚)	φ (˚)
$R_{cm}, \vartheta, \varphi$	3.67813	17.493	36.973
$R_{cm}, \vartheta, \pi + \varphi$	3.67813	17.493	216.973
$R_{cm}, \pi - \vartheta, 2\pi - \varphi$	3.67813	162.507	323.027
$R_{cm}, \pi - \vartheta, \pi - \varphi$	3.67813	162.507	143.027
	α (Å)	β (Å)	γ (Å)
Ar	0.88328	0.66494	3.50804
	–0.88328	–0.66494	3.50804
	0.88328	–0.66494	–3.50804
	–0.88328	0.66494	–3.50804

The position of Ar with respect to the inertial axes of the PCA monomer may also be rationalized by considering the fitted nuclear quadrupole coupling constants of table 4.2 and 4.4 and the diagonalized components in terms of principal nuclear axes. These are discussed in detail in section 4.6 and are summarized in table 4.9. In order to derive structural information from the coupling of the monomer and that of the Ar complex, we need to assume that changes in the electric field gradient at the N nucleus caused by complexation are negligible. Examining the fitted nuclear quadrupole coupling constants of PCA and PCA···Ar, the α-axis of PCA is almost co-linear with the c-axis of PCA···Ar, $\chi_{aa}^{PCA}(N) = 1.8974 \cong \chi_{cc}^{Ar}(N) = 1.8649$ MHz. From the values of the diagonalized components, it follows that the x-nuclear axis on N is almost colinear with the α-axis of PCA and the c-axis of PCA···Ar. From the rotation matrix, the angle between the z-axis (on the N) and the a-axis of PCA···Ar is 21(4)°. The complementary angle between the vector along R_{CM} and the α-axis is within the uncertainty of that value. This is in support of the proposal that the Ar coordinates above or below the plane of PCA. However, given that the rotation matrix depends on the calculated values of $\chi_{ab}(N)$ for PCA and PCA···Ar, this approach will eventually be inconclusive regarding the exact position of Ar since there is no experimental $\chi_{ab}(N)$ values available.

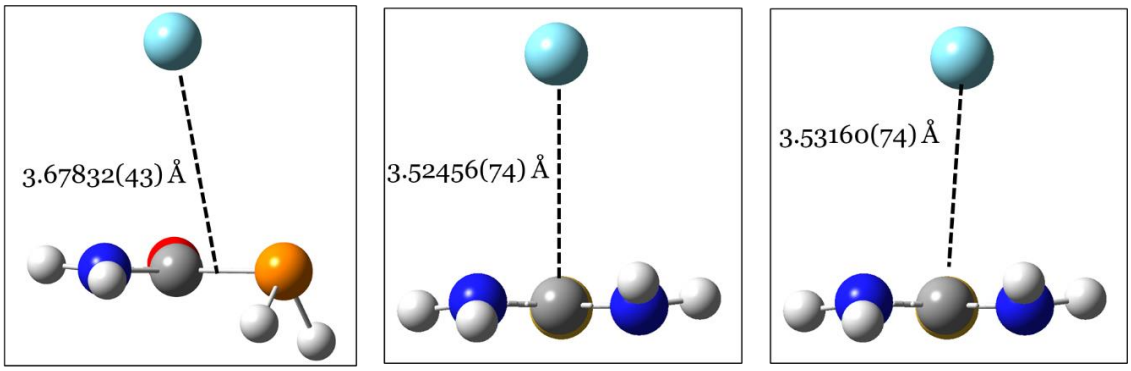

Figure 4.10. The R_{CM} length in the PCA···Ar, urea···Ar and thiourea···Ar indicated as a dashed line.

The R_{CM} length in PCA···Ar, urea···Ar and thiourea···Ar are displayed in figure 4.10. The differences in that coordinate between the three complexes is mainly due to the position of the center of mass in each of PCA, urea and thiourea. This distance is significantly longer in PCA···Ar due to the center of mass of PCA being between the C and P atoms. Given the high symmetry of urea and thiourea, the center of mass is placed very close to the C in each molecule.

4.6 Nuclear Quadrupole Coupling Constants of PCA and PCA···Ar

The ^{14}N nucleus, with nuclear spin $I = 1$, in PCA is responsible for the hyperfine splitting of the rotational transitions in both PCA and PCA···Ar. Upon rotation, the electric field gradient (efg) at the ^{14}N nucleus couples the efg of the oscillating electric field resulting in the said hyperfine splitting. The nuclear quadrupole coupling constants $\chi_{aa}(N)$ and $[\chi_{bb}(N) - \chi_{cc}(N)]$ determined for PCA and PCA···Ar can be used as a probe to detect changes that may occur in the electronic environment around the ^{14}N nuclei. These changes may be induced by, for example, Van der Waals forces between PCA and Ar or as it has been shown by Pinacho and co-workers in the case of ethylcarbamate,[60] as a result of progressive hydration and hydrogen bonding cooperativity. Complete determination of all nuclear quadrupole coupling components, both diagonal and off-diagonal components, can provide an insight into the electric field gradient at a given quadrupolar nucleus. However, often, only the diagonal components can be determined experimentally as the off-diagonal ones are usually small and thus only poorly determined.

The experimentally measured nuclear quadrupole constants of PCA and PCA···Ar are shown in tables 4.2 and 4.4, respectively. These are referenced in the principal inertial axes system, therefore direct comparisons of the quadrupole coupling of the ^{14}N nucleus in PCA and PCA···Ar cannot be made since the inertial axes are differently oriented. A common reference system needs to be implemented where a set of mutually perpendicular axes (principal nuclear axes), x, y, z, are placed on the ^{14}N nucleus. The principal nuclear quadrupole coupling components $\chi_{aa}(N)$, $\chi_{bb}(N)$ and $\chi_{cc}(N)$ are diagonalized such that the $\chi_{xx}(N)$, $\chi_{yy}(N)$ and $\chi_{zz}(N)$ components are generated along the x, y, z axes, respectively, using the program QDIAG, available from the PROSPE website.[54] This method has been discussed in detail in chapter 2 and the relative equations used for the transformations are 2.59 and 2.60.

Planarity around the heavy atoms O, C, N and P of PCA is established by the structure determination methods discussed earlier and previous X-ray crystallography data. In PCA, the out-of-plane *c*-axis is parallel to one of the principal nuclear axes on the ^{14}N atom whilst the *a*- and *b*-inertial axes are rotated by an angle of ϕ. However, in PCA···Ar, the inertial axes are rearranged as shown in figure 4.1 meaning that the *a*-axis goes through the plane of PCA within the complex. It follows that the *z*-nuclear axis on N is parallel to the *c*-axis of PCA and to the *a*-axis of PCA···Ar.

The nuclear quadrupole coupling constants in terms of principal nuclear axes $\chi_{xx}(N)$, $\chi_{yy}(N)$ and $\chi_{zz}(N)$ for PCA and PCA···Ar are shown in table 4.9. Assuming that changes to the efg on the N nucleus of PCA caused by attachment of Ar are negligible, the results reliably indicate that the assignment of PCA and PCA···Ar as molecular carriers is correct. Negligible changes to the efg of quadrupolar nuclei upon Ar attachment have also been discussed for other complexes.[59,61] The main differences between the diagonalized nuclear quadrupole coupling components in PCA and PCA···Ar mainly arise from low lying vibrations consistent with the weak van der Waals forces.

Table 4.8. The diagonalized nuclear quadrupole coupling constants χ_{xx}, χ_{yy} and χ_{zz} for PCA, urea and thiourea and their van der Waals complexes with Ar.

	PCA	Urea	Thiourea
$\chi_{xx}(N)$	1.764(42)[a]	1.715(54)	1.635(99)
$\chi_{yy}(N)$	2.118(42)	2.174(54)	2.433(99)
$\chi_{zz}(N)$	–3.8817(40)	–4.0889(29)	–4.0684(28)
η[b]	0.092(15)	0.112(19)	0.196(34)
	PCA···Ar	Urea···Ar	Thiourea···Ar
$\chi_{xx}(N)$	1.8649(94)	1.676(54)	1.843(84)
$\chi_{yy}(N)$	2.21(33)	2.149(86)	1.922(20)
$\chi_{zz}(N)$	–4.08(33)	–3.825(95)	–3.776(78)
η	0.085(81)	0.124(27)	0.021(23)

[a] Numbers in parentheses are one standard deviation in units of the last significant figure.

[b] The asymmetry parameter calculated as $\eta = \frac{\chi_{xx}(N)-\chi_{yy}(N)}{\chi_{zz}(N)}$ implies the nuclear axes orientation[53].

The diagonalized nuclear quadrupole coupling constants are further explored for urea and thiourea and their Ar complex analogues (urea···Ar and thiourea···Ar unpublished work by Mullaney *et al.*). The calculated values of χ_{ab} for PCA, urea and thiourea are –0.1719, –0.2227 and –0.3971 MHz, respectively, at the B3LYP(D3BJ)/aug-cc-pVTZ level. For their Ar complexes these values are 2.0286, –0.6235 and –0.9176 MHz. The values of the χ_{xx} and χ_{yy} components for PCA, urea and thiourea do not vary significantly across the series and the level of precision is relatively high, particularly for the out-of plane χ_{zz} component. For PCA and urea, the values of the χ_{xx} and χ_{yy} components are within the standard

deviation of one another, highlighting the similarities in the electronic environment around the N nucleus between the two molecules. These similarities may arise from the chemical composition of the amide site in both PCA and urea as well as the established planarity around the N, C and O atoms. For thiourea, an increase is observed for the χ_{yy} component which may be consistent with the presence of 3p-orbitals in the valence shell of S resulting in a better charge delocalization. However, the values of χ_{xx} and χ_{yy} are less accurately determined when compared to PCA and urea so no further conclusions can be drawn by looking at χ_{xx} and χ_{yy} alone. Of course, the values of the χ_{xx} and χ_{yy} for PCA, urea and thiourea are somewhat dependent on the chosen value of χ_{ab} upon which the rotation is reliant. However, the value of χ_{ab} is consistently calculated to be small across the three molecules and a standard deviation of 25% of its calculated value was assumed when the axes rotations were performed.

The value of the χ_{zz} component of PCA is determined to be significantly smaller than that of urea and thiourea. This may be explained by electron density being donated by the $2p_z$ orbital on N into the σ* orbitals of the P-H bonds on the phosphine group due to partial orbital overlap. To support this argument, an orbital population analysis was performed for the 2p orbitals on N for PCA, urea and thiourea following the Townes-Dailey model[62] and the equations used are given and explained in other works,[63,64] where $2p_z$ is the lone pair orbital. The model also allows for calculation of the ionic character of the N-H and N-C bonds, labelled as $i_\sigma(NH)$ and $i_\sigma(NC)$, respectively, as well as the covalent character of the N-C bond, $\pi_c(NC)$. The results of the analysis are summarized in table 4.10. The equations were used as reported in previous studies.

Table 4.9. Some parameters calculated for PCA, urea and thiourea by consideration of their nuclear quadrupole coupling constants.

	PCA	Urea	Thiourea
χ_{zz} (MHz)	–3.8817(40)	–4.0889(29)	–4.0684(28)
δ	2.36(40)%	3.06(51)%	5.32(93)%
$i_\sigma(NH)$	0.32	0.32	0.38
$i_\sigma(NC)$	0.29	0.28	0.30
$\pi_c(NC)$	0.22	0.19	0.13
$2p_x$	1.31	1.30	1.34
$2p_y$	1.32	1.32	1.38
$2p_z$	1.78	1.81	1.87

The lowest lone pair orbital population is observed for PCA supporting the assumption that electron density may be donated into the σ-orbitals of the P-H bonds on the phosphine group. The highest covalent character for the N-C bond, $\pi_c(NC)$, is also observed for PCA suggesting that the electron density concentrated at the amide site is high. The comparably highly populated orbitals on the N of thiourea are consistent the with the increase in the values of at χ_{xx} and χ_{yy} as discussed earlier.

The extent of electron transfer from the N atom toward the π-system may be evaluated by means of Goldstein's parameter,[46,53,65] δ, following the expression;

$$\delta = \frac{2}{3}\frac{\chi_{xx} - \chi_{yy}}{eQq_{n10}}$$

where eQq_{n10} is the contribution of a single p-electron to the total nuclear quadrupole coupling. It has been determined that eQq_{n10} for the N nucleus it is equal to –10 MHz. The Goldstein parameter may be rationalized as the difference in electron density between the p_x and p_y orbitals on N. The N lone pair in the p_z orbital is delocalized over the π-system of PCA as seen in the resonance canonicals in figure 4.1. It follows that δ is defined as the electron density deficit in the p_y orbital with respect to a fully occupied by a lone pair orbital. The value of δ may give an insight into the double bond character of the N–C bond and subsequently into the degree of electron delocalization across PCA.

For PCA, the value of δ is calculated to be 2.36% which is the smallest value across the PCA, urea, thiourea series suggesting that the N-C bond in PCA has low double bond character. The electron delocalization across PCA is relatively low with the phosphine group having minimal contribution to the resonance canonicals as it was also discussed by Goichoechea *et al*[2]. The electron density is shared across the O and N of the amide group. This argument is in harmony with the high degree of covalent character $\pi_c(NC)$ in PCA when compared to urea and thiourea. The highest double bond character is observed for the N-C bond in thiourea with that of urea being the intermediate case.

It must be noted that these analyses may only provide an initial insight into the orbital populations and the bond properties in PCA, urea and thiourea. These results will be dependent, to a certain extent, on the selected off-diagonal terms χ_{ab} calculated for each molecule. This determines the rotation of the quadrupole axes which in turn will determine the values of χ_{xx} and χ_{yy}. As DFT methods mainly consider charges in the valance shell of an atom and the value of χ_{ab} arises from unequal distribution of nuclear charges, the accuracy of this value will be affected. Even though an uncertainty of 25% was given to χ_{ab}, it is likely that its value will be somewhat dependant on the level of theory used to calculate it. It should also be noted that these analyses were primarily developed for halogen-bearing molecules, *i.e.* H-Cl, H-Br etc, for which the off-diagonal χ_{ab} components vanish and therefore the analysis depends on purely experimental data.[53]

4.7 Conclusions

The microwave spectra of three isotopologues of PCA (parent, ^{13}C, ^{15}N) and the van der Waals complex PCA···Ar were recorded in the 7.0-18.5 GHz frequency range with the CP-FTMW spectrometer at Newcastle University. Rotational constants, centrifugal distortion constants and nuclear quadrupole coupling constants are determined experimentally for both PCA and PCA···Ar. Rotational constants were evaluated to generate the r_s atomic coordinates of C and N for gas phase PCA and to determine the position of Ar with respect to the PCA skeleton. It is remarkable that a steeply pyramidal configuration is adopted at the $–PH_2$ site with the two H atoms pointing out of the plane defined by the heavy atoms of PCA. The electronic charge distribution around the N nucleus in PCA was explored and compared to that of its structural analogues, urea and thiourea. A concentration of electronic charge around the amide site of PCA is observed with the phosphine site having minimal contributions to delocalization of charges. The N-C bond in PCA was shown to have low double bond character when compared to urea and thiourea. PCA is one of a few examples of primary air-stable phosphines and its stability may arise from a large HOMO-LUMO gap and mixing of π-orbitals.

4.8 References

1 J. T. Fleming and L. J. Higham, Primary phosphine chemistry, Coord. *Chem. Rev.*, 2015, **297–298**, 127–145.

2 A. R. Jupp and J. M. Goicoechea, Phosphinecarboxamide: A Phosphorus-Containing Analogue of Urea and Stable Primary Phosphine, *J. Am. Chem. Soc.*, 2013, **135**, 19131–19134.

3 T. Kulakovskaya, *Biochem. Physiol. Open Access*, 2014, 04, 1–4.

4 A. E. White, New insights into bacterial acquisition of phosphorus in the surface ocean, *Proc. Natl. Acad. Sci.*, 2009, **106**, 21013 LP-21014.

5 J. Chantzos, V. M. Rivilla, A. Vasyunin, E. Redaelli, L. Bizzocchi, F. Fontani and P. Caselli, The first steps of interstellar phosphorus chemistry, *Astron. Astrophys.*, 2020, **633**, DOI:10.1051/0004-6361/201936531.

6 L. M. Ziurys, Detection of interstellar PN - The first phosphorus-bearing species observed in molecular clouds, *Astrophys. J.*, 1987, **321**, L81.

7 M. Guelin, J. Cernicharo, G. Paubert and B. Turner, Free CP in IRC+ 10216, *Astron. Astrophys.* (Berlin. Print), 1990, **230**, L9–L11.

8 M. Agúndez, J. Cernicharo and M. Guélin, Discovery of Phosphaethyne (HCP) in Space: Phosphorus Chemistry in Circumstellar Envelopes, *Astrophys. J.*, 2007, **662**, L91–L94.

9 E. D. Tenenbaum, N. J. Woolf and L. M. Ziurys, Identification of Phosphorus Monoxide (X 2Πr) in VY Canis Majoris: Detection of the First P–O Bond in Space, *Astrophys. J.*, 2007, **666**, L29–L32.

10 D. T. Halfen, D. J. Clouthier and L. M. Ziurys, Detection of the CCP Radical (X2Πr) in IRC +10216: A New Interstellar Phosphorus-containing Species, *Astrophys. J.*, 2008, **677**, L101–L104.

11 M. Agúndez, J. Cernicharo, L. Decin, P. Encrenaz and D. Teyssier, Confirmation of circumstellar phosphine, *Astrophys. J. Lett.*, 2014, **790**, L27.

12 L. N. Fletcher, G. S. Orton, N. A. Teanby and P. G. J. Irwin, *Icarus*, 2009, **202**, 543–564.

13 H. P. Larson, U. Fink and R. R. Treffers, Phosphine in Jupiter's atmosphere - The evidence from high-altitude observations at 5 micrometers, *Astrophys. J.*, 1977, **211**, 972.

14 H. P. Larson, U. Fink, H. A. Smith and D. S. Davis, The middle-infrared spectrum of Saturn - Evidence for phosphine and upper limits to other trace atmospheric constituents, *Astrophys. J.*, 1980, **240**, 327.

15 M. Jura and D. G. York, Observations of interstellar chlorine and phosphorus, Astrophys. J., 1978, 219, 861.

16 R. L. Snell, F. P. Schloerb, J. S. Young, a. Hjalmarson and P. Friberg, Observations of HC3N, HC5N, and HC7N in molecular clouds, *Astrophys. J.*, 1981, **244**, 45.

17 M. C. McCarthy, E. S. Levine, A. J. Apponi and P. Thaddeus, Experimental Structures of the Carbon Chains HC7N, HC9N, and HC11N by Isotopic Substitution, *J. Mol. Spectrosc.*, 2000, **203**, 75–81.

18 G. R. Adande, N. J. Woolf and L. M. Ziurys, Observations of interstellar formamide: availability of a prebiotic precursor in the galactic habitable zone, *Astrobiology*, 2013, **13**, 439–453.

19 A. Belloche, A. A. Meshcheryakov, R. T. Garrod, V. V Ilyushin, E. A. Alekseev, R. A. Motiyenko, L. Margulès, H. S. P. Müller and K. M. Menten, Rotational spectroscopy, tentative interstellar detection, and chemical modeling of *N*-methylformamide, *A&A.*, 2017, **601**

20 A. Belloche, R. T. Garrod, H. S. P. Müller, K. M. Menten, I. Medvedev, J. Thomas and Z. Kisiel, Re-exploring Molecular Complexity with ALMA (ReMoCA): interstellar detection of urea, *A&A.*, 2019, **628**

21 I. Fourré, L. Rosset, H. Chevreau and Y. Ellinger, About the detection of urea in the interstellar medium: the energetic aspect, *A&A.*, 2019, **628**

22 S. Kassi, D. Petitprez and G. Wlodarczak, Microwave spectrum of isotopic species of urea (NH2)2CO, *J. Mol. Spectrosc.*, 2004, **228**, 293–297.

23 U. Kretschmer, D. Consalvo, A. Knaack, W. Schade, W. Stahl and H. Dreizler, The 14N quadrupole hyperfine structure in the rotational spectrum of laser vaporized urea observed by molecular beam Fourier transform microwave spectroscopy, *Mol. Phys.*, 1996, **87**, 1159–1168.

24 R. D. Brown, P. D. Godfrey and J. Storey, The microwave spectrum of urea, *J. Mol. Spectrosc.*, 1975, **58**, 445–450.

25 P. D. Godfrey, R. D. Brown and A. N. Hunter, The shape of urea, *J. Mol. Struct.*, 1997, **413**, 405–414.

26 A. Lesarri, S. Mata, S. Blanco, J. C. López and J. L. Alonso, A rotational study of laser ablated thiourea, *J. Chem. Phys.*, 2004, **120**, 6191–6196.

27 S. B. Hendricks, The crystal structure of urea and the molecular symmetry of thiourea, *J. Am. Chem. Soc.*, 1928, **50**, 2455–2464.

28 J. C. Mullaney, C. Medcraft, D. P. Tew, L. Lewis-Borrell, B. T. Golding, N. R. Walker and A. C. Legon, Cooperative hydrogen bonds form a pseudocycle stabilizing an isolated complex of isocyanic acid with urea, *Phys. Chem. Chem. Phys.*, 2017, **19**, 25080–25085.

29 P. M. Schaber, J. Colson, S. Higgins, D. Thielen, B. Anspach and J. Brauer, Thermal decomposition (pyrolysis) of urea in an open reaction vessel, *Thermochim. Acta,* 2004, **424**, 131–142.

30 L. H. Jones, J. N. Shoolery, R. G. Shulman and D. M. Yost, The Molecular Structure of Isocyanic Acid from Microwave and Infra-Red Absorption Spectra, *J. Chem. Phys.*, 1950, **18**, 990–991.

31 K. Yamada, Molecular structure and centrifugal distortion constants of isocyanic acid from the microwave, millimeter wave, and far-infrared spectra, *J. Mol. Spectrosc.*, 1980, **79**, 323–344.

32 S. G. Kukolich, A. C. Nelson and B. S. Yamanashi, Molecular-beam microwave spectra of isocyanic acid and isocyanic acid-d, *J. Am. Chem. Soc.*, 1971, **93**, 6769–6771.

33 W. H. Hocking, M. C. L. Gerry and G. Winnewisser, The Microwave and Millimetre Wave Spectrum, Molecular Constants, Dipole Moment, and Structure of Isocyanic Acid, HNCO, *Can. J. Phys.*, 1975, **53**, 1869–1901.

34 J. J. Oh, I. Park, R. J. Wilson, S. A. Peebles, R. L. Kuczkowski, E. Kraka and D. Cremer, Structure of the chlorobenzene-argon dimer: Microwave spectrum and ab initio analysis, *J. Chem. Phys.*, 2000, **113**, 9051–9059.

35 T. Brupbacher and A. Bauder, Rotational spectrum and dipole moment of the benzene-argon van der Waals complex, *Chem. Phys. Lett.*, 1990, **173**, 435–438.

36 F. Lorenzo, A. Lesarri, J. C. López and J. L. Alonso, Rotational spectrum and structure of the oxetane-argon Van der Waals complex, *Chem. Phys. Lett.*, 1998, **286**, 272–276.

37 U. Kretschmer, W. Stahl and H. Dreizler, *Zeitschrift fur Naturforsch. - Sect. A J. Phys. Sci.,* 1993, **48**, 1107–1110.

38 W. Caminati, P. G. Favero and B. Velino, Adducts of aromatic molecules with rare gases: rotational spectrum of pyrazole–argon, *Chem. Phys.*, 1998, **239**, 223–227.

39 S. Melandri, J. C. López, P. G. Favero, W. Caminati and J. L. Alonso, Rotational spectrum and dynamics of tetrahydrofuran–argon, *Chem. Phys.*, 1998, **239**, 229–234.

40 L. Kang, A. R. Keimowitz, M. R. Munrow and S. E. Novick, Rotational spectra of argon acetone: A two-top internally rotating complex, *J. Mol. Spectrosc.*, 2002, **213**, 122–129.

41 T. A. Hu, D. G. Prichard, L. H. Sun, J. S. Muenter and B. J. Howard, The vibration-rotation spectrum of the argon-acetylene van der Waals complex, *J. Mol. Spectrosc.*, 1992, **153**, 486–496.

42 J. K. G. Watson, Determination of centrifugal distortion coefficients of asymmetric-top molecules. III. Sextic coefficients, *J. Chem. Phys.*, 1968, **48**, 4517–4524.

43 C. Western, PGOPHER, a program for rotational, vibrational and electronic spectra, *J. Quant. Spectrosc. Radiat. Transf.*, 2015, **186**, 221–242.

44 S. Thorwirth, H. S. P. Müller and G. Winnewisser, Millimeter- and submillimeter-wave spectrum of HC3N in the ground and vibrationally excited states, *J. Mol. Spectrosc.*, 2000, **204**, 133–144.

45 A. Bauer, Rotational spectrum of acetonitrile CH3C14N and CH3C15N in a doubly excited degenerate vibrational state, *J. Mol. Spectrosc.*, 1971, **40**, 183–206.

46 W. S. Wilcox, J. H. Goldstein and J. W. Simmons, The microwave spectrum of vinyl cyanide, *J. Chem. Phys.*, 1954, **22**, 516–518.

47 L. H. Coudert, F. J. Lovas, R. D. Suenram and J. T. Hougen, New measurements of microwave transitions in the water dimer, *J. Chem. Phys.*, 1987, **87**, 6290–6299.

48 S. Thorwirth, V. Lattanzi and M. C. McCarthy, Phosphorus and silicon analogs of isocyanic acid: Microwave detection of HPCO and HNSiO, *J. Mol. Spectrosc.*, 1987, **310**, 119–125.

49 H. W. Kroto, J. F. Nixon and K. Ohno, The microwave spectrum of phosphabutadiyne, HCCCP, *J. Mol. Spectrosc.*, 1981, **90**, 512–516.

50 L. Bizzocchi, C. Degli Esposti and P. Botschwina, Vibrationally excited states of HC5P: millimetre-wave spectroscopy and coupled cluster calculations, *Phys. Chem. Chem. Phys.*, 2003, **5**, 4090–4095.

51 J. Kraitchman, Determination of Molecular Structure from Microwave Spectroscopic Data, *Am. J. Phys.*, 1953, **21**, 17–24.

52 C. C. Costain, Determination of molecular structures from ground state rotational constants, *J. Chem. Phys.*, 1958, **29**, 864–874.

53 W. Gordy and R. L. Cook, Microwave molecular spectra, John Wiley & Sons, Ltd, New York, 3rd., 1984.

54 Z. Kisiel, PROSPE - Programs for ROtational SPEctroscopy, http://www.ifpan.edu.pl/~kisiel/prospe.htm.

55 C. C. Costain, Further comments on the accuracy of rs substitution structures., *Trans. Am. Crystallogr. Assoc.*, 1966, **2**, 157–61, discussion 161-4.

56 Z. Kisiel, Least-squares mass-dependence molecular structures for selected weakly bound intermolecular clusters, *J. Mol. Spectrosc.*, 2003, **218**, 58–67.

57 A. C. Legon and D. G. Lister, Van der Waals stretching and bending force constants from the rotational spectrum of argon... 1,3,5-trioxane, *Chem. Phys. Lett.*, 1993, **204**, 139–144.

58 A. C. Legon and D. G. Lister, The rotational spectrum of the argon-thiirane van der Waals molecule, *Chem. Phys. Lett.*, 1992, **189**, 149–152.

59 R. D. Suenram, G. T. Fraser, F. J. Lovas, C. W. Gillies and J. Zozom, Microwave spectrum, structure, and electric dipole moment of the Ar-formamide van der Waals complex, *J. Chem. Phys.*, 1988, **89**, 6141–6146.

60 P. Pinacho, J. C. López, Z. Kisiel and S. Blanco, Microsolvation of Ethyl Carbamate Conformers: Effect of Carrier Gas on the Formation of Complexes, Phys. Chem. Chem. Phys., 2020, DOI:10.1039/D0CP03093G.

61 S. Melandri, G. Maccaferri, A. Maris, A. Millemaggi, W. Caminati and P. G. Favero, Observation of the rotational spectra of van der Waals complexes by free jet absorption millimeter wave spectroscopy: Pyridine-argon, *Chem. Phys. Lett.*, 1996, **261**, 267–271.

62 S. E. Novick, Extended Townes–Dailey analysis of the nuclear quadrupole coupling tensor, *J. Mol. Spectrosc.*, 2011, **267**, 13–18.

63 T. Betz, S. Zinn, J. B. Graneek and M. Schnell, Nuclear Quadrupole Coupling Constants of Two Chemically Distinct Nitrogen Atoms in 4-Aminobenzonitrile, *J. Phys. Chem. A*, 2014, **118**, 5164–5169.

64 R. G. Bird, J. L. Neill, V. J. Alstadt, J. W. Young, B. H. Pate and D. W. Pratt, Correction to "Ground State 14N Quadrupole Couplings in the Microwave Spectra of N,N′-Dimethylaniline and 4,4′-Dimethylaminobenzonitrile", *J. Phys. Chem. A*, 2014, **118**, 1964.

65 J. H. Goldstein, Quadrupole Coupling and Bond Character in the Vinyl Halides, *J. Chem. Phys.*, 1956, **24**, 106–109.

Chapter 5. Bifunctional Hydrogen Bonding of Imidazole with Water Explored by Rotational Spectroscopy and DFT Calculations

Publication: Eva Gougoula, Daniel J. Cole and Nicholas R. Walker, *The Journal of Physical Chemistry A*, 2020, 124, 13, 2649-2659, doi.org/10.1021/acs.jpca.0c00544

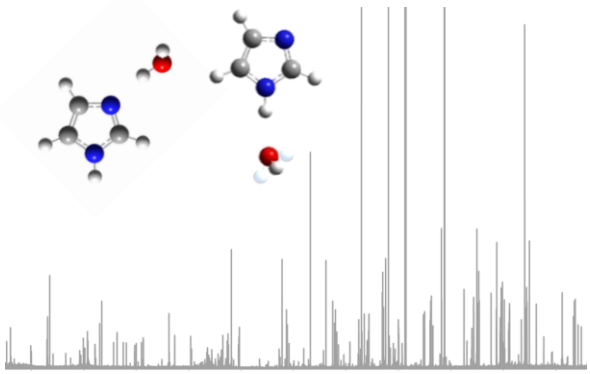

5.1 Introduction

Imidazole ($C_3H_4N_2$), figure 5.1, is a five-membered heteroaromatic ring that is an important building block of fundamental biomolecules such as the nucleobase adenine and the amino-acid histidine. Histidine's imidazole subunit can interact with hemoglobin[1] via either the pyrrolic (N1) or pyridinic (N3) nitrogen, acting as either a proton donor or acceptor, respectively. Anti-cancer agents such as *cis*-Pt drugs bind to DNA's guanine or adenine while stabilized by secondary interactions *via* the pyridinic nitrogen of the imidazole subunit[2]. Due to the presence of a basic nitrogen atom (N3) within the ring, imidazole, alongside thiazole and oxazole, also belongs to the class of alkaloids.[3] This may partially account for their diverse biochemical activity, meaning they can be found in antibiotics,[4] antifungal,[5] antithyroid[6] and anti-HIV[7] medication among others. Rationalizing the various possible binding sites of imidazoles is crucial to our understanding of their properties and biochemical activity.

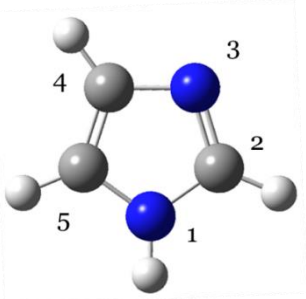

Figure 5.1. The imidazole monomer. Heavy atoms are numbered following the convention for aromatic molecules.

The structure of crystalline imidazole has been established through neutron[8] and X-ray diffraction.[9,10] Alternating linkages between the pyrrolic and the pyridinic nitrogen of individual imidazole molecules were observed in the crystal structure. The gas phase structure of isolated imidazole was determined by microwave spectroscopy.[11,12] Microwave spectroscopy also allows for structure determination of gas phase complexes that contain imidazole interacting with some other smaller molecule.[13,14] The imidazole dimer was studied by Mullaney *et al.*[13] The two imidazole monomers interact through an intermolecular hydrogen bond between the pyrrolic nitrogen of one monomer and the pyridinic nitrogen of the other monomer. The observed molecular geometry and the presence of an intermolecular hydrogen bond is consistent with that described for crystalline solid imidazole.

The stepwise hydration of various aromatic molecules in the gas phase has been studied extensively with microwave spectroscopy. Monohydrates of *N*-containing aromatic molecules including pyrrole[15] (C_4H_5N), thiazole[16] (C_3H_3OS), isoxazole[17] (C_3H_3NO), indole[18] (C_8H_7N), pyridine[19] (C_5H_5N), pyrazine[20] ($C_4H_4N_2$), pyrimidine[21] ($C_4H_4N_2$), pyridazine[22] ($C_4H_4N_2$), and triazine[23] ($C_3H_3N_3$) have been studied with microwave spectroscopy giving an insight into the first step of their solvation in water. Unlike in pyrazole ($C_3H_4N_2$), the pyridinic and the pyrrolic nitrogen of imidazole are spatially arranged so that they do not immediately affect each other. It follows that an individual water molecule may interact with either the pyridinic or the pyrrolic nitrogen site but not with both simultaneously. The binding site where the first water molecule interacts, and the intermolecular interaction type are determined by the chemical environment of the aromatic molecule. For example, a hydrogen bond is formed between the H on the pyrrolic nitrogen and the O of water in the $H_2O\cdots$pyrrole and the $H_2O\cdots$indole complexes[15,18] with the pyrrolic nitrogen being the proton donor. In each of pyridine[19], pyrazine[20], pyrimidine,[21] pyridazine[22] and triazine,[23] a hydrogen bond is observed with the pyridinic nitrogen accepting a proton from an individual water molecule.

Imidazole and water are both ubiquitous in biology and biochemistry so rationalizing the preferred binding modes between the two is crucial. IR spectroscopy in He-nanodroplets suggest a 1:1 ratio between the binding modes in the imid$\cdots H_2O$ and $H_2O\cdots$imid isomers.[24] A more recent study with IR spectroscopy[25] probing complexes formed between imidazole and water within a free jet expansion failed to detect the $H_2O\cdots$imid isomer. The

observation was interpreted as a result of that isomer not being kinetically stable in a free jet and effectively relaxing into imid···H_2O. Further gas phase IR experiments[26] probing benzimidazole and water identified two isomers, benzim···H_2O and H_2O···benzim, where water is a proton donor and a proton acceptor, respectively. In this chapter, the simultaneous isolation of two isomers of a complex between imidazole and water, imid···H_2O and H_2O···imid, probed in a free jet expansion is reported for the first time. The microwave spectra of both isomers in the 7.0-18.5 GHz frequency range are reported and analyzed. Isotopologues containing D and ^{18}O are also considered in order to confirm the assignment of molecular carriers and to determine structural parameters regarding the H_2O subunit in both isomers. Large amplitude motions associated with the H_2O subunit in the H_2O···imid isomer are modelled and discussed.

5.2 Experimental Details

This is the first experiment that was performed after the implementation of the fundamental 1064 nm harmonic in the laser ablation source. Imidazole was used as a test molecule to examine if laser ablation was possible with that wavelength. Imidazole (Sigma-Aldrich, ≥99.5%) mixed with silver iodide (ACROS Organics™, 99%) in a 1:1 by mass ratio and pressed into a 13mm cylindrical rod. Argon gas was kept at a constant pressure of 7 bar. No deliberate actions were taken to introduce water into the experiment; water may be present within the gas lines, the solid sample itself or the adsorbed on the walls of the vacuum chamber or pulse valve.

5.3 Quantum Chemical Calculations

Geometry optimizations of imid···H_2O and H_2O···imid were performed. The optimized geometries are shown in figure 5.2. The B3LYP functional in conjunction with dispersion correction D3BJ, was initially used alongside Dunning's aug-cc-pVTZ basis set. Geometry optimizations were subsequently performed with the ωB97X-D functional and quadrupole-ζ aug-cc-pVQZ basis set with tight convergence criteria. Grimme's D2 dispersion correction is included in the functional. Calculated values of rotational constants and dipole moment components are presented in Table 5.1. The complete set of DFT-calculated atomic coordinates is presented in Table A3 and A4 of appendix A. For H_2O···imid, one-dimensional potential energy surfaces (PES) were scanned to describe large amplitude motions for two internal coordinates. These respectively probe the torsional and wagging motions of H_2O with respect to the imidazole ring and are presented in Section 6.5. These PES calculations were kindly performed by Dr Daniel J. Cole at Newcastle University. Calculated rotational constants (A_e, B_e and C_e), dipole moment components ($|\mu_a|$, $|\mu_b|$ and $|\mu_c|$) and relative energies of the two complexes are summarised in Table 5.1. Structural parameters calculated at the ωB97X-D/aug-cc-pVQZ level will be used in the comparisons to follow due to its strong performance across a wide range of benchmark tests.

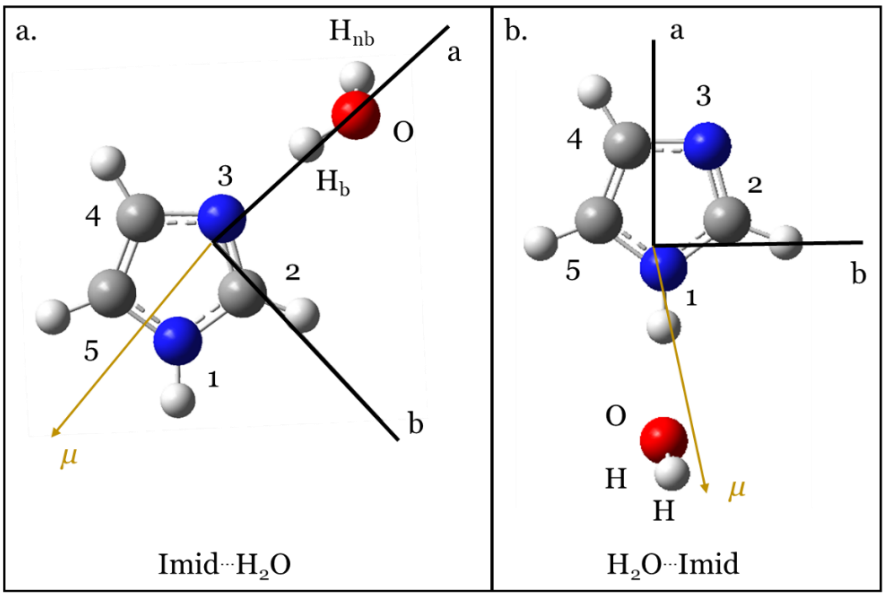

Figure 5.2. Equilibrium geometries of imid···H_2O and H_2O···imid calculated at the ωB97XD/aug-cc-pVQZ level of theory. The electric dipole moment components are propagated from positive to negative charge.

Table 5.1. Spectroscopic parameters calculated for imid···H_2O and H_2O···imid at the B3LYP(D3BJ)/aug-cc-pVTZ and ωB97X-D/aug-cc-pVQZ levels of theory.

B3LYP(D3BJ)/aug-cc-pVTZ		
	imid···H_2O	H_2O···imid
A_e (MHz)[a]	9522.83	9524.35
B_e (MHz)[a]	1788.40	1677.16
C_e (MHz)[a]	1512.19	1435.68
$\chi_{aa}(\mathbf{N1})$ (MHz)	1.1920	0.8152
$\chi_{bb}-\chi_{cc}(\mathbf{N1})$ (MHz)	3.8580	3.4511
$\chi_{ab}(\mathbf{N3})$ (MHz)	−0.0939	−0.0755
$\chi_{aa}(\mathbf{N3})$ (MHz)	−3.7828	−2.2672
$\chi_{bb}-\chi_{cc}(\mathbf{N3})$ (MHz)	−0.4900	−2.6799
$\chi_{ab}(\mathbf{N3})$ (MHz)	1.1492	−2.9629
$\lvert\mu_a\rvert$, $\lvert\mu_b\rvert$, $\lvert\mu_c\rvert$ (D)	|5.3|, |1|, |1.2|	|6.4|, |1.2|, |0|
ΔE (cm^{-1}, kJ mol^{-1})	0, 0	263, 3.15
ωB97X-D/aug-cc-pVQZ		
	imid···H_2O	H_2O···imid
A_e (MHz)[a]	9608	9570.97
B_e (MHz)[a]	1778.24	1695.37
C_e (MHz)[a]	1507.59	1449.96
$\chi_{aa}(\mathbf{N1})$ (MHz)	1.1446	0.8388
$\chi_{bb}-\chi_{cc}(\mathbf{N1})$ (MHz)	3.7922	3.2956
$\chi_{ab}(\mathbf{N3})$ (MHz)	0.1337	0.1110
$\chi_{aa}(\mathbf{N3})$ (MHz)	−3.8686	−2.0030
$\chi_{bb}-\chi_{cc}(\mathbf{N3})$ (MHz)	−0.7299	−3.3344
$\chi_{ab}(\mathbf{N3})$ (MHz)	−1.1681	3.0535
$\lvert\mu_a\rvert$, $\lvert\mu_b\rvert$, $\lvert\mu_c\rvert$ (D)	|5.3|, |1.1|, |1.2|	|6.2|, |0.6|, |0|
ΔE (cm^{-1}, kJ mol^{-1})	0, 0	606, 7.25

[a] Calculated equilibrium A_e, B_e and C_e rotational constants..

5.4 Spectral Analysis

The initial geometries used for the DFT calculations were generated based on the geometry of previously studied complexes like pyridine···H_2O and H_2O···pyrrole. A detailed conformational analysis for the two complexes imid···H_2O and H_2O···imid was not necessary given the well-established geometry of both imidazole and H_2O and the presence of chemically distinct coordination sites available for H-bonding on imidazole. The optimized equilibrium geometry of both imid···H_2O and H_2O···imid appears to be a near-prolate asymmetric top where all the heavy atoms lie in the plane defined by the imidazole ring. The total electric dipole moment component is calculated to be almost co-linear with the *a*-inertial axis in both isomers.

The jet-cooled rotational spectrum recorded under the experimental conditions described earlier is displayed in figure 5.3. The most intense transitions are readily identified based on previous studies and are ascribed to the imidazole monomer.[11,12] Transitions of $(imid)_2$, imid···Ar, AgI and $(H_2O)_2$ were also assigned with reference to previous studies.[13,14,27,28] Products of fragmentation of imidazole and subsequent gas phase chemical reactions are also present in the spectra. These include HC_3N, HC_5N, HC_7N, CH_3CN, ICN, IC_3N, C_4H_3N (methylcyanoacetylene), C_4H_3N (cyanoallene) and C_3H_2N (vinyl cyanide).[29–37] The observation of fragmentation products is unsurprising and has previously been reported and described.[13,38,39]

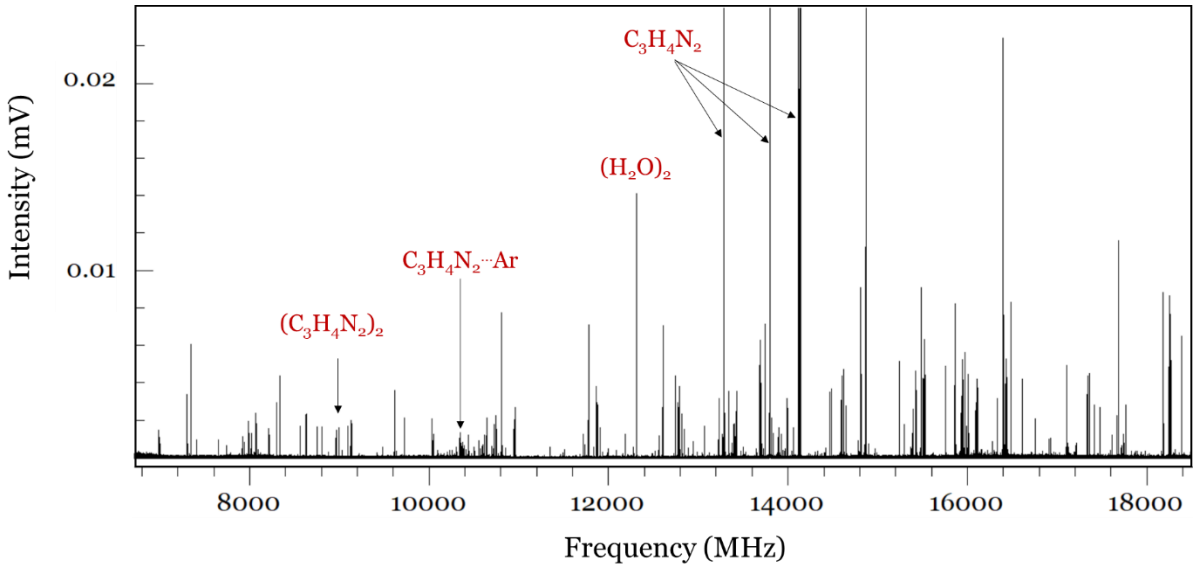

Figure 5.3. Broadband microwave spectrum between 7.0 and 18.5 GHz recorded over 240k FID's under the experimental conditions described in Section 5.2.

Several transitions remain unassigned and these are consistent with expectations for the spectra of $H_2O\cdots$imid and imid$\cdots H_2O$. The transitions exhibit hyperfine splitting confirming the presence of two distinct N nuclei within the molecular carriers of these spectra. These transitions were fit to Watson's S-reduced Hamiltonian[40,41] in the I^r representation for a semi-rigid asymmetric top as implemented in Pgopher[42];

$$H = H_R - \frac{1}{6}\mathbf{Q}(\mathrm{N1}):\nabla\mathbf{E}(\mathrm{N1}) - \frac{1}{6}\mathbf{Q}(\mathrm{N3}):\nabla\mathbf{E}(\mathrm{N3})$$

Here, two different nuclear quadrupole moment dyadics $\mathbf{Q}$ and electric field gradient dyadics $\nabla\mathbf{E}$ to account for the presence of two distinct quadrupolar nuclei. The rotational constants A_0, B_0 and C_0, centrifugal distortion constants D_J and D_{JK} for the parent isotopologue of both imid$\cdots H_2O$ and $H_2O\cdots$imid are included in the H_R and their values are summarized in table 5.2. The diagonalized components of the nuclear quadrupole coupling tensor χ_{aa} and $(\chi_{bb} - \chi_{cc})$ for both N1 and N3 in each isomer are also summarized in table 5.9. When fitting the transitions for imid$\cdots H_2{}^{18}O$, imid$\cdots H_bOD_{nb}$ and the 0^+ state of HDO$\cdots$imid it was necessary to include additional centrifugal distortion term, d_1, to generate a satisfactory fit. The detailed form of the Hamiltonian was given in chapter 2.

Rotational transitions were initially assigned to the imid$\cdots H_2O$ complex based on the consistence between DFT calculated and fitted rotational constants. The spectroscopic parameters determined through fitting several *a*-type transitions with $\Delta J = 1$ and $\Delta K = 0$ with Watson's S-reduced Hamiltonian are summarized in table 5.2. Previous studies of pyridine$\cdots H_2O$, isoxazole$\cdots H_2O$ and pyrazine$\cdots H_2O$ complexes, among others, report the presence of two different tunneling states arising from large amplitude motions associated with the H_2O subunit within the complexes. Such splittings were not observed for the imid$\cdots H_2O$ complex, being consistent with the results[21,43] reported for 2-fluoropyridine$\cdots H_2O$ and pyrimidine$\cdots H_2O$. Observation of only *a*- and *b*-type transitions and absence of *c*-type transitions for all observed isotopologues of imid$\cdots H_2O$ is consistent with the planarity of the complex.

Further examination of the recorded spectra led to independent assignment of two different sub-states, denoted as 0^- and 0^+, of the spectrum with the molecular carrier being the $H_2O\cdots$imid complex. The rotational constants and centrifugal distortion constants

determined for these sub-states are also displayed in table 5.2. These parameters do not vary significantly between the two sub-states suggesting subtle rearrangement of masses. A statistical weight ratio of approximately 3:1 is observed for most transitions assigned for the 0^- and 0^+ sub-states, respectively. A set of 0^- and 0^+ sub-states with 3:1 statistical weight was reported in the spectra for $H_2O\cdots$indole and $H_2O\cdots$pyrrole and thus supporting the initial assignment that the molecular carrier of these spectra is the $H_2O\cdots$imid complex.

Table 5.2. Experimentally determined spectroscopic parameters fitted to Watson's S-reduced Hamiltonian for each of imid$\cdots H_2O$ and $H_2O\cdots$imid.

	imid$\cdots H_2O$	$H_2O\cdots$imid	
		0^-	0^+
$\boldsymbol{A_0}$ (MHz)	9502.79(43)[a]	9436.97(54)	9520.99(26)
$\boldsymbol{B_0}$ (MHz)	1826.3929(13)	1663.0101(11)	1662.91298(73)
$\boldsymbol{C_0}$ (MHz)	1531.9303(10)	1421.1251(13)	1420.74502(72)
$\boldsymbol{D_J}$ (kHz)	1.269(20)	0.487(18)	0.2349(96)
$\boldsymbol{D_{JK}}$ (kHz)	63.03(21)	49.77(25)	59.20(15)
$\boldsymbol{\chi_{aa}}$(N1) (MHz)	1.143(19)	0.923(75)	0.916(45)
[$\boldsymbol{\chi_{bb}}$(N1)−$\boldsymbol{\chi_{cc}}$(N1)] (MHz)	3.712(56)	3.80(46)	4.07(23)
$\boldsymbol{\chi_{aa}}$(N3) (MHz)	−2.889(21)	−1.932(71)	−1.859(44)
[$\boldsymbol{\chi_{bb}}$(N3)−$\boldsymbol{\chi_{cc}}$(N3)] (MHz)	−1.07(11)	−2.66(44)	−2.47(25)
$\boldsymbol{\kappa}^b$	−0.926115(4)	−0.939648(4)	−0.9402073(31)
$\boldsymbol{P_{aa}}$ (u Å^2)	276.7053(12)	302.9729(15)	303.2656(13)
$\boldsymbol{P_{bb}}$ (u Å^2)	53.1839(12)	52.6377(15)	52.4401(13)
$\boldsymbol{P_{cc}}$ (u Å^2)	−0.0029(12)	0.9141(15)	0.6391(13)
Δ_0 (u Å^2)	0.0059(24)	−1.8282(31)	−1.2783(15)
$\boldsymbol{N}$ [c]	60	37	24
$\boldsymbol{\sigma_{RMS}}$ (kHz)[c]	13.7	13.6	5.8

[a] Numbers in parentheses are one standard deviation in units of the last significant figure.

[b] Ray's asymmetry parameter is calculated as $\kappa = \frac{2B_0 - A_0 - C_0}{A_0 - C_0}$

[c] N and σ_{RMS} are respectively the number of measured transitions and the standard deviation of the fit.

Pickett's SPFIT/SPCAT suite of programs[44] was used in an attempt to produce a simultaneous, global fit of transitions of both 0^- and 0^+ sub-states. The Hamiltonian was selected to include one or more Coriolis coupling constants to account for the large amplitude motion causing the splitting. Several procedures were employed, one of which

was to fix the quadrupole coupling to the values shown in table 5.2, fit the rotational constants and some selected Coriolis terms, followed by adjustment of these terms prior to repeating the fit. It was not possible to produce a unique solution and constrain the fit due to large amplitude motions associated with the H_2O subunit. As it will be discussed later, a wagging and a torsional motion were identified, and both appear to contribute a significant amount to the large amplitude motions within this complex. The Hamiltonians implemented in SPFIT/SPCAT are unable to account for these motions and subsequently did not allow determination of Coriolis coupling terms. Significant differences are also observed for D_J and D_{JK} between the 0^- and 0^+ sub-states consistent with the proposal of complex internal dynamics and large amplitude motions.

Isotopic experiments were performed with isotopic water HDO and $H_2{}^{18}O$ to confirm the geometry and subsequently the assignment of molecular carriers to the identified spectra. A total of four isotopologues of the imid···H_2O (imid···H_2O, imid···DOH, imid···$H^{18}OH$ and imid···HOD) and three isotopologues of the H_2O···imid (H_2O···imid, $H_2{}^{18}O$···imid and HDO···imid) were assigned and their determined spectroscopic parameters are summarized table 5.3 and 5.4. The changes in the rotational constants of the D and ^{18}O isotopologues are consistent with expected isotopic shifts. The $5_{05}\rightarrow4_{04}$ transitions of the H_2O···imid and HDO···imid isotopologues is shown in figure 5.4. It is immediately apparent that the splitting between the 0^- and 0^+ sub-states decreases upon deuteration supporting the proposal of large amplitude motions associated with the protons of the H_2O subunit. Observation of the spectrum of only one HDO···imid isotopologue suggests that the two protons are equivalent within the complex and isotopic substitution of either one of them creates an equal change in the moment of inertia of that complex. Only one sub-state of the $H_2{}^{18}O$···imid isotopologue was observed with significantly low intensity and that was assigned to the 0^- sub-state. The experimentally determined rotational constants for imid···H_2O and H_2O···imid alongside their percentage deviations from their corresponding calculated values are shown in table 5.5.

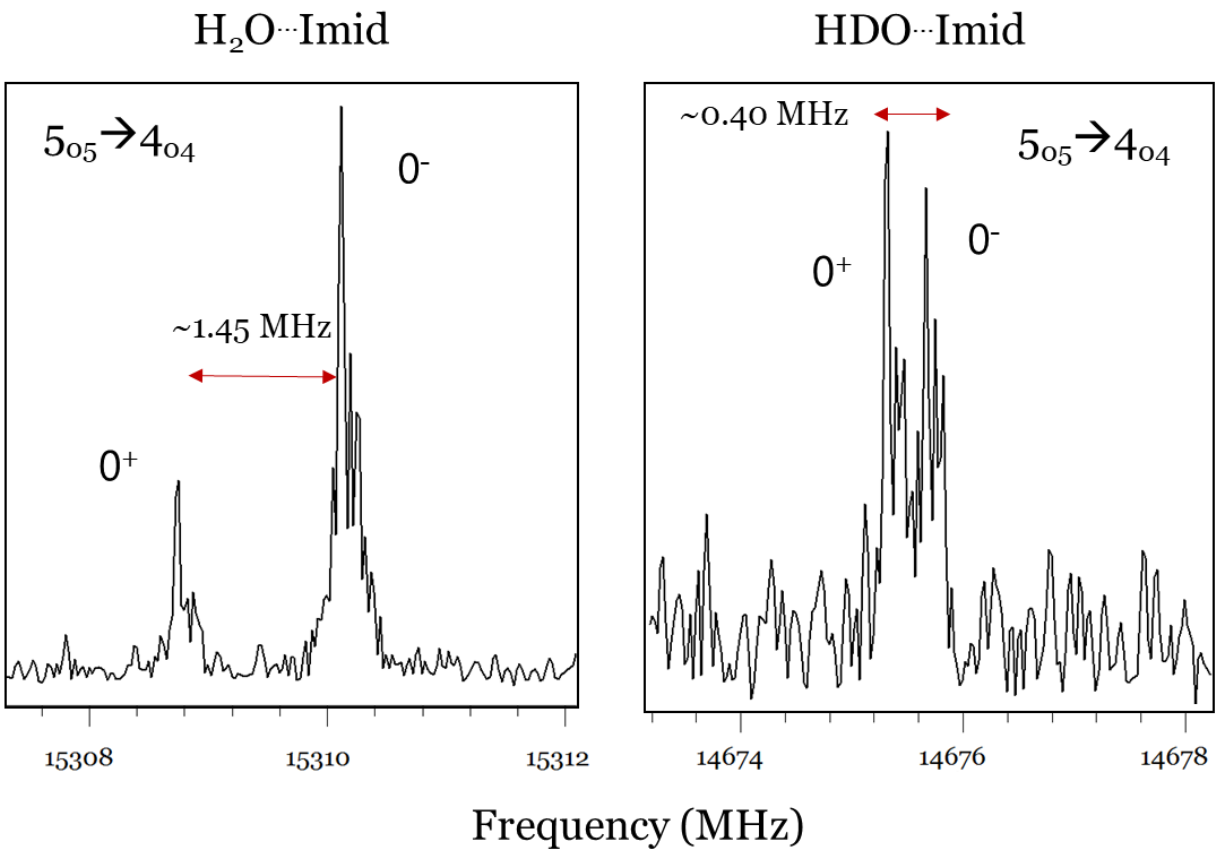

Figure 5.4. (a, left panel) Expanded section of the $5_{05}\rightarrow4_{04}$ transition of $H_2O\cdots$imid and (b, right panel) the same transition of the HDO···imid isotopologue. Rotational transitions are split into 0^- and 0^+ states. The splitting between the 0^- and 0^+ states decreases upon deuteration implying an internal motion of the water molecule.

Table 5.3. Spectroscopic parameters determined for isotopologues of imid···H_2O.

	imid···D_bOH_{nb}	imid···$H_2{}^{18}O$	imid···H_bOD_{nb}
$\boldsymbol{A_0}$ (MHz)	9481.55(46)[a]	9499.20(45)	9422.95(34)
$\boldsymbol{B_0}$ (MHz)	1793.3641(15)	1707.6406(23)	1742.7498(29)
$\boldsymbol{C_0}$ (MHz)	1508.1838(10)	1447.3811(20)	1472.3732(15)
$\boldsymbol{D_J}$ (kHz)	1.320(26)	1.427(22)	1.088(21)
$\boldsymbol{D_{JK}}$ (kHz)	60.97(25)	57.83(12)	57.29(19)
$\boldsymbol{d_1}$(kHz)	–	–0.276(23)	–0.139(24)
$\boldsymbol{\chi_{aa}}$(N1) (MHz)	[1.143(19)]	[1.143(19)]	[1.143(19)]
[$\boldsymbol{\chi_{bb}}$(N1)−$\boldsymbol{\chi_{cc}}$(N1)] (MHz)	[3.712(56)]	[3.712(56)]	[3.712(56)]
$\boldsymbol{\chi_{aa}}$(N3) (MHz)	[–2.889(21)]	[–2.889(21)]	[–2.889(21)]
[$\boldsymbol{\chi_{bb}}$(N3)−$\boldsymbol{\chi_{cc}}$(N3)] (MHz)	[–1.07(11)]	–1.07(11)]	[–1.07(11)]
$\boldsymbol{\kappa}$	–0.92847(6)	–0.93535(6)	–0.93199(5)
$\boldsymbol{P_{aa}}$ (u Å^2)	281.797(21)	295.959(22)	289.799(16)
$\boldsymbol{P_{bb}}$ (u Å^2)	53.294(21)	53.209(22)	53.442(16)
$\boldsymbol{P_{cc}}$ (u Å^2)	0.008(21)	–0.007(22)	0.191(16)
Δ_0 (u Å^2)	–0.015(42)	0.014(44)	–0.381(32)
$\boldsymbol{N}$ [b]	19	41	25
$\boldsymbol{\sigma_{RMS}}$ (kHz)[b]	9.2	13.3	10.3

[a] Numbers in parentheses are one standard deviation in units of the last significant figure.

[b] N and σ_{RMS} are respectively the number of hyperfine transitions and the standard deviation of the fit.

Table 5.4. Spectroscopic parameters determined for isotopologues of H_2O···imid.

	HDO···imid		$H_2{}^{18}O$···imid
	0^-	0^+	
A_0 (MHz)	9384.56(67)[a]	9430.41(50)	9437.55(38)
B_0 (MHz)	1586.6402(18)	1586.7041(26)	1557.5747(16)
C_0 (MHz)	1366.8028(15)	1366.6089(20)	1343.3755(18)
D_J (kHz)	0.633(23)	1.138(17)	0.711(23)
D_{JK} (kHz)	37.59(35)	34.62(29)	[49.77]
d_1 (kHz)	–	−0.613(18)	–
χ_{aa}(N1) (MHz)	[0.923]	[0.916]	[0.923]
$[\chi_{bb}(\mathrm{N1})-\chi_{cc}(\mathrm{N1})]$ (MHz)	[3.80]	[4.07]	[3.80]
χ_{aa}(N3) (MHz)	[−1.932]	[−1.859]	[−1.932]
$[\chi_{bb}(\mathrm{N3})-\chi_{cc}(\mathrm{N3})]$ (MHz)	[−2.66]	[−2.47]	[−2.66]
κ	−0.945163(4)	−0.9454129(35)	−0.9470732(26)
P_{aa} (u Å^2)	317.2037(18)	317.3548(15)	323.5506(11)
P_{bb} (u Å^2)	52.5403(18)	52.4416(15)	52.6414(11)
P_{cc} (u Å^2)	1.3104(18)	1.1465(15)	0.9071(11)
Δ_0 (u Å^2)	−2.621(4)	−2.2930(29)	−1.8143(22)
N[b]	15	15	11
σ_{RMS} (kHz)[b]	12.7	8.4	10.6

[a] Numbers in parentheses are one standard deviation in units of the last significant figure.

[b] N and σ_{RMS} are respectively the number of hyperfine transitions and the standard deviation of the fit.

Table 5.5. Calculated rotational constants of imid···H_2O and H_2O···imid and their percentage deviations from the experimentally determined ground state rotational constants.

	B3LYP(D3BJ)/aug-cc-pVTZ				
	imid···H_2O		H_2O··· imid		
				0^-	0^+
$\boldsymbol{A_e}$ (MHz)	9522.83	0.21%[a]	9516.67	0.84%	–0.05%
$\boldsymbol{B_e}$ (MHz)	1788.40	–2.12%	1677.86	0.89%	0.89%
$\boldsymbol{C_e}$ (MHz)	1512.19	–1.31%	1436.02	1.04%	1.6%
$\lvert\boldsymbol{\mu_a}\rvert$, $\lvert\boldsymbol{\mu_b}\rvert$, $\lvert\boldsymbol{\mu_c}\rvert$ (D)	|5.3|, |1.0|, |1.2|		|6.4|, |1.2|, |0|		
$\Delta\boldsymbol{E}$ (cm^{-1}, kJ mol^{-1})[b]	0		263, 3.15		
	ω-B97XD/aug-cc-pVQZ				
	imid···H_2O		H_2O···imid		
				0^-	0^+
$\boldsymbol{A_e}$ (MHz)	9608	1.10%	9570.98	1.4%	0.52%
$\boldsymbol{B_e}$ (MHz)	1778.24	–2.71%	1695.37	1.91%	1.92%
$\boldsymbol{C_e}$ (MHz)	1507.59	–1.62%	1449.96	1.99%	2.01%
$\lvert\boldsymbol{\mu_a}\rvert$, $\lvert\boldsymbol{\mu_b}\rvert$, $\lvert\boldsymbol{\mu_c}\rvert$ (D)	|5.3|, |1.1|, |1.2|		|6.2|, |0.6|, |0|		
$\Delta\boldsymbol{E}$ (cm^{-1}, kJ mol^{-1})[b]	0		606, 7.3		

[a] Percentage deviation calculated as $\frac{A_{calc}-A_{exp}}{A_{exp}} \times 100$ where the comparison is between results for the parent isotopologues of imid···H_2O and H_2O···imid.

[b] Imid···H_2O is calculated to be the global minimum by both methods. The energy of the H_2O···imid isomer is given relative to the energy of imid···H_2O.

5.5 Geometry Interpretation

In chapter 4, it was explained how an initial insight into the geometry of a complex may be obtained by evaluating the experimentally determined rotational constants to derive the values of the planar moments P_{aa}, P_{bb} and P_{cc} and the inertial defect Δ_0. It has been explained that a Δ_0 value of zero is obtained for a planar molecule at equilibrium. However, at the zero-point, Δ_0 is expected to be contaminated by low lying vibrations. Typically, in-plane vibrations have a positive contribution to Δ_0 whereas out-of-plane vibrations (and mass) result in negative contributions. The value of $\Delta_0 = 0.0059(24)$ u Å^2 for the parent isotopologue of imid···H_2O is very close to zero suggesting that this isomer is effectively planar at the zero-point. Looking at the values of Δ_0 and P_{cc}, these vary significantly between the two sub-states of the parent isotopologue of the H_2O···imid isomer. The value of $\Delta_0 = -1.8282$ u Å^2 for the 0^- sub-state is close to that expected for a molecule with two rigid hydroxylic protons. However, for the 0^+ sub-state, a value of -1.2783 u Å^2 is calculated suggesting that the protons of the H_2O subunit are brought closer to the *ab*-plane of H_2O···imid. This observation is consistent with large amplitude motions occurring at the H_2O subunit, particularly involving the two protons, at the timescale of molecular rotation.

Atomic coordinates of the O and H atoms in the H_2O subunit in both imid···H_2O and H_2O···imid are determined by evaluating the shifts in rotational constants caused by isotopic substitution. The Kraitchman method was used to generate the substitution r_s coordinates and these are collectively shown in table 5.6 and compared to the calculated r_e coordinates. The method can only produce the magnitudes of the relative coordinates and for that reason the signs were those determined for the equilibrium geometry at the ωB97X-D/aug-cc-pVQZ level. Costain's errors are displayed in parentheses alongside the relative coordinates. In imid···H_2O, the *c*-axis coordinate of the O atom is returned as an imaginary number, so it was set to zero. This is consistent with the proposed planarity of that complex indicated by the small value of the calculated Δ_0. The *c*-axis coordinate of the bonding H participating in the intermolecular bond is only $|c|$=0.104(17) Å. Even though the position of H atoms is generally not well determined with the r_s method due to elongation effects[45], the results are in good agreement with the calculated coordinates. The non-bonding hydrogen, not participating in the intermolecular bond, is calculated to lie 0.4521(38) Å above the *ab*-plane. The DFT calculated *c*-axis coordinate is 0.6829 Å. These

numbers may be connected to the planar geometry implied by the small value of Δ_0 of the parent imid···H_2O by invoking a rapid motion of the non-bonding hydrogen of water rapidly switching between equivalent positions above and below the *ab*-plane of the complex. A similar interpretation was given to the discrepancies between the calculated and experimental geometry of the 2-flyoropyridine···H_2O complex[43]. For the imid···H_bOD_{nb} isotopologue, Δ_0 is calculated to be –0.381(32) u Å^2, significantly larger than that of the parent isotopologue and subsequently implying that the non-bonding deuterium atom is lying out of the *ab*-plane, both at equilibrium and at the zero-point. This may be rationalized by considering that the r_s method does not account for the elongation of the O-D bond when compared to O-H and therefore neglects differences in vibrational energy of the isotopologues caused by that bond elongation.

It was discussed earlier that two distinct sub-states are observed in the spectrum of the H_2O···imid isomer indicating that the H_2O moiety undergoes one or more large amplitude motions. Rigid rotor assumptions about the structure are not effective. However, it is possible to calculate the r_s coordinate of the O atom. Considering the geometry of H_2O···imid depicted in figure 5.1, the O atom of the water subunit is involved in the intermolecular hydrogen bond acting as a proton donor. This will, to a certain extent, constrain the position of the O atom. Only one state of the $H_2{}^{18}O$···imid was observed and that was assigned to the 0^- state which gives the most consistent results between the r_e, r_s and r_0 coordinates. It is also in agreement with the intensities of the 0^- and 0^+ states of H_2O···imid and HDO···imid where the 0^- state was statistically more intense than the 0^+ state in both isotopologues. It is expected that 0^- of $H^{18}O$···imid is three times more intense than 0^+. The *c*-axis coordinate was calculated to be an imaginary number suggesting the intermolecular hydrogen bond is in the *ab*-plane of the imidazole ring. The magnitude of the calculated *b*-coordinate is small indicating that O lies very close to the *a*-axis of the complex. These observations confirm the calculated geometry of the H_2O···imid isomer and stand along the earlier assumption that the O atom is relatively constrained.

Table 5.6. Experimentally-determined (r_0, r_s) and DFT-calculated (r_e) atomic coordinates for imid···H_2O and H_2O···imid.

		imid···H_2O		
		a / Å	*b* / Å	*c* / Å
H_b	r_e (calc.)	2.253901	0.141020	–0.054538
	r_s (exp.)	2.25889(77)[a]	0.3339(53)	–0.104(17)
	r_0 (exp.)	2.230(5)	0.187(25)	0[b]
O	r_e (calc.)	3.203723	–0.048453	–0.124829
	r_s (exp.)	3.13460(50)	–0.115(14)	0[c]
	r_0 (exp.)	3.151(2)	–0.0770(6)	0[b]
H_{nb}	r_e (calc.)	3.584692	0.289172	0.682930
	r_s (exp.)	3.62122(47)	0.5218(33)	0.4521(38)
	r_0 (exp.)[a]	3.636(21)	0.749(14)	0[b]
		H_2O···imid		
	Å	*a*	*b*	*c*
O	r_e (calc.)	–3.15362	0.077918	0.00007
	r_s (exp.)	–3.24141(48)	0.042(38)	0[c]
	r_0 (exp.)	–3.2518(37)	0.0258(58)	0

[a] Numbers in parentheses are one standard deviation in units of the last significant figure.
[b] The r_0 coordinates are those determined under one of two alternative model geometries which fit the rotational constants with high accuracy (see text for details). The coordinates shown are those obtained when the r_0 parameters are as shown in Table 4.
[c] Imaginary result is obtained so r_s coordinate is assumed equal to zero.

Given that some structural information has been obtained through the r_s coordinates of the two isomers, it is possible to determine some r_0 parameters, provided some reasonable assumptions are made. Numbering of heavy atoms in imidazole follows that of figure 5.1 and 5.2 whilst the hydrogens are labelled based on the heavy atom their attached. The atom connectivity for the initial *z*-matrix is established through the r_s geometry determined above. Planarity of imid···H_2O is established based on the value of Δ_0. The r_0 parameters were determined using STRFIT. The r_0 parameters that were determined for imid···H_2O are $r(H_b \cdots N3)$ that described the length of the intermolecular hydrogen bond and the angles $\angle(H_b \cdots N3 - C2)$ and $\angle(O - H_b \cdots N3)$ which describe the position and orientation of the water molecule with respect to the *ab*-plane of imidazole. It is also assumed that the geometry of imidazole and water is unaffected by complexation and for

that reason the individual r_0 geometries of the two subunits were used. As in the case of pyrimidine···H_2O, there are four possible orientations for the water subunit whilst still fulfilling the condition that the complex is planar. The orientation can be defined by the dihedral angles $\angle(H_{nb} - O - H_b \cdots N3)$ and $\angle(O - H_b \cdots N3 - C2)$ both of which can obtain a value of 0 or 180°. The four possible orientations are depicted in figure 5.5.

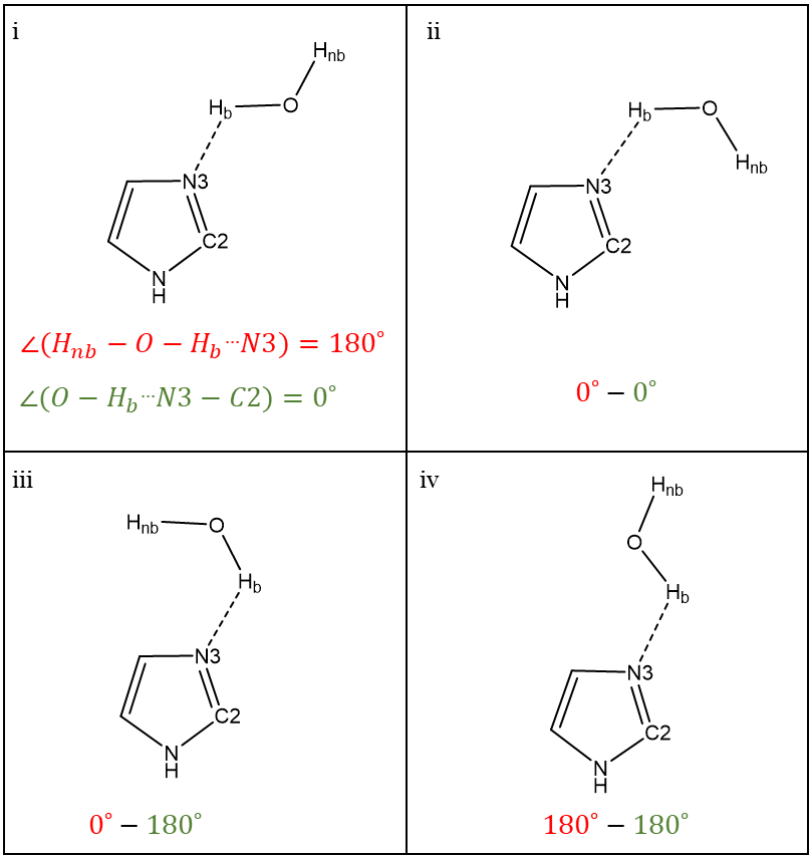

Figure 5.5. The four possible orientations of the H_2O subunit with respect to the imidazole ring in imid···H_2O. The two relative dihedral angles are justified in red and green, respectively.

Fits were performed for all four possible structures. When assuming that $\angle(H_{nb} - O - H_b \cdots N3) = 0°$, the fit does not converge, eliminating structures ii and iii. Fits performed assuming $\angle(H_{nb} - O - H_b \cdots N3) = 180°$ generated two structures, i and iv, for both of which structural parameters were determined with high precision. The structural parameters in table 5.7 were determined while assuming $\angle(O - H_b \cdots N3 - C2) = 0°$. An alternative set of structural parameters is obtained when $\angle(O - H_b \cdots N3 - C2) = 180°$ which is not included here. Two sets of structural parameters were determined for the isoxazole···H_2O and pyrimidine···H_2O, both of which fitted the experimentally determined rotational constants and moment of inertia. In the case of isoxazole···H_2O, the correct

structure was determined based on the experimentally determined nuclear quadrupole coupling constants $\chi_{aa}(N)$. For imid···H_2O, the atomic coordinates of N1 and N3 are effectively the same in structures i and iv, within 1% of the magnitude of the coordinates, with the standard deviations of the measured values of $\chi_{aa}(N1)$ and $\chi_{aa}(N3)$ being of comparable magnitude, therefore making this test inconclusive. However, looking at the DFT calculated geometry, it is clear that $\angle(O - H_b \cdots N3 - C2) = 0^\circ$. Setting that dihedral angle to the DFT value, the best agreement between fitted and calculated structural parameters is obtained. The results in table 5.6 and 5.7 are calculated on the assumption that $\angle(O - H_b \cdots \mathrm{N3} - C2) = 0^\circ$. When assuming $\angle(O - H_b \cdots N3 - C2) = 180^\circ$, the values of the fitted structural parameters are $r(H_b \cdots N3)$ = 2.006(41) Å, $\angle(H_b \cdots N3 - C2)$ = 89.7(42)° and $\angle(O - H_b \cdots N3)$ = 146.9(29)°. This structure brings H_b in close proximity to H2 at only 2.24 Å apart which is too short an interaction given that the sum of the van der Waals radii for two hydrogen atoms is 2.4 Å. A list of atomic r_0 coordinates of both structures i and iv can be found in table A5 appendix A.

Table 5.7. Experimentally-determined (r_0) and DFT-calculated (r_e) structural parameters of imid···H_2O and H_2O···imid.

Parameter[a]		imid···H_2O	Parameter[a]		H_2O···imid
$r(H_b \cdots N3)$ (Å)	r_e	1.931	$r(H1 \cdots O)$ (Å)	r_e	1.953
	r_0	2.024(29)[b,c]		r_0	2.007(4)[b]
$\angle(H_b \cdots N3 - C2)$ (°)	r_e	116	$\angle(H1 \cdots O \cdots \mathrm{X})$ (°)	r_e	153
	r_0	89.5(32)		r_0	152(6)
$\angle(O - H_b \cdots N3)$ (°)	r_e	171			
	r_0	172.2(26)			

[a] See text and Figure 5.5 for parameter definitions.

[b] Numbers in parentheses are one standard deviation in units of the last significant figure.

[c] The r_0 parameters are those determined under one of two alternative model geometries which fit the rotational constants with high accuracy (see text for details).

A hydrogen bond deviating from linearity is observed in imid···H_2O, consistent with results for pyridine···H_2O, pyrimidine···H_2O and pyridazine···H_2O. This is the result of secondary interactions between the O atom of the H_2O subunit and hydrogen atoms on carbon atoms adjacent to the pyridinic nitrogen in each of imidazole, pyridine, pyrimidine

and pyridazine. In the case of imidazole, the secondary interaction is observed between O and the H2 hydrogen on the C2 carbon. The angle $\angle(O - H_b \cdots N3)$ is calculated to be 171° at the ωB97X-D/aug-cc-pVQZ level being in excellent agreement with the experimental value of 172.1(26)°. From the r_0 fit, the $r(O \cdots H2)$ distance is derived to be 3.13(8) Å which is significantly lower than the DFT calculated 3.54 Å value. This may be rationalized by the fact that DFT calculates the equilibrium geometry while the fitted rotational constants used for the r_0 fit are determined for imid···H_2O the zero-point. The primary hydrogen bonding interaction is characterized within reasonable precision at the ωB97X-D/aug-cc-pVQZ level whilst the weak, secondary interaction is significantly underestimated.

It was discussed earlier that large amplitude motions occur in H_2O···imid which mainly involves the two hydrogen atoms of the water subunit. The angle $\angle(O \cdots H1 - N1)$ which defines the position of the O atoms with respect to the imidazole ring was fixed to the DFT value of 174.7°. The values of the inertial defects Δ_0 and planar moments P_{cc} calculated earlier for the two spectral states that were assigned to that isomer and its isotopologues, suggest that only the hydroxylic protons lie outside the plane. Based on that, the dihedral $\angle(O \cdots H1 - N1 - C2)$ was fixed to 180°, placing the O atom in the plane of the imidazole ring. A dummy atom X was placed between the two hydrogen atoms and on the C_2 axis dissecting the plane of the water subunit. The dummy atom also lies in the plane of the imidazole ring such that $\angle(X \cdots O \cdots H1 - N1) = 0°$. This assumption is based on the DFT calculated geometry suggesting that the hydrogen atoms are symmetrically located on either side of the imidazole plane.

The fitted r_0 structural parameters obtained under the constraints described above yield the values summarized in table 5.6 and 5.7. These are r_0(O···H1) = 2.000(4) Å and $\angle(X \cdots O \cdots H1) = 159(7)°$ and in good agreement with the DFT calculated structures; however, it is not possible to determine more structural parameters unless more assumptions are made. If it is assumed that $\angle(X \cdots O \cdots H1 - N1) = 180°$, then $r(O \cdots H1) = 2.001(4)$ Å and $\angle(X \cdots O \cdots H1) = 151(7)°$. Both assumptions yield results within the range of the large amplitude motions of wagging and torsion within the water molecule, as it will be shown in section 5.6. Within the PES scans, transitions states are identified at $\angle(X \cdots O \cdots H1 - N1) = 90°$ or 270°. Pursuing the fit while assuming the above angles yields similar values for both $r(O \cdots H1)$ and $\angle(X \cdots O \cdots H1)$ but at the expense of greater uncertainties. The

residuals that describe the differences between measured values of rotational constants and those implied by the fitted structures are higher for A_0 than for B_0 and C_0. This suggests that large amplitude motions are mainly associated with a torsional motion around the $\angle(X-O\cdots H1-N1)$ coordinate and a wagging motion defined by the angle $\angle(X\cdots O\cdots H1)$. Similar interpretations for the large amplitude motions identified for similar complexes such as H_2O···indole and H_2O···pyrrole.

5.6 Potential Energy Scans of Intermolecular Coordinates of H_2O···imid

The large amplitude motions in H_2O···imid were modelled with DFT calculations characterizing the PES's of those motions. The PES's were produced at the ωB97X-D/aug-cc-pVQZ level while all internal coordinates, except for the scanned ones described below, were fixed. The dummy atom X that was used in the structure fits was also implemented here for the definition of the scanned coordinates. The PES calculated when varying the angle $\angle(X \cdots O \cdots H1)$ between 130° and 210° is depicted in figure 5.6. This coordinate corresponds to the wagging motion of the water molecule, mainly involving the hydrogen atoms. The PES is relatively flat and exhibits two shallow minima at 154° and 200° separated by a barrier of approximately 10 cm^{-1}.

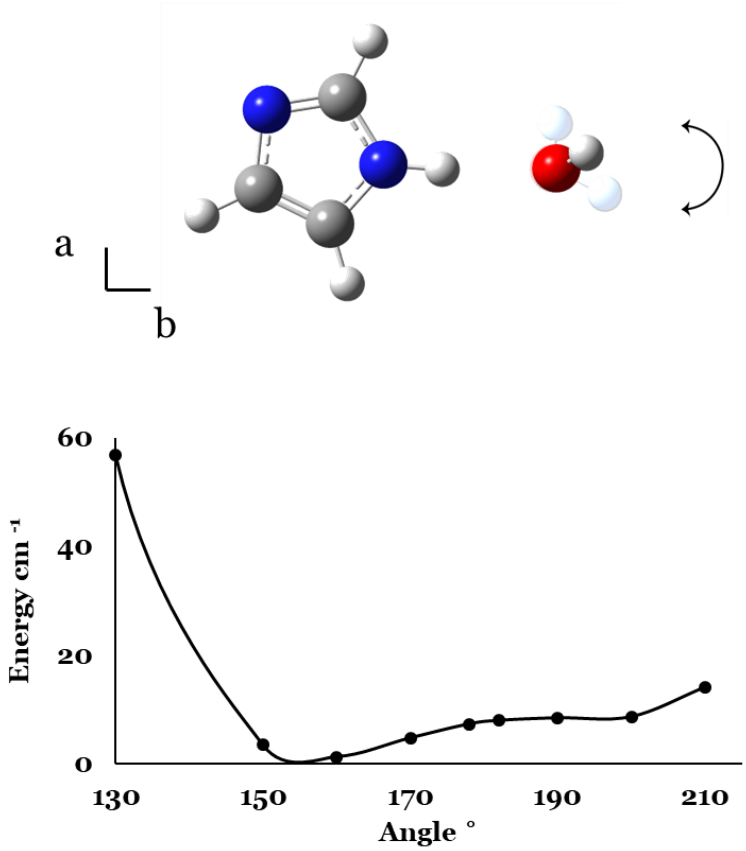

Figure 5.6. Calculated potential energy surface tracing the wagging motion of H_2O···imid at the ωB97X-D/aug-cc-pVQZ level. The transparent white spheres are drawn to illustrate the molecular geometries when $\angle(X \cdots O \cdots H1)$ is 90° or 200°. The trend rises steeply towards higher energy beyond the limits of this plot.

The PES describing a torsional motion of the H_2O subunit is shown in figure 5.7. The coordinate that was scanned describes the angle formed between the X···O vector and the imidazole plane between 0 and 180°. Two minima are observed at both 0 and 180° and the barrier to interconversion is approximately 143 cm^{-1}. It is very likely that both motions may contribute to the large amplitude motions causing the spectral splitting in H_2O···imid.

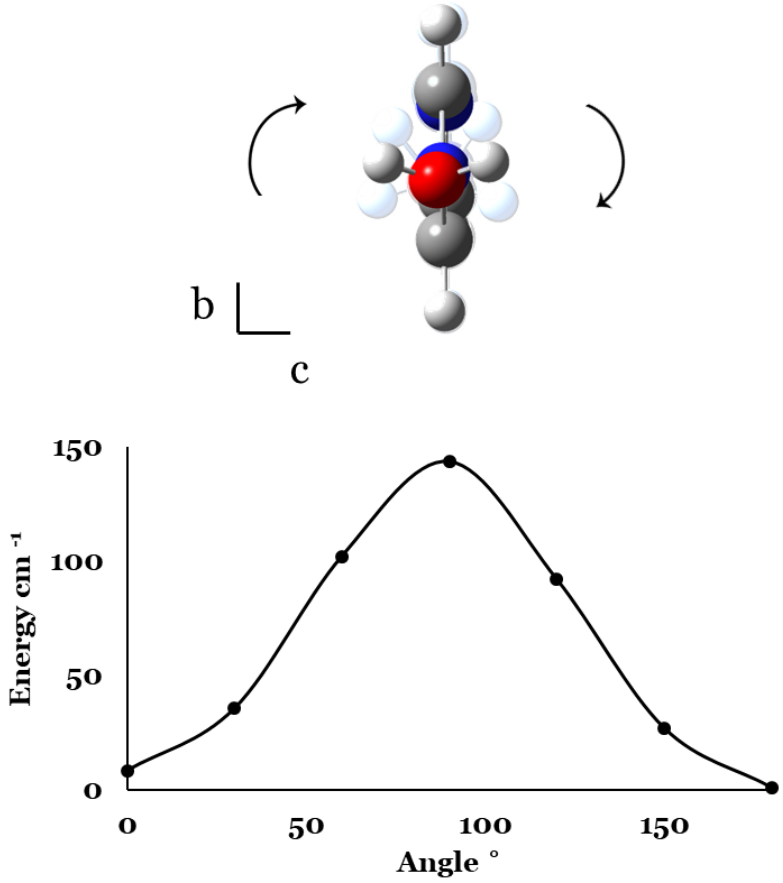

Figure 5.7. 1D potential energy surface of a torsional motion in H_2O···imid defined by the angle formed by the X···O vector and the imidazole plane between 0 and 180° at the ωB97X-D/aug-cc-pVQZ level. The opaque white spheres indicate the molecular geometries where this angle is equal to 30° or 120° respectively.

5.7 Force Constant and Dissociation Energy of the N···H-O and O···H-N non-Covalent Bonds

The intermolecular stretching force constants k_s for imid···H_2O and H_2O···imid may be evaluated by a model introduced by Millen, described in detail elsewhere.[46] The model approaches complexes by means of a pseudodiatomic model which considers the geometry of the complex subunits. In order to apply the model, it is required that *a*-axis of the complex is aligned or almost aligned with the axis of the intermolecular hydrogen bond, which applies for both imid···H_2O and H_2O···imid. The model assumes that contributions to the fitted value of the centrifugal distortion D_J by stretching modes other than that of the intermolecular interaction are negligible. It also assumes that upon complexation, the geometry of the subunits remains unaffected. The model is strictly designed for equilibrium values of rotational and centrifugal distortion constants but given that these are rarely available, zero-point quantities may be used. The stretching force constant k_s is expressed as;

$$k_s = 16\pi^4(\mu R_{CM})^2[4B_0^4 + C_0^4 - (B_0^4 - C_0^4)^2(B_0^4 + C_0^4)^2]/(hD_J) \qquad (Eq.5.1)$$

where μ is the reduced mass of the pseudodiatomic, expressed as $\mu = \frac{M_I M_W}{M_I + M_W}$ where M_I and M_W are the mass of the imidazole and water subunits, respectively. The distance between the centers of mass between the two subunits is defined by R_{CM}. The stretching frequency[47] of the intermolecular interaction v is given by the expression;

$$v = \frac{1}{2\pi c}\sqrt{\frac{k_s}{\mu}} \qquad (Eq.5.2)$$

where c is the speed of light.

Results for imid···H_2O and H_2O···imid alongside those for other complexes of six- and five-membered *N*-heteroaromatics with water are summarized in table 5.8. These are calculated from the rotational and centrifugal distortion constants determined here and from previous studies. For pyridine···H_2O and H_2O···imid, two values are calculated for k_s and v, each one corresponding to the rotational and centrifugal distortion constants determined for the individual substates. Looking at table 5.8, it is apparent that values for k_s and v are generally larger for complexes between *N*-heteroaromatics and water where

the latter is acting as the proton acceptor. The force constant describing the hydrogen bond in imid···H_2O is twice the magnitude of those in each state of pyridine···H_2O. Comparing imid···H_2O to pyrimidine···H_2O, pyridazine···H_2O and 1,3,5-triazine···H_2O, k_s and v are of similar magnitude. This highlights the similarities in the intermolecular hydrogen bond in these complexes. The values of k_s and v for the 0^- state of H_2O···imid are similar to those determined for the respective state in H_2O···pyrrole. The values of k_s and v determined for the two states of H_2O···imid are significantly different from one another. It is likely that the effects of the internal motions described earlier are affecting the values of the centrifugal distortion constants and this reflects on the force constants and stretching frequencies of these bonds. The assumption that stretching modes other than that for the intermolecular hydrogen bond have a negligible contribution to the measured centrifugal distortion constants is therefore unreliable. Secondary interactions like those described for the complexes in table 5.7 will have a significant contribution to the values of the centrifugal distortion constants and subsequently to k_s and v. For these reasons, it is not possible to draw further conclusions about the strength of these interactions by looking at the force constants alone.

Table 5.8. Stretching force constants k_s, and stretching wavenumbers v/c, determined for the hydrogen bonded complexes discussed in this work and in references 15,17,19, 21-23.

	k_s (kg m s^{-2})	v/c (cm^{-1})
imid···H_2O	10.69(17)[a]	112.9(9)
isoxazole···H_2O	26.9(10)	178.6(33)
pyridine···H_2O[b]	4.36(11)/5.95(16)	71.0(9)/82.9(11)
pyrimidine···H_2O	13.8	126
pyridazine···H_2O	13.1	122.8
1,3,5-triazine···H_2O	9.05	108.1
H_2O···imid[b]	22.0(8)/45.6(1.9)	162(3)/233(5)
H_2O···pyrrole	28	180

[a] Numbers in parentheses are one standard deviation in units of the last significant figure.
[b] The two results shown for each of pyridine···H_2O and H_2O···imid are those determined for the 0^- and 0^+ states respectively. For pyridine···H_2O, values for k_s and v were deduced from the spectroscopic parameters determined in the original work of R. B. Mackenzie *et al.*[19]

5.8 Nuclear Quadrupole Coupling Constants

Measured nuclear quadrupole coupling constants χ_{aa} and $\chi_{bb} - \chi_{cc}$ of N1 and N3 in imid···H_2O and H_2O···imid are sensitive to subtle changes in the electronic environment around the N nuclei. To perform direct comparisons on the coupling between imid···H_2O and H_2O···imid and the imidazole monomer, the diagonalized coupling terms χ_{xx}, χ_{yy} and χ_{zz} are calculated with QDIAG following the procedure described for PCA in chapter 4 and the underpinning theory in chapter 2. The off-diagonal term χ_{ab} was calculated at the B3LYP(D3BJ)/aug-cc-pVTZ level for each complex (table 5.1) and 25% uncertainty of its value was given. The orientation of the *x*-, *y*- and *z*-nuclear axes placed on N1 and N3 are based on the convention established by Cristen *et al.*[12] for the imidazole monomer. For N1, it holds that $\chi_{zz} \approx \chi_{cc}$, and for N3, $\chi_{yy} \approx \chi_{cc}$ because the complexes are essentially approaching planarity. The angle between the *x*-axis (for N1) or *y*-axis (for N3) and the *a*-axis is defined as φ. The derived values of χ_{xx}, χ_{yy} and χ_{zz} for N1 and N3 are in good agreement with those determined for the imidazole monomer and they are summarized in table 5.9.

No significant changes in the electronic environment around the N1 and N3 nuclei in imidazole are observed upon attachment of H_2O. The magnitude and sign of the χ_{xx}, χ_{yy} and χ_{zz} coupling component is consistent across imid···H_2O, H_2O···imid and the imidazole monomer. As it was discussed in chapter 4, the values of χ_{xx}, χ_{yy} and χ_{zz} will be somewhat dependent on the calculated values of χ_{ab}. The measured values of the nuclear quadrupole coupling components are expected to be impacted by internal motions occurring at the water subunit causing changes at the efg on N1 and N3.

Table 5.9. Diagonal nuclear quadrupole coupling terms χ_{xx}, χ_{yy} and χ_{zz} for imid···H_2O, H_2O···imid and imidazole monomer.

	Imid···H_2O	H_2O···Imid	Imidazole[a]
$\boldsymbol{\chi_{xx}}$(N1) (MHz)	1.096(27)	0.912(74)	0.890(52)
$\boldsymbol{\chi_{yy}}$(N1) (MHz)	1.332(54)	1.45(51)	1.633(58)
$\boldsymbol{\chi_{zz}}$(N1) (MHz)	–2.428(30)	–2.36(23)	–2.524(12)
$\boldsymbol{\eta}$[b]	0.097(25)	0.23(22)	0.1361(59)
$\boldsymbol{\chi_{xx}}$(N3) (MHz)	1.23(19)	1.92(78)	1.835(23)
$\boldsymbol{\chi_{yy}}$(N3) (MHz)	1.980(56)	2.30(22)	2.278(24)
$\boldsymbol{\chi_{zz}}$(N3) (MHz)	–3.21(15)	–4.21(74)	–4.113(34)
$\boldsymbol{\eta}$[b]	0.234(63)	0.09(19)	0.060(20)

[a] Results from Christen *et al.*[12]

[b] Asymmetry parameter $\eta = (\chi_{xx} - \chi_{yy})/\chi_{zz}$

5.9 Discussion

A notable outcome of this work is that both imid···H_2O and H_2O···imid were formed and isolated in a free jet expansion of argon buffer gas. A previous FT-IR study by Zischang *et al.* featuring co-expansion of imidazole, from a heated reservoir, and water in a helium buffer only identified the imid···H_2O isomer.[25] The authors reported that their sample preparation conditions did not yield the H_2O···imid isomer and suggested that it effectively relaxes into imid···H_2O. The competition between kinetic and thermodynamic control within an expanding gas sample was previously explored by Ruoff *et al.*[48] According to their work, conformational relaxation to lower energy configurations occurs more effectively in a gas sample that contains a high concentration of krypton or argon. Higher energy conformations are more readily accessible within an expanding gas sample containing neon or helium. The supersonic expansion dynamics were briefly discussed in chapter 2. Considering that in this work the two isomers were formed in an argon buffer expansion and the observation of Ruoff *et al.*,[48] it is anticipated that both isomers might be observable in a neon or helium supersonic expansion. A similar conclusion was drawn by FT-IR experiments on benzimidazole[26] and *N*-methylbenzimidazole.[49]

The question "where does the first water molecule go in imidazole?" was posed by Zischang *et al.* in their aforementioned work[25] and it was concluded that imid···H_2O is the lowest energy isomer. In this work, imid···H_2O was observed with a higher intensity than H_2O···imid despite the fact that the latter is calculated to have a larger dipole moment than the former ($|\mu_a| = 5.3$ D and $|\mu_a| = 6.2$ D). The spectrum of H_2O···imid was split into two components, 0^- and 0^+, due to internal motions associated with the water subunit which may result in an overall decrease of signal intensity. In our experiment, it is not possible to directly correlate signal intensity with the relative energy of the two isomers. DFT calculations suggest that imid···H_2O is lower in energy than H_2O···imid, however, this cannot be determined by the experimental results.

Geometrical parameters for a number of *N*-heteroaromatic monohydrates are shown in table 5.10. A primary hydrogen bond is observed between the pyridinic nitrogen of pyrazine, pyridine, pyridazine, 1,3,5-triazine, 2-fluoropyridine, oxazole and imidazole (this work) and water as well as a secondary interaction with C-H bonds adjacent to each pyridinic nitrogen. The interplay between primary and secondary interactions determines the orientation of the water subunit in each monohydrate, particularly the $\angle(O - Hb \cdots N3)$ angle. In table 5.10, it is observed that the primary hydrogen bond deviates from

linearity with the $\angle(O - Hb \cdots N3)$ angle varying between 141.12˚ in oxazole and 172.2˚ in imidazole. The length of the primary hydrogen in imid···H_2O is similar to that in pyridine···H_2O, as it is expected considering the similarities in the immediate chemical environment.[19] The calculated $r(H_b \cdots N)$ in pyridine···H_2O is 1.95 Å whilst the experimentally determined value of $r(H_b \cdots N3)$ in imid···H_2O is 1.927(27) Å. The length of the secondary interaction in imidazole $r(O \cdots H2)$ was determined to be 3.05 Å which longer than the respective secondary interaction in pyridine···H_2O by approximately 0.36 Å. Fewer complexes with a primary hydrogen bond at the pyrrolic nitrogen of an *N*-heteroaromatic are available. The $\angle(O \cdots H1 - N1)$ angle of H2O···imid is calculated to be 174.7° implying that linearity of the hydrogen bond is compromised by some secondary interaction between the imidazole ring and the water subunit. The $\angle(X \cdots O \cdots H1)$ angle ranges from 143° for H2O···pyrrole to 165° for H2O···indole. Structural parameters in all these molecules are expected to be somewhat contaminated by the large amplitude molecules concerning the water subunit in each one of them.

Table 5.10. Lengths and geometries of hydrogen bonds reported for complexes described in references 17, 18, 19, 21-23, 15.

Proton donor = H_2O	$\boldsymbol{r(H_b \cdots N3)}$ (Å)	$\boldsymbol{\angle(O–H_b \cdots N3)}$ (º)
6-membered rings		
pyrazine···H_2O	1.94(2)	152(4)
pyridine···H_2O [a]	1.95	156
pyrimidine···H_2O	1.98	164.7
pyridazine···H_2O	2.04	165.5
5-membered rings		
imid···H_2O [b]	2.024(23)	172.2(26)
isoxazole···H_2O	2.1467	141.12
Proton donor = N-heteroaromatic	$r(H1 \cdots O)$ (Å)	$\angle(H1 \cdots O \cdots X)$ (º)
H_2O···pyrrole	-	143(5)
H_2O···imid [b]	2.007(4)	152(6)
H_2O···indole	2.007(5)	165(5)

[a.] DFT result calculated at the M06-2X/6-311++G(3df,3pd) level.

[b.] Experimentally-determined r_0 parameters (this work).

5.10 Outlook

The broadband rotational spectra of two isomers of a monohydrate complex formed between imidazole and water, imid···H_2O and H_2O···imid, were recorded in the 7.0-18.5 GHz region. Rotational constants, centrifugal distortion constants and nuclear quadrupole coupling constants were determined experimentally for both species. A non-linear hydrogen bond is observed in imid···H_2O as a result of a secondary interactions. Secondary interactions also appear to affect the linearity of the hydrogen bond in the H_2O···imid isomer too. Two substates, 0^- and 0^+, were observed in the spectra of H_2O···imid as a result of large amplitude motions within the water moiety. Observation of both isomers in an argon free jet expansion suggests that both isomers are similar in energy.

5.11 References

1 J. S. Olson, A. J. Mathews, R. J. Rohlfs, B. A. Springer, K. D. Egeberg, S. G. Sligar, J. Tame, J. P. Renaud and K. Nagai, The role of the distal histidine in myoglobin and haemoglobin, *Nature*, 1988, **336**, 265–266.

2 T. C. Johnstone, K. Suntharalingam and S. J. Lippard, The Next Generation of Platinum Drugs: Targeted Pt(II) Agents, Nanoparticle Delivery, and Pt(IV) Prodrugs, *Chem. Rev.*, 2016, **116**, 3436–3486.

3 Z. Jin, Imidazole, oxazole and thiazole alkaloids, *Nat. Prod. Rep.*, 2006, **23**, 464–496.

4 Beena, N. Kumar, R. K. Rohilla, N. Roy and D. S. Rawat, Synthesis and antibacterial activity evaluation of metronidazole-triazole conjugates, *Bioorganic Med. Chem. Lett.*, 2009, **19**, 1396–1398.

5 H. Takahashi, M. Abe, T. Sugawara, K. Tanaka, Y. Saito, S. Fujimura, M. Shibuya and Y. Sato, Clotrimazole, an imidazole antimycotic, is a potent inhibitor of angiogenesis, *Japanese J. Cancer Res.*, 1998, **89**, 445–451.

6 M. Garner, D. R. Armstrong, J. Reglinski, W. E. Smith, R. Wilson and J. H. McKillop, The structure of methimazole and its consequences for current therapeutic models of graves' disease., *Bioorganic Med. Chem. Lett.*, 1994, **4**, 1357–1360.

7 S. Ganguly, V. V. Vithlani, A. K. Kesharwani, R. Kuhu, L. Baskar, P. Mitramazumder, A. Sharon and A. Dev, Synthesis, antibacterial and potential anti-HIV activity of some novel imidazole analogs, *Acta Pharm.*, 2011, **61**, 187–201.

8 B. M. Craven, R. K. McMullan, J. D. Bell and H. C. Freeman, The crystal structure of imidazole by neutron diffraction at 20°C and –150°C, *Acta Crystallogr. Sect. B Struct. Crystallogr. Cryst. Chem.*, 1977, **33**, 2585–2589.

9 J. Epstein, J. R. Ruble and B. M. Craven, The charge density in imidazole by X-ray diffraction at 103 and 293 K, *Acta Crystallogr. Sect. B Struct. Crystallogr. Cryst. Chem.*, 1982, **38**, 140–149.

10 S. Martinez-Carrera, The crystal structure of imidazole at –150°C, *Acta Crystallogr.*, 1966, *20*, 783–789.

11 G. L. Blackman, R. D. Brown, F. R. Burden and I. R. Elsum, Nuclear quadrupole coupling in the microwave spectrum of imidazole, *J. Mol. Spectrosc.*, 1976, **60**, 63–70.

12 D. Christen, J. H. Griffiths and J. Sheridan, *Zeitschrift fur Naturforsch. - Sect. A J. Phys. Sci.*, 1981, **36**, 1378–1385.

13 J. C. Mullaney, D. P. Zaleski, D. P. Tew, N. R. Walker and A. C. Legon, Geometry of an Isolated Dimer of Imidazole Characterised by Rotational Spectroscopy and *Ab Initio* Calculations, *ChemPhysChem*, 2016, **17**, 1154–1158.

14 W. Caminati, S. Melandri, A. Millemaggi and P. G. Favero, Rotational spectrum of the imidazole-argon complex, *Chem. Phys. Lett.*, 1998, **294**, 377–380.

15 M. J. Tubergen, A. M. Andrews and R. L. Kuczkowski, Microwave spectrum and structure of a hydrogen-bonded pyrrole-water complex, *J. Phys. Chem.*, 1993, **97**, 7451–7457.

16 W. Li, J. Chen, Y. Xu, T. Lu, Q. Gou and G. Feng, Unveiling the structural and energetic properties of thiazole-water complex by microwave spectroscopy and theoretical calculations, *Spectrochim. Acta Part A Mol. Biomol. Spectrosc.*, 2020, **242**, 118720.

17 S. McGlone, P. Moreschini, T. K. Ha and A. Bauder, Microwave spectra and structure of an isoxazole-water complex, *Mol. Phys.*, 2001, **99**, 1353–1364.

18 S. Blanco, J. C. Lopez, J. L. Alonso, P. Ottaviani and W. Caminăti, Pure rotational spectrum and model calculations of indole–water, *J. Chem. Phys.*, 2003, **119**, 880–886.

19 R. B. Mackenzie, C. T. Dewberry, R. D. Cornelius, C. J. Smith and K. R. Leopold, Multidimensional large amplitude dynamics in the pyridine-water complex, *J. Phys. Chem. A*, 2017, **121**, 855–860.

20 W. Caminati, L. B. Favero, P. G. Favero, A. Maris and S. Melandri, Intermolecular Hydrogen Bonding between Water and Pyrazine, *Angew. Chemie Int. Ed.*, 1998, **37**, 792–795.

21 S. Melandri, M. E. Sanz, W. Caminati, P. G. Favero and Z. Kisiel, The Hydrogen Bond between Water and Aromatic Bases of Biological Interest: An Experimental and Theoretical Study of the 1:1 Complex of Pyrimidine with Water, *J. Am. Chem. Soc.*, 1998, **120**, 11504–11509.

22 W. Caminati, P. Moreschini and P. G. Favero, The Hydrogen Bond between Water and Aromatic Bases of Biological Interest: Rotational Spectrum of Pyridazine−Water, *J. Phys. Chem. A*, 1998, **102**, 8097–8100.

23 A. Maris, S. Melandri, M. Miazzi and F. Zerbetto, Interactions of Aromatic Heterocycles with Water: The Driving Force from Free-Jet Rotational Spectroscopy and Model Electrostatic Calculations, *ChemPhysChem*, 2008, **9**, 1303–1308.

24 M. Y. Choi and R. E. Miller, Infrared laser spectroscopy of imidazole complexes in helium nanodroplets: Monomer, dimer, and binary water complexes, *J. Phys. Chem. A*, 2006, **110**, 9344–9351.

25 J. Zischang, J. J. Lee and M. A. Suhm, Communication: Where does the first water molecule go in imidazole?, *J. Chem. Phys.*, 2011, **135**, 61102.

26 A. Bhattacherjee and S. Wategaonkar, Water bridges anchored by a C–H···O hydrogen bond: the role of weak interactions in molecular solvation, *Phys. Chem. Chem. Phys.*, 2016, **18**, 27745–27749.

27 J. Hoeft and K. P. R. Nair, Millimeter-wave rotational transitions and molecular constants of the diatomic silver iodide, *Chem. Phys. Lett.*, 1986, **129**, 538–540.

28 L. H. Coudert, F. J. Lovas, R. D. Suenram and J. T. Hougen, New measurements of microwave transitions in the water dimer, *J. Chem. Phys.*, 1987, **87**, 6290–6299.

29 S. Thorwirth, H. S. P. Müller and G. Winnewisser, Millimeter- and submillimeter-wave spectrum of HC3N in the ground and vibrationally excited states, *J. Mol. Spectrosc.*, 2000, **204**, 133–144.

30 T. F. Giesen, M. E. Harding, J. Gauss, J.-U. Grabow and H. S. P. Müller, Determination of accurate rest frequencies and hyperfine structure parameters of cyanobutadiyne, HC5N, *J. Mol. Spectrosc.*, 2020, **371**, 111303.

31 C. Kirby, H. W. Kroto and D. R. M. Walton, The microwave spectrum of cyanohexatriyne, HC_7N, *J. Mol. Spectrosc.*, 1980, **83**, 261–265.

32 C. C. Costain, Determination of molecular structures from ground state rotational constants, *J. Chem. Phys.*, 1958, **29**, 864–874.

33 J. B. Simpson, J. G. Smith and D. H. Whiffen, Microwave spectrum of ICN including $IC^{15}N$, *J. Mol. Spectrosc.*, 1972, **44**, 558–570.

34 T. Bjorvatten, Molecular structure and microwave spectra of isotopic chloro-, bromo-, and iodocyanoacetylene, *J. Mol. Struct.*, 1974, **20**, 75–82.

35 M. Bester, M. Tanimoto, B. Vowinkel, G. Winnewisser and K. Yamada, *Zeitschrift fur Naturforsch. - Sect. A J. Phys. Sci.*, 1983, **38**, 64–67.

36 C. C. Costain and B. P. Stoicheff, Microwave spectrum, molecular structure of vinyl cyanide and a summary of CC, CH bond lengths in simple molecules, *J. Chem. Phys.*, 1959, **30**, 777–782.

37 A. Bouchy, J. Demaison, G. Roussy and J. Barriol, Microwave spectrum of cyanoallene, *J. Mol. Struct.*, 1973, **18**, 211–217.

38 J. C. Mullaney, C. Medcraft, D. P. Tew, L. Lewis-Borrell, B. T. Golding, N. R. Walker and A. C. Legon, Cooperative hydrogen bonds form a pseudocycle stabilizing an isolated complex of isocyanic acid with urea, *Phys. Chem. Chem. Phys.*, 2017, **19**, 25080–25085.

39 G. A. Cooper, C. Medcraft, E. Gougoula and N. R. Walker, Conformational isomers of trans -urocanic acid observed by rotational spectroscopy, *Phys. Chem. Chem. Phys.*, 2019, **21**, 9495–9503.

40 J. K. G. Watson, Determination of centrifugal distortion coefficients of asymmetric-top molecules. III. Sextic coefficients, *J. Chem. Phys.*, 1968, **48**, 4517–4524.

41 J. K. G. Watson, Determination of Centrifugal Distortion Coefficients of Asymmetric-Top Molecules, *J. Chem. Phys.*, 1967, **46**, 1935–1949.

42 C. Western, PGOPHER, a program for rotational, vibrational and electronic spectra, *J. Quant. Spectrosc. Radiat. Transf.*, 2015, **186**, 221–242.

43 Q. Gou, L. Spada, M. Vallejo-Lopez, S. Melandri, A. Lesarri, E. J. Cocinero and W. Caminati, Intermolecular Hydrogen Bonding in 2-Fluoropyridine-Water, *ChemistrySelect*, 2016, **1**, 1273–1277.

44 B. J. Drouin, Practical uses of SPFIT, *J. Mol. Spectrosc.*, 2017, **340**, 1–15.

45 A. R. Ubbelohde and K. J. Gallagher, Acid-base effects in hydrogen bonds in crystals, *Acta Crystallogr.*, 1955, **8**, 71–83.

46 D. J. Millen, Determination of stretching force constants of weakly bound dimers from centrifugal distortion constants, *Can. J. Chem.*, 1985, **63**, 1477–1479.

47 W. Gordy and R. L. Cook, *Microwave molecular spectra*, John Wiley & Sons, Ltd, New York, 3rd., 1984.

48 R. S. Ruoff, T. D. Klots, T. Emilsson and H. S. Gutowsky, Relaxation of conformers and isomers in seeded supersonic jets of inert gases, *J. Chem. Phys.*, 1990, **93**, 3142–3150.

49 A. Bhattacherjee and S. Wategaonkar, Conformational preferences of monohydrated clusters of imidazole derivatives revisited, *Phys. Chem. Chem. Phys.*, 2015, **17**, 20080–20092.

Chapter 6. Barriers to Internal Rotation in Methylimidazole Isomers

Publication: Eva Gougoula, Chris Medcraft, Juliane Heitkämper, and Nicholas R. Walker, *The Journal of Chemical Physics*, **151**, 2019, 10.1063/1.5119997

6.1 Introduction

The imidazole monomer[1,2] was discussed in chapter 5 in the context of stepwise microsolvation. Imidazole, alongside pyridine, pyrimidine, and pyrrole, among others, is an *N*-heterocyclic compound with a significant role in chemistry,[3] medicine,[4] biochemistry,[5] and photochemistry.[6] Structural isomers of methylimidazole exhibit very different physical properties as well as different toxicity levels.[7] Some imidazoles can be key compounds around tumor growth and development of certain cancers.[6,8] To a certain extent, their properties can be controlled by addition of functional groups resulting in functionalized imidazoles with anti-cancer,[6] anti-fungal[9] and anti-HIV[4] activity, among others. Substitution across an aromatic ring with CH_3 groups is common and will modify its physical and chemical properties.[7,10] Microwave spectroscopy is a powerful method in probing the energetic hindering potential of internal rotation of CH_3 groups.[11]

A large number of methylated aromatic molecules have been characterized by microwave spectroscopy and barriers to internal rotation of the methyl group have been determined.[12–17] It is crucial to determine and rationalize energetic barriers and obtain information on bonding preferences in order to establish fundamental conformational preferences. Gas phase measurements at temperatures as low as 2 K allow for precise determination of such properties by analysis of the rotational signatures of individual molecules.[18] The barrier to internal rotation of the methyl group in toluene is effectively unhindered. Fluorination of toluene[19,20] at the *ortho*- and *meta*-positions hinders the essentially free internal rotation of the methyl group and creates a threefold periodic barrier which will be denoted as V_3. The presence of fluorine substituents at one of the *ortho*- positions in toluene leads to a barrier in the order of 200 cm^{-1}. Lower barriers are observed when a single fluorine atom is at a *meta*- or *para*- position, of the order of 5-16 cm^{-1}. The V_3 barriers to internal rotation of the CH_3 group in isomers of methylthiazole[18,21,22] and methyloxazole[23] depend on the position where the CH_3 is attached. The V_3 barrier in 2-methyloxazole is 252 cm^{-1} while in 4-methyloxazole and 5-methyloxazole that value becomes 428 and 478 cm^{-1}, respectively.

In this chapter, the microwave spectra of *N*-methylimidazole (*N*-MI), 2-methylimidazole (2-MI), 4-methylimidazole (4-MI) and 5-methylimidazole (5-MI) in the 7.0-18.5 GHz frequency range are reported and analyzed. The geometry of the isomers and the internal rotation parameters are also approached by DFT calculations. Supersonic expansion and laser ablation methods described in chapter 3 were used to probe the molecules of interest. Data for 2-MI were collected and provided by Chris Medcraft and Juliane Heitkämper. 4-MI and 5-MI co-exist as a tautomeric mixture and were thus probed within the same experiment. The V_3 for these two isomers was determined by B. Harris as part of their PhD thesis[24] and these values are 311.9362(78) and 378.416(68) cm^{-1}, respectively. *N*-MI, which is a liquid under ambient conditions, was placed in the reservoir described in section 3.3 and seeded directly into the flow of the expanding argon carrier gas.

6.2 Experimental

The microwave spectra of *N*-MI, 2-MI, 4-MI and 5-MI were recorded in the 7.0-18.5 GHz frequency range. *N*-MI (Sigma-Aldrich, 99%) was vaporized from the reservoir described in chapter 3, section 3.3, and seeded directly into the flow of argon in the supersonic expansion. The 4(5)-MI (Sigma-Aldrich, 98%) tautomeric pair was mixed with Cu powder (Sigma-Aldrich, <75 μm, 99%) and $MgSO_4$ (Sigma-Aldrich, ≥99.5%) and pressed into a 13 mm diameter rod in 1:1:1 by mass ratio. Rods containing 2-MI (Sigma-Aldrich, 98%) and Cu 1:1 by mass ratio were prepared by Chris Medcraft and Juliane Heitkämper. Vaporized material from the rods were entrained into the supersonic jet of expanding Ar which was kept at 7 bar constant backing pressure for laser ablation experiments and 2 bar for *N*-MI.

6.3 Density Functional Theory

Density Functional Theory (DFT) calculations on *N*-MI, 4-MI and 5-MI (figure 6.1) were performed prior to experiments using Gaussian 09. Geometry optimizations were carried out using the B3LYP functional, with D3BJ correction. The functional was used in conjunction with three basis sets: cc-pVTZ, aug-cc-pVTZ and Def2-TZVP. Calculated rotational constants are benchmarked against experimentally determined constants and their percentage deviations are summarized in table 6.1. Given the level of consistency with the experiment at the B3LYP(D3BJ)/aug-cc-pVTZ level, atomic r_e coordinates of optimized geometries, the off-diagonal nuclear quadrupole coupling terms $x_{ab}(N1)$ and $x_{ab}(N3)$, centrifugal distortion constants D_J, D_{JK}, D_K, d_1, d_2 and potential energy curves of estimated V_3 barriers to internal rotation are calculated at that level too. The relative coordinate that was scanned to estimate the V_3 barriers to internal rotation was the dihedral $\angle(H-C6-N1-C2)$, $\angle(H-C6-C2-N3)$, $\angle(H-C6-C4-C5)$ and $\angle(H-C6-C5-N1)$ for each of *N*-, 2-, 4- and 5-MI, respectively. Calculations on 2-MI at the B3LYP(D3BJ)/aug-cc-pVTZ level were performed by C. Medcraft and J. Heitkämper and are used here for comparisons.

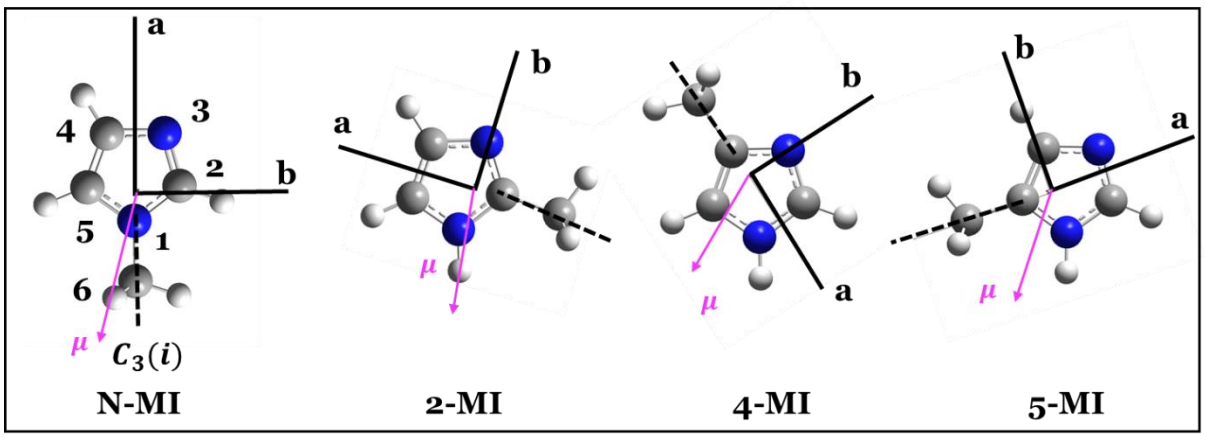

Figure 6.1. Calculated equilibrium geometries of *N*-, 2-, 4-, and 5-MI. Dipole moments are drawn to extend from positive to negative charges.

6.4 Initial Assumptions and Observations

The calculated geometries of *N*-, 2-, 4- and 5-MI are displayed in figure 6.1. Considering the calculated geometries and calculated rotational constants, all four isomers are asymmetric tops close to the prolate limit with the *a*-inertial axis being almost co-linear with the H_3C-N bond of *N*-MI and the H_3C-C bond of 2-, 4- and 5-MI. The molecular skeleton of the aromatic ring lies within the plane defined by the *a*- and *b*-inertial axes which are mutually perpendicular to the *c*-axis. The electric dipole moment is dependent on the arrangement of the pyrrolic and pyridinic nitrogen within the ring with respect to the *a*- and *b*-inertial axes. In all cases, the dipole moment lies within the plane of the aromatic ring. The microwave spectra of *N*-, 2-, 4- and 5-MI in the 7.0-18.5 GHz frequency range are displayed in figure 2.2, 2.4 and 2.5 and were collected over the course of 1.14, 0.9 and 2.6 M FID's, respectively, with 4- and 5-MI co-existing in the same spectrum. Expanded portions of the spectra with selected transitions are displayed in figure 2.3 and 2.6. At first glance, the spectra carry hyperfine structure induced by the presence of pyrrolic and pyridinic nitrogen (nuclear spin $I = 1$) in the aromatic rings. A total of 150 to 300 hyperfine transitions were assigned to the spectrum of each isomer. The ratio of identified transitions of *a*- and *b*-type is consistent with the ratio of the $|\mu_a|$ and $|\mu_b|$ dipole moment components in each isomer.

It was discussed before that laser ablation of organic molecules, particularly those containing nitrogen, generates a series of gas phase reaction products. It is believed that these products are generated by fragmentation of the precursor organic molecules and, potentially, subsequent recombination of these fragments in the gas phase. In the spectra of 2-, 4- and 5-MI, identified fragmentation products[2,25–31] include HC_3N, HC_5N, HC_7N, CH_3CN, CH_2=CHCN (vinyl cyanide), CH_3CCCN (methylcyanoacetylene) and $C_5N_2H_3$ (imidazole). In previous studies of imidazole (chapter 5) and *trans*-urocanic acid,[32] to name a few, essentially the same range of side-products was observed when they we laser ablated under similar experimental conditions. After assignment of the spectra of MI isomers, there is a large number of remaining unassigned lines with only a fraction the intensity of the parent MI. As it will be discussed in the chapter 7, some of these lines were assigned to weakly bound complexes formed between methylimidazole isomers and H_2O and Ar.

Presence of a CH_3 within each MI isomer suggests that internal rotation of that group coupling to the overall molecular rotation is possible. Considering previous studies of

similar methylated aromatic and heteroaromatic molecules, *e.g.* toluene,[33] isomers of methylpyridine,[34–36] methylpyrimidine,[37] methylpyrrole,[38,39] methylthiazole,[18,21,22] and methyloxazole,[18] where internal rotation of the CH_3 group was examined, it is likely that the CH_3 in MI isomers is also rotating internally. Evidence supporting this assumption is provided by the calculated V_3 barriers to internal rotation as well as the presence of "doublets" in the spectra. Rotational levels are split into *A*- and *E*-states ($m = 0$ and $m = \pm 1$, respectively) when a group of 3-fold symmetry is present within the molecule and undergoes internal rotation. Details on the underpinning theory of internal rotational is provided in Chapter 2 section 2.9. Fitting of *A*-states[B] was possible using a semi-rigid asymmetric Hamiltonian (section 2.7). A global fit of both *A*- and *E*-states requires the inclusion of terms accounting for the internal rotation (section 2.9). The fitting procedures as well as the information derived from the fits will be discussed in detail in the following sections.

[B] Fit for 2-MI was performed by Chris Medcraft and Julianne Heitkämper.

6.5 Fitting of A-States

Fitting of *A*-States molecular transitions was performed with Pgopher[40] using Watson's S-reduced Hamiltonian[41] (chapter 2, section 2.7). The Hamiltonian contains information about A_0, B_0 and C_0 rotational constants and D_J, D_{JK}, D_K, d_1 and d_2 distortion constants. The nuclear quadrupole coupling terms for the pyrrolic and pyridinic nitrogen, N1 and N3, respectively, are denoted as χ_{aa} and $\chi_{bb}-\chi_{cc}$. Upon rotation, the nuclear spin of N, $I = 1$, couples to the rotational angular momentum J resulting in formation of the quantum number F expressing the total angular momentum (chapter 2, figure 2.5 and 2.6). On this basis, the quadrupole matrix is built in blocks of F. For MI isomers where two N nuclei are present, N1 and N3, we have $J + I_{N1} = F_1$ and $J + I_{N3} = F$.

Experimentally determined spectroscopic parameters derived from fitting of *A*-states are summarized in table 6.2. Calculated rotational constants A_e, B_e and C_e are benchmarked against the experimentally determined ones (table 6.1) for the *A*-states which from now on will be denoted as A_0', B_0' and C_0' and called *effective* rotational constants. It was not possible to obtain an experimental value for d_1 and d_2 for *N*-MI and for d_2 for 2-MI. In these cases, the DFT calculated values for these parameters were included and kept fixed in the fits. The fits for 2-MI, 4-MI and 5-MI benefit significantly by inclusion of d_1 and d_2, resulting in reduced standard deviation of the fits (11.3, 10.8 and 12.8 kHz respectively) and reduced uncertainty in the rest of the fitted spectroscopic parameters (rotational constants, centrifugal distortion constants and nuclear quadrupole coupling constants). In the case of *N*-MI, inclusion of d_1 and d_2 does not affect the standard deviation or the uncertainties. However, for the sake of completeness and in order to adopt a consistent approach for all isomers, d_1 and d_2 were kept fixed at the DFT values. The fitted values of D_J and D_{JK} are consistently small for all MI isomers, as expected for semi-rigid aromatic molecules. Centrifugal distortion constants determined for similar aromatic molecules containing a methyl top are similar in magnitude.[18,22,23,42]

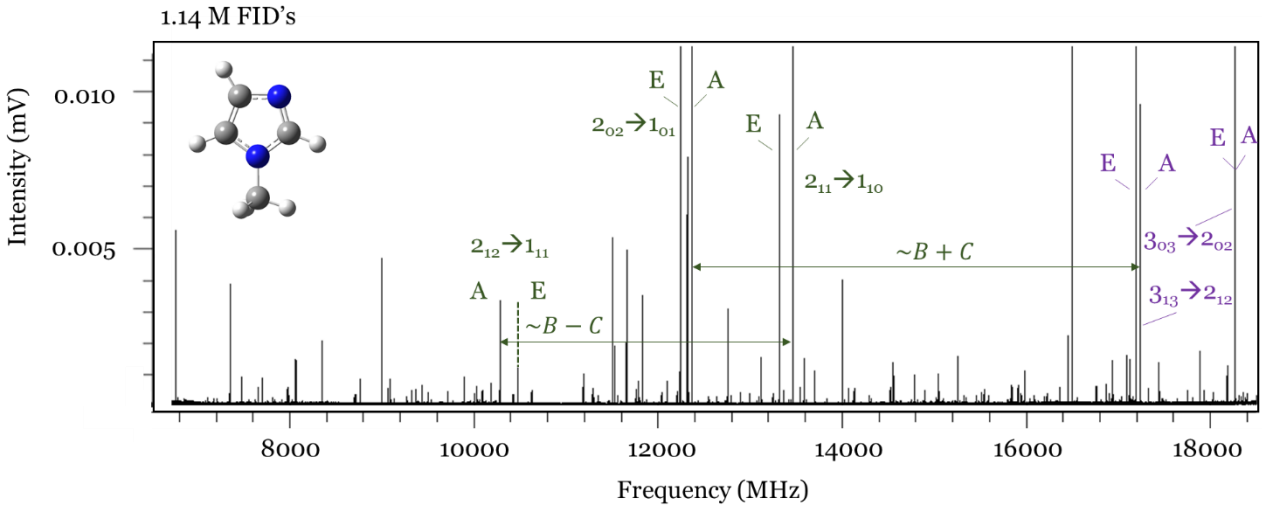

Figure 6.2. The microwave spectrum of *N*-MI in the 7.0-18.5 GHz region collected over the course of 1.15 M FID's.

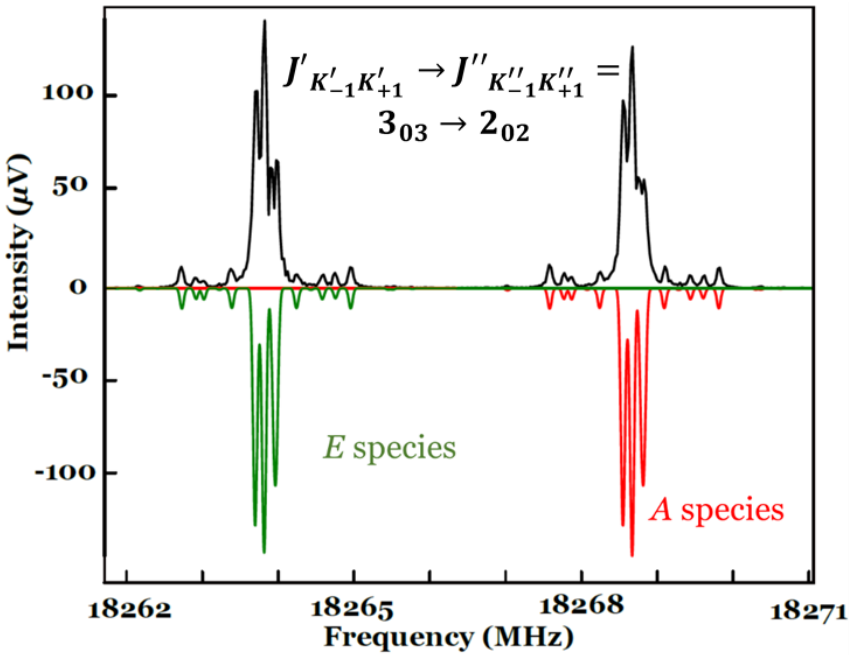

Figure 6.3. Expanded portion of the spectrum displayed in figure 2. The $3_{03} \rightarrow 2_{02}$ transition of *N*-MI averaged over 1.15 million FID's illustrating transitions of both *A* (m = 0) and *E* (m = ±1) symmetry states. Hyperfine splittings are introduced by the two nitrogen nuclei which are very similar for both *A*- and *E*-states. The experimental spectrum is shown at the top (black) and the simulation at the bottom (green and red). The simulation for the *E*-states is generated by shifting the simulation for the *A*-states the appropriate amount of MHz.

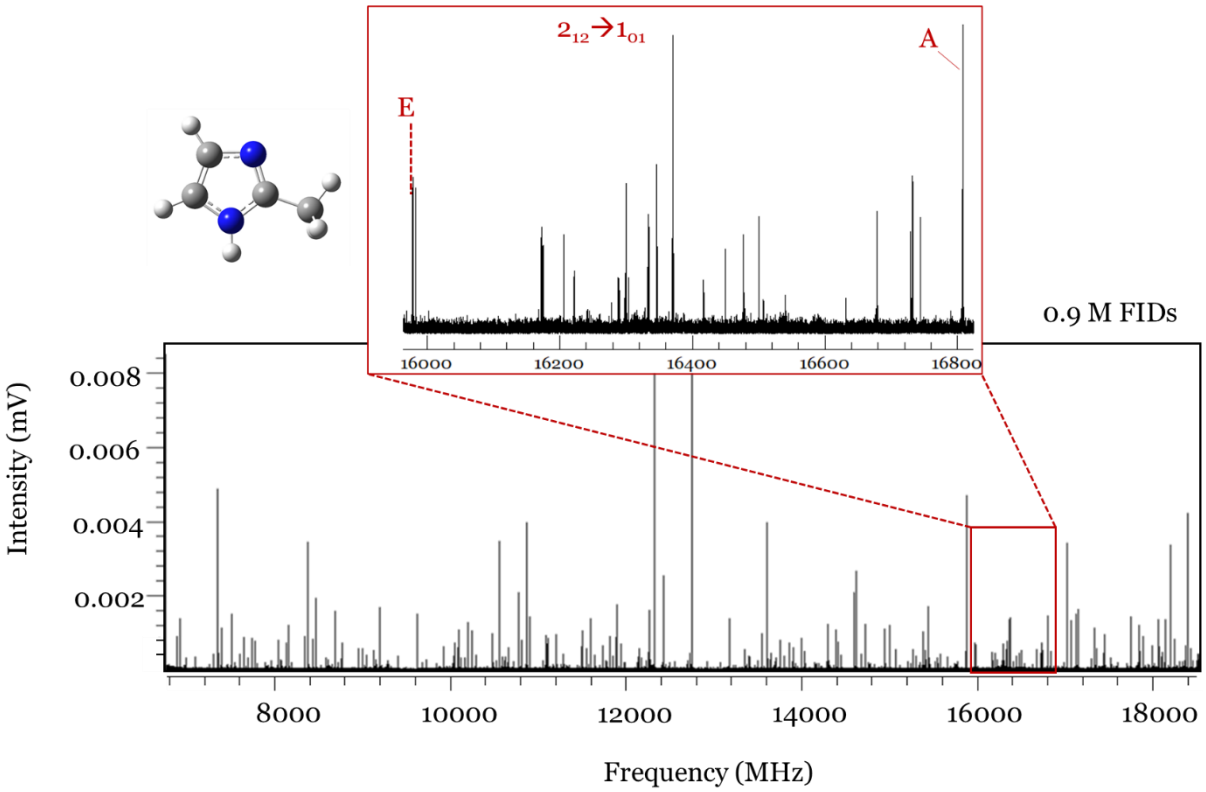

Figure 6.4. The microwave spectrum of 2-MI in the 7.0-18.5 GHz region collected over the course of 0.9 M FID's.

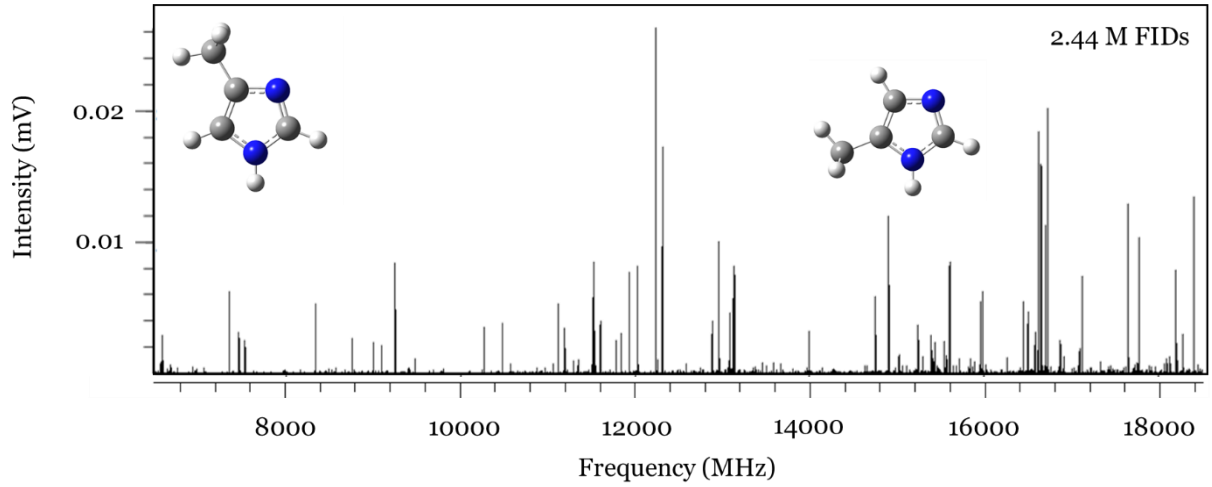

Figure 6.5. The microwave spectrum of 4- and 5-MI in the 7.0-18.5 GHz region collected over the course of 2.6 M FID's.

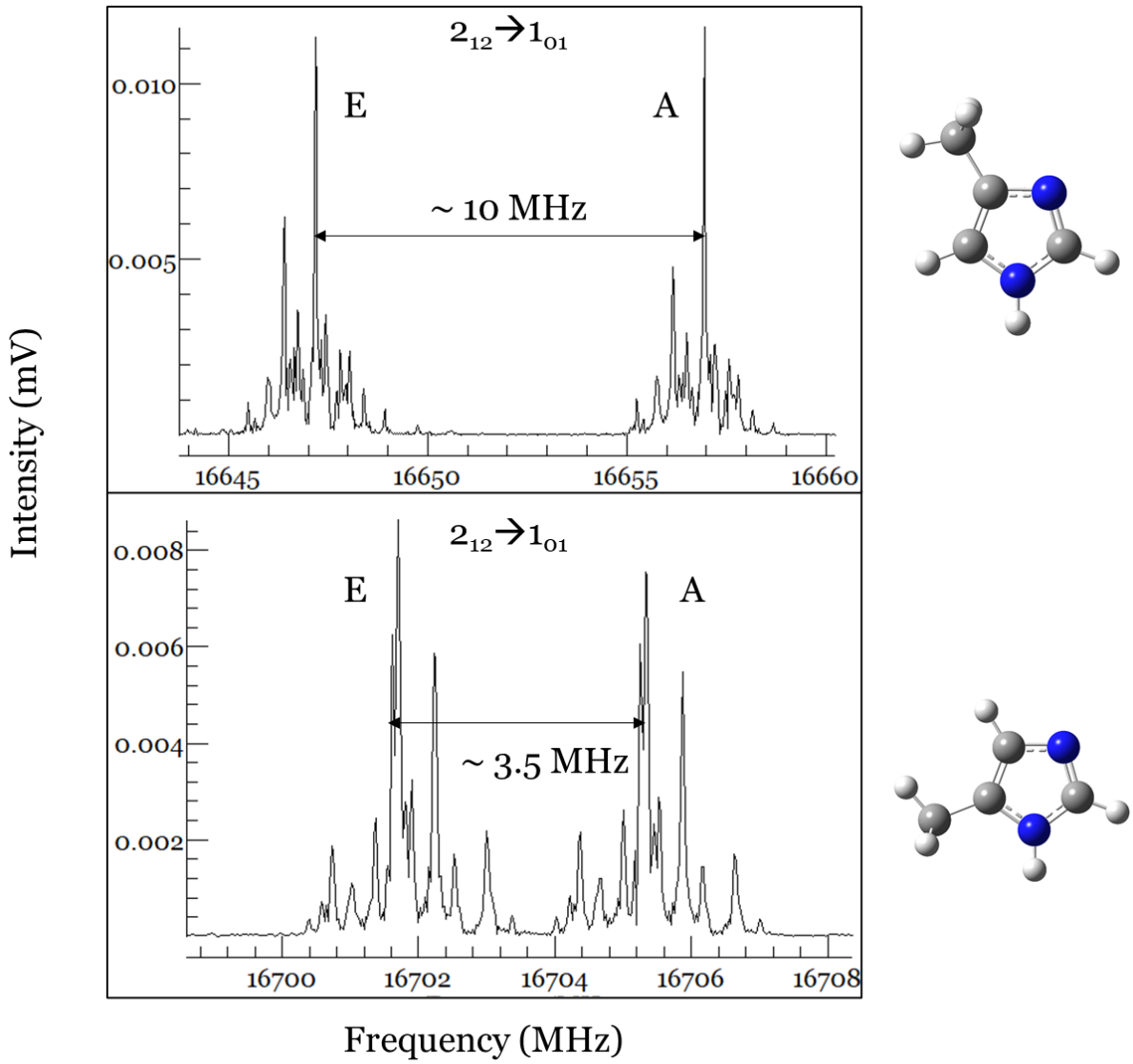

Figure 6.6. Expanded portions of the spectrum of 4- and 5-MI. The $2_{12} \rightarrow 1_{01}$ transitions of 4- and 5-MI averaged over 2.6 M FID's. The transitions are split into two components, *A*- and *E*-states, which is an outcome of internal rotation of the CH_3 group in both molecules. The energy separation between the two states is proportional to the barrier to internal rotation, *i.e.* the calculated barrier for 5-MI is higher than that of 4-MI, being consistent with a larger energy separation in 4-MI.

Table 6.1. Calculated rotational constants for *N*-, 2-, 4- and 5-MI. Percentage deviations of calculated rotational constants are calculated for performance benchmarking.

	N-Methylimidazole					
	B3LYP(D3BJ)					
	Def2-TZVP		cc-pVTZ		aug-cc-pVTZ	
A_e (MHz)[a]	9207.27	0.55%[b]	9207.62	0.55%[b]	9206.40	0.54%[b]
B_e (MHz)	3626.73	0.46%	3625.86	0.44%	3625.11	0.42%
C_e (MHz)	2645.17	0.48%	2644.64	0.46%	2644.17	0.44%
$\lvert\mu_a\rvert$, $\lvert\mu_b\rvert$, $\lvert\mu_c\rvert$ (D) [c]	3.9, 1.1, 0		3.9, 1, 0		4, 1, 0	
	2-Methylimidazole					
	B3LYP(D3BJ)					
	Def2-TZVP		cc-pVTZ		aug-cc-pVTZ	
A_e (MHz)	8978.77	0.96%	8976.79	0.94%	8981.74	1.00%
B_e (MHz)	3606.09	0.14%	3606.79	0.16%	3604.12	0.08%
C_e (MHz)	2614.67	0.38%	2614.78	0.38%	2613.80	0.34%
$\lvert\mu_a\rvert$, $\lvert\mu_b\rvert$, $\lvert\mu_c\rvert$ (D)	0.6, 3.6, 0		0.6, 3.5, 0		0.6, 3.5, 0	
	4-Methylimidazole					
	B3LYP(D3BJ)					
	Def2-TZVP		cc-pVTZ		aug-cc-pVTZ	
A_e (MHz)	9044.46	0.87%	9041.35	0.83%	9044.12	0.86%
B_e (MHz)	3518.21	0.28%	3519.09	0.30%	3517.24	0.25%
C_e (MHz)	2614.67	0.45%	2573.26	0.46%	2572.51	0.43%
$\lvert\mu_a\rvert$, $\lvert\mu_b\rvert$, $\lvert\mu_c\rvert$ (D)	2.1, 2.7, 0		2, 2.6, 0		2, 2.7. 0	
	5-Methylimidazole					
	B3LYP(D3BJ)					
	Def2-TZVP		cc-pVTZ		aug-cc-pVTZ	
A_e (MHz)	9116.30	0.68%	9117.85	0.69%	9116.59	0.68%
B_e (MHz)	3486.59	0.43%	3486.06	0.41%	3485.96	0.41%
C_e (MHz)	2562.23	0.51%	2561.96	0.50%	2561.83	0.49%
$\lvert\mu_a\rvert$, $\lvert\mu_b\rvert$, $\lvert\mu_c\rvert$ (D)	2.7, 2.9, 0		2.7, 2.9, 0		2.8, 2.9, 0	

[a] DFT-calculated rotational constants.

[b] Percentage deviations from experimental constants are calculated by means of equation $[(A_e - A_0)/A_0] \times 100$

[c] Calculated electric dipole moment components along the principal inertial axes.

Table 6.2. Effective rotational constants A_0', B_0' and C_0' alongside other spectroscopic parameters determined by fitting A-state transitions of *N*-, 2-, 4- and 5-MI.

	N-MI	2-MI	4-MI	5-MI
A_0' (MHz)	9194.5817(17)[a]	8992.75911(97)	8971.89077(89)	9057.12512(100)
B_0' (MHz)	3609.78192(71)	3600.99984(38)	3508.27356(31)	3471.61329(36)
C_0' (MHz)	2632.63930(68)	2604.96676(32)	2561.66742(25)	2549.43964(33)
D_J (kHz)	0.244(47)	0.1947(56)	0.2560(37)	0.2206(40)
D_K (kHz)	44.51(91)	97.06(11)	7.882(18)	3.080(33)
D_{JK} (kHz)	1.135(91)	1.942(53)	1.358(37)	1.759(34)
d_1 (kHz)	[–0.065776][b]	-0.0684(18)	–0.0746(16)	–0.0622(25)
d_2 (kHz)	[–0.00108]	[0.00512]	–0.01540(93)	–0.0146(11)
$\chi_{aa}(N1)$ (MHz)	1.7347(51)	1.3010(59)	1.4065(49)	1.1630(66)
$[\chi_{bb}(N1)–\chi_{cc}(N1)]$ (MHz)	3.6373(83)	4.178(10)	3.8163(88)	4.167(10)
$\chi_{ab}(N1)$ (MHz)[c]	[–0.0793]	[0.1263]	[–0.1051]	[–0.0643]
$\chi_{aa}(N3)$ (MHz)	–2.0837(52)	1.3742(64)	0.9529(55)	–2.0975(57)
$[\chi_{bb}(N3)–\chi_{cc}(N3)]$ (MHz)	–2.200(10)	–5.399(10)	–5.1394(82)	–2.415(12)
$\chi_{ab}(N3)$ (MHz)[c]	[–2.9276]	[1.7777]	[2.2221]	[2.9711]
$\lvert\mu_a\rvert, \lvert\mu_b\rvert, \lvert\mu_c\rvert$ (D)[d]	4, 1, 0	0.6, 3.5, 0	2, 2.7, 0	2.8, 2.9, 0
Δ_0' (uÅ^2)	–3.02267(6)	–2.536524(29)	–3.097382(24)	–3.142257(30)
P_{cc}' (uÅ^2)	1.511333(29)	1.268262(14)	1.548691(12)	1.571128(15)
N[e]	150	195	236	251
σ_{RMS} (kHz)[f]	9.9	11.3	10.8	12.8

[a] Numbers in parentheses are one standard deviation in units of the last significant figures; [b] Numbers in square brackets are fixed to results calculated using DFT at the B3LYP(D3BJ)/aug-cc-pVTZ level; [c] Off-diagonal nuclear quadrupole coupling term, χ_{ab} fixed to DFT-calculated value; [d] DFT-calculated results; [e] Number of hyperfine components included in the fit; [f] Root mean square deviation of the fit.

It was not possible to determine the off-diagonal nuclear quadrupole coupling terms, $\chi_{ab}(N1)$ and $\chi_{ab}(N3)$, through fitting of the available spectroscopic data. $\chi_{ab}(N1)$ and $\chi_{ab}(N3)$ were kept fixed at their DFT values and will be used for diagonalization of the $\chi_{aa}(N1)$, $\chi_{bb}(\mathrm{N1}) - \chi_{cc}(N1)$, $\chi_{aa}(N3)$ and $\chi_{bb}(\mathrm{N3}) - \chi_{cc}(N3)$) nuclear quadrupole coupling terms in section 6.8. Diagonalization results in determination of χ_{zz}, χ_{yy} and χ_{xx} coupling terms which are expressed in terms of mutually perpendicular principal nuclear axes z, y and x placed on the individual quadrupolar nuclei N1 and N3 in each MI isomer.

The signal to noise (S:N) ratio of the spectra of the parent *N*-, 2-, 4- and 5-MI was approximately 250:1, which allowed for observation of ^{13}C and ^{15}N isotopologues in their natural isotopic abundance. In section 6.6 molecular geometries, it will be shown how experimentally determined rotational constants for the available ^{13}C and ^{15}N isotopologues resulted in determination of atomic coordinates of heavy atoms in the molecular skeleton of each MI isomer. The experimentally determined spectroscopic parameters of the available ^{13}C and ^{15}N isotopologues are detailed in table 6.3 and 6.4. The nuclear quadrupole coupling constants χ_{aa} and $\chi\chi_{bb} - \chi_{cc}$ for N1 and N3 were kept fixed to the values determined for the respective parent isotopologue.

Table 6.3. Experimentally determined effective rotational constants for the torsional ground state of ^{13}C and ^{15}N isotopologues of *N*- and 2-MI.

	N-Methylimidazole					
	^{15}N(1)	^{13}C(2)	^{15}N(3)	^{13}C(4)	^{13}C(5)	^{13}C(6)
A_0' (MHz)	9194.9288(38)[a,b]	9010.820(95)	9114.31(22)	9123.37(11)	8986.80(11)	9194.72(15)
B_0' (MHz)	3598.4477(22)	3609.2353(16)	3558.0319(39)	3558.9266(15)	3609.5046(21)	3498.3721(19)
C_0' (MHz)	2626.6414(18)	2617.0542(11)	2598.50601(28)	2599.7298(13)	2615.1501(12)	2572.8642(16)
N [c]	13	31	7	25	28	25
$\sigma_{\text{r.m.s}}$ [d] (kHz)	9.9	10.9	11.3	10.9	12.1	13.4
	2-Methylimidazole					
	^{15}N(1)	^{13}C(2)	^{15}N(3)	^{13}C(4)	^{13}C(5)	^{13}C(6)
A_0' (MHz)	8814.6319(18)	8992.8302(11)	8792.1062(42)	8915.8214(17)	8926.2872(14)	8992.7498(14)
B_0' (MHz)	3600.6798(11)	3590.29885(71)	3600.9490(24)	3552.2344(10)	3548.18883(98)	3487.68163(79)
C_0' (MHz)	2589.6296(10)	2599.38473(67)	2587.8671(18)	2572.97540(96)	2571.75208(87)	2545.13613(77)
N [c]	18	48	7	46	43	47
$\sigma_{\text{r.m.s}}$ [d] (kHz)	11.8	11.5	15.1	17.4	13.5	13.4

[a] Numbers in parentheses are standard deviations in units of the last significant figure.

[b] Each column presents the data for a different isotopologue. The column header indicates the identity of the atom substituted into the parent isotopologue where the atom numbering is that shown in Figure 1. For example, the results shown in the first column are those for isotopologues where ^{15}N is present in the N(1) position. The values of all other parameters are fixed to those determined for the corresponding isomer as shown in Table S3.

[c] Number of hyperfine components included in the fit.

[d] Root mean square deviation of the fit.

Table 6.4. Experimentally determined effective rotational constants for the torsional ground state of ^{13}C and ^{15}N isotopologues of 4- and 5-MI.

	4-Methylimidazole					
	^{15}N(1)	^{13}C(2)	^{15}N(3)	^{13}C(4)	^{13}C(5)	^{13}C(6)
A_0' (MHz)	8916.089(14)[a,b]	8885.3930(18)	8777.7047(39)	8971.9848(21)	8775.4655(16)	8971.8365(14)
B_0' (MHz)	3459.545(11)	3467.6755(11)	3508.2093(21)	3496.8472(14)	3507.8617(10)	3396.53395(80)
C_0' (MHz)	2531.7195(67)	2532.96827(81)	2545.6403(17)	2555.58829(99)	2545.16947(73)	2501.55747(70)
N [c]	7	30	9	24	24	23
$\sigma_{r.m.s}$ [d] (kHz)	18.7	13.1	14.8	12.9	9.7	8
	5-Methylimidazole					
	^{15}N(1)	^{13}C(2)	^{15}N(3)	^{13}C(4)	^{13}C(5)	^{13}C(6)
A_0' (MHz)	-	8989.8304(58)	-	8859.5298(18)	9061.7295(39)	9057.0010(34)
B_0' (MHz)	-	3426.5369(17)	-	3471.4965(11)	3461.1415(30)	3360.8398(10)
C_0' (MHz)	-	2519.94907(90)	-	2532.97377(84)	2542.8130(24)	2489.41542(95)
N [c]	-	9	-	8	6	9
$\sigma_{r.m.s}$ [d] (kHz)	-	8.2	-	6.8	9.2	10.5

[a] Numbers in parentheses are standard deviations in units of the last significant figure.

[b] Each column presents the data for a different isotopologue. The column header indicates the identity of the atom substituted into the parent isotopologue where the atom numbering is that shown in Figure 1. For example, the results shown in the first column are those for isotopologues where ^{15}N is present in the N(1) position. The values of all other parameters are fixed to those determined for the corresponding isomer as shown in Table S3.

[c] Number of hyperfine components included in the fit.

[d] Root mean square deviation of the fit.

6.6 Molecular Geometry

A first insight into the geometry of each MI isomer is obtained in terms of planar (second) moments. The relative equations have been discussed in previous chapters. The planar moment assigned to the *c*-inertial axis, P_{cc}, was evaluated for a range of molecules by R. K. Bohn *et al.*[43] It was shown that for a relatively small and rigid, singly-methylated molecule, where the only contributions to the out-of-plane mass are due to the protons on the CH_3 group, results in a value of P_{cc} of approximately 1.6 u Å^2. For *N*-, 2-, 4- and 5-MI, P_{cc} was calculated using the experimentally determined rotational constants summarized in table 6.2 for each isomer by means of equation 2.72.

The P'_{cc} values determined for *N*-, 2-, 4- and 5-MI are 1.50055(3), 1.26843(3), 1.54873(1) and 1.57117(2) u Å^2, respectively. In the case of 4- and 5-MI those values are sufficiently close to the expected 1.6 u Å^2 value for a planar and rigid molecule where the only out-of-plane contributions are coming from the CH_3 protons. Evidently, this is not the case for *N*- and 2-MI where these values significantly deviate from the expected value. This observation is consistent with the proposal that internal rotation of a CH_3 group may affect the *effective* rotational constants of a rotating molecule (obtained by fitting of *A*-state transitions as described in section 6.5). In section 6.7, it will be shown how the V_3 barrier to internal rotation for CH_3 may be evaluated by means of the inertial defect Δ'_0.

Determination of atomic coordinates of all carbon and nitrogen atoms in *N*-, 2- and 4-MI and all carbon atoms in 5-MI was performed using Kraitchman's method[44,45] (r_s). As described in chapter 2, section 2.10.2, the method determines the position of an atom based on shifts in rotational constants caused by isotopic substitution of that atom. Atomic coordinates of C and N atoms in *N*-, 2-, 4- and 5-MI are displayed in table 6.5 alongside their Costain errors[46] in parentheses. The method only generates the magnitude of the relative coordinates so for that reason signs were implied by the DFT calculated coordinates of the optimized structures. Given that only an *A*-states fit could be performed on the ^{13}C and ^{15}N isotopologues, the *effective* rotational constants were used to calculate the atomic coordinates without affecting the precision and quality of these coordinates. It is obvious in table 6.5 that the resulting r_s coordinates are in good agreement with the DFT r_e coordinates calculated for each isomer. Considering that an equilibrium structure is calculated by DFT whilst the r_s method determines the zero-point structure, some discrepancies are observed between theory and experiment, *e.g.* C(4) in 5-MI. Imaginary

coordinates are obtained for some atoms, *i.e.* C(5) of 5-MI, which lie close to an inertial axis or the center of mass suggesting that the magnitude of these coordinates is very small and they were therefore set to zero.

Atomic coordinates were evaluated with the program EVAL, also available from the PROSPE website,[47] and bond lengths between the heavy atoms in *N*-, 2-, 4- and 5-MI were determined. These are summarized in table 6.6 and compared against values obtained for unmethylated imidazole. Data from X-ray[48,49] and neutron[50] diffraction experiments are available for imidazole and they are displayed alongside its r_0 and r_s bond lengths. A crystal structure[51] is only available for 2-MI and the results are consistent with the r_s structure determined here through microwave spectroscopy. The differences between the structure obtained through X-ray crystallography and the gas phase structure mainly arise due to lattice and crystal packing effects in the former. The C(2)-N(3), N(3)-C(4), C(4)-C(5) and C(2)-C(6) bonds in the gas phase structure are elongated by an average value of approximately 0.018 Å whilst the N(1)-C(2) bond is approximately 0.03 Å shorter.

Table 6.5. Experimentally determined (r_s) and calculated (r_e) atomic coordinates of C and N atoms in *N*-, 2-, 4-, and 5-MI on the *a*- and *b*-axes assuming a planar geometry around the heavy atoms ($|c| = 0$).

		N(1)		C(2)		N(3)	
		a	*b*	*a*	*b*	*a*	*b*
N-MI	r_s / Å	–0.6689(22)[a]	0.0[b]	0.145(10)	-1.0635(14)	1.4337(11)	0.7094(23)
	r_e / Å	–0.6716	–0.0105	0.1295	-1.1303	1.4278	0.7083
2-MI	r_s / Å	0.112(13)	–1.0738(14)	–0.6496(23)	0.0[b]	0.045(34)	1.1411(13)
	r_e / Å	0.1314	–1.0695	–0.6595	0.0457	0.0791	1.1324
4-MI	r_s / Å	1.4323(11)	–0.6051(25)	1.3003(12)	0.7509(20)	0.051(29)	1.1248(13)
	r_e / Å	1.4227	–0.6046	1.3036	0.7510	0.0459	1.1192
5-MI	r_s / Å	-	-	–1.3867(11)	–0.6560(23)	-	-
	r_e / Å	–0.0855	–1.0559	–1.3898	–0.6484	–1.4789	0.6568
		C(4)		C(5)		C(6)	
		a	*b*	*a*	*b*	*a*	*b*
N-MI	r_s / Å	1.4171(11)	–0.6656(23)	0.103(15)	–1.1324(13)	–2.1209(7)	0.0[b]
	r_e / Å	1.4173	–0.6651	0.1295	–1.1303	–2.1199	0.0154
2-MI	r_s / Å	1.3902(11)	0.7071(21)	1.4481(10)	–0.6578(23)	–2.1448(7)	–0.008(191)
	r_e / Å	1.3898	0.7084	1.4477	–0.6550	–2.1463	–0.0053
4-MI	r_s / Å	–0.6891(22)	0.0[b]	0.130(12)	–1.1279(13)	–2.1865(7)	–0.019(79)
	r_e / Å	–0.6965	–0.0448	0.1446	–1.1253	–2.1858	–0.0197
5-MI	r_s / Å	–0.070(22)	1.1205(13)	0.6667(23)	0.0[b]	2.20012(68)	0.029(53)
	r_e / Å	–0.1792	1.1152	0.7089	0.0731	2.1950	0.0209

[a] Numbers in parentheses are Costain errors (in units of the last significant figure) calculated as $\delta z = 0.0015 / |z|$ Å where z is the value of the coordinate.

[b] An imaginary result was obtained so this coordinate is assumed equal to zero.

Table 6.6. Calculated (r_e) and experimentally determined (r_s, X-ray and neutron diffraction) bond lengths between the heavy atoms in imidazole and methylimidazole isomers.

Structural parameters		N(1)-C(2)	C(2)-N(3)	N(3)-C(4)	C(4)-C5)	C(5)-N(1)	X-C(6)
N-MI	r_s	1.340(27)	1.336(10)	1.3750(33)	1.394(14)	1.371(28)	1.4518(24)
	r_e	1.372	1.338	1.381	1.395	1.380	1.458
2-MI	r_s	1.316(58)	1.336(63)	1.414(32)	1.3662(31)	1.400(13)	1.4952(26)
	r_e	1.377	1.337	1.385	1.390	1.3803	1.497
100 K [a]	*X-ray*	*1.347(2)*	*1.327(2)*	*1.384(2)*	*1.356(3)*	*1.370(2)*	*1.487(2)*
4-MI	r_s	1.3624(32)	1.304(28)	1.367(54)	1.346(54)	1.404(11)	1.4976(26)
	r_e	1.372	1.334	1.387	1.394	1.383	1.500
5-MI	r_s	-	-	-	1.341(14)	-	1.5337(26)
	r_e	1.376	1.334	1.385	1.394	1.385	1.498
Imidazole [b]	r_0	1.3704	1.3164	1.3875	1.3676	1.3788	-
	r_s	1.3643	1.3135	1.3822	1.3638	1.3774	-
123 K [c]	*X-*	*1.349*	*1.326*	*1.378*	*1.358*	*1.369*	-
293 K [d]	*ray*	*1.337*	*1.311*	*1.381*	*1.311*	*1.373*	-
103 K [e]	*n-diff*	*1.347(1)*	*1.323(1)*	*1.375(1)*	*1.368(1)*	*1.369(1)*	-
293 K [e]		*1.358(1)*	*1.333(1)*	*1.389(1)*	*1.378(1)*	*1.381(1)*	-

[a] Reference 51; [b] Reference 2; [c] Reference 49; [d] Reference 48; [e] Reference 50

6.7 Internal Rotation of CH_3 - Global Fit of *A*- and *E*-States

Internal rotation has been explored in numerous aromatic molecules containing one or more CH_3 groups.[12,17,18,21–23,33,39,42,52] Internal rotation of a group with 3-fold symmetry is represented by a periodic potential function describing how the potential energy varies with rotating angle. As we saw in chapter 2, section 2.9, this can be generally described by the relationship Eq.2.61.

It was shown that the V_3 barrier to internal rotation in isomers of methylthiazole[18,21,22] (MT) and methyloxazole[23] (MO) varies significantly depending on the position where the CH_3 group substitutes. V_3 barriers of 34.9, 358 and 332 cm^{-1} were reported for each of 2-, 4- and 5-MT. Likewise, the V_3 barriers in 2-, 4- and 5-MO were determined to be 251, 428 and 478 cm^{-1}, respectively. Another outstanding example of varying V_3 barrier with substitution position is observed for the seven isomers of methylindole[53] (MIN), 1-, 2-, 3-, 4-, 5-, 6- and 7-MIN (the numbering was decided by the authors), with values varying from 121 to 426 cm^{-1}.

The V_3 barriers to internal rotation in *N*-, 2-, 4- and 5-MI were calculated with DFT methods as described in section 6.3. The calculated barriers are 190, 115, 295 and 377 cm^{-1} for each isomer, respectively, suggesting a correlation between barrier height and position of CH_3 substitution. Potential energy curves with the relative V_3 barriers are shown in figure 6.7. In this section, the PAM (theory section 2.9.1) was initially employed to

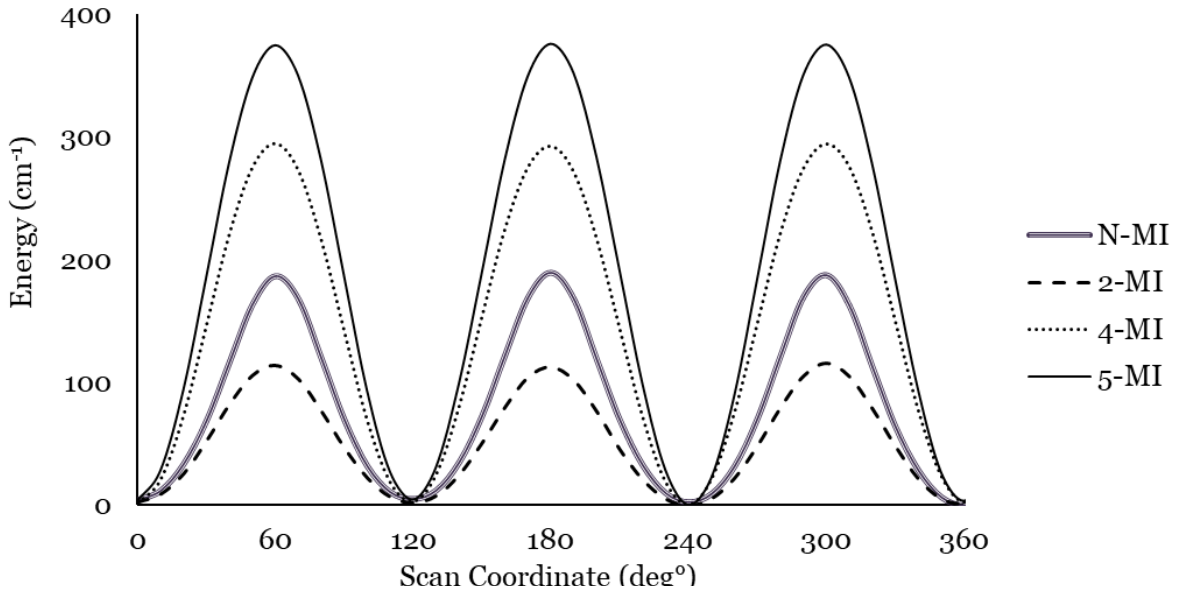

Figure 6.7. Potential energy surfaces of the relative dihedral angles describing internal rotation of the CH_3 in *N*-, 2-, 4- and 5-MI.

estimate the V_3 barrier to internal rotation for each MI isomer. Given the limitations of the PAM, a complete analysis and a global fit considering both *A*- and *E*-states is performed using the IAM (theory section 2.9.2) as implemented in the program XIAM.[54]

N-, 2-, 4-, and 5-MI fulfill the requirements explained in chapter 2, section 2.9.1 and it is possible to approach the V_3 barriers in each one of them using PAM. To summarize, those requirements are that the local C_3 axis of the threes-fold CH_3 group is co-linear or almost co-linear with the *a*-inertial axis of the molecule. Also, out-of-plane contributions to the inertial defect Δ_0 are negligible at the zero-point and the value of Δ_0 primarily arises from the CH_3 protons.

Examining figure 6.1 where the optimized equilibrium geometries of *N*-, 2-, 4- and 5-MI are shown, it is apparent that the *a*-axis is almost co-linear with the N-CH_3 or C-CH_3 bond. This is also supported by the r_s coordinates determined in section 6.6. As expected for small, rigid, aromatic molecules, contributions of out-of-plane vibrations to the inertial defect Δ_0 are negligible at the zero-point and the value of Δ_0 mainly arises from the CH_3 protons. Within the PAM, there are two limiting cases; i. where the CH_3 group undergoes unhindered internal rotation about its C_3 axis or ii. the CH_3 group is essentially rigid with two out-of-plane protons, resulting in the molecule behaving as a rigid-rotor. It has been shown[18] that in the first case of unhindered internal rotation, the A_0' rotational constant can exceed that expected for a molecule with a rigid CH_3 group by approximately 187 MHz. The inertial defect of the molecule relies exclusively on the rest of the molecular skeleton and the CH_3 does not contribute to it. In the latter case of essentially rigid behavior, differences between *effective* rotational constants and rigid rotor constants are expected to be much smaller (approaching zero) and the inertial defect Δ_0 to have a value of approximately –3.2 u Å^2. On this basis, the *effective* rotational constants A_0', B_0' and C_0' determined in section 6.5 can be compared against the rotational constants expected for a rigid rotor, denoted as A_{RR}, B_{RR} and C_{RR}, to estimate the V_3 barrier to internal rotation in MI isomers.

STRFIT[55] was used to calculate A_{RR}, B_{RR} and C_{RR}. For the initial *z*-matrix, the r_s geometry of the C and N atoms in each of *N*-, 2-, and 4-MI were used. The positions of the H-atoms were implied by the DFT calculated geometries at the B3LYP(D3BJ)/aug-cc-pVTZ level. In the case of 5-MI where no isotopic data are available for the N atoms, the r_s geometry of unsubstituted imidazole[2] was used, assuming that the imidazole subunit remains

unchanged upon methylation. For all isomers, it was further assumed that in the CH_3 group the $r(C-H)$ distance is 1.09 Å and the $\angle(C-C-H)$ angle 110°. Based on the expression;

$$F_\alpha = \frac{h}{8\pi^2 I_\alpha} \qquad (Eq.\,6.1)$$

where F_α is the standard rotational constant for an sp^3 hybridized methyl top, h is the Planck constant, it follows that the moment of inertia of the CH_3 top is $I_\alpha \cong 3.2$ u Å^2.

The rotational constants resulting when assuming rigid rotor behavior are summarized in table 6.7 alongside the *effective* rotational constants of *N*-, 2-, 4- and 5-MI. The inertial defect Δ_0' is calculated by means of equation 2.73 using the *effective* rotational constants. For 2-MI, the A_0' rotational constant exceeds A_{RR} by approximately 100 MHz whilst the difference between B_0' and C_0' and B_{RR} and C_{RR}, respectively, is significantly lower. This behavior is also observed for *N*-MI and, to a lesser extent, for 4- and 5-MI. At a first approximation and whilst considering these observations, it is expected that the lowest V_3 barrier will be found for 2-MI, followed by *N*-MI, 4-MI and 5-MI, consistent with the DFT calculated barriers.

Table 6.7. Effective rotational constants compared to rigid rotor rotational constants.

	N-MI[a]	2-MI [a]	4-MI [a]	5-MI[a, b]
A_0' (MHz)	9194.5817(17)[c]	8992.75911(97)	8971.89077(89)	9057.12512(100)
A_{RR} (MHz)	9153.91	8907.60	9002.00	9023.03
B_0' (MHz)	3609.78192(71)	3600.99984(38)	3508.27356(31)	3471.61329(36)
B_{RR} (MHz)	3626.68	3616.00	3515.11	3468.67
C_0' (MHz)	2632.63930(68)	2604.96676(32)	2561.66742(25)	2549.43964(33)
C_{RR} (MHz)	2640.99	2614.51	2569.10	2545.88
Δ_0' / u Å^2	−3.02267(6)[d]	−2.536524(29)	−3.097382(24)	−3.142257(30)

[a] Values of rotational constants implied by a rigid rotor (RR) geometry and the r_s coordinates of the carbon and nitrogen atoms given in Table 6.5. Internal coordinates that establish the positions of hydrogen atoms are assumed equal to the results of DFT calculations.

[b] Rigid rotor rotational constants defined as in footnote (a) while making the additional assumptions that r(N(1)–C(2)), r(N(3)–C(2)), r(N(3)–C(4)) and angles internal to the imidazole ring are equal to r_s results for imidazole.

[c] Effective rotational constants (A_0', B_0' and C_0') determined by fitting to A-species transitions (full details of fits including the values of centrifugal distortion and hyperfine constants are provided in Table 6.2).

[d] The assumption of rigid rotor behavior leads to $\Delta_0' \cong 3.2$ u Å^2 for each isomer.

The procedure followed to estimate V_3 barriers with PAM will only be described in detail for *N*- and 2-MI. Within the "high-barrier approximation" described in detail elsewhere[18,45], higher potential terms are neglected, *i.e.* $V_6 = V_9 = \ldots = 0$. Contributions to the B_0' and C_0' rotational constants due to the non-zero direction cosine between the C_3 axis of the CH_3 group and the *b*- and *c*-axis are also neglected. The *effective* Hamiltonian appropriate for the ground torsional state (A-states, m=0) can be expressed in terms of Herschbach's barrier dependent perturbation coefficient[45], $W_{v\sigma}^{(n)}$, and is described by the following relationship;

$$\hat{H}_{v=0,\sigma=0} = \left(A + F\rho_a^2 W_{00}^{(2)}\right)\hat{P}_a^2 + B\hat{P}_b^2 + C\hat{P}_c^2 \qquad (Eq.\,6.2)$$

where $\hat{P}_a$, $\hat{P}_b$ and $\hat{P}_c$ are the rotational angular momentum operators along the *a*-, *b*- and *c*-axes, respectively. A, B and C are the rotational constants for a generic, rigid molecule, the standard rotational constant for an sp^3 hybridized methyl top $F = h/[8\pi^2 I_\alpha(1-\rho_\alpha)]$, $\rho_\alpha = I_\alpha/I_a$, and $W_{00}^{(2)}$ is Herschbach's barrier dependent perturbation coefficient. $W_{00}^{(2)}$ depends on the reduced barrier $s = 4V_3/9F$, according to Microwave Molecular Spectra[45] and the tables by Hayashi and Pierce[56]. The perturbation coefficient can be expressed in terms of moments of inertia and inertial defect;

$$W_{00}^{(2)} = \left(1 + \frac{\Delta'}{I_\alpha}\right)\left(1 + \frac{\Delta'}{I_a'}\right) \qquad (Eq.\,6.3)$$

where Δ' is the *effective* inertial defect, I_α is the moment of inertia of the sp^3 hybridized CH_3 group and I_a' is the *effective* moment of inertia along the *a*-inertial axis of the molecule.

In-plane vibrational contributions to the inertial defect of the imidazole subunit at the zero-point are small resulting in a value of $\Delta_0 = +0.029$ u Å^2. These were subtracted from Δ_0'

shown in table 6.7. On this basis, it is calculated that $W_{00}^{(2)}$ for *N*-MI and 2-MI is approximately 0.042 and 0.182 (unitless quantities), respectively. With reference to reduced barrier tables in Microwave Molecular Spectra[45] and the work of Hayashi and Pierce[56], these values correlate to values of reduced barriers s of 17.1 and 10.2. It is estimated that $V_3 \cong 215$ and 128 cm^{-1} for *N*- and 2-MI, respectively. These values are sensitive to assumptions made for the molecules, for example, if $I_\alpha = 3.10$ u Å^2 is assumed, then $V_3 \cong 141$ cm^{-1} for 2-MI. Relatively good agreement is also observed between these values and the DFT calculated ones (190 and 115 cm^{-1}).

It should be noted that this procedure is appropriate for molecules with low barriers where $\left|\frac{\Delta'}{I_\alpha}\right| \ll 1$ and systems where vibrational contributions (and/or contributions arising by mass distribution directly) to Δ' are small. For these reasons, PAM does not provide a reliable measure of the V_3 barrier height particularly for 4- and 5-MI where the barriers are intermediate to high, as it will be discussed later. For the same reasons, PAM was not used in the process of determining the V_3 barriers in the weakly-bound complexes of MI isomers with H_2O in chapter 7.

The IAM was used to produce global fits with inclusion of both ground and first excited torsional *A*- and *E*-states ($m = 0$, $m = \pm 1$). The *A*- and *E*-states for a given transition in the spectrum of an asymmetric molecule share the same set of quantum numbers J, K_{-1} and K_{+1}. Considering the DFT calculated barrier heights, it is expected that the splitting between the two states will be in the range of 500 kHz to 10 MHz, with the lowest barrier accounting for the largest splitting. The global fits produce experimental values of rotational constants A_0, B_0 and C_0, and centrifugal distortion constants D_J, D_{JK}, D_K, d_1 and d_2, as appropriate. Parameters describing the internal rotation in each MI isomer include F_0, which was defined earlier as the rotational constants for and sp^3 hybridized CH_3 internal rotor, V_3 barriers to internal rotation and fitted angles between the local C_3 axis of the CH_3 group and the *a*-, *b*- and *c*-inertial axes of the molecules denoted as $\angle(i,a)$, $\angle(i,b)$ and $\angle(i,c)$.

In order to perform a fit with XIAM, an input file is required. The *effective* rotational constants and centrifugal distortion constants were used as the starting points for the global fits of transitions yielded by each isomer. The initial values of the polar coordinates of the internal rotation axis in the principal axes system, δ and ε, are deduced from the DFT

geometries. A definition of these coordinates was provided in chapter 2, section 2.9.2. The DFT calculated V_3 barriers are also used as initial values. The line-list of transitions consists of the *A*-state transitions, initially fitted with Pgopher, along with an identified *E*-state transition frequency. Identifying the correct *E*-state transition frequencies through spectral inspection can be challenging, however, the two states will typically exhibit very similar hyperfine structure and signal intensity due to statistical weights. Given that XIAM is not coded to treat internal rotation in a molecule with two quadrupolar nuclei, it was necessary to neglect the hyperfine structure and exclude the quantum numbers F_1 and F from the line-list. For this reason, the transition frequency centers were estimated, and iterative corrections of those center-frequencies were made after a few fit cycles and after inclusion of more *E*-state transitions. The precision of the fits is greatly underestimated by this procedure, however, the fitted V_3 barriers are in excellent agreement with their calculated values. The spectra were examined for further torsional excited states with $|m| > 1$, however, no transitions were identified that might reasonably be related to such states. Considering the low rotational temperature of the supersonic expansion, it is expected that states with $|m| > 1$ will not be populated.

Watson's S-reduced Hamiltonian[41] with the appropriate internal rotation terms as implemented in XIAM was used and the results of the global fits are summarized in table 6.8. For each of *N*-, 2-, 4- and 5-MI, the fitted values of $\angle(i, a)$ imply that the *a*-axis is essentially aligned with the C_3 axis (0 or 180°) of the C-CH_3 (or N-CH_3) bond. The planarity of the imidazole subunit is further supported by the fitted values of the $\angle(i, c)$ angles which are very close to 90°. The fitted V_3 barriers are 185.104(11), 122.7529(38), 317.20(14) and 386.001(19) cm^{-1} for *N*-, 2-, 4- and 5-MI, respectively. These values are consistent with those determined with PAM and in good agreement with the values reported by B. Harris[24] for 4- and 5-MI. A fitted value for F_0 is obtained for *N*-, 2-, and 4-MI, 157.9291(88), 157.6901(44) and 157.784(60) GHz, respectively, which correspond to an approximate value of $I_\alpha \cong 3.20$ Å. It was not possible to determine F_0 for 5-MI so during the fits it was kept fixed to 157.68 GHz.

Table 6.8. Results of "global" fits of spectroscopic parameters to *A* and *E*-species transition frequencies to determine rotational constants and internal rotation parameters for *N*-, 2-, 4- and 5-MI.

	N-MI	2-MI	4-MI	5-MI
$\boldsymbol{A_0'}$ (MHz)	9156.7503(50)[a]	8892.9063(26)	8966.7590(10)	9054.9327(15)
$\boldsymbol{B_0'}$ (MHz)	3609.9582(16)	3601.19596(95)	3508.41729(51)	3471.74371(51)
$\boldsymbol{C_0'}$ (MHz)	2632.4462(16)	2604.8287(98)	2561.52449(47)	2549.30663(32)
D_J (kHz)	0.16(11)	[0.1947(56)][b]	0. 288(20)	0.271(11)
D_K (kHz)	32.07(1.10)	–21.51(45)	7.98(33)	1.76(36)
D_{JK} (kHz)	–2.99(14)	7.44(10)	1.566(74)(34)	1.592(58)
d_1 (kHz)	[–0.065776][c]	–0.0764(90)	–0.0719(47)	–0.0586(46)
d_2 (kHz)	[–0.00108][c]	[0.00512][c]	–0.0146(23)	–0.0183(20)
$\boldsymbol{V_3}$ (cm^{-1})	185.104(11)	122.7529(38)	317.20(14)	386.001(19)
$\boldsymbol{F_0}$ (GHz)	157.9291(88)	157.6901(44)	157.784(60)	[157.68]
$\angle(\boldsymbol{i},\boldsymbol{a})$(°) [d]	0.33(20)	176.0705(94)	187.79(12)	187.539(66)
$\angle(\boldsymbol{i},\boldsymbol{b})$(°) [d]	90.00(32)	86.25(11)	96.37(16)	84.93(15)
$\angle(\boldsymbol{i},\boldsymbol{c})$(°) [d]	90.33(61)	88.8240(84)	85.53(15)	84.44(14)
$\boldsymbol{\kappa}$[e]	–0.70	–0.68	–0.70	–0.72
$\boldsymbol{\Delta_0}$ (u $Å^2$)	–3.20701(14)	–3.1497(7)	–3.11278(4)	–3.140029(34)
$\boldsymbol{P_{cc}}$(u $Å^2$)	1.60351(7)	1.5748(4)	1.556392(21)	1.570015(17)
σ_{RMS} (kHz)[f]	8.9	13.8	4.5	3.4
N[f]	32	46	47	44

[a] Numbers in parentheses are one standard deviation in units of the last significant figure.; [b] Fixed to D_J determined by fitting to transitions of the *A* species of 2-MI (see Table 6.2).; [c] Fixed to DFT-calculated results.; [d] Angle between the three-fold axis of the methyl group (i) and the respective inertial axes (a, b, c).; [e] Ray's asymmetry parameter, κ.; [f] Number of transitions included in the fit and root mean square deviation of the fit.

6.8 Nuclear Quadrupole Coupling Constants (NQCC)

The diagonal nuclear quadrupole coupling terms χ_{xx}, χ_{yy} and χ_{zz} were calculated with QDIAG for *N*-, 2-, 4-, and 5-MI. The results are summarized in table 6.9 alongside the values for unsubstituted imidazole[2], and 2- and 4-iodoimidazole[57]. The axes orientation on N1 and N3 is common across all molecules and a detailed description was given in chapter 5 for the case of the imidazole-water complex. For N1, the *z*-axis is almost parallel to the *c*-axis resulting in $\chi_{cc}(N1) \approx \chi_{zz}(N1)$ whilst for N3 this is permuted to the *y*-axis so it holds $\chi_{cc}(\mathrm{N3}) \approx \chi_{yy}(\mathrm{N3})$. The off-diagonal component χ_{ab} was calculated at the B3LYP(D3BJ)/aug-cc-pVTZ level for each isomer and was given a 25% uncertainty.

Within the limitations of our analysis, no significant changes are observed in the electronic environment of N1 and N3 of imidazole upon substitution with a CH_3 group or an I atom. The sign and the magnitude of the diagonalized nuclear quadrupole coupling constants are consistent across each molecule. The uncertainty in χ_{xx} and χ_{yy} in N1 is relatively large, in the second or third significant figure, so it is not possible to perform meaningful comparisons for these components. Likewise, χ_{xx} and χ_{zz} in N3 carry relatively large uncertainties.

Table 6.9. Diagonalization of nuclear quadrupole coupling terms to determine χ_{xx}, χ_{yy} and χ_{zz}.

	N-MI	2-MI	4-MI	5-MI	Imidazole	2-iodoim	4-iodoim
χ_{xx}(N1) (MHz)	0.943(10)	1.225(28)	1.160(21)	1.1512(86)	0.890(52)	0.98(26)	1.386(23)
χ_{yy}(N1) (MHz)	1.7427(64)	1.514(29)	1.451(20)	1.514(13)	1.633(58)	1.77(26)	1.136(21)
χ_{zz}(N1) (MHz)	–2.6860(49)	–2.7395(58)	–2.6114(50)	–2.6650(60)	–2.524(12)	–2.7561(47)	–2.5223(86)
η^a	0.294(31)	0.2977(44)	0.106(21)	0.111(81)	0.1361(59)	0.29(13)	0.099(12)
χ_{xx}(N3) (MHz)	2.04(69)	1.97(26)	1.94(41)	2.000(71)	1.835(23)	2.0097(47)	1.75(23)
χ_{yy}(N3) (MHz)	2.1419(27)	2.0124(59)	2.0933(49)	2.2563(66)	2.278(24)	2.17(14)	2.0051(86)
χ_{zz}(N3) (MHz)	–4.18(69)	–3.98(27)	–4.0360(31)	–4.25(71)	–4.113(34)	–4.18(14)	–3.76(23)
η	0.0244(80)	0.011(17)	0.011(65)	0.04(10)	0.060(20)	0.038(34)	0.068(61)

[a] The asymmetry parameter $\boldsymbol{\eta} = \frac{\chi_{xx}-\chi_{yy}}{\chi_{zz}}$

6.9 Discussion

The V_3 barriers to internal rotation are compared across the series of isomers of methylimidazole (MI) (this work), methylpyrrole[38,39] (MP), methylthiazole[18,21,22] (MT), methyloxazole[23] (MO) and methylindole[53] (MIN) and summarized in table 6.10. A graphical outlook on the V_3 barriers across a wide range of methylated *N*-heteroaromatic molecules is given in Figure 6.8. It is immediately apparent that the barrier height greatly depends on the substitution position of the CH_3 group across each ring. For the isomers of MI, MT and MO, the broad trend in barrier height is that the lowest V_3 value is observed for each of 2-MI, 2-MT and 2-MO. Likewise, the highest V_3 barrier in each of the series is observed for 5-MI, 5-MT and 5-MO with 4-MI, 4-MT and 4-MO being the intermediate case. The heteroatoms appear to have a great influence on the barrier height. For example, V_3 barrier for 2-MT is 35 cm^{-1} whilst for 2-MI and 2-MO that value becomes 123 and 252 cm^{-1}, respectively. Significant differences are also observed between MI and MP isomers. The V_3 barrier in *N*-MI is 186 cm^{-1} whilst in *N*-MP this value decreases by a factor of three. Comparing 2-MI and 2-MP, the V_3 barrier of the latter is approximately twice that of the former.

In molecules where a highly symmetric environment is observed around the CH_3 group, like in toluene and *N*-MP, only a low V_6 barrier is determined. Lowering the symmetry to a C_s point-group like in 2-MP, results in a hindered V_3 potential arising from steric and electronic effects. Comparing *N*-MI and *N*-MP, the V_3 barrier of the latter exceeds that of the former by a factor of three, despite the fact that the local, immediate, chemical environment of two C-H bonds adjacent to the N-CH_3 is the same in both molecules. This suggests that electronic effects induced by the presence of the second heteroatom in *N*-MI can propagate across the aromatic system and hinder the internal rotation. In each of 2-MI, 2-MT and 2-MO which exhibit the lowest V_3 in each series, two heteroatoms are adjacent to the C-CH_3 bond suggesting that the local environment is more symmetric in comparison to 4-MI, 4-MT and 4-MO and 5-MI, 5MT and 5-MO, respectively. Particularly 5-MI, 5-MT and 5-MO exhibit the highest V_3 barriers and the most asymmetric environment with a heteroatom and a C-H bond adjacent to each C-CH_3 in each series. Similar arguments were put in place in the cases of 2-MT and 2-MP. These interpretations, however, arise from empirical and intuitive observations so it is not possible to draw generalized conclusions that apply to all aromatic systems.

The effects of steric and electronic interactions were considered by Spangler[11] who emphasized on how significant effects are observed on the V_3 barriers when π-orbitals from aromatic rings interact with π-like orbitals on the adjacent CH_3 group. In cases where high symmetry is present[33,38] like in toluene and *N*-MP, contributions to the hindering potential that result from overlap between the π-orbitals and π-like orbitals are of equal magnitude but opposite sign. A low V_6 barrier is observed in toluene and *N*-MP. Spangler's model accounts for the differences between *N*-MP and *N*-MI and explains the arrangement of the H atoms of the CH_3 with respect to the plane of the two molecules. In *N*-MP, the hindering potential is a six-fold V_6 barrier meaning the H atoms of the CH_3 are staggered with the pyrrole ring. The three-fold V_3 barrier in *N*-MI (and the other of the isomers) results in an eclipsed projection of the CH_3 protons, with one of them being in the plane of the imidazole ring.

In methylimidazole where the symmetry is reduced, the overlap between π-orbitals and π-like orbitals accounts for the differences in the V_3 barriers to internal rotation between the four isomers. The magnitudes of these barriers are strongly related to the relative populations and energies of these orbitals. Mulliken charges orbital population analyses were performed for each isomer, however, the calculation results are dependent on the level of theory used and are as such inconclusive and unreliable. The V_3 barrier to internal rotation of the CH_3 group in 2-MO and 2-MT were determined to be 252 and 35 cm^{-1}, respectively. It was suggested that a higher degree of aromatic character is associated with the latter which explains the low V_3 while 2-MO is less aromatic since the barrier is higher. That would imply an intermediate degree of aromatic character associated with 2-MI.

The values of χ_{xx}, χ_{yy} and χ_{zz} derived from the measured values of χ_{aa} and $\chi_{bb} - \chi_{cc}$ for N1 and N3 in methylimidazole isomers suggests that methylation of imidazole results in minimal changes in the electronic environment around N1 and N3. However, these values alone, do not provide an insight into the aromaticity of the imidazole ring. It is possible to perform orbital population analyses using the extended Townes-Dailey model[58,59] as in chapter 4 for PCA; however, this analysis will only give sufficient information regarding the p-orbitals on the N atoms. The accuracy of the analysis may also be compromised by the lack of experimentally determined values for the off-diagonal component χ_{ab} so it was not performed.

Table 6.10. Barrier to internal rotation in methylated 5-membered heteroaromatic rings. (from references 16, 39, 21-23, 39)

	V_3 (cm^{-1})	F_0 (GHz)
N-MI	185.104(11)	157.9291(88)
2-MI	122.7529(38)	157.6901(44)
4-MI	317.20(14)	157.784(60)
5-MI	386.001(19)	157.68
N-methylpyrrole	67.8021(38)	-
2-methylpyrrole	279.7183(26)	167.0422
2-methylthiazole	34.938(20)	165.1886
4-methylthiazole	357.59(11)	166.79(6)
5-methylthiazole	332.03(8)	164.20(36)
2-methyloxazole	251.83(12)	167.52(68)
4-methyloxazole	427.99(8)	167.67(27)
5-methyloxazole	477.88(13)	168.52(37)

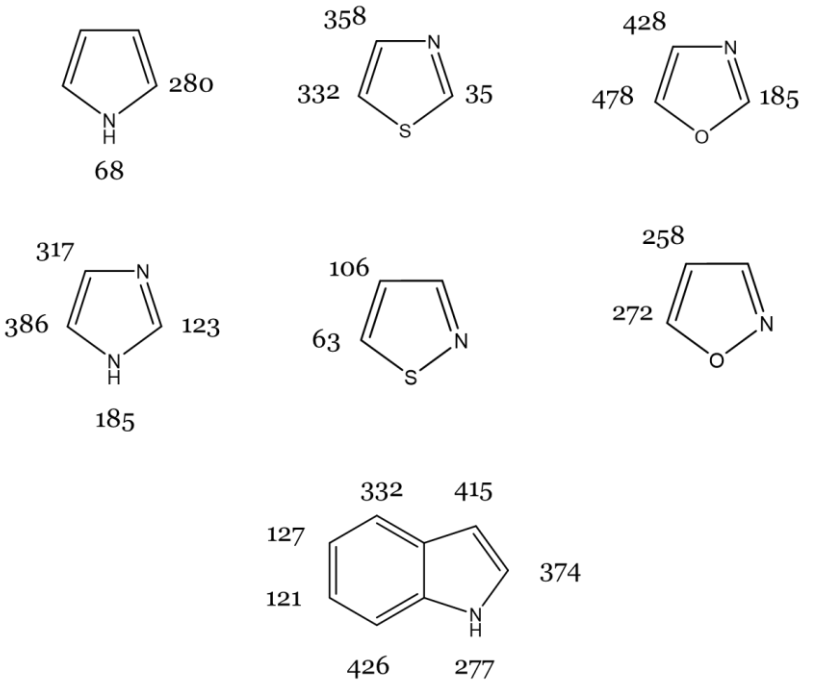

Figure 6.8. From left to right; pyrrole, thiazole, oxazole, imidazole, isothiazole, isoxazole, indole. The numbers next to each carbon indicate the measured barrier to internal rotation (in cm^{-1}) for the respective methylated analogue. (references 15, 16, 39, 21-23, 39, 53, 60)

6.10 Conclusions

The ground state rotational spectra of *N*-, 2-, 4- and 5-MI were recorded in the 7.0-18.5 GHz frequency range. Rotational constants, centrifugal distortion constants, barriers to internal rotation of the CH_3 groups and nuclear quadrupole coupling constants of the N atoms were determined experimentally and computationally. r_s structure determination was performed by evaluation of changes in the moment of inertia of each isomer by analyzing the observed spectra of ^{13}C and ^{15}N isotopologues. The gas phase structure of 2-MI was compared to the structure determined by X-ray diffraction[51]. Differences between the two mainly arise from lattice and crystal packing effects in the latter. Planarity is observed within the heavy atoms' skeleton of the aromatic ring in each isomer with the only contributions to the out-of-plane mass arising from two protons of the CH_3 group. Spectroscopic parameters related to the internal rotation of the CH_3 groups were evaluated including the values of the V_3 barrier heights. A strong correlation between the value of V_3 and the position where the CH_3 group is substituting in the ring was observed, consistent with observations for isomers of MT and MO. Driving force for that variation in V_3 is likely dominated by electronic effects and, to a lesser extent, by steric hindrance around the CH_3 group obstructing its internal motion. The nuclear quadrupole coupling constants χ_{xx}, χ_{yy} and χ_{zz} in terms of principal nuclear axes (*x,y,z*) located on each individual N atoms are reported and compared to those determined for other imidazole derivatives. Subtle differences are observed between the different molecules suggesting that nuclear charges in the N atoms are not significantly affected by methylation or halogenation.

6.11 References

1 G. L. Blackman, R. D. Brown, F. R. Burden and I. R. Elsum, Nuclear quadrupole coupling in the microwave spectrum of imidazole, *J. Mol. Spectrosc.*, 1976, **60**, 63–70.

2 D. Christen, J. H. Griffiths and J. Sheridan, Microwave spectra of isotopic pyrazoles and molecular structure of pyrazole, *Zeitschrift fur Naturforsch. - Sect. A J. Phys. Sci.*, 1981, **36**, 1378–1385.

3 M. Gatchell, M. Goulart, L. Kranabetter, M. Kuhn, P. Martini, B. Rasul and P. Scheier, Complexes of gold and imidazole formed in helium nanodroplets, *Phys. Chem. Chem. Phys.*, 2018, **20**, 7739–7745.

4 S. Ganguly, V. V. Vithlani, A. K. Kesharwani, R. Kuhu, L. Baskar, P. Mitramazumder, A. Sharon and A. Dev, Synthesis, antibacterial and potential anti-HIV activity of some novel imidazole analogs, *Acta Pharm.*, 2011, **61**, 187–201.

5 Z. Jin, Imidazole, oxazole and thiazole alkaloids, Nat. Prod. Rep., 2006, 23, 464–496.

6 N. K. Gibbs, J. Tye and M. Norval, Recent advances in urocanic acid photochemistry, photobiology and photoimmunology, *Photochem. Photobiol. Sci.*, 2008, **7**, 655–667.

7 K. Nishie, A. C. Waiss and A. C. Keyl, Toxicity of methylimidazoles, *Toxicol. Appl. Pharmacol.*, 1969, **14**, 301–307.

8 S. E. Ullrich, Mechanisms underlying UV-induced immune suppression, *Mutat. Res. - Fundam. Mol. Mech. Mutagen.*, 2005, **571**, 185–205.

9 H. Takahashi, M. Abe, T. Sugawara, K. Tanaka, Y. Saito, S. Fujimura, M. Shibuya and Y. Sato, Clotrimazole, an imidazole antimycotic, is a potent inhibitor of angiogenesis, *Japanese J. Cancer Res.*, 1998, **89**, 445–451.

10 L. Luca, Naturally Occurring and Synthetic Imidazoles: Their Chemistry and Their Biological Activities, Curr. *Med. Chem.*, 2012, **13**, 1–23.

11 L. H. Spangler, Structural Information From Methyl Internal Rotation Spectroscopy, *Annu. Rev. Phys. Chem.*, 1997, **48**, 481–510.

12 K. P. R. Nair, S. Herbers and J. U. Grabow, Structure and methyl torsion of halogenated toluenes: Rotational spectrum of 3,4-difluorotoluene, *J. Mol. Spectrosc.*, 2019, **355**, 19–25.

13 N. Hansen, H. Mäder and T. Bruhn, A molecular beam Fourier transform microwave study of 0-tolunitrile: ^{14}N nuclear quadrupole coupling and methyl internal rotation effects, *Mol. Phys.*, 1999, **97**, 587–595.

14 P. J. Mjöberg, W. M. Ralowski and S. O. Ljunggren, Microwave Spectrum and Barrier to Internal Rotation of 5-Methylisoxazole, *Zeitschrift fur Naturforsch.ung - Sect. A J. Phys. Sci.*, 1975, **30**, 1279–1281.

15 H. W. Nicolaisen, J. U. Grabow, N. Heineking and W. Stahl, The Microwave Spectrum of 4-Methylisothiazole, *Zeitschrift fur Naturforsch. - Sect. A J. Phys. Sci.*, 1991, **46**, 635–638.

16 S. Huber, T. K. Ha and A. Bauder, Microwave spectra of isotopic N-methylpyrroles, quadrupole coupling constants and substitution structure, *J. Mol. Struct.*, 1997, **413–414**, 93–100.

17 V. Van, W. Stahl and H. V. L. Nguyen, Two equivalent methyl internal rotations in 2,5-dimethylthiophene investigated by microwave spectroscopy, *Phys. Chem. Chem. Phys.*, 2015, **17**, 32111–32114.

18 J. U. Grabow, H. Hartwig, N. Heineking, W. Jäger, H. Mäder, H. W. Nicolaisen and W. Stahl, The microwave spectrum of 2-methylthiazole: Methyl internal rotation and 14N nuclear quadrupole coupling, *J. Mol. Struct.*, 2002, **612**, 349–356.

19 H. D. Rudolph and H. Seiler, *Zeitschrift fur Naturforsch. - Sect. A J. Phys. Sci.*, 1965, **20**, 1682–1686.

20 J. Susskind, Microwave spectrum, barrier to internal rotation, and torsion-vibration interaction in ortho-fluoro toluene, *J. Chem. Phys.*, 1970, **53**, 2492–2501.

21 W. Jäger and H. Mäder, The Microwave Spectrum of 4-Methylthiazole: Methyl Internal Rotation, ^{14}N Nuclear Quadrupole Coupling and Electric Dipole Moment, *Zeitschrift für Naturforsch. A*, 1987, **42**, 1405.

22 W. Jäger and H. Mäder, The microwave spectrum of 5-methylthiazole: methyl internal rotation, ^{14}N nuclear quadrupole coupling and electric dipole moment, *J. Mol. Struct.*, 1988, **190**, 295–305.

23 E. Fliege, H. Dreizler, M. Meyer, K. Iqbal and J. Sheridan, ^{14}N Nuclear Quadrupole Coupling and Methyl Internal Rotation of 2-, 4-, and 5-Methyl Oxazole, *Zeitschrift fur Naturforsch. - Sect. A J. Phys. Sci.*, 1986, **41**, 623–636.

24 B. Harris, University of Virginia, 2014.

25 S. Thorwirth, H. S. P. Müller and G. Winnewisser, Millimeter- and submillimeter-wave spectrum of HC_3N in the ground and vibrationally excited states, *J. Mol. Spectrosc.*, 2000, **204**, 133–144.

26 T. F. Giesen, M. E. Harding, J. Gauss, J.-U. Grabow and H. S. P. Müller, Determination of accurate rest frequencies and hyperfine structure parameters of cyanobutadiyne, HC_5N, *J. Mol. Spectrosc.*, 2020, **371**, 111303.

27 C. Kirby, H. W. Kroto and D. R. M. Walton, The microwave spectrum of cyanohexatriyne, HC_7N, *J. Mol. Spectrosc.*, 1980, **83**, 261–265.

28 M. C. McCarthy, E. S. Levine, A. J. Apponi and P. Thaddeus, Experimental Structures of the Carbon Chains HC_7N, HC_9N, and $HC_{11}N$ by Isotopic Substitution, *J. Mol. Spectrosc.*, 2000, **203**, 75–81.

29 A. Bauer, Rotational spectrum of acetonitrile $CH_3C^{14}N$ and $CH_3C^{15}N$ in a doubly excited degenerate vibrational state, *J. Mol. Spectrosc.*, 1971, **40**, 183–206.

30 H. V. L. Nguyen, A. Jabri, V. Van and W. Stahl, Methyl Internal Rotation in the Microwave Spectrum of Vinyl Acetate, *J. Phys. Chem. A*, 2014, **118**, 12130–12136.

31 M. Bester, M. Tanimoto, B. Vowinkel, G. Winnewisser and K. Yamada, Rotational Spectrum of Methylcyanoacetylene. A New Millimeter Wave Spectrometer, *Zeitschrift fur Naturforsch. - Sect. A J. Phys. Sci.*, 1983, **38**, 64–67.

32 G. A. Cooper, C. Medcraft, E. Gougoula and N. R. Walker, Conformational isomers of trans -urocanic acid observed by rotational spectroscopy, *Phys. Chem. Chem. Phys.*, 2019, **21**, 9495–9503.

33 V. Amir-Ebrahimi, A. Choplin, J. Demaison and G. Roussy, Microwave spectrum of the 13C-ring-monosubstituted toluenes and structure of toluene, *J. Mol. Spectrosc.*, 1981, **89**, 42–52.

34 S. Wörmke, K. Brendel, U. Andresen and H. Mäder, A molecular beam Fourier transform microwave study of 2-methylpyridine and its complex with argon: Structure, methyl internal rotation and14N nuclear quadrupole coupling, *Mol. Phys.*, 2004, **102**, 1625–1639.

35 K. Inoue, N. Kuze, M. Tanabe, H. Takeuchi, T. Egawa and S. Konaka, Determination of the molecular structure of γ-picoline in the gas phase and in liquid crystal solvents, *J. Mol. Struct.*, 1997, **413–414**, 81–91.

36 Z. Rong, H. G. Kjaergaard and B. R. Henry, Internal methyl rotation in the CH stretching overtone spectra of 2-, 3-, and 4-Methylpyridine, *J. Phys. Chem. A*, 2002, **106**, 4368–4376.

37 W. Caminati, G. Cazzoli and A. M. Mirri, Microwave spectrum, barrier to internal rotation and dipole moment in 5-methyl-pyrimidine, *Chem. Phys. Lett.*, 1975, **31**, 104–107.

38 S. Huber, J. Makarewicz and A. Bauder, Rotational spectra, structure and barrier to internal rotation of *N*-methylpyrrole and its argon complexes, *Mol. Phys.*, 1998, **95**, 1021–1043.

39 T. Nguyen, C. Dindic, W. Stahl, H. V. L. Nguyen and I. Kleiner, ^{14}N Nuclear quadrupole coupling and methyl internal rotation in the microwave spectrum of 2-methylpyrrole, *Mol. Phys.*, 2019, **118**, 1668572.

40 C. Western, PGOPHER, a program for rotational, vibrational and electronic spectra, *J. Quant. Spectrosc. Radiat. Transf.*, 2015, **186**, 221–242.

41 J. K. G. Watson, Determination of Centrifugal Distortion Coefficients of Asymmetric-Top Molecules, *J. Chem. Phys.*, 1967, **46**, 1935–1949.

42 J. Makarewicz, S. Huber, B. Brupbacher-Gatehouse and A. Bauder, Internal rotation dependent quadrupole hyperfine splittings of rotational transitions of *N*-methylpyrrole, *J. Mol. Struct.*, 2002, **612**, 117–123.

43 R. K. Bohn, J. A. Montgomery, H. H. Michels and J. A. Fournier, Second moments and rotational spectroscopy, *J. Mol. Spectrosc.*, 2016, **325**, 42–49.

44 J. Kraitchman, Determination of Molecular Structure from Microwave Spectroscopic Data, *Am. J. Phys.*, 1953, **21**, 17–24.

45 W. Gordy and R. L. Cook, *Microwave molecular spectra*, John Wiley & Sons, Ltd, New York, 3rd., 1984.

46 C. C. Costain, Further comments on the accuracy of r_s substitution structures., *Trans. Am. Crystallogr. Assoc.*, 1966, **2**, 157–61, discussion 161-4.

47 Z. Kisiel, PROSPE - Programs for ROtational SPEctroscopy, http://www.ifpan.edu.pl/~kisiel/prospe.htm.

48 J. Epstein, J. R. Ruble and B. M. Craven, The charge density in imidazole by X-ray diffraction at 103 and 293 K, *Acta Crystallogr. Sect. B Struct. Crystallogr. Cryst. Chem.*, 1982, **38**, 140–149.

49 S. Martinez-Carrera, The crystal structure of imidazole at –150°C, *Acta Crystallogr.*, 1966, **20**, 783–789.

50 B. M. Craven, R. K. McMullan, J. D. Bell and H. C. Freeman, The crystal structure of imidazole by neutron diffraction at 20°C and –150°C, *Acta Crystallogr. Sect. B Struct. Crystallogr. Cryst. Chem.*, 1977, **33**, 2585–2589.

51 B. Hachuła, M. Nowak and J. Kusz, Crystal and Molecular Structure Analysis of 2-Methylimidazole, *J. Chem. Crystallogr.*, 2010, **40**, 201–206.

52 K. P. R. Nair, S. Herbers, J. U. Grabow and A. Lesarri, Internal rotation in halogenated toluenes: Rotational spectrum of 2,3-difluorotoluene, *J. Mol. Spectrosc.*, 2018, **349**, 37–42.

53 R. M. Gurusinghe and M. J. Tubergen, Probing the Electronic Environment of Methylindoles using Internal Rotation and ^{14}N Nuclear Quadrupole Coupling, *J. Phys. Chem. A*, 2016, **120**, 3491–3496.

54 H. Hartwig and H. Dreizler, The microwave spectrum of trans-2,3-dimethyloxirane in torsional excited states, *Zeitschrift fur Naturforsch. - Sect. A J. Phys. Sci.*, 1996, **51**, 923–932.

55 Z. Kisiel, Least-squares mass-dependence molecular structures for selected weakly bound intermolecular clusters, *J. Mol. Spectrosc.*, 2003, **218**, 58–67.

56 M. Hayashi and L. Pierce, Tables for the internal rotation problem, *J. Chem. Phys.*, 1961, **35**, 1148–1149.

57 G. A. Cooper, C. J. Anderson, C. Medcraft and N. R. Walker, Rotational spectra and nuclear quadrupole coupling constants of 4- and 2-iodoimidazole, *J. Mol. Spectrosc.*, 2018, **354**, 15–23.

58 S. E. Novick, Extended Townes–Dailey analysis of the nuclear quadrupole coupling tensor, *J. Mol. Spectrosc.*, 2011, **267**, 13–18.

59 C. H. Townes and B. P. Dailey, Determination of Electronic Structure of Molecules from Nuclear Quadrupole Effects, *J. Chem. Phys.*, 1949, **17**, 782–796.

60 R. Gurusinghe and M. Tubergen, Probing the Electronic Environment of Methylindoles using Internal Rotation and 14N Nuclear Quadrupole Coupling, *J. Phys. Chem. A*, 2016, **120**, 3491–3496.

Chapter 7. Hydrogen Bonding of Methylimidazole Isomers with Water: The Effect on the Barrier Height

7.1 Introduction

It was discussed in chapters 5 and 6 that imidazole is a biologically significant molecule. It is the building block of adenine, guanine, histamine, histidine, to name a few, meaning imidazole is abundant in the human body. Functionalizing imidazole results in molecules with biochemical activity, *i.e.* the anti-fungal drug chlotrimazol,[1] the antibiotic and antiprotozoal drug metronidazole[2] and various antivirals inhibiting replication of hepatitis viruses[3] (HAV, HBV, HCV etc). These molecules, once present in the human body, are expected to interact with others, including water, as part of their mode of action. Understanding conformational and bonding preferences by targeting prototype "building blocks" like imidazole is an imperative part of the process of synthesizing novel drugs that will make it through the phases of clinical trials.

Hydrogen bonds are the primary type of intermolecular interactions that are manifested in the structures of the weakly bound complexes formed between the imidazole building block and other molecules. Rotational spectroscopy is a powerful tool that allows for characterization of these interactions on a macroscopic scale. Conformational and bonding trends may be rationalized and an insight into the dynamics of imidazole-bearing complexes is given at internal temperatures as low as 2 K. Several microwave spectroscopy studies have explored the effect that complex formation imposes on the barrier to internal rotational of a group of three-fold symmetry in a molecule.[4–10] In toluene,[11] a six-fold barrier of approximately 4.9 cm^{-1} is observed suggesting essentially free rotation of the CH_3 group. The symmetry is reduced to three-fold upon attachment of SO_2 to toluene[6] resulting in a V_3 of 83.2 cm^{-1}.

The binding of water to imidazole was explored in chapter 5 where two monohydrate complexes of imidazole were simultaneously isolated within an argon free-jet expansion. In chapter 6, the barriers to internal rotation in methylimidazole isomers were determined with rotational spectroscopy.[12] The stepwise solvation of various aromatic and heteroaromatic molecules has been explored with microwave spectroscopy,[13–18] however, there is very limited information on the stepwise microsolvation of their methylated analogues and the effect of microsolvation on the barrier height. To the author's best

knowledge, this is the first comparative study of the effect of the first step of microsolvation on the barrier height of *N*-, 2-, 4-, and 5-MI.

7.2 Experimental Details

The experimental details are given in chapter 6 section 6.2. The spectra of *N*-, 2-, 4- and 5-MI···H_2O were recorded alongside the spectra of their monomers *N*-, 2-, 4- and 5-MI, respectively. No deliberate actions were taken to introduce water in the experiments; it is likely a contaminant present in the gas line or the walls of the vacuum chamber, as also seen in chapter 5, section 5.2, or within the respective methylimidazole sample. Isotopic experiments with D_2O (Sigma-Aldrich, 99.9% D atom) were performed to confirm the assignment of molecular carriers and partially elucidate the geometry of the complexes. Approximately 0.1 mL of D_2O was placed in the reservoir described in chapter 3 and that amount was sufficient to collect data for all complexes in three individual experiments.

For *N*-MI···H_2O, an additional experiment was performed where the reservoir attached on the valve faceplate was heated to 90˚C. The heater was placed around the reservoir and the temperature was monitored by a K-type thermocouple attached to a temperature controller. *N*-MI vapour co-expanded with argon at a constant pressure of 5 bar into the vacuum chamber. The resulting spectrum was collected over the course of 2.34 M FID averages. For isotopic substitution of the H atoms in the water subunit, D_2O (Sigma-Aldrich, 99.9% D atom) was placed in a reservoir attached to the gas line, approximately 20 cm before the pulse valve. This experiment was part of a series where the performance, reliability and safety of the heater was evaluated as an alternative method to laser vaporization.

7.3 Computational Methods

Geometry optimizations of the *N*-, 2-, 4- and 5-MI···H_2O complexes (figure 7.1) were performed. The starting points were directed by the work in chapters 5 and 6. The optimized geometries of *N*-, 2-, 4- and 5-MI were used and a water molecule was placed in close proximity to the pyridinic nitrogen of each methylimidazole monomer. Geometry optimizations were also performed for alternative monohydrates where water coordinates at the pyrrolic nitrogen of 2-, 4- and 5- MI, in a manner seen in chapter 5 for H_2O···imid. The coordinates for the H_2O···2-MI, H_2O···4-MI and H_2O···5-MI at the B3LYP(D3BJ)/aug-cc-pVTZ level are displayed in appendix A tables A31-A33. In chapter 6, where the geometry and barriers to internal rotation of the *N*-, 2-, 4- and 5-MI are discussed, given the level of consistency between theory and experiment, the B3LYP(D3BJ)/aug-cc-pvtz method[19–24] was used for structural comparisons and prediction of the V_3 barriers to internal rotation. Geometry optimizations of *N*-, 2-, 4- and 5-MI···H_2O were therefore performed at the same level. Optimizations were also performed with the ωB97X-D/aug-cc-pVQZ method in order to evaluate its performance with these complexes, like in chapter 5 for imid···H_2O and H_2O···imid. Finally, the geometries were also calculated at the MP2/aug-cc-pVDZ level. The V_3 barriers to internal rotation for each complex are predicted with all methods by scanning the dihedral angles $\angle(H-C6-N1-C2)$, $\angle(H-C6-C2-N3)$, $\angle(H-C6-C4-C5)$ and $\angle(H-C6-C5-N1)$ for each of *N*-, 2-, 4- and 5-MI···H_2O, respectively. The calculated rotational constants (A_e, B_e and C_e), nuclear quadrupole coupling constants and dipole moment components ($|\mu_a|$, $|\mu_b|$ and $|\mu_c|$) are summarized in tables 7.1-7.3. The V_3 barriers to internal rotation and energies ΔE for each complex at each level are summarized in tables 7.9 and 7.10 alongside their percentage deviations of calculated rotational constants from experimentally determined ones. The calculated optimized geometries for each of *N*-, 2-, 4- and 5-MI···H_2O at B3LYP(D3BJ)/aug-cc-pvtz are shown in figure 7.1.

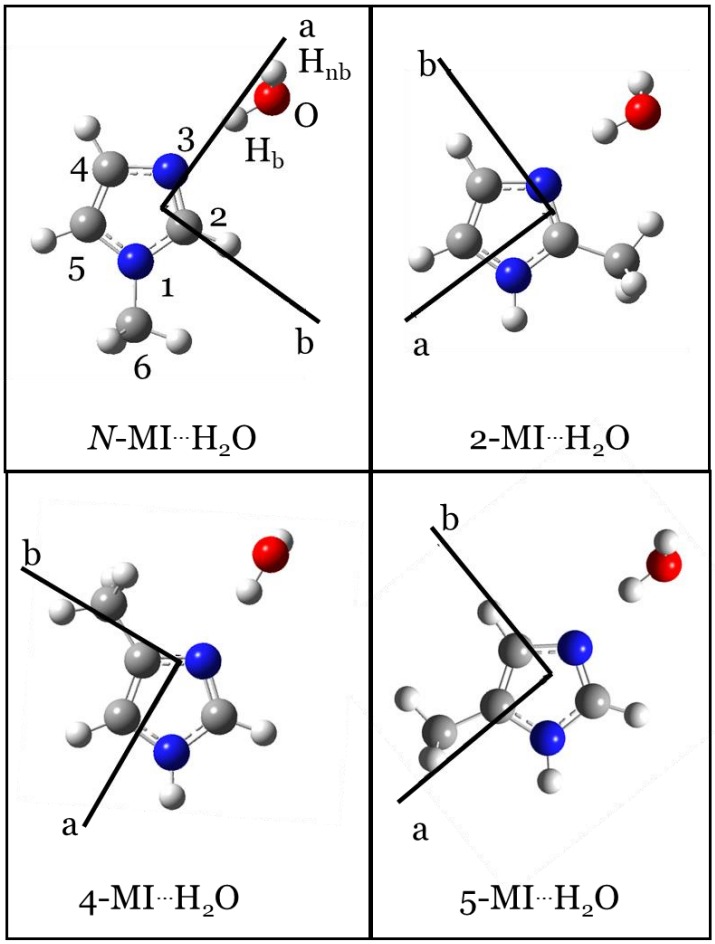

Figure 7.1. Optimized equilibrium geometries of *N*-, 2-, 4-, and 5-MI···H_2O at the B3LYP(D3BJ)/aug-cc-pVTZ.

Table 7.1. Calculated spectroscopic parameters at the B3LYP(D3BJ)/aug-pVTZ level.

	B3LYP(D3BJ)/aug-cc-pVTZ			
Spectroscopic parameters	*N*-MI···H_2O	2-MI···H_2O	4-MI···H_2O	5-MI···H_2O
A_e (MHz)	5754.89	4182.14	3812.17	7574.94
B_e (MHz)	1313.14	1769.10	1752.87	1183.73
C_e (MHz)	1079.70	1255.94	1216.30	1033.88
$\chi_{aa}(N1)$ (MHz)	1.3800	1.3054	1.2926	1.2282
$\chi_{bb} - \chi_{cc}(N1)$ (MHz)	3.8624	4.2411	3.8734	4.1386
$\chi_{ab}(N1)$ (MHz)	–0.3646	–0.1060	–0.1275	–0.1279
$\chi_{aa}(N3)$ (MHz)	–3.9395	–3.2677	–3.7995	–3.4384
$\chi_{bb} - \chi_{cc}(N3)$ (MHz)	–0.1405	–0.4252	–0.1113	–0.8268
$\chi_{ab}(N3)$ (MHz)	–0.1242	1.6956	–0.4669	1.7300
$\lvert\mu_a\rvert$, $\lvert\mu_b\rvert$, $\lvert\mu_c\rvert$ (D)	5.5, 0.4, 1.4	4.4, 1.7, 1	5.4, 0.5, 1.3	5.8, 1.5, 1.2

Table 7.2. Calculated spectroscopic parameters at the ωB97X-D/aug-cc-pVQZ level.

	ωB97X-D/aug-cc-pVQZ			
Spectroscopic parameters	*N*-MI···H_2O	2-MI···H_2O	4-MI···H_2O	5-MI···H_2O
A_e (MHz)	6111.37	4197.93	3993.46	7828.80
B_e (MHz)	1277.08	1758.92	1740.95	1176.29
C_e (MHz)	1067.06	1252.42	1230.17	1032.29
$\chi_{aa}(N1)$ (MHz)	1.3700	1.2408	1.2838	1.1703
$\chi_{bb} - \chi_{cc}(N1)$ (MHz)	3.6886	4.1757	3.7182	4.0763
$\chi_{ab}(N1)$ (MHz)	0.3987	–0.1415	–0.1741	–0.1667
$\chi_{aa}(N3)$ (MHz)	–3.9955	–3.3702	–3.7285	–3.4338
$\chi_{bb} - \chi_{cc}(N3)$ (MHz)	–0.3999	–0.6404	–0.4053	–1.1633
$\chi_{ab}(N3)$ (MHz)	0.4037	1.6781	–0.9716	1.8540
$\lvert\mu_a\rvert$, $\lvert\mu_b\rvert$, $\lvert\mu_c\rvert$ (D)	6.1, 0.1, 1.2	4.5, 1.8, 1.1	5.4, 0.3, 1.2	5.7, 1.6, 1.2

Table 7.3. Calculated spectroscopic parameters at the MP2/aug-cc-pVDZ level.

	MP2/aug-cc-pVDZ			
Spectroscopic parameters	*N*-MI···H_2O	2-MI···H_2O	4-MI···H_2O	5-MI···H_2O
A_e (MHz)	5034.14	4149.27	3987.81	8291.84
B_e (MHz)	1424.65	1739.08	1714.32	1164.63
C_e (MHz)	1121.24	1243.81	1215.47	1030.84
$\chi_{aa}(N1)$ (MHz)	0.9915	1.0375	1.1681	0.9680
$\chi_{bb} - \chi_{cc}(N1)$ (MHz)	3.1973	3.6275	3.2083	3.5815
$\chi_{ab}(N1)$ (MHz)	–0.3833	0.1489	–0.1779	–0.1465
$\chi_{aa}(N3)$ (MHz)	–3.5256	–2.6000	–2.8887	–2.4216
$\chi_{bb} - \chi_{cc}(N3)$ (MHz)	–0.1978	–0.3701	–0.0461	–0.7368
$\chi_{ab}(N3)$ (MHz)	0.5722	–1.5757	–1.0735	1.8503
$\lvert\mu_a\rvert$, $\lvert\mu_b\rvert$, $\lvert\mu_c\rvert$ (D)	5.3, 0.3, 1.1	4.2, 1.2, 0	5.5, 0.4, 1.2	5.2, 1.5, 1.2

7.4 Spectral Analysis

Numerous lines remain unassigned alongside the microwave spectra of *N*-, 2-, 4-, and 5-MI in the 7.0-18.5 GHz range (chapter 6, figure 6.2, 6.4, and 6.5), excluding the identified species discussed in chapter 6. Considering the presence of transitions[25] assigned to $(H_2O)_2$, formation of water complexes may be favored.[25] The monohydrate complexes of *N*-, 2-, 4- and 5-MI···H_2O (figure 7.1) are calculated to be near prolate asymmetric tops with their electronic charges distributed such that the total dipole moment components are almost aligned with *a*-inertial axis. Considering the predicted values and magnitudes of the V_3 barriers, A/E splitting of transition frequencies is expected to be resolvable by our experiment. The spectra that were recorded in each of the three individual experiments were examined and the *N*-, 2-[c], 4-, and 5-MI···H_2O complexes were searched for. The spectra were recorded over the course of 2.34, 1.2 and 2.6 M FID averages, respectively. Consistent with the broad expectations described above, *a*-type patterns are immediately identifiable in each spectrum. The partially resolved hyperfine structure is consistent with the presence of two nitrogen nuclei, N1 and N3, in the imidazole ring. *A*-state transition frequencies were fit with Watson's S-reduced Hamiltonian[26,27] as implemented in Pgopher[28] to produce the measured values of the spectroscopic parameters summarized table 7.4. [26,27] The detailed form of the Hamiltonian has been described in chapter 2. The calculated value of the χ_{ab} nuclear quadrupole terms for N1 and N3 in each complex was included in the fits. This was so the measured values of χ_{aa} and $\chi_{bb} - \chi_{cc}$ would be used for the generation of the diagonal coupling terms χ_{zz}, χ_{xx} and χ_{yy}, a procedure described in chapters 2-6. Discussion of the diagonalized nuclear quadrupole coupling constants is beyond the scope of the chapter so these values are summarized in appendix A, table A43. Measured values of *effective* rotational constants A_0', B_0', and C_0', centrifugal distortion constants, nuclear quadrupole coupling constants are summarized in table 7.4 alongside derived values for the planar moment P_{cc}' and inertial defect Δ_0'. A definition of *effective* rotational constants was given in chapter 6.

[c] Fit for 2-MI···H_2O was performed by Chris Medcraft and Julianne Heitkämper.

Table 7.4. Effective rotational constants A_0', B_0', and C_0' and other spectroscopic parameters determined with Pgopher for *A*-state transitions of *N*-, 2-, 4-, and 5-MI···H_2O.

Spectroscopic parameters	*N*-MI ···H_2O	2-MI ···H_2O	4-MI ···H_2O	5-MI ···H_2O
A_0' (MHz)	5015.939(64)[a]	4238.129(36)	4084.506(22)	8440.90(44)
B_0' (MHz)	1409.9347(14)	1733.7787(15)	1707.3390(15)	1167.56380(82)
C_0' (MHz)	1107.2937(14)	1240.3116(12)	1214.3010(11)	1032.85910(75)
D_J (kHz)	2.3593(68)	0.451(16)	0.119(11)	0.2633(48)
D_K (kHz)	–	–69.1(55)	–	–
D_{JK} (kHz)	–16.723(57)	6.49(11)	28.876(76)	27.320(39)
d_k (kHz)	–0.0708(64)	–	–0.3145(70)	–0.0369(37)
d_j (kHz)	–0.882(10)	–0.148(12)	–0.133(11)	–
$\chi_{aa}(N1)$ (MHz)	1.245(16)	1.218(21)	1.199(16)	1.650(62)
$\chi_{bb}-\chi_{cc}(N1)$ (MHz)	3.909(56)	4.127(46)	3.819(52)	4.78(15)
$\chi_{ab}(N1)$ (MHz)	[–0.3646]	[–0.1060]	[–0.1275]	[–0.1279]
$\chi_{aa}(N3)$ (MHz)	–3.609(13)	–2.979(16)	–3.356(12)	–2.739(54)
$\chi_{bb}-\chi_{cc}(N3)$ (MHz)	–0.065(43)	–0.313(47)	–0.416(62)	–1.31(38)
$\chi_{ab}(N3)$ (MHz)	[–0.1242][b]	[1.6956]	[–0.4669]	[1.7300]
$\lvert\mu_a\rvert$, $\lvert\mu_b\rvert$, $\lvert\mu_c\rvert$ (D)	5.5, 0.4, 1.4	4.4, 1.7, 1	5.4, 0.5, 1.3	5.8, 1.5, 1.2
Δ_0' (u Å^2)	–2.7868(15)	–3.2743(11)	–3.5453(8)	–3.4207(32)
P_{cc}' (u Å^2)	1.3934(7)	1.6371(6)	1.7727	1.7104(16)
N [c]	111	80	84	68
σ_{RMS} (kHz) [d]	16.5	14.4	11.6	14.3

[a] Numbers in parentheses are one standard deviation in units of the last significant figures.

[b] Numbers in square brackets fixed to the calculated value at the B3LYP(D3BJ)/aug-cc-pVTZ level.

[c] Number of *A*-state hyperfine components included in the fit.

[d] Root mean square deviation of the fit.

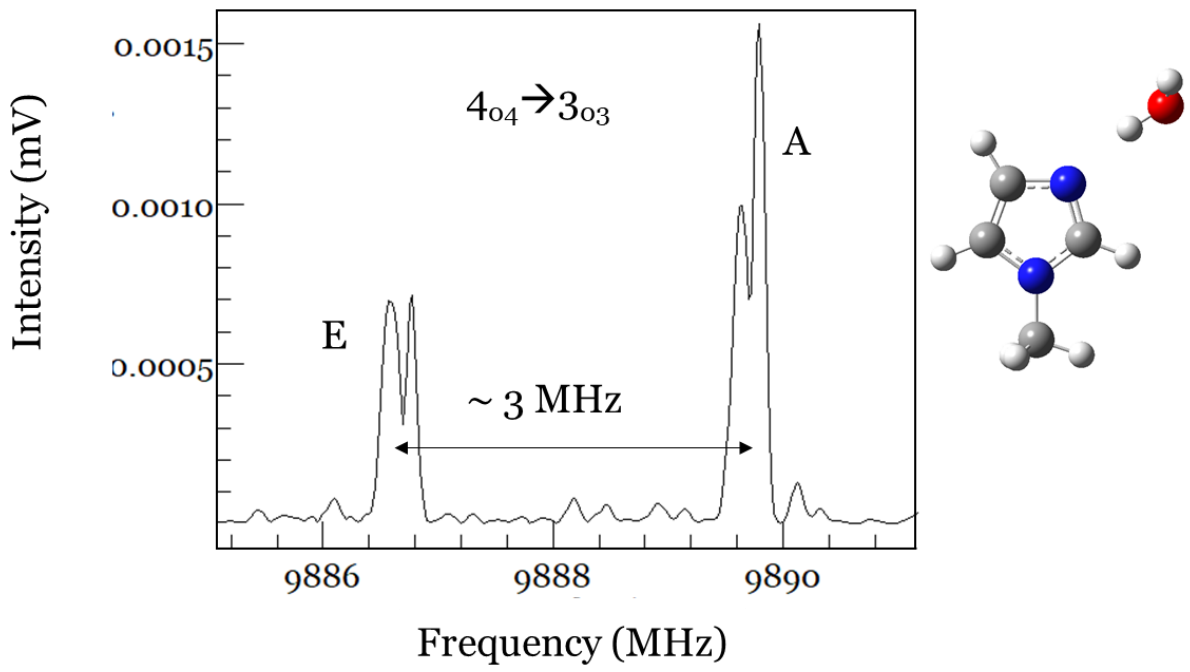

Figure 7.2. Expanded portion of the spectrum of *N*-MI collected over the course 2.34 M FID's. The $4_{04}\rightarrow3_{03}$ transition of *N*-MI···H_2O split into *A*- and *E*-states and their energy separation is related to the V_3 barrier height.

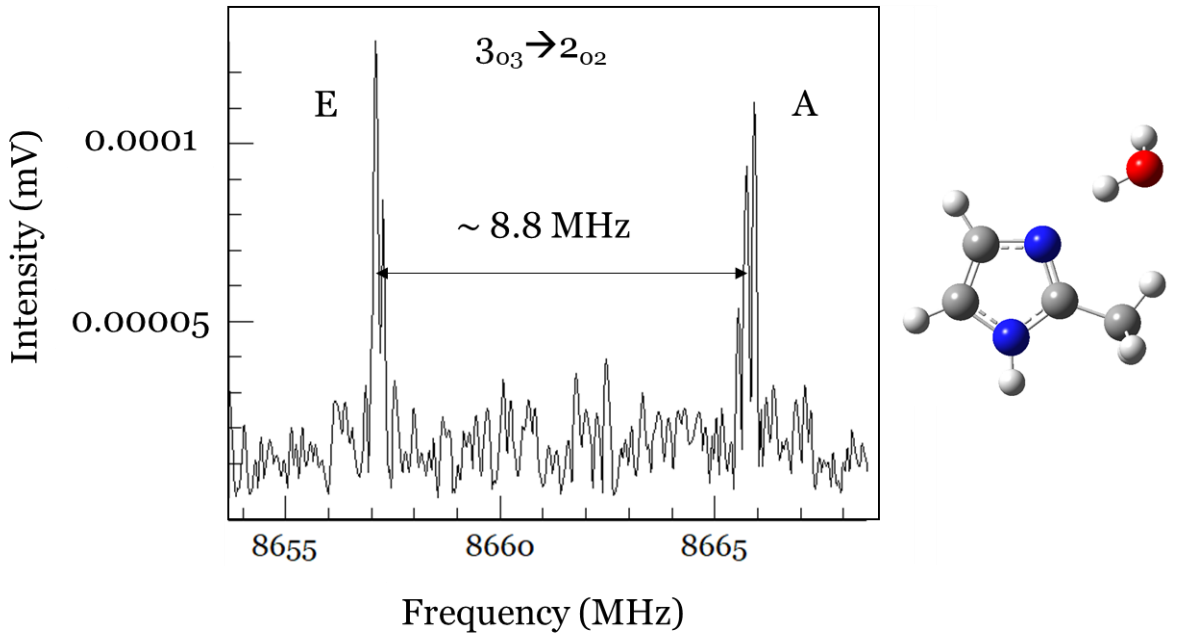

Figure 7.3. Expanded portion of the spectrum of 2-MI collected over the course 1.2 M FID's. The $3_{03}\rightarrow2_{02}$ transition of 2-MI···H_2O split into *A*- and *E*-states and their energy separation is related to the V_3 barrier height.

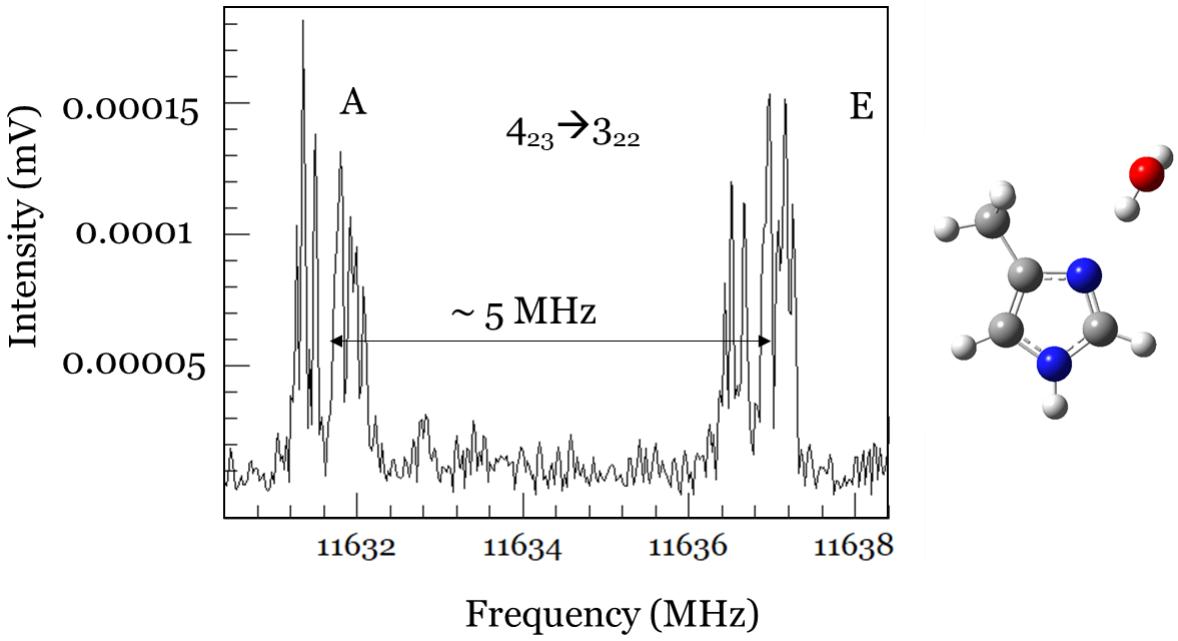

Figure 7.4. Expanded portion of the spectrum of 4-MI collected over the course 2.6 M FID's. The $4_{23}\rightarrow3_{22}$ transition of 4-MI···H_2O split into *A*- and *E*-states and their energy separation is related to the V_3 barrier height.

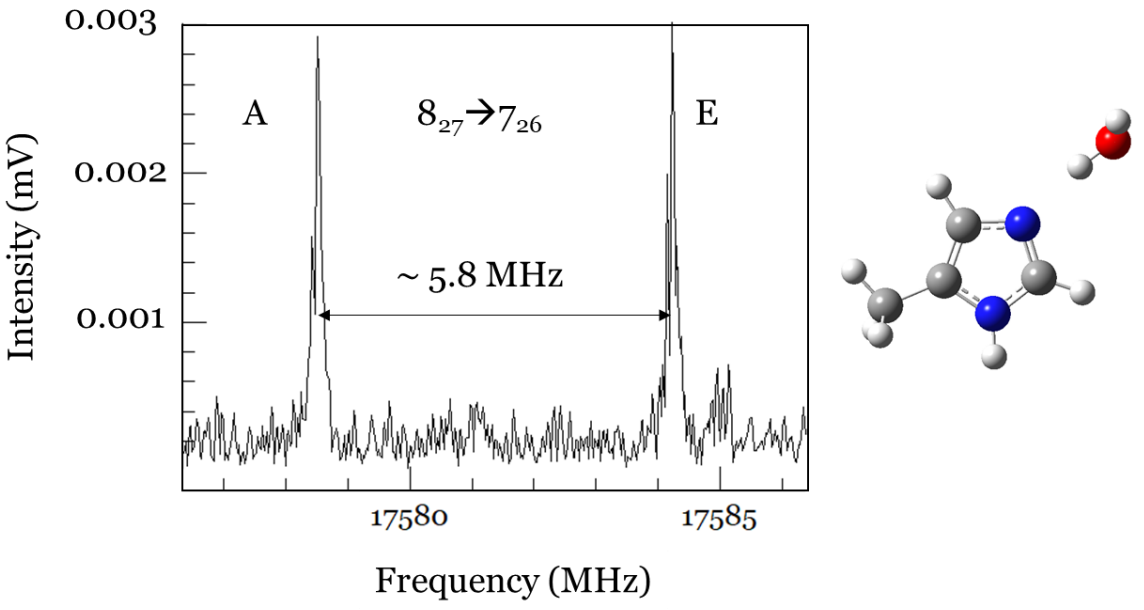

Figure 7.5. Expanded portion of the spectrum of 5-MI collected over the course 2.6 M FID's. The $8_{27}\rightarrow7_{26}$ transition of 5-MI···H_2O split into *A*- and *E*-states and their energy separation is related to the V_3 barrier height.

The assignment of molecular carriers to the fitted spectra was further confirmed with isotopic experiments with D_2O. Two singly deuterated isotopologues were observed for each complex, with deuterium either substituting at the position of the bonding hydrogen participating in the intermolecular interaction, H_b, or at the position of the non-bonding hydrogen, H_{nb}. The fitted spectroscopic parameters obtained through fitting of *A*-state transitions with Watson's S-reduction are summarized in table 7.5. The spectra of the deuterated isotopologues were recorded over the course of 1.44, 0.9, and 2.9 M FID's, respectively.

In chapter 5, no splitting due to large amplitude motions (LAM) in the water subunit was observed in the spectrum of the imid···H_2O, where water is the proton donor[29]. The *A*-state transitions of *N*-, 2-, 4-, and 5-MI···H_2O were explored for evidence of LAM other than that of the CH_3 undergoing internal rotation. No evidence was found that the water subunit undergoes LAM that couple the overall rotation and internal rotation in each of *N*-, 2-, 4-, and 5-MI···H_2O, consistent with observations[29,30] for imid···H_2O and 2-fluoropyridine···H_2O. Absence of *c*-type transitions in the spectra of the four complexes discussed here, indicate that wagging and flipping motions at the water subunit are unhindered or that the complexes are rigidly planar. In chapter 5, we also reported the formation of the H_2O···imid complex where water is the proton acceptor and interacting *via* the pyrrolic N-H site of imidazole. The spectrum was split into two components, labelled as 0^- and 0^+, as a result of a torsional motion associated with the water subunit. The overall intensity of that spectrum was lower than that of imid···H_2O, despite H_2O···imid having a larger dipole moment, possibly as a result of the splitting described above and the relative energies favouring formation of the former. The spectra of H_2O···2-MI, H_2O···4-MI and H_2O···5-MI[D] were searched for but not detected under these experimental conditions. Assuming that their geometry would be similar to that of H_2O···imid and that LAM associated with the H_2O subunit and the CH_3 group couple each other, the spectrum would be expected to be split into four components, $A0^-$, $A0^+$, $E0^-$, and $E0^+$. No evidence for spectra following these expectations are observed under these experimental conditions. The calculated energies of H_2O···2-MI, H_2O···4-MI and H_2O···5-MI at the B3LYP(D3BJ)/aug-cc-pVTZ level sugest that these monohydrate isomers are higher in energy by approximately 1000 cm^{-1}.

[D] The H atom on the pyrrolic N1 site in *N*-MI is replaced by a CH_3 group, making that site unavailable for H-bonds.

Table 7.5. Effective rotational constants and other spectroscopic parameters determined with Pgopher for A-state transitions of *N*-, 2-, 4-, and 5-MI···HOD and ···DOH isotopologues.

Spectroscopic parameters	*N*-MI···DOH	*N*-MI···HOD	2-MI···DOH	2- MI···HOD
A_0 (MHz)	5036.633(58)[a]	4981.903(86)	4216.458(58)	4187.992(50)
B_0 (MHz)	1380.3352(17)	1351.3770(25)	1708.8034(25)	1662.8773(22)
C_0 (MHz)	1089.9312(13)	1070.2310(23)	1225.7080(21)	1200.1827(18)
D_J (kHz)	2.2804(77)	2.035(12)	0.442(27)	0.473(22)
D_K (kHz)	–	–	–71.8(97)	–63(10)
D_{JK} (kHz)	–18.13(11)	–15.51(26)	6.31(19)	6.32(13)
d_j (kHz)	–0.8060(89)	–0.523(15)	–0.126(20)	–0.157(16)
N [b]	53	30	45	61
σ_{RMS} (kHz) [c]	13.7	18.7	18.2	17.7
Spectroscopic parameters	4-MI···DOH	4-MI···HOD	5-MI···DOH	5-MI···HOD
A_0 (MHz)	4064.330(26)	4034.596(34)	8391.57(52)	8351.24(60)
B_0 (MHz)	1683.07260(77)	1638.98921(94)	1148.45060(76)	1123.68324(69)
C_0 (MHz)	1200.18317(88)	1176.7805(11)	1017.18919(75)	998.12784(79)
D_J (kHz)	0.103(10)	0.109(13)	0.2545(58)	0.2376(52)
D_{JK} (kHz)	29.03(13)	29.06(22)	26.930(100)	24.766(95)
d_k (kHz)	–0.3088(67)	–0.2663(86)	–0.0365(40)	–0.0317(43)
d_j (kHz)	–0.133(11)	–0.133(11)	–	–
N	61	44	37	39
σ_{RMS} (kHz)	12.7	13.4	12.5	12

[a] Numbers in parentheses are one standard deviation in units of the last significant figures.

[b] Number of *A*-state hyperfine components included in the fit.

[c] Root mean square deviation of the fit.

7.5 Geometry

It has been discussed in chapters 4, 5, and 6, that a first insight into the geometry of a complex or molecule may be obtained by evaluating the planar moments and inertial defect from the measured rotational constants with no assumptions about the structure. The reliability of this approach, however, is expected to be affected by the internal rotation of the CH_3 group not being aligned with any inertial axis and low lying vibrations in the water subunit in *N*-, 2-, 4-, and 5-MI···H_2O. The evaluated values of P'_{cc}, Δ'_0 and P_{cc} and Δ_0 follow broad expectations for planar complexes with an internal three-fold CH_3 rotor. It has been shown that inclusion of *E*-states in the fits produces a different set of rotational constants to the *A*-state fit. This accounts for the differences in the values of P'_{cc}, Δ'_0 and P_{cc} and Δ_0 in each of *N*-, 2-, 4-, and 5-MI···H_2O.

Substitution coordinates (r_s) of the H atoms in the water subunit were determined using the Kraitchman method[27,31] described in chapter 2, section 2.10.2. These coordinates are summarized in table 7.6 alongside their Costain errors[32,33] to account for vibration-rotation coupling effects. DFT Calculated r_e coordinates are also shown and the results are in good agreement. As in previous chapters, the coordinate signs were implied by the DFT calculated coordinates and the ones that were calculated as imaginary numbers due to being positioned close to an axis were set to zero. In *N*-MI···H_2O, for H_b it is calculated that $|c|$ =0.030(52) Å. The uncertainty in the coordinate is large compared to its magnitude which is consistent with the H_b atom being positioned in the plane defined by *N*-MI. Often the Kraitchman method performs poorly when it comes to determining the position of a H atom, mainly due to the elongation[34] and the differences in vibrational energy of the bond caused by D which may explain the high uncertainty in that coordinate. In 2-, 4-, and 5-MI···H_2O, the value of $|c|$ consistently shows that H_b involved in the intermolecular interaction lies in the plane of the respective methylimidazole. Similarly, the H_b atom in imid···H_2O is in the plane of imidazole (chapter 5). It was calculated that the non-bonding H_{nb} in the imid···H_2O complex points above (or below) the plane defined by the imidazole ring with $|c|$ =0.4521(38) Å. It is consistently observed that in each of *N*-, 2-, 4-, and 5-MI···H_2O the magnitude and value of the $|c|$ coordinate of H_{nb} are similar with one another and with that for imid···H_2O.

In table 7.6, for *N*-MI···H_2O and 4-MI···H_2O, some inconsistencies are observed between the experimental and calculated *b*-coordinate of H_{nb}. In both complexes, the magnitude of $|b|$ is underestimated by approximately 0.5 Å with both DFT methods. The agreement

improves slightly at the MP2/aug-cc-pVDZ level. Rovibrational calculations were performed for *N*- and 4-MI···H_2O to check whether the optimization calculations had landed on a saddle point or local minimum geometry. No imaginary frequencies were found so each calculation is concerned with a global minimum. These inconsistencies could be rationalized by the fact that DFT methods cannot always account for long range interactions with high precision. Benchmarking has been performed for various systems in a number of studies that support this statement.[22,35,36] The complex internal dynamics of internal rotation of the CH_3 and motions associated with the water subunit may influence the accuracy of these calculations. As it will be seen in the following sections, the calculated V_3 barriers for *N*- and 4-MI···H_2O are somewhat incosistent when compared to the experimental values. It should be noted that these methods calculate an equilibrium structure whilst the zero-point geometry is probed by the experiment and often the two structures differ from one another.

Table 7.6. Experimental (r_s) and calculated (r_e) coordinates of the H atoms in the water subunit in *N*-, 2-, 4-, and 5-MI···H_2O.

			a/ Å	b/ Å	c/ Å
N-MI···H_2O	H_{nb}	r_s	3.91722(42)[a]	–0.7145(23)	0.4670(35)
		r_e	3.9972[b]	–0.2262	0.7223
	H_b	r_s	2.77970(57)	0[c]	–0.030(52)
		r_e	2.6691	–0.1954	–0.0341
2-MI···H_2O	H_{nb}	r_s	–3.50137(45)	1.1870(13)	0.3506(45)
		r_e	–3.4265	1.0444	0.6827
	H_b	r_s	–2.06203(77)	0.8779(20)	–0.097(16)
		r_e	–2.1105	0.7120	–0.0300
4-MI···H_2O	H_{nb}	r_s	–3.46242(46)	–1.1470(14)	0.5651(29)
		r_e	–3.4750	–0.6450	0.7373
	H_b	r_s	–2.06768(74)	–0.7993(19)	0[c]
		r_e	–2.1438	–0.6345	–0.0151
5-MI···H_2O	H_{nb}	r_s	–4.08392(49)	0.6321(33)	–0.5224(40)
		r_e	–3.9921	0.6187	–0.7450
	H_b	r_s	–2.68608(56)	0.5923(33)	0.096(20)
		r_e	–2.7079	0.3405	0.0369

[a] Costain's errors in units of the last significant figures in parentheses calculated as fractional uncertainties by means of $\delta_z = 0.0015/|z|$, where $|z|$ is the absolute value of a coordinate.

[b] Calculated equilibrium r_e coordinates at the ωB97X-D/aug-cc-pVQZ level.

[c] Where imaginary results were obtained, the coordinate was set to zero.

7.6 Internal Rotation

The V_3 barriers to internal rotation in *N*-, 2-, 4-, and 5-MI were determined[12] and discussed in chapter 6. Two methods were used, PAM and IAM, with the resulting value for each isomer being dependent on the position where the CH_3 group substitutes on the imidazole ring. The PAM[27,37] is appropriate for molecules with low barriers in which the local C_3 axis of the CH_3 group is close to parallel with the *a*-inertial axis and out-of-plane contributions to Δ_0' mainly arise from the CH_3 protons. With that in mind, *N*-, 2-, 4-, and 5-MI···H_2O do not fulfill the requirements of the PAM, so the V_3 barriers will only be approached by the IAM[27] implemented in the XIAM program.[38]

XIAM allows for simultaneous fitting of both ground and first excited torsional *A*- and *E*-state transitions ($m = 0$ and $m = \pm 1$) with the IAM. For a given *A*- and *E*-state transition pair for an asymmetric top molecule, the quantum numbers J, K_{-1} and K_1 are the same for both states. The V_3 barriers at various levels of theory for *N*-, 2-, 4-, and 5-MI···H_2O are summarized in tables 7.9 and 7.10. Considering their calculated values, the *A*- and *E*-state splittings are expected to be resolvable in our experiment and varying between 100 kHz to 8 MHz. As it was seen in chapter 6, the lowest V_3 barrier typically accounts for the largest splitting whilst the highest V_3 barrier will generate *A*- and *E*-state transition pairs that are close in energy and, as such, the smallest splitting. Rotational constants A_0, B_0 and C_0 and centrifugal distortion constants D_J, D_{JK}, D_K, d_1 and d_2 found in table 7.7 are generated through least squares fitting of *A*- and *E*-state transitions of *N*-, 2-, 4-, and 5-MI···H_2O, as appropriate. Internal rotation parameters that were determined for each complex include the V_3 barrier to internal rotation and the angles (i, a), (i, b) and (i, c). It was not possible to fit the F_0 standard rotational constant for an sp^3 hybridized CH_3 top so that parameter was kept fixed to the values determined experimentally for the respective methylimidazole monomer in chapter 6.

The fitting procedure described in chapter 6 was followed here for *N*-, 2-, 4-, and 5-MI···H_2O. For the XIAM input file, the rotational constants and centrifugal distortion constants that were experimentally determined through fitting of the *A*-state transitions and are summarized in table 7.4 were used as starting points. The polar coordinates ε and δ that define the orientation of the CH_3 group with respect to each inertial axis and the V_3 barrier were based on the DFT calculated geometries at the B3LYP(D3BJ)/aug-cc-pVTZ level. The hyperfine structure induced by the presence of two N nuclei in methylimidazole was not fit as XIAM does not deal with two quadrupolar nuclei. The center frequency of

each A-state transition was selected and the F_1 and F quantum numbers were omitted from the line-lists. The appropriate E-state transitions sharing the same J, K_{-1} and K_1 quantum numbers as the respective A-state were identified for a number of transitions. As more E-state transtions were identified and progressively added to each line-list, the frequency centers were corrected after a few fit cycles, as described in chapter 6. Transitions with $|m| > 1$ were not detected and this is an outcome of effective adiabatic cooling of molecules in the supersonic expansion.

The spectroscopic parameters displayed in table 7.7 were obtained through global fits of A- and E-state transitions of N-, 2-, 4-, and 5-MI···H_2O with Watson's S-reduction.[27,39] The fitted values of the V_3 barriers are 210.611(46), 154,1193(50), 321.05(11) and 380.230(54) cm^{-1} for N-, 2-, 4-, and 5-MI···H_2O, respectively. The values of (i, a) imply that the CH_3 top is no longer closely aligned with the a-inertial axis like in their respective monomers. The (i, c) values suggest that the CH_3 is effectively in the plane defined by each imidazole ring. For 5-MI···H_2O, the (i, a), (i, b) and (i, c) angles were kept fixed to their calculated values as it was not possible to simulataneously fit the angles and the V_3. The projection of the CH_3 on each inertial axis is small and the fitted V_3 value was essentially insensitive to the value given to the polar coordinates ε and δ.

The fitted V_3 values were used to benchmark the performance of quantum chemical calculations and the percentage deviations are shown in table 7.9 and 7.10. The percentage deviations are relatively large, however, discrepancies are somewhat expected at these levels of theory especially when long range interactions cannot be accounted for with high precision. The highest level of consistency between theory and experiment is observed at the B3LYP(D3BJ)/aug-cc-pVTZ level with deviations in the range of 14-32%. The agreement between theory and experiment is generally high for N-, 2- and 5-MI···H_2O, particularly for the latter. The V_3 barrier to internal rotation in 4-MI···H_2O is significantly underestimated by all three methods. Considering the complexity of the N-, 2-, 4-, and 5-MI···H_2O arising from weak interactions and large amplitude motions, convergence of the energy of each molecular system may be hard to achieve. It should also be noted that these methods calculate the V_3 barrier starting at equilibrium geometry whereas the experimental values correspond to the zero-point. Low lying vibrations like those described for imid···H_2O are also expected to affect the barrier height, either through spatial interaction or electronic effects propagating across each aromatic system.

Table 7.7. Global fits for *A*- and *E*-state transitions of *N*-, 2-, 4-, and 5-MI···H_2O produced in XIAM.

Spectroscopic parameters	*N*-MI ···H_2O	2-MI ···H_2O	4-MI ···H_2O	5-MI ···H_2O
$\boldsymbol{A_0}$ (MHz)	5009.614(42)[a]	4234.235(14)	4083.925(11)	8439.68(56)
$\boldsymbol{B_0}$ (MHz)	1409.1474(13)	1732.53380(83)	1707.18034(71)	1167.58629(93)
$\boldsymbol{C_0}$ (MHz)	1107.5777(12)	1240.29861(72)	1214.30238(51)	1032.84575(85)
$\boldsymbol{D_J}$ (kHz)	2.2076(56)	0.4472(59)	0.0814(54)	0.3116(68)
$\boldsymbol{D_K}$ (kHz)	–	[–69.1]	–	
$\boldsymbol{D_{JK}}$ (kHz)	–20.494(74)	6.204(24)	26.686(49)	27.218(72)
$\boldsymbol{d_k}$ (kHz)	[–0.0708][b]	–	–0.3104(39)	[–0.0188]
$\boldsymbol{d_j}$ (kHz)	0.8456(76)	–0.1393(55)	–0.1544(52)	–
F_0 (GHz)	{157.9291}[c]	{157.6901}	{157.784}	{157.68}
V_3 (cm^{-1})	210.611(46)	154.1193(50)	321.05(11)	380.230(54)
$\angle(\boldsymbol{i},\boldsymbol{a})/°$	91.1034(23)	125.8477(35)	271.9571(75)	171 [f]
$\angle(\boldsymbol{i},\boldsymbol{b})/°$	12.740(43)	35.9318(40)	7.936(72)	99 [f]
$\angle(\boldsymbol{i},\boldsymbol{c})/°$	77.310(43)	87.8600(69)	82.312(72)	90 [f]
$\boldsymbol{\Delta_0'}$ (u $Å^2$)	–3.2313(10)	–3.5891(5)	–3.5909(4)	–3.415(4)
$\boldsymbol{P_{cc}}$ (u $Å^2$)	1.6156(5)	1.79457(24)	1.79546(20)	1.7073(20)
N [d]	54	44	50	48
σ (kHz) [e]	10.9	5.3	4.7	16.6

[a] Numbers in parentheses are one standard deviation in units of the last significant figure.

[b] Values in square brackets were kept fixed to the values determined in Pgopher fits in table 7.4.

[c] Values in curly brackets were kept fixed to the values determined in chapter 6 for the *N*-, 2-, 4-, and 5-MI monomers.

[d] Total number of *A*- and *E*-state transitions included in the fit.

[e] Root mean square deviation of the fit.

[f] Angles fixed to the calculated values.

7.7 Discussion

To the author's best knowledge, there are no other studies on the effect of complex formation with water on the V_3 barrier height in five- and six-membered, methylated, heteroaromatic rings. The spectra of corresponding microsolvated, unmethylated analogues[13,14,40] in water, *i.e.* oxazole···H_2O, pyridine···H_2O, pyrimidine···H_2O were mentioned in chapter 5 and used for comparisons with the imid···H_2O complex. A number of studies have explored the effect of microsolvation in non-aromatic molecules such as in acetic acid,[5] methyl glycidate,[41] methyl carbamate,[42] pyruvic acid,[43] *o*-toluic acid[44] and *p*-toluic acid,[4] to name a few. In the case of acetic acid, the V_3 barrier decreases upon progressive hydration with water whilst in methyl carbamate, the opposite trend is observed and the V_3 barrier increases. It is suggested that the barriers are influenced by the strength of the hydrogen bonds in the microsolvated networks. In *p*-toluic acid, the V_3 barrier remains essentially unchanged upon attachment of H_2O.

It is worth considering how the V_3 barrier to internal rotation in *N*-, 2-, 4-, and 5-MI is influenced by the first step of their microsolvation with H_2O. The V_3 barriers are collectively shown in table 7.8 for *N*-, 2-, 4-, and 5-MI···H_2O and their respective methylimidazole monomers. Calculated values at the B3LYP(D3BJ)/aug-cc-pVTZ level are also shown alongside the experimental values. Attachment of one H_2O molecule to 4- and 5-MI has very minimal effects on the barrier height, causing the V_3 to increase by 4 cm^{-1} and decrease by 6 cm^{-1}, respectively. More profound changes are observed upon hydration of *N*- and 2-MI where an increase of approximately 25 and 32 cm^{-1} is observed, respectively. As it has been discussed in chapter 6, steric and electronic effects may cause the barrier to internal rotation of a three-fold group in a molecule to increase or decrease.

Assuming that the H_2O subunit is positioned in a manner similar to that seen in imid···H_2O where a secondary interaction r(O···H2) is observed, we can assume that the three-fold potential in 2-MI···H_2O is hindered by similar secondary interactions between the O atom and the protons in the CH_3 group in 2-MI. In imid···H_2O, the r(O···H2) distance was calculated to be approximately 3.5 Å with DFT and was derived to be approximately 3.13(8) Å with the r_0 fit. It also follows that in 2-MI···H_2O the dihedral angles that define the orientation of the H_2O subunit are are $\angle(H_{nb} - O - H_b \cdots N3) = 180^\circ$ and $\angle(O - H_b \cdots N3 - C2) = 0^\circ$. The intermolecular distance between the O of the water and the in-plane proton r(O···H_{Me}) of the CH_3 group is calculated to be approximately 2.64 Å and the r(O···C6) distance is 3.51 Å at the ωB97X-D/aug-cc-pVQZ level. These values are

comparable to those determined for imid···H_2O and indicate that secondary interactions between the O and the CH_3 protons result in an increase in the V_3 barrier height as the CH_3 internal rotation is sterically hindered. Isotopic data with ^{18}O would likely allow for derivation of the r(O···C6) distance, however, it is highly unlikely to generate a geometry that contradicts the current assumptions and conclusions.

The V_3 barrier height increase upon hydration of *N*-MI may be due to a combination of steric and electronic effects. As it was discussed in chapter 6, the variation of the V_3 barrier height across methylimidazole isomers is correlated to the overlap between π-orbitals on C-H bonds adjacent to the CH_3 and π-like orbitals at the CH_3. If the immediate, local chemical environment around the CH_3 is symmetric like in toluene[45] and *N*-MP,[46] then a small V_6 is detected and if the symmetry is reduced, the barrier height increases. Hydration of *N*-MI is expected to further reduce the symmetry around the N-CH_3 bond. Based on the geometry assumptions made earlier for 2-MI···H_2O, secondary interactions involve the H2 on the C2 adjacent to the N-CH_3 bond. The lone pair from the non-bonding orbital on the O of water donates its electrons into the anti-bonding σ^* of H2. Propagation of electronic effects across the aromatic system is also expected to be affected by attachment of H_2O. However, the current experiment and the available computational methods are not able to provide a detailed insight into the electronic effects involved.

Following similar arguments and assumptions about the orientation of the water subunit in 4- and 5-MI···H_2O, it follows that the O atom of water is not in close proximity to the CH_3 in 4- and 5-MI and thus sterical hinderence does not directly influence internal rotation. Electronic effects caused by attachement of H_2O are also subtle considering that no secondary interactions occur around the local chemical environment around the CH_3. Considering the resonance canonicals of 4- and 5-MI, it is apparent that delocalization of charges is not concerned with the site of the C4 and C5 carbons. The resonance canonicals are displayed in figure 7.6 highlighting that 4- and 5-MI are tautomers of each other.

The performance of the computational methods described in section 7.3 was benchmarked against the experimentally determined rotational constants and their percentage deviations are summarized in tables 7.10 and 7.11. The calculated V_3 barriers were also checked against the experimentally determined ones. The highest level of consistency between the rotational constants is observed at the MP2/aug-cc-pVDZ level with deviations in the range of 0.2-2.5 %. Comparing the calculated V_3 values with the experimentally determined

ones, the highest consistency is observed at the B3LYP/aug-cc-pVTZ level with some disagreements for *N*- and 4-MI···H_2O, as described in previous paragraphs.

Table 7.8. Comparison of calculated and experimentally determined V_3 barriers for N-, 2-, 4-, and 5-MI and *N*-, 2-, 4-, and 5-MI···H_2O.

	N-MI	2-MI	4-MI	5-MI
V_3^{XIAM} (cm^{-1}) [a]	185.104(11) [b]	122.7529(38)	317.20(14)	386.001(19)
V_3^{B3LYP}(cm^{-1}) [c]	189.74	115.28	295.17	376.57
	N-MI···H_2O	2-MI···H_2O	4-MI···H_2O	5-MI···H_2O
V_3^{XIAM}(cm^{-1})	210.611(46)	154.1193(50)	321.05(11)	380.230(54)
V_3^{B3LYP}(cm^{-1})	185.01	173.38	244.18	363.61

[a] Experimental values.

[b] Numbers in parentheses are one standard deviation in units of the last significant figures.

[c] Calculated values at the B3LYP(D3BJ)/aug-cc-pVTZ level.

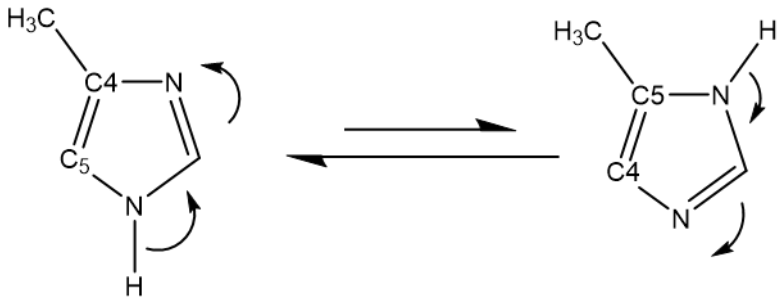

Figure 7.6. Resonance canonicals of the 4- and 5-MI tautomeric pair. Based on the calculated electric dipole moments and the relative intensity of the two molecules in the spectra, 4-MI is more abundant than 5-MI in the gas phase.

Table 7.9. Percentage deviations of calculated rotational constants and V_3 barrier heights from experimentally determined ones. Deviations calculated by means of $\frac{A_{calc}-A_{exp}}{A_{exp}} \times 100$. (Continues to table 4)

	B3LYP(D3BJ)/aug-cc-pVTZ							
	N-MI ···H_2O		2-MI ···H_2O		4-MI ···H_2O		5-MI ···H_2O	
A_e (MHz)	5754.89	12.9 %	4183.14	–1.31 %	3812.17	–7.14 %	7574.94	–11.43 %
B_e (MHz)	1313.14	–7.4 %	1769.10	2.0 %	1752.87	2.60 %	1183.73	1.37 %
C_e (MHz)	1079.70	–2.6 %	1255.94	1.2 %	1216.30	0.16 %	1033.88	0.10 %
V_3 (cm^{-1})	185.01	–13.84 %	173.38	11.11 %	244.18	–31.48 %	363.61	–4.57 %
	MP2/aug-cc-pVDZ							
	N-MI ···H_2O		2-MI ···H_2O		4-MI ···H_2O		5-MI ···H_2O	
A_e (MHz)	5034.14	0.39 %	4149.27	0.26 %	3987.81	–2.43 %	8291.84	–1.80 %
B_e (MHz)	1424.65	1.1 %	1739.08	0.31 %	1714.32	0.41 %	1164.63	–0.25 %
C_e (MHz)	1121.24	1.2 %	1243.81	0.28 %	1215.47	0.10 %	1030.84	–0.20 %
V_3 (cm^{-1})	185.58	–13.49 %	121.18	–27.18 %	241.29	–33.06 %	344.28	–10.44 %

Table 7.10. Percentage deviations of calculated rotational constants and V_3 barrier heights from experimentally determined ones. Deviations calculated by means of $\frac{A_{calc}-A_{exp}}{A_{exp}} \times 100$.

	N-MI ···H_2O		2-MI ···H_2O		4-MI ···H_2O		5-MI ···H_2O	
	ωB97X-D/aug-cc-pVQZ							
A_e (MHz)	6111.37	17.94 %	4197.93	–0.96 %	3993.46	–2.27 %	7828.8	–7.82 %
B_e (MHz)	1277.08	–10.40 %	1758.92	1.43 %	1740.95	1.93 %	1176.29	0.74 %
C_e (MHz)	1067.08	–3.77 %	1252.42	0.97 %	1230.17	1.29 %	1032.29	–0.06 %
V_3 (cm^{-1})	230.02	24.33%	223.09	28.67%	289.06	18.38%	384.68	5.80%

7.8 Conclusions

The microwave spectra of *N*-, 2-, 4-, and 5-MI···H_2O monohydrate complexes were recorded in the 7.0-18.5 GHz frequency range with CP-FTMW spectrometer at Newcastle University. The geometry of *N*-, 2-, 4-, and 5-MI···H_2O is consistent with that determined for imid···H_2O in chapter 5, meaning the pyridinic N3 nitrogen is involved in the intermolecular hydrogen bond. Alternative isomers of the monohydrates, H_2O···2-MI, H_2O···4-MI and H_2O···5-MI were not observed under the current experimental conditions. Internal rotation of the CH_3 group occurs at the timescale of the experiment and couples the overall rotation resulting in splitting of the energy levels into *A*- and *E*-states. Spectrocopic parameters including rotational, centrifugal and nuclear quadrupole coupling constants were determined through fitting of *A*-state transitions. Global fits including both *A*- and *E*-state transitions were perfomormed and internal rotation paramaters were determined. The V_3 barriers to internal rotation in these complexes vary significantly from one another and these values are dependent on the position where the CH_3 group substitutes on the imidazole ring. Attachment of H_2O on methylimidazole via a primary hydrogen bond at the N3 position does not significantly affects the V_3 in 4- and 5-MI. More profound effects are observed for *N*- and 2-MI upon H_2O attachment at the N3 position. The variation in V_3 is driven by electronic effects propagating across the aromatic system and steric factors around the immediate environment of each CH_3. The geometry of *N*-, 2-, 4-, and 5-MI···H_2O is consistent with that determined for imid···H_2O in chapter 5, meaning the pyridinic N3 nitrogen is involved in the intermolecular hydrogen bond. Alternative isomers of the monohydrates, H_2O···2-MI, H_2O···4-MI and H_2O···5-MI were not observed under the current experimental conditions.

7.9 References

1 H. Takahashi, M. Abe, T. Sugawara, K. Tanaka, Y. Saito, S. Fujimura, M. Shibuya and Y. Sato, Clotrimazole, an imidazole antimycotic, is a potent inhibitor of angiogenesis, Japanese J. Cancer Res., 1998, 89, 445–451.

2 Beena, N. Kumar, R. K. Rohilla, N. Roy and D. S. Rawat, Synthesis and antibacterial activity evaluation of metronidazole-triazole conjugates, Bioorganic Med. Chem. Lett., 2009, 19, 1396–1398.

3 S.-C. Tsay, S.-Y. Lin, W.-C. Huang, M.-H. Hsu, K. C. Hwang, C.-C. Lin, J.-C. Horng, I.-C. Chen, J. R. Hwu, F.-K. Shieh, P. Leyssen and J. Neyts, Synthesis and Structure-Activity Relationships of Imidazole-Coumarin Conjugates against Hepatitis C Virus, Molecules, 2016, 21, 228.

4 E. G. Schnitzler, N. A. Seifert, I. Kusuma and W. Jäger, Rotational Spectroscopy of p-Toluic Acid and Its 1:1 Complex with Water, J. Phys. Chem. A, 2017, 121, 8625–8631.

5 B. Ouyang and B. J. Howard, The monohydrate and dihydrate of acetic acid: A high-resolution microwave spectroscopic study, Phys. Chem. Chem. Phys., 2009, 11, 366–373.

6 A. Taleb-Bendiab, K. W. Hillig and R. L. Kuczkowski, Microwave spectrum of toluene·SO2: Structure, barrier to internal rotation, and dipole moment, J. Chem. Phys., 1993, 98, 3627–3636.

7 A. Huff, K. Leopold and C. Smith, in Proceedings of the 74th International Symposium on Molecular Spectroscopy, University of Illinois at Urbana-Champaign, Urbana, Illinois, 2019, pp. 1–1.

8 W. Caminati, J. C. López, S. Blanco, S. Mata and J. L. Alonso, How water links to cis and trans peptidic groups: the rotational spectrum of N-methylformamide–water, Phys. Chem. Chem. Phys., 2010, 12, 10230–10234.

9 S. Huber, J. Makarewicz and A. Bauder, Rotational spectra, structure and barrier to internal rotation of N-methylpyrrole and its argon complexes, Mol. Phys., 1998, 95, 1021–1043.

10 S. Wörmke, K. Brendel, U. Andresen and H. Mäder, A molecular beam Fourier transform microwave study of 2-methylpyridine and its complex with argon: Structure,

methyl internal rotation and14N nuclear quadrupole coupling, Mol. Phys., 2004, 102, 1625–1639.

11 V. Amir-Ebrahimi, A. Choplin, J. Demaison and G. Roussy, Microwave spectrum of the 13C-ring-monosubstituted toluenes and structure of toluene, J. Mol. Spectrosc., 1981, 89, 42–52.

12 E. Gougoula, C. Medcraft, J. Heitkämper and N. R. Walker, Barriers to internal rotation in methylimidazole isomers determined by rotational spectroscopy, J. Chem. Phys., 2019, 151, 144301.

13 R. B. Mackenzie, C. T. Dewberry, R. D. Cornelius, C. J. Smith and K. R. Leopold, Multidimensional large amplitude dynamics in the pyridine-water complex, J. Phys. Chem. A, 2017, 121, 855–860.

14 S. Melandri, M. E. Sanz, W. Caminati, P. G. Favero and Z. Kisiel, The Hydrogen Bond between Water and Aromatic Bases of Biological Interest: An Experimental and Theoretical Study of the 1:1 Complex of Pyrimidine with Water, J. Am. Chem. Soc., 1998, 120, 11504–11509.

15 M. J. Tubergen, A. M. Andrews and R. L. Kuczkowski, Microwave spectrum and structure of a hydrogen-bonded pyrrole-water complex, J. Phys. Chem., 1993, 97, 7451–7457.

16 W. Caminati, P. Moreschini and P. G. Favero, The Hydrogen Bond between Water and Aromatic Bases of Biological Interest: Rotational Spectrum of Pyridazine−Water, J. Phys. Chem. A, 1998, 102, 8097–8100.

17 A. Maris, S. Melandri, M. Miazzi and F. Zerbetto, Interactions of Aromatic Heterocycles with Water: The Driving Force from Free-Jet Rotational Spectroscopy and Model Electrostatic Calculations, ChemPhysChem, 2008, 9, 1303–1308.

18 W. Caminati, L. B. Favero, P. G. Favero, A. Maris and S. Melandri, Intermolecular Hydrogen Bonding between Water and Pyrazine, Angew. Chemie Int. Ed., 1998, 37, 792–795.

19 A. D. Becke, Density-functional thermochemistry. III. The role of exact exchange, J. Chem. Phys., 1993, 98, 5648–5652.

20 B. Miehlich, A. Savin, H. Stoll and H. Preuss, Results obtained with the correlation energy density functionals of becke and Lee, Yang and Parr, Chem. Phys. Lett., 1989, 157, 200–206.

21 S. Grimme, S. Ehrlich and L. Goerigk, Effect of the damping function in dispersion corrected density functional theory, J. Comput. Chem., 2011, 32, 1456–1465.

22 S. Grimme and M. Steinmetz, Effects of London dispersion correction in density functional theory on the structures of organic molecules in the gas phase, Phys. Chem. Chem. Phys., 2013, 15, 16031–16042.

23 T. Hashimoto, K. Hirao and H. Tatewaki, Comment on Dunning's correlation-consistent basis sets, Chem. Phys. Lett., 1995, 243, 190–192.

24 R. A. Kendall, T. H. Dunning and R. J. Harrison, Electron affinities of the first-row atoms revisited. Systematic basis sets and wave functions, J. Chem. Phys., 1992, 96, 6796–6806.

25 L. H. Coudert and J. T. Hougen, Analysis of the microwave and far infrared spectrum of the water dimer, J. Mol. Spectrosc., 1990, 139, 259–277.

26 J. K. G. Watson, Determination of centrifugal distortion coefficients of asymmetric-top molecules. III. Sextic coefficients, J. Chem. Phys., 1968, 48, 4517–4524.

27 W. Gordy and R. L. Cook, Microwave molecular spectra, John Wiley & Sons, Ltd, New York, 3rd., 1984.

28 C. Western, PGOPHER, a program for rotational, vibrational and electronic spectra, J. Quant. Spectrosc. Radiat. Transf., 2015, 186, 221–242.

29 E. Gougoula, D. J. Cole and N. R. Walker, Bifunctional Hydrogen Bonding of Imidazole with Water Explored by Rotational Spectroscopy and DFT Calculations, J. Phys. Chem. A, 2020, 124, 2649–2659.

30 Q. Gou, L. Spada, M. Vallejo-Lopez, S. Melandri, A. Lesarri, E. J. Cocinero and W. Caminati, Intermolecular Hydrogen Bonding in 2-Fluoropyridine-Water, ChemistrySelect, 2016, 1, 1273–1277.

31 J. Kraitchman, Determination of Molecular Structure from Microwave Spectroscopic Data, Am. J. Phys., 1953, 21, 17–24.

32 C. C. Costain, Determination of molecular structures from ground state rotational constants, J. Chem. Phys., 1958, 29, 864–874.

33 C. C. Costain, Further comments on the accuracy of rs substitution structures., Trans. Am. Crystallogr. Assoc., 1966, 2, 157–61, discussion 161-4.

34 A. R. Ubbelohde and K. J. Gallagher, Acid-base effects in hydrogen bonds in crystals, Acta Crystallogr., 1955, 8, 71–83.

35 L. Goerigk and S. Grimme, A thorough benchmark of density functional methods for general main group thermochemistry, kinetics, and noncovalent interactions, Phys. Chem. Chem. Phys., 2011, 13, 6670–6688.

36 S. Oswald and M. A. Suhm, Soft experimental constraints for soft interactions: a spectroscopic benchmark data set for weak and strong hydrogen bonds, Phys. Chem. Chem. Phys., 2019, 21, 18799–18810.

37 J. U. Grabow, H. Hartwig, N. Heineking, W. Jäger, H. Mäder, H. W. Nicolaisen and W. Stahl, The microwave spectrum of 2-methylthiazole: Methyl internal rotation and 14N nuclear quadrupole coupling, J. Mol. Struct., 2002, 612, 349–356.

38 H. Hartwig and H. Dreizler, Zeitschrift fur Naturforsch. - Sect. A J. Phys. Sci., 1996, 51, 923–932.

39 J. K. G. Watson, Determination of Centrifugal Distortion Coefficients of Asymmetric-Top Molecules, J. Chem. Phys., 1967, 46, 1935–1949.

40 S. McGlone, P. Moreschini, T. K. Ha and A. Bauder, Microwave spectra and structure of an isoxazole-water complex, Mol. Phys., 2001, 99, 1353–1364.

41 J. T. A. Gall, J. Thomas, F. Xie, Z. Wang, W. Jäger and Y. Xu, Rotational spectroscopy of the methyl glycidate–water complex: conformation and water and methyl rotor tunnelling motions, Phys. Chem. Chem. Phys., 2017, 19, 29508–29515.

42 P. Pinacho Morante, Universidad de Valladolid, 2018.

43 E. G. Schnitzler, N. A. Seifert, S. Ghosh, J. Thomas, Y. Xu and W. Jäger, Hydration of the simplest α-keto acid: a rotational spectroscopic and ab initio study of the pyruvic acid–water complex, Phys. Chem. Chem. Phys., 2017, 19, 4440–4446.

44 E. G. Schnitzler, B. L. M. Zenchyzen and W. Jäger, Rotational spectroscopy of the atmospheric photo-oxidation product o-toluic acid and its monohydrate, Phys. Chem. Chem. Phys., 2016, 18, 448–457.

45 J. Susskind, Microwave spectrum, barrier to internal rotation, and torsion-vibration interaction in ortho-fluoro toluene, J. Chem. Phys., 1970, 53, 2492–2501.

46 J. Makarewicz, S. Huber, B. Brupbacher-Gatehouse and A. Bauder, Internal rotation dependent quadrupole hyperfine splittings of rotational transitions of N-methylpyrrole, J. Mol. Struct., 2002, 612, 117–123.

Chapter 8. Overview, Conclusions and Future Work

The CP-FTMW spectrometer at Newcastle University was used to record the microwave spectra of phosphine carboxamide and phosphine carboxaminde-argon (chapter 4), two isomers of a complex between imidazole and water (chapter 5), isomers of methylimidazole (chapter 6) and microsolvated methylimidazole complexes with water (chapter 7) in the 7.0-18.5 GHz frequency range. This work focuses on probing weak intermolecular interactions and internal motions in molecules and complexes by means of gas phase microwave spectroscopy. The species of interest are generated through supersonic gas expansion in conjunction with laser ablation methods.

In chapter 4, the spectrum of phosphine carboxamide (PCA), a phosphorus-bearing analogue of urea, was recorded for the first time with MW spectroscopy. The molecule was synthesized in the group of Prof Jose M. Goichoechea at Oxford University.[1] Despite it being a primary phosphine, which are typically known for being hard to handle, it was stable at room temperature. Laser ablation was used to vaporize PCA from a solid target prior to in interaction with MW chirped pulses. Detection of ^{13}C and ^{15}N isotopologues of PCA in their natural isotopic abundance allowed for determination of the atomic coordinates of C and N, which are in good agreement with the previously determined crystal structure and DFT calculations. The H atoms at the PH_2 site adopt a steeply pyramidal arrangement both in the crystal and gas phase PCA. The NH_2 site configuration is consistent with that observed for urea at the zero point.[2,3] Recording the spectra of deuterated isotopologues of PCA would give a more accurate insight into the PH_2 and NH_2 sites. Experiments with ^{18}O-PCA are likely to be to be harder but would allow to experimentally measure the carbonyl length. Attachment of an Ar atom onto PCA follows the broad trend that has been observed for various van der Waals complexes between an organic molecule and Ar; the Ar atom coordinates at the point where the electronic on the organic molecule is concentrated.

Two isomers of a complex between imidazole and water[4] (imid···H_2O and H_2O···imid) were discussed in chapter 5. Imidazole has two chemically distinct nitrogen atoms, pyrrolic (N1) and pyridinic (N3), which can act either as a proton donor or a proton acceptor, respectively. A hydrogen bond is formed between the nitrogen atoms of imidazole and the oxygen or hydrogen of water. Large amplitude internal motions associated with the water subunit were detected in the spectra of the H_2O···imid complex. The intermolecular hydrogen bond in imid···H_2O is non-linear as an outcome of secondary long-range interactions at the O atom. In H_2O···imid, the intermolecular hydrogen also slightly

deviates from linearity as the chemical environment around the $N-H\cdots O$ bond is not symmetric.

The barriers to internal rotation of the CH_3 groups in methylimidazole isomers[5] were determined and discussed in chapter 6. To the author's best knowledge this is the first comparative study of their V_3 barriers and the first time their spectra are reported in the 7.0-18.5 GHz frequency range. A correlation between the height of the barrier and the position where the CH_3 group substitutes on the ring was observed. The trend agrees with previous studies of methylthiazole and methyloxazole isomers where two heteroatoms are present in the ring and separated by a C atom. Consistently, the lowest and highest barriers are observed for each 2-methyl- and 5-methyl-analogues, respectively. The variation in the barrier arises from a combination of steric and electronic effects.

Complexes between methylimidazole isomers and water were reported in chapter 7. The scope of that chapter explored the effect of microsolvation on the V_3 barrier height of each methylimidazole isomer. Internal rotation if further hindered upon complex formation of *N*- and 2-methylimidazole with water while for 4- and 5-methylimidazole only subtle changes are observed. The increase in the barrier of the former two isomers was rationalized in terms of steric and electronic effects around the CH_3 environment. It appears that attachment of one water molecule preserves the general barrier height trend which is dependent on the position where the CH_3 group substitutes on the ring; 2-methylimidazole$\cdots H_2O$ exhibits the lowest barrier and 5-methylimidazole$\cdots H_2O$ the lowest barrier.

In previous works, the Newcastle group has reported the benefits of using copper or silver iodide[6–8] as a binder in conjunction with an organic precursor for formation of rods to be used with laser ablation. In this work, the use of new binding materials was explored. Zinc powder was used with PCA as a more affordable alternative to copper and silver iodide. Given that copper powder may ignite and considering the potential risk of releasing PH_3 whilst handling PCA, zinc was deemed as a safer alternative for that experiment. It is worth exploring the effect that copper may have on the signal intensity of PCA and whether it prompts formation of more fragmentation products by acting as a catalyst during laser ablation. However, for that matter, more PCA need to be synthesized and transported to Newcastle University which has not been possible during the pandemic. In chapter 6, it was also reported that $MgSO_4$ can be mixed with copper and hygroscopic organic substances or substances with low melting points prior to rod formation, *i.e.* 4(5)-

methylimidazole. $MgSO_4$ combined with copper powder was also used for various experiments which are not reported here and successfully allowed us to measure their spectra, *i.e.* pyrazole, serinol, *N*,*N*'-dimethylserinol which are all hygroscopic.

It is worth exploring the formation higher microsolvated clusters of methylimidazole isomers and rationalize the effect on the barrier height. It is also important to establish which intermolecular interactions are fundamental and drive the shape of each microsolvated cluster. Across the different methylimidazole isomers, different positions are available for hydrogen bonding of the type $C-H\cdots O$ and as such the shape of the microsolavated clusters is expected to vary. Hydrogen bond cooperativity has been observed in water clusters $[(H_2O)_n,\ n = 2,3,\ldots,10]$.[9–16] A key point about future studies would be whether the water molecules in the microsolvated cluster maintain the arrangement observed in the free-water clusters. It also important to determine the highest microsolvated methylimidazole cluster that can be detected with MW spectroscopy.

8.1 References

1 A. R. Jupp and J. M. Goicoechea, Phosphinecarboxamide: A Phosphorus-Containing Analogue of Urea and Stable Primary Phosphine, *J. Am. Chem. Soc.*, 2013, **135**, 19131–19134.

2 S. Kassi, D. Petitprez and G. Wlodarczak, Microwave spectrum of isotopic species of urea $(NH_2)_2CO$, *J. Mol. Spectrosc.*, 2004, **228**, 293–297.

3 P. D. Godfrey, R. D. Brown and A. N. Hunter, The shape of urea, *J. Mol. Struct.*, 1997, **413–414**, 405–414.

4 E. Gougoula, D. J. Cole and N. R. Walker, Bifunctional Hydrogen Bonding of Imidazole with Water Explored by Rotational Spectroscopy and DFT Calculations, *J. Phys. Chem. A*, 2020, **124**, 2649–2659.

5 E. Gougoula, C. Medcraft, J. Heitkämper and N. R. Walker, Barriers to internal rotation in methylimidazole isomers determined by rotational spectroscopy, *J. Chem. Phys.*, 2019, **151**, 144301.

6 C. Medcraft, E. Gougoula, D. M. Bittner, J. C. Mullaney, S. Blanco, D. P. Tew, N. R. Walker and A. C. Legon, Molecular geometries and other properties of H2O···AgI and H3N···AgI as characterised by rotational spectroscopy and ab initio calculations, *J. Chem. Phys.*, 2017, **147**, DOI:10.1063/1.5008744.

7 J. C. Mullaney, D. P. Zaleski, D. P. Tew, N. R. Walker and A. C. Legon, Geometry of an Isolated Dimer of Imidazole Characterised by Rotational Spectroscopy and Ab Initio Calculations, *ChemPhysChem*, 2016, **17**, 1154–1158.

8 C. Medcraft, J. C. Mullaney, N. R. Walker and A. C. Legon, A complex Ar···AgI produced by laser ablation and characterised by rotational spectroscopy and *ab initio* calculations: Variation of properties along the series Ar···AgX (X=F, Cl, Br and I), J. *Mol. Spectrosc.*, 2017, **335**, 61–67.

9 L. H. Coudert, F. J. Lovas, R. D. Suenram and J. T. Hougen, New measurements of microwave transitions in the water dimer, *J. Chem. Phys.*, 1987, **87**, 6290–6299.

10 M. R. Viant, J. D. Cruzan, D. D. Lucas, M. G. Brown, K. Liu and R. J. Saykally, Pseudorotation in Water Trimer Isotopomers Using Terahertz Laser Spectroscopy, *J. Phys. Chem. A*, 1997, **101**, 9032–9041.

11 J. D. Cruzan, M. R. Viant, M. G. Brown and R. J. Saykally, Terahertz Laser Vibration−Rotation Tunneling Spectroscopy of the Water Tetramer, *J. Phys. Chem. A*, 1997, **101**, 9022–9031.

12 K. Liu, M. G. Brown, J. D. Cruzan and R. J. Saykally, Terahertz Laser Spectroscopy of the Water Pentamer: Structure and Hydrogen Bond Rearrangement Dynamics, *J. Phys. Chem. A*, 1997, **101**, 9011–9021.

13 C. Pérez, M. T. Muckle, D. P. Zaleski, N. A. Seifert, B. Temelso, G. C. Shields, Z. Kisiel and B. H. Pate, Structures of cage, prism, and book isomers of water hexamer from broadband rotational spectroscopy, *Science*, 2012, **336**, 897–901.

14 J. O. Richardson, C. Pérez, S. Lobsiger, A. A. Reid, B. Temelso, G. C. Shields, Z. Kisiel, D. J. Wales, B. H. Pate and S. C. Althorpe, Concerted hydrogen-bond breaking by quantum tunneling in the water hexamer prism, *Science*., 2016, **351**, 1310 LP-1313.

15 W. T. S. Cole, J. D. Farrell, D. J. Wales and R. J. Saykally, Structure and torsional dynamics of the water octamer from THz laser spectroscopy near 215 μm, *Science*, 2016, **352**, 1194 LP-1197.

16 C. Pérez, D. P. Zaleski, N. A. Seifert, B. Temelso, G. C. Shields, Z. Kisiel and B. H. Pate, Hydrogen Bond Cooperativity and the Three-Dimensional Structures of Water Nonamers and Decamers, *Angew. Chemie Int. Ed.*, 2014, **53**, 14368–14372.

Appendix A

Complete lists of calculated and experimental (where available) atomic coordinates of the molecules and complexes discussed in this thesis may be found here. The tables are organized such that the order of molecules or complexes follows the order in which they appear in the main thesis body. Other information that cannot be embedded in the main chapters are also summarized here.

Table A1. PCA (Chapter 4), B3LYP(D3BJ)/aug-cc-pVTZ

	PCA		
	a/Å	b/Å	c/Å
O1	–1.094458	–1.167516	–0.000935
C1	–0.550289	–0.083719	0.020713
N3	–1.230127	1.093383	–0.008232
H_{N1}	–2.237238	1.063770	–0.014605
H_{N2}	–0.770800	1.976956	0.111132
P4	1.333920	0.029060	–0.063484
H_{P1}	1.529555	–0.824327	1.047635
H_{P2}	1.496605	1.224800	0.689504

Table A2. PCA···Ar (Chapter 4), B3LYP(D3BJ)/aug-cc-pVTZ

	PCA···Ar		
	a/Å	b/Å	c/Å
O1	0.843774	–1.128886	–1.182195
C1	1.077455	–0.639920	–0.096916
N3	0.905107	–1.307179	1.074269
H_{N1}	0.582815	–2.261047	1.039542
H_{N2}	1.177062	–0.916460	1.956914
P4	1.560270	1.181292	0.033603
H_{P1}	2.642825	1.058020	–0.868845
H_{P2}	2.377451	1.089091	1.194166
Ar	–2.358731	0.212435	0.016026

Table A3. Some experimentally (r_0, r_s) and calculated (r_e) structural parameters for PCA as well as some structural parameters from X-ray crystallography. Parameters for the structural analogues urea and thiourea are also summarized.

	PCA				Urea		Thiourea	
	r_s	r_0	r_e	X-ray	r_s/r_0	r_e	r_s	r_e
$r(N-C)$	1.346(23)	1.3329(15)	1.360	1.329(2)	1.3779	1.3911	1.368(3)	1.3640
$r(P-C)$	–	–	1.900	1.865(1)	–	–	–	–
$r(C-O)$	–	–	1.213	1.230(2)	1.2211	1.2179	–	–
$r(C-S)$	–	–	–	–	–	–	1.645(4)	1.6480
$r(P-H_1)$	–	–	1.4146	1.27(2)	–	–	–	–
$r(P-H_2)$	–	–	1.4224	1.30(2)	–	–	–	–
$r(N-H_1)$	–	–	1.0030	0.85(2)	0.9978	1.0099	–	1.0058
$r(N-H_2)$	–	–	1.0076	0.88(2)	1.0212	1.0100	–	1.0075
$\angle(N-C-P)$	–	117(2)°	116.50	117.3(1)	–	–	–	–
$\angle(N-C-N)$	–	–	–	–	114.71	113.11	–	–
$\angle(N-C-O)$	–	126.4(6) °	123.30	124.1(1)	122.64	123.45	–	–
$\angle(N-C-S)$	–	–	–	–	–	–	123.0(2)	123.07

Table A4. Imidazole-water (Chapter 5)

B3LYP(D3BJ) /aug-cc-pVTZ	imid···H_2O		
	a/Å	b/Å	c/Å
N1	–1.615374	0.806280	–0.019777
H1	–2.295863	1.544682	–0.048017
C2	–0.266459	0.960219	0.040607
H2	0.217182	1.921485	0.063646
N3	0.337720	–0.204622	0.060796
C4	–0.657821	–1.152979	0.010598
H4	–0.434988	–2.205138	0.010900
C5	–1.880242	–0.545453	–0.039670
H5	–2.880648	–0.933539	–0.087331
H_b	2.239001	–0.154897	–0.009942
O	3.195103	0.037564	–0.084533
H_{nb}	3.591841	–0.338637	0.705064
ωB97XD/aug-cc-pVQZ	imid···H_2O		
	a/Å	b/Å	c/Å
N1	–1.622908	–0.800110	–0.013285
H1	–2.301568	–1.537156	–0.038116
C2	–0.280639	–0.952715	0.041072
H2	0.201260	–1.915388	0.064178
N3	0.327091	0.203692	0.057305
C4	–0.664420	1.147949	0.010111
H4	–0.443213	2.200765	0.008406
C5	–1.883636	0.545509	–0.033524
H5	–2.881975	0.939680	–0.078315
H_b	2.253901	0.141020	–0.054538
O	3.203723	–0.048453	–0.124829
H_{nb}	3.584692	0.289172	0.682930

Table A5. Water-imidazole (Chapter 5)

B3LYP(D3BJ)/aug-cc-pVTZ	$H_2O\cdots$imid		
	a/Å	b/Å	c/Å
N1	–0.256587	–0.022689	–0.000509
H1	–1.268207	–0.016502	–0.000985
C2	0.559694	1.065756	–0.000144
H2	0.178600	2.073051	–0.000169
N3	1.827879	0.723135	0.000329
C4	1.834559	–0.652136	0.000255
H4	2.754350	–1.211039	0.000657
C5	0.552955	–1.133820	–0.000238
H5	0.178600	2.073051	–0.000169
H	–3.787567	0.135023	–0.766216
O	–3.224258	–0.008568	0.000097
H	–3.784036	0.130190	0.769885
ωB97XD/aug-cc-pVQZ	$H_2O\cdots$imid		
	a/Å	b/Å	c/Å
N1	–0.192148	0.081550	0.000004
H1	–1.201279	0.141483	0.000026
C2	0.536766	–1.058420	0.000019
H2	0.077839	–2.033225	0.000060
N3	1.822306	–0.820108	–0.000022
C4	1.931681	0.545367	–0.000062
H4	–1.201279	0.141483	0.000026
C5	0.696116	1.122257	–0.000047
H5	0.377954	2.148809	–0.000070
H	–3.657410	–0.200079	–0.763499
O	–3.153620	0.077918	0.000070
H	–3.657362	–0.200038	0.763686

Table A6. Calculated atomic coordinates and residuals for the alternative, experimentally determined, fitted geometries of imid···H_2O described under "Molecular Geometry". The geometry determined while assuming ∠(H_{nb}–O–H_b···N3) = 180°, ∠(O–H_b···N3–C2) = 0° leads to the parameters and coordinates displayed in Tables xx and xx. All c-coordinates are constrained to zero by the assumption that the molecule is planar.

	imid···H_2O (∠(H_{nb}–O–H_b···N3) = 180°, ∠(O–H_b···N3–C2) = 0°)			
	a/Å	da/Å	b/Å	db/Å
N1	–1.327352	0.03877	–1.007995	0.01910
H1	–1.739547	0.07363	–1.916895	0.03491
C2	0.008189	0.02808	–0.729346	0.03212
H2	0.756980	0.05787	–1.505955	0.06083
N3	0.240898	0.02150	0.563375	0.04104
C4	–1.010423	0.04401	1.150464	0.00695
H4	–1.119783	0.08512	2.222400	0.01114
C5	–1.988557	0.00756	0.200093	0.04446
H5	–3.064932	0.01016	0.267765	0.08574
O	3.150931	0.00196	–0.077040	0.00062
H_b	2.230131	0.00531	0.187332	0.02450
H_{nb}	3.635990	0.02058	0.749084	0.01376

imid···H_2O (□ (H_{nb}–O–H_b···N3) = 180°, □ (O–H_b···N3–C2) =180°)				
	a/Å	da/Å	b/Å	db/Å
N1	–1.332272	0.04004	–1.006938	0.01996
H1	0.004611	0.02924	–0.734802	0.03313
C2	0.243618	0.02205	0.556769	0.04262
H2	–1.004826	0.04561	1.149950	0.00695
N3	–1.987581	0.00806	0.204359	0.04598
C4	–1.748893	0.07606	–1.913818	0.03650
H4	0.749607	0.06022	–1.515053	0.06271
C5	–1.108959	0.08819	2.222407	0.01109
H5	–3.063613	0.01095	0.277276	0.08871
O	3.151083	0.00203	0.050184	0.00056
H_b	2.229504	0.00543	-0.211456	0.02547
H_{nb}	3.633691	0.02135	-0.777375	0.01409

Table A7. *N*-MI (Chapter 6), B3LYP(D3BJ)/aug-cc-pVTZ

N-MI	*a*/Å	*b*/Å	*c*/Å
N1	–0.671589	–0.010546	–0.000257
C2	0.164773	1.065843	0.000059
H2	–0.208941	2.076622	–0.000491
N3	1.427750	0.708278	0.000040
C4	1.417344	–0.665138	0.000081
H4	2.329221	–1.236962	–0.000145
C5	0.129453	–1.130294	0.000008
H5	–0.282531	–2.123332	–0.000186
C6	–2.119924	0.015399	0.000135
H6	–2.453094	1.050263	–0.002045
H6	–2.514527	–0.480577	–0.886250
H6	–2.514275	–0.476812	0.888769

Table A8. *N*-MI (Chapter 6), B3LYP(D3BJ)/cc-pVTZ

N-MI	*a*/Å	*b*/Å	*c*/Å
N1	–0.671716	–0.010801	–0.000259
C2	0.165565	1.065244	0.000142
H2	–0.208824	2.075956	–0.000233
N3	1.428222	0.708301	0.000038
C4	1.416403	–0.665106	–0.000078
H4	2.328243	–1.237354	–0.000319
C5	0.129042	–1.130662	0.000150
H5	–0.283701	–2.123456	0.000343
C6	–2.119452	0.016375	0.000045
H6	–2.452444	1.051497	–0.001406
H6	–2.515673	–0.478611	–0.886406
H6	–2.515513	–0.476082	0.888006

Table A9. *N*-MI (Chapter 6), B3LYP(D3BJ)/Def2-TZVP

N-MI	a/Å	b/Å	c/Å
N1	–0.671580	–0.010651	–0.000350
C2	0.165044	1.065510	0.000129
H2	–0.208776	2.077409	–0.000328
N3	1.427498	0.708010	0.000067
C4	1.416946	–0.664774	–0.000048
H4	2.329613	–1.237322	–0.000232
C5	0.129039	–1.130336	0.000125
H5	–0.283438	–2.124228	0.000315
C6	–2.119070	0.015762	0.000107
H6	–2.452585	1.051614	–0.001897
H6	–2.514816	–0.480400	–0.886989
H6	–2.514511	–0.476887	0.889334

Table A10. 2-MI (Chapter 6), B3LYP(D3BJ)/aug-cc-pVTZ

2-MI	a/Å	b/Å	c/Å
N1	0.131449	–1.069486	–0.000246
H1	–0.187075	–2.022056	0.000731
C2	–0.659470	0.045650	–0.000267
N3	0.079149	1.132386	–0.000138
C4	1.389822	0.708437	0.000168
H4	2.207784	1.407596	0.000088
C5	1.447651	–0.655045	0.000191
H5	2.268020	–1.349010	0.000022
C6	–2.146268	–0.005266	0.000201
H6	–2.532377	–0.527768	–0.877458
H6	–2.532391	–0.511186	0.887578
H6	–2.527935	1.011894	–0.009134

Table A11. 2-MI (Chapter 6), B3LYP(D3BJ)/cc-pVTZ

2-MI	a/Å	b/Å	c/Å
N1	0.132006	–1.069709	–0.000250
H1	–0.186108	–2.022520	0.000665
C2	–0.658611	0.045462	–0.000278
N3	0.078490	1.133078	–0.000147
C4	1.388509	0.708635	0.000181
H4	2.206618	1.407943	0.000055
C5	1.447504	–0.654875	0.000201
H5	2.268336	–1.348418	0.000050
C6	–2.145654	–0.005896	0.000213
H6	–2.526469	1.011601	–0.010825
H6	–2.532471	–0.529918	–0.876508
H6	2.532635	–0.510393	0.888310

Table A12. 2-MI (Chapter 6), B3LYP(D3BJ)/Def2-TZVP

2-MI	a/Å	b/Å	c/Å
N1	0.131648	–1.069531	–0.000302
H1	–0.186776	–2.023007	0.000390
C2	–0.658666	0.045679	–0.000304
N3	0.078912	1.132745	–0.000213
C4	1.388741	0.708580	0.000197
H4	2.207303	1.408626	0.000217
C5	1.447159	–0.655132	0.000257
H5	2.268458	–1.349578	0.000197
C6	–2.145571	–0.005609	0.000271
H6	–2.527224	1.012570	–0.008665
H6	–2.532290	–0.528198	–0.878396
H6	–2.532082	–0.512237	0.888387

Table A13. 4-MI (Chapter 6), B3LYP(D3BJ)/aug-cc-pVTZ

4-MI	a/Å	b/Å	c/Å
N1	1.422668	–0.604647	0.000132
H1	2.278863	–1.129297	–0.000699
C2	1.303572	0.750978	–0.000095
H2	2.156988	1.407971	0.000231
N3	0.045917	1.119184	0.000021
C4	–0.696509	–0.044770	–0.000031
C5	0.144606	–1.125349	–0.000020
H5	–0.042055	–2.183755	–0.000015
C6	–2.185769	–0.019663	0.000019
H6	–2.594856	–1.029204	–0.001738
H6	–2.564317	0.503578	0.879385
H6	–2.564072	0.506298	–0.877793

Table A14. 4-MI (Chapter 6), B3LYP(D3BJ)/cc-pVTZ

4-MI	a/Å	b/Å	c/Å
N1	1.422640	–0.604419	0.000246
H1	2.278803	–1.129241	–0.000810
C2	1.302572	0.750890	–0.000068
H2	2.156133	1.408001	0.000386
N3	0.045161	1.119848	–0.000066
C4	–0.695608	–0.044562	–0.000069
C5	0.145180	–1.125402	–0.000153
H5	–0.041518	–2.183834	0.000017
C6	–2.185281	–0.020537	0.000090
H6	–2.594442	–1.030212	–0.002411
H6	–2.564520	0.501992	0.501992
H6	–2.564470	0.506126	–0.877099

Table A15. 4-MI (Chapter 6), B3LYP(D3BJ)/Def2-TZVP

4-MI	a/Å	b/Å	c/Å
N1	1.422527	–0.604166	0.000059
H1	2.279163	–1.129527	–0.000338
C2	1.302864	0.750952	–0.000104
H2	2.156847	1.409092	0.000058
N3	0.045349	1.119059	0.000069
C4	–0.696080	–0.044412	–0.000006
C5	0.145375	–1.125355	0.000029
H5	–0.041358	–2.184773	–0.000037
C6	–2.185471	–0.020159	–0.000012
H6	–2.594045	–1.031030	–0.000857
H6	–2.564950	0.503925	0.879647
H6	–2.564637	0.505002	–0.879144

Table A16. 5-MI (Chapter 6), B3LYP(D3BJ)/aug-cc-pVTZ

5-MI	a/Å	b/Å	c/Å
N1	–0.085541	–1.055933	–0.000258
H1	0.240684	–2.006276	0.001134
C2	–1.389786	–0.648393	0.000137
H2	–2.213010	–1.342822	–0.000013
N3	–1.478914	0.656782	0.000271
C4	–0.179216	1.115247	–0.000172
H4	0.046878	2.168033	–0.000131
C5	0.708947	0.073143	–0.000510
C6	2.194976	0.020924	0.000303
H6	2.584868	–0.490467	0.883702
H6	2.586135	–0.493480	–0.880801
H6	2.596860	1.032181	–0.001206

Table A17. 5-MI (Chapter 6), B3LYP(D3BJ)/cc-pVTZ

5-MI	a/Å	b/Å	c/Å
N1	–0.084959	–1.056188	–0.000428
H1	0.242420	–2.006225	0.001548
C2	–1.388716	–0.648637	0.000284
H2	–2.211627	–1.343694	0.000129
N3	–1.479597	0.656697	0.000256
C4	–0.180308	1.114604	–0.000191
H4	0.045975	2.167506	–0.000080
C5	0.708751	0.073209	–0.000585
C6	2.194955	0.021959	0.000355
H6	2.596844	1.033320	0.000595
H6	2.585605	–0.490642	0.882960
H6	2.587455	–0.490944	–0.881132

Table A18. 5-MI (Chapter 6), B3LYP(D3BJ)/Def2-TZVP

5-MI	a/Å	b/Å	c/Å
N1	–0.085141	–1.055727	–0.000285
H1	0.242194	–2.006535	0.001425
C2	–1.388927	–0.648654	0.000132
H2	–2.212946	–1.343926	–0.000097
N3	–1.478849	0.656354	0.000306
C4	–0.180429	1.115091	–0.000173
H4	0.045781	2.168924	–0.000224
C5	0.708738	0.073166	–0.000547
C6	2.194836	0.021422	0.000326
H6	2.596618	1.033744	–0.000752
H6	2.585706	–0.490500	0.884292
H6	2.586974	–0.492715	–0.881824

Table A19. *N*-MI···H_2O (Chapter 7), B3LYP(D3BJ)/aug-cc-pVTZ

N-MI···H_2O	a/Å	b/Å	c/Å
N1	–1.330478	0.255040	–0.000158
C2	–0.043393	0.686423	–0.052153
H2	0.218220	1.730760	–0.082357
N3	0.804207	–0.318391	–0.054274
C4	0.037076	–1.455940	–0.000861
H4	0.479275	–2.436560	0.012755
C5	–1.288805	–1.121664	0.032639
H5	–2.183253	–1.715961	0.076763
C6	–2.521220	1.082404	0.020034
H6	–2.223673	2.127296	–0.009033
H6	–3.148722	0.871611	–0.845055
H6	–3.094074	0.905843	0.929499
O	3.532356	0.543698	0.085819
H_b	2.639465	0.148974	0.012775
H_{nb}	4.004428	0.249346	–0.697002

Table A20. *N*-MI···H_2O (Chapter 7), ωB97XD/aug-cc-pVQZ

N-MI···H_2O	a/Å	b/Å	c/Å
N1	–1.357174	–0.231787	0.008588
C2	–0.099160	–0.721263	0.062897
H2	0.107524	–1.778352	0.101293
N3	0.796658	0.232451	0.061732
C4	0.087957	1.400243	0.001122
H4	0.576279	2.358912	–0.015310
C5	–1.247427	1.133689	–0.033036
H5	–2.110130	1.773649	–0.079802
C6	–2.581119	–0.998193	–0.035331
H6	–2.347795	–2.048243	0.119485
H6	–3.260370	–0.673033	0.750364
H6	–3.070516	–0.885539	–1.001446
O	3.588113	–0.506146	–0.093761
H_b	2.669123	–0.195381	–0.034050
H_{nb}	3.997168	–0.226173	0.722259

Table A21. *N*-MI···H_2O (Chapter 7), MP2/aug-cc-pVDZ

N-MI···H_2O	a/Å	b/Å	c/Å
N1	–1.250018	0.313323	–0.002740
C2	0.083145	0.568578	–0.053451
H2	0.485217	1.568292	–0.086878
N3	0.795493	–0.551020	–0.049914
C4	–0.123051	–1.565507	0.005593
H4	0.174734	–2.599887	0.022576
C5	–1.400976	–1.048537	0.035326
H5	–2.371202	–1.512340	0.079258
C6	–2.313094	1.299515	0.013147
H6	–1.866313	2.289075	–0.027705
H6	–2.963131	1.166356	–0.848892
H6	–2.896086	1.209756	0.927172
O	3.394397	0.612111	0.080198
H_b	2.610614	0.032603	0.017017
H_{nb}	3.967917	0.316053	–0.631072

Table A22. 2-MI···H_2O (Chapter 7), B3LYP(D3BJ)/aug-cc-pVTZ

2-MI···H_2O	a/Å	b/Å	c/Å
N1	1.603938	–0.647532	–0.015257
H1	2.190785	–1.462578	–0.033754
C2	0.240795	–0.647284	0.012197
N3	–0.206695	0.591265	0.028442
C4	0.898245	1.413602	0.009686
H4	0.804606	2.485060	0.015127
C5	2.036041	0.663316	–0.017158
H5	3.077609	0.925265	–0.037233
C6	–0.588906	–1.881515	0.015798
H6	–1.638034	–1.600982	0.062643
H6	–0.427178	–2.470469	–0.889087
H6	–0.356450	–2.514454	0.874356
O	–3.045496	0.564008	–0.064429
H_b	–2.081383	0.736065	–0.013024
H_{nb}	–3.442650	1.113129	0.615955

Table A23. 2-MI···H_2O (Chapter 7), ωB97XD/aug-cc-pVQZ

2-MI···H_2O	a/Å	b/Å	c/Å
N1	1.610674	–0.633079	–0.001090
H1	2.201624	–1.442578	–0.005724
C2	0.254852	–0.642298	0.012642
N3	–0.207781	0.583735	0.014195
C4	0.886215	1.411753	–0.001147
H4	0.782666	2.482594	–0.005503
C5	2.027401	0.675993	–0.010290
H5	3.066282	0.949231	–0.020542
C6	–0.560578	–1.885871	0.004610
H6	–1.606181	–1.625183	0.146866
H6	–0.463607	–2.409208	–0.947316
H6	–0.254048	–2.566814	0.798947
O	–3.070668	0.553547	–0.054869
H_b	–2.110527	0.712036	–0.029976
H_{nb}	–3.426471	1.044396	0.682725

Table A24. 2-MI···H_2O (Chapter 7), MP2/aug-cc-pVDZ

2-MI···H_2O	a/Å	b/Å	c/Å
N1	1.583337	0.702515	–0.000029
H1	2.129130	1.556638	–0.000077
C2	0.211056	0.634247	–0.000280
N3	–0.182056	–0.646256	–0.000268
C4	0.973370	–1.407665	0.000074
H4	0.943939	–2.494831	0.000139
C5	2.091470	–0.583319	0.000218
H5	3.158128	–0.791355	0.000293
C6	–0.684241	1.834555	0.000046
H6	–1.728081	1.493961	–0.004419
H6	–0.519442	2.454772	0.895935
H6	–0.513264	2.459848	–0.891142
O	–3.037817	–0.563371	0.000392
H_b	–1.728081	1.493961	–0.004419
H_{nb}	–2.084434	–0.800073	0.000555

Table A25. 4-MI···H_2O (Chapter 7), B3LYP(D3BJ)/aug-cc-pVTZ

4-MI···H_2O	a/Å	b/Å	c/Å
N1	1.870120	–0.868293	–0.043074
H1	2.728321	–1.387301	–0.095133
C2	0.621837	–1.389741	0.057352
H2	0.428439	–2.448118	0.092281
N3	–0.281032	–0.438458	0.096908
C4	0.401381	0.759759	0.017047
C5	1.743010	0.506274	–0.070759
H5	2.593341	1.158247	–0.149572
C6	–0.313427	2.065786	0.031183
H6	0.382815	2.892382	–0.101688
H6	–1.058570	2.105091	–0.763686
H6	–0.842013	2.209794	0.974676
O	–3.140825	–0.527326	–0.118771
H_b	–2.168511	–0.535988	–0.003616
H_{nb}	–3.501102	–0.592596	0.769095

Table A26. 4-MI···H_2O (Chapter 7), ωB97XD/aug-cc-pVQZ

4-MI···H_2O	a/Å	b/Å	c/Å
N1	1.941139	–0.739671	–0.061845
H1	2.838440	–1.180048	–0.130529
C2	0.753656	–1.365743	0.074275
H2	0.659562	–2.437288	0.124620
N3	–0.229594	–0.507434	0.130291
C4	0.338700	0.740064	0.023908
C5	1.689477	0.610459	–0.096659
H5	2.471627	1.339865	–0.201342
C6	–0.489483	1.976621	0.049423
H6	0.122770	0.122770	–0.136110
H6	–1.273002	1.926754	–0.705396
H6	–0.978062	2.094295	1.016643
O	–3.106219	–0.588991	–0.141629
H_b	–2.143797	–0.634498	–0.015075
H_{nb}	–3.475006	–0.644980	0.737299

Table A27. ωB97XD/aug-cc-pVQZ, MP2/aug-cc-pVDZ

4-MI···H_2O	a/Å	b/Å	c/Å
N1	1.988208	–0.690030	–0.056537
H1	2.912514	–1.100527	–0.119247
C2	0.810711	–1.377742	0.063179
H2	0.760377	–2.462908	0.102556
N3	–0.226208	–0.537975	0.115235
C4	0.304233	0.740378	0.023893
C5	1.690341	0.660192	–0.084282
H5	2.458685	1.423500	–0.176448
C6	–0.572166	1.957151	0.048599
H6	0.028469	2.866755	–0.101313
H6	–1.33614	1.899056	–0.741455
H6	–1.097720	2.039333	1.012754
O	–3.099972	–0.608227	–0.133924
H_b	–2.130426	–0.677558	–0.004234
H_{nb}	–3.468150	–0.847570	0.725421

Table A28. 5-MI···H_2O (Chapter 7), B3LYP(D3BJ)/aug-cc-pVTZ

5-MI···H_2O	a/Å	b/Å	c/Å
N1	1.023574	–1.102553	0.012058
H1	1.616286	–1.913179	0.049428
C2	–0.337382	–1.106472	–0.034833
H2	–0.924631	–2.008638	–0.035864
N3	–0.805450	0.116508	–0.071624
C4	0.295138	0.945315	–0.046934
H4	0.194861	2.016657	–0.064656
C5	1.448845	0.211931	0.005242
C6	2.882872	0.601370	0.050214
H6	2.968267	1.685872	0.035712
H6	3.373556	0.240634	0.956981
H6	3.437205	0.211716	–0.806557
O	–3.659745	0.296181	0.106923
H_b	–2.685398	0.326215	0.015165
H_{nb}	–4.002053	0.675593	–0.706235

Table A29. 5-MI···H_2O (Chapter 7), ωB97XD/aug-cc-pVQZ

5-MI···H_2O	a/Å	b/Å	c/Å
N1	1.002383	–1.098151	0.004024
H1	1.573438	–1.921990	0.025376
C2	–0.351629	–1.067247	–0.024578
H2	–0.960065	–1.956016	–0.026559
N3	–0.794369	0.159067	–0.043840
C4	0.322208	0.957079	–0.026096
H4	0.247986	2.031079	–0.033202
C5	1.454364	0.200042	0.003646
C6	2.897329	0.555415	0.031836
H6	3.008467	1.637052	0.033872
H6	3.389340	0.166990	0.924735
H6	3.424462	0.166183	–0.840477
O	–3.675852	0.269815	0.085592
H_b	–2.707901	0.340493	0.036971
H_{nb}	–3.675852	0.269815	0.085592

Table A30. 5-MI···H_2O (Chapter 7), MP2/aug-cc-pVDZ

5-MI···H_2O	a/Å	b/Å	c/Å
N1	0.891780	–1.101082	–0.003291
H1	1.378247	–1.990552	0.015246
C2	–0.469382	–0.934760	–0.036241
H2	–1.174721	–1.762384	–0.044557
N3	–0.788922	0.361634	–0.049753
C4	0.417476	1.038700	–0.024055
H4	0.462654	2.125964	–0.026239
C5	1.488538	0.148975	0.005180
C6	2.971745	0.354561	0.040838
H6	3.186265	1.432730	0.040644
H6	3.421345	–0.080881	0.948322
H6	3.466050	–0.090285	–0.838407
O	–3.647949	0.153675	0.092743
H_b	–2.707391	0.421925	0.029209
H_{nb}	–4.055775	0.545579	–0.689097

Table A31. $H_2O\cdots$2-MI (Chapter 8), B3LYP(D3BJ)/aug-cc-pVTZ

$H_2O\cdots$2-MI	a/Å	b/Å	c/Å
N1	-0.249934	-0.389696	-0.000700
H1	-1.260937	-0.391259	-0.000841
C2	0.554366	0.712140	-0.000035
N3	1.824479	0.365086	0.000514
C4	1.841629	-1.011629	0.000257
H4	2.765552	-1.563714	0.000577
C5	0.565636	-1.500189	-0.000481
H5	0.171544	-2.500093	-0.000931
C6	0.030945	2.105394	0.000014
H6	0.872259	2.793120	0.000303
H6	-0.582389	2.305104	0.880993
H6	-0.581956	2.305349	-0.881215
H	-3.798818	-0.451262	-0.768112
O	-3.232170	-0.335771	0.000462
H	-3.797733	-0.466479	0.767398

Table A32. $H_2O\cdots$4-MI (Chapter 8), B3LYP(D3BJ)/aug-cc-pVTZ

$H_2O\cdots$4-MI	a/Å	b/Å	c/Å
N1	-0.728193	0.059688	-0.002902
H1	-1.726551	-0.101213	-0.003310
C2	-0.104116	1.265813	-0.000782
H2	-0.645484	2.197070	-0.000578
N3	1.203090	1.136900	0.001145
C4	1.449154	-0.220294	0.000323
C5	0.259202	-0.901207	-0.002082
H5	0.033063	-1.952113	-0.003695
C6	2.836819	-0.762924	0.001703
H6	2.830888	-1.852476	0.002782
H6	3.388220	-0.423712	-0.876849
H6	3.387123	-0.421919	0.880229
H	-4.244585	-0.282076	-0.763403
O	-3.671119	-0.387117	0.001692
H	-4.236673	-0.279836	0.772355

Table A33. H_2O···5-MI (Chapter 8), B3LYP(D3BJ)/aug-cc-pVTZ

H_2O···5-MI	a/Å	b/Å	c/Å
N1	-0.249815	0.341360	-0.003985
H1	-1.261402	0.345219	-0.005836
C2	0.562048	1.437082	-0.002162
H2	0.174823	2.442265	-0.003785
N3	1.829064	1.100229	0.001968
C4	1.837627	-0.277305	0.003015
H4	2.758532	-0.835867	0.006099
C5	0.559922	-0.773858	-0.000491
C6	0.026559	-2.162451	-0.001000
H6	0.851170	-2.872893	0.003830
H6	-0.583927	-2.364095	-0.884329
H6	-0.591992	-2.361593	0.877260
H	-3.774813	0.576355	-0.761188
O	-3.232776	0.354250	0.001874
H	-3.764169	0.571328	0.773826

Table A34. Diagonalized nuclear quadrupole coupling components χ_{xx}, χ_{yy} and χ_{zz} for *N*-, 2-, 4-, and 5-MI···H_2O.

	N-MI ···H_2O	2-MI ···H_2O	4-MI ···H_2O	5-MI ···H_2O	Imid···H_2O
χ_{xx}(N1) (MHz)	0.921(95)	1.178(27)	1.07(11)	1.744(75)	1.096(27)
χ_{yy}(N1) (MHz)	1.656(97)	1.496(50)	2.235(96)	1.48(12)	1.332(54)
χ_{zz}(N1) (MHz)	–2.577(29)	–2.673(25)	–2.509(28)	–3.215(79)	–2.428(30)
η	0.285(53)	0.119(21)	0.464(58)	–0.082(44)	0.097(25)
χ_{xx}(N3) (MHz)	1.837(23)	1.646(25)	1.886(32)	1.44(48)	1.23(19)
χ_{yy}(N3) (MHz)	1.775(49)	1.92(27)	1.474(70)	2.03(20)	1.980(56)
χ_{zz}(N3) (MHz)	–3.612(13)	–3.57(26)	–3.359(12)	–3.46(32)	–3.21(15)
η	–0.017(15)	0.077(76)	–0.123(23)	0.17(15)	0.234(63)

The calculation of diagonalized nuclear quadrupole coupling components χ_{xx}, χ_{yy} and χ_{zz} of N1 and N3 with QDIAG from experimentally measured values of nuclear quadrupole coupling χ_{aa}, χ_{bb} and χ_{cc} was described in previous chapters. The orientation of the nuclear axes on the individual N nuclei in the imidazole ring follows that described by Christen *et al.* for the imidazole monomer which was also followed for imid···H_2O and methylimidazole isomers. The χ_{ab} values for N1 and N3 for each complex are displayed in the tables 7.1-7.3 in chapter 7.